

Universitat Politècnica de Catalunya
Departament de Matemàtiques

PhD Thesis

**On the role of oscillatory dynamics
in neural communication**

Alberto Pérez Cervera

Advisors: Gemma Huguet and Tere M-Seara

Memòria presentada per aspirar al grau de Doctor en Matemàtiques
Programa de doctorat en Matemàtica Aplicada. Universitat Politècnica de Catalunya

Contents

Introduction	6
1 Mean field models	12
1.1 The Wilson-Cowan equations	13
1.2 Dynamical Analysis	14
1.3 Bifurcation Diagram	18
1.4 Periodic orbits Γ_{HB} and Γ_{SN}	23
2 Periodically forced oscillators beyond the weak coupling limit	26
2.1 The stroboscopic map	28
2.2 Bifurcation Analysis for the fixed points of the Stroboscopic Map	28
2.3 Dynamics of the stroboscopic map F_A	31
2.4 Discussion	39
3 Neural Oscillations, phase and isochrons	44
3.1 Phase Variable and Isochrons	45
3.2 Phase-Amplitude Variables, Isochrons and A-Curves	46

3.3	Non Autonomous Perturbation	48
3.3.1	Phase Reduction Approach	48
3.3.2	Phase-Amplitude Approach and Phase-Amplitude Response Functions	50
3.4	The 2D case	52
3.4.1	Numerical computation of $K(\theta, \sigma)$	53
3.4.2	Globalizing $\mathcal{I}_\theta, \mathcal{A}_\sigma$ and $K(\theta, \sigma)$	55
3.4.3	Study of perturbations: the rotation number	59
3.5	The 3D case	67
3.5.1	A formal solution for the invariance equation	68
3.5.2	Numerical Implementation	71
3.5.3	Globalizing $\mathcal{I}_\theta, \mathcal{A}_\sigma$ and $K(\theta, \sigma)$	73
3.5.4	A 3 dimensional study of perturbations	78
3.5.5	Preliminary study of perturbations	84
3.6	Discussion	86
4	Computation of PRCs by means of the parameterization method	88
4.1	Mathematical Formalism	89
4.2	Computation of the PRC by means of the parameterization method. Theoretical results	92
4.2.1	Stroboscopic approach	92
4.2.2	Proof of Theorem 4.2.2	95
4.3	Computation of the PRC by means of the parameterization method. Computational results	102
4.3.1	Computation of the invariant curve	102

4.3.2	Computation of PRCs beyond the existence of the invariant curve	107
4.3.3	Computation of the PRC and ARC	109
4.4	Numerical Examples	111
4.4.1	Large Amplitude Perturbations	119
4.5	Discussion	122
5	The uncoupled limit of identical Hopf bifurcations	126
5.1	Study of two coupled identical systems undergoing Hopf Bifurcations	127
5.1.1	Normal Form of system (5.1)	128
5.1.2	Normal Form Computation	129
5.1.3	Numerical computations	131
5.2	Dynamical analysis of the truncated normal form	133
5.2.1	Normal Form in Polar Coordinates	133
5.2.2	The uncoupled system ($\epsilon = 0$)	135
5.2.3	Hopf bifurcations of the origin for $\epsilon > 0$	136
5.2.4	The Oscillating Solutions \mathcal{S}_{osc}^{\pm}	138
5.3	Bifurcation diagrams of the reduced system	146
5.3.1	Case $\beta_{\epsilon 0R} > 0$ and $C_{det} + \beta_{\epsilon 0R} > 0$ (or $\beta_{\epsilon 0R} < 0$ and $C_{det} + \beta_{\epsilon 0R} < 0$) . .	148
5.3.2	Case $\beta_{\epsilon 0R} < 0$ and $C_{det} + \beta_{\epsilon 0R} > 0$ (or $\beta_{\epsilon 0R} > 0$ and $C_{det} + \beta_{\epsilon 0R} < 0$) . .	151
5.3.3	Case $\beta_{\epsilon 0R} = 0$ and $C_{det} > 0$ (or $\beta_{\epsilon 0R} = 0$ and $C_{det} < 0$)	153
5.4	Application to two coupled Wilson-Cowan oscillators	155
5.4.1	Case $b_{sp} < 0$	157
5.4.2	Case $b_{sp} > 0$	157

5.4.3 Case $b_{sp} = 0$ 159

5.4.4 Dynamics beyond the weak coupling limit 160

5.5 Discussion 162

Introduction

Oscillations are ubiquitous in a wide range of biological processes [20]. Some classical examples are the cardiac pacemakers [58], the flashing fireflies [22] or the circadian rhythms [54]. In this Thesis, we focus on oscillations in neuroscience. Oscillatory activity in the brain is widely observed at different levels of organization. At the single cell level, neurons show oscillatory activity of their membrane potential [21]. Indeed, neurons integrate inputs from neighbouring neurons across dendrites. When these inputs cause the neuron membrane potential to reach a certain critical value or threshold, the neuron responds with a characteristic voltage change of large amplitude and short time duration (≈ 1 ms) known as action potential or *spike*. The generation of an action potential is the result of a mechanism involving an accurate concatenation of opening and closing of ionic channels. Under the appropriate conditions, the neurons can show sustained oscillatory activity, either subthreshold oscillations of the membrane potential or repetitive firing [51].

Macroscopic oscillatory activity in the brain arises from the activity of individual neurons and its interactions through synapses. When a neuron is excited it emits an action potential which travels along the axon of the neuron to the axon or pre-synaptic terminal causing the release of neurotransmitters in the synaptic cleft. These neurotransmitters bind to the receiver in the post-synaptic terminals of other neurons. The binding between neurotransmitter and receiver leads to the opening of ionic channels. Neurons can be excitatory or inhibitory, depending on the effect of the connection (synapse) on the receiving neuron: inputs from an excitatory (E) (inhibitory (I)) neuron depolarize (hyperpolarize) the membrane potential of the receiving neuron [26].

Macroscopic neural oscillations were first observed in 1929 by Hans Berger [8], and, nowadays, are classified in the following bands: delta (1-4 Hz), theta (4-8 Hz), alpha (8-13), beta (13-30 Hz) and gamma (30-70 Hz). Although some of these oscillations have been associated to specific tasks or behaviours, their functional role is not completely understood [10].

Many mechanisms have been proposed to explain macroscopic oscillatory activity, which remains an active area of research [77, 83]. In this Thesis, we focus on those mechanisms involving the interaction between excitation and inhibition (E-I). Consider a neuronal network consisting of a single population of excitatory neurons and a single population of inhibitory neurons (E-I

network). Under the appropriate stimulus, the firing of the excitatory population activates the inhibitory population that, on its turn, suppresses the excitatory activity. Once the inhibitory effect has vanished, if the stimulus remains, the excitatory neurons will fire again generating an oscillatory pattern [78]. As a consequence of this oscillatory mechanism, due to the inhibitory action, the excitability of the excitatory population is not the same for all the phases of the cycle. Indeed, when the excitatory population receives an external input at the phase in which the inhibition is not present, the excitatory cells can respond effectively, while if the inhibition is present, the input might be ignored.

The communication through coherence (CTC) theory [30] proposes that repetitive changes in the excitability of neuronal populations, as the one described above, might play a role in neuronal communication. In particular, it conjectures that for an effective communication between an emitting population and a receiving population, the input from the emitting population must arrive at a time in which the receiving population is at its excitable phase. Thus, the CTC theory proposes a flexible mechanism on top of the fixed brain connectivity for an effective communication. The mathematical community has explored different approaches to implement the CTC mechanism in computational models [79]. In this Thesis we propose a mathematical set-up based on mean field models [87] to study this phenomenon. Mathematically, oscillations correspond to limit cycles. In this Thesis we study how different types of perturbations affect the ongoing oscillatory activity of a neural population with different intrinsic properties. To tackle this problem, we use different tools from dynamical systems: classical perturbation theory, the stroboscopic map of a time periodically forced system, the parameterization method to compute invariant manifolds [13], as well as recent tools such as the phase-amplitude reduction [39, 82, 85]. Next, we describe in detail the organization and main results of this Thesis.

In Chapter 1 we introduce the Wilson-Cowan model [87] (§1.1) and review its bifurcations (§1.2). This model describes the generation of oscillatory activity across the E-I mechanism via two different types of bifurcations: a Hopf and a SNIC bifurcation (§1.3) [9]. These cycles respond qualitatively different to external perturbations. For this reason most of the studies carried out along this Thesis will be applied to oscillators near these bifurcation regimes, which will be denoted by Γ_{HB} and Γ_{SN} , respectively (§1.4).

According to the CTC theory, two neuronal groups with underlying oscillatory activity communicate much effectively when they are properly phase-locked so that the windows for inputs and outputs are open at the same times. To explore this scenario, in Chapter 2 we consider the following mathematical setting: we take the Wilson-Cowan equations and choose parameters so that the system is in an oscillatory regime, either Γ_{HB} and Γ_{SN} , modelling the receiving population, and we perturb it with an external time periodic perturbation $p(t)$ modelling the input from the emitting population.

We consider the stroboscopic map for this system (§2.1) and compute the bifurcation diagram

for its fixed points and periodic points as the amplitude and the frequency of the perturbation are varied (§2.2). We highlight that we have developed the numerical software to compute the bifurcation diagram instead of relying on existing software packages, thus providing more control on the calculations performed.

The techniques that we use to do the bifurcation analysis have no restriction neither on the amplitude nor on the frequency of the perturbation. From the bifurcation diagram, we can identify the phase-locked states as well as different areas involving bistability between two invariant objects (§2.3). We discuss the possible implications of the phase-locked states and the bistable scenarios that we find for the mathematical implementations of the CTC theory (§2.4).

Studying the phase response of an oscillator to an external input is related to the CTC framework. Indeed, phase shifts of the receiving population may create/destroy effective windows for communication. This is the motivation underlying Chapter 3. This Chapter starts by introducing the phase reduction for oscillators (§3.1), and exploits recent techniques based on phase-amplitude variables to describe the phase dynamics of an oscillator under different perturbations [5]. More precisely, we extend the applications of the parameterization method to compute a change of variables $x = K(\theta, \sigma), x \in \mathbb{R}^n$ that describes correctly the dynamics near a limit cycle in terms of the phase $\theta \in \mathbb{T}$ and the amplitude $\sigma \in \mathbb{R}^{n-1}$ [39, 49] (§3.2). This change provides two remarkable manifolds used in neuroscience: the sets of constant phase (the isochrons \mathcal{I}_θ) and the sets of constant amplitude (the A-curves/surfaces or isostables \mathcal{A}_σ). Moreover, we compute the functions describing the phase and amplitude changes caused by a perturbation arriving at different phases of the cycle, known as Phase and Amplitude Response Curves, PRCs and ARCs, respectively. The parameterization $K(\theta, \sigma)$ provides also the extension of these curves outside of the limit cycle, defined as the Phase and Amplitude Response Functions, PRFs and ARFs, respectively (§3.3) [17].

For the 2-dimensional case (§3.4), we consider the same perturbed Wilson-Cowan model as in Chapter 2 and we study its dynamics by means of the phase and phase-amplitude variables. We check that the phase-amplitude approach description of the dynamics is more accurate than the classical phase reduction. Combining results from Chapters 2 and 3, it allows us to understand the differences in the phase-locking areas that we found in Chapter 2 for Γ_{HB} and Γ_{SN} . Furthermore, we use the diagrams in Chapter 2 to understand the domains of applicability of the phase-amplitude description in the considered problem.

Next, as the isochrons foliate the attracting manifold of the limit cycle [38], we use the parameterization method to compute the local approximation of the isochrons and their globalization for $d = 3$ for different models in neuroscience (§3.5). Namely, a thalamic spiking model [72], a reduced Hodgkin-Huxley model [47], an extended Wilson-Cowan model with dynamic synaptic input and an exact neural mean field model [19]. An important point to successfully extend these methods to dimension $d > 2$ is the use of Floquet theory [49, 18] to diagonalize the linear part of

the equation. Moreover, for a spiking neuron model we explore the performance of two possible dynamical reductions, namely, the phase reduction and the reduction to the slow manifold in the description of the dynamics resulting from a periodic perturbation consisting of a train of pulsatile inputs followed by a resting period.

In Chapter 4 we focus on the applications of the parameterization method to the computation of the Phase Response Curves (PRCs) for a transient stimulus of arbitrary amplitude and duration. The underlying idea for the method is to construct a particular periodic perturbation consisting of the repetition of the transient stimulus followed by a resting period when no perturbation acts (§4.2). For this periodic system we consider the corresponding stroboscopic map and we prove that, under certain conditions, the map has an invariant curve. The core mathematical result of this Chapter is Theorem 4.2.2, which gives the existence of the invariant curve and provides the relationship between the PRC and the internal dynamics of the curve. Moreover, we link the existence properties of this invariant curve as the amplitude of the perturbation is increased with changes in the PRC waveform and with the geometry of isochrons. The theorem provides a method to numerically compute the PRCs alternative to the adjoint method (§4.3). The invariant curve and its dynamics will be computed by means of the parameterization method consisting of solving an invariance equation [15]. We show that the method to compute the PRC can be extended beyond the breakdown of the curve by means of introducing a modified invariance equation. The method also computes the amplitude response functions (ARCs) which provide information on the displacement away from the oscillator due to the effects of the perturbation. Finally, we apply the method to several classical models in neuroscience (§4.4) to illustrate how the results herein extend the framework of computation and interpretation of the PRC and ARC for perturbations of large amplitude and not necessarily pulsatile.

In Chapter 5 we study the dynamics arising when two identical oscillators are coupled near a Hopf bifurcation, where we assume a parameter ϵ uncouples the system at $\epsilon = 0$. Using the truncated normal form for $N = 2$ identical systems undergoing a Hopf bifurcation (§5.1) introduced in [6], we perform a theoretical dynamical analysis (§5.2) and study its possible bifurcations (§5.3). Matching the normal form coefficients to a coupled Wilson-Cowan oscillator network gives an understanding of different types of behaviour that arise in a model of perceptual bistability [69]. Notably, we find bistability between in-phase and anti-phase solutions. Using numerical continuation (§5.4) we confirm our theoretical analysis for small coupling strength and explore the bifurcation diagrams for large coupling strength, where the normal form approximation breaks down. We finally discuss the implications of this dynamical study in models of perceptual bistability (§5.5).

We conclude by summarizing the main achievements of this Thesis as well as some open questions for future work.

For Chapter 2, concerning periodically forced oscillators beyond the weak coupled limit,

- we have proposed a setting based on mean field models that implements mathematically some aspects of the CTC theory,
- we have identified the 1:1 and 1:2 phase-locked areas with no restrictions on the frequency nor on the amplitude of the perturbation,
- we have found areas of bistability corresponding to different communication regimes in the CTC context.
- As future work, we plan to repeat the analysis for a perturbation consisting of an active and a silent phase. We propose to use these results to deepen in the analysis of the effects onto the receiving population of two pulses arriving with a phase shift using the 1:1 and 1:2 phase locking states. Furthermore, we aim to consider perturbations in the inhibitory population.

For Chapter 3, concerning the phase-amplitude descriptions of 2 and 3-dimensional limit cycles,

- we have used the phase-amplitude variables to describe the oscillatory dynamics for the Wilson-Cowan equations under a continuous periodic perturbation,
- we have extended the computation of the parameterization $K(\theta, \sigma)$ to \mathbb{R}^3 and used these results to obtain the isochrons and the A-surfaces for several 3-dimensional neural models,
- we have proposed several reductions of the dynamics based on phase and phase amplitude variables and have quantified its performance in a perturbed 3-dimensional single neuron model.
- As future work, we aim to study the applicability of the proposed dynamical reductions for different perturbations and 3-dimensional models.

For Chapter 4, concerning the computation of PRCs by means of the parameterization method,

- we have presented a new approach to PRCs based on the parameterization method with solid theoretical results, which extends the framework of computation and geometrical interpretation of the PRC and ARC for perturbations of large amplitude and not necessarily pulsatile.

- As future work, we plan to extend the results, both theoretical and computational, to \mathbb{R}^n , $n \geq 2$.

For Chapter 5, concerning the uncoupled limit of two identical Hopf bifurcations,

- we have proven analytically, using the normal form, the bifurcations occurring for small coupling strength,
- we have performed a numerical bifurcation analysis for two coupled Wilson-Cowan oscillators that confirms the theoretical predictions and extends the analysis beyond the weak coupling.
- As future work, we plan to study in more detail the implications of this work in perceptual bistability.

Chapter 1

Mean field models

The aim of this Chapter is to introduce the seminal Wilson-Cowan model for an excitatory-inhibitory network, and some basic terminology about bifurcations to address the problems in the next Chapters.

Spiking models of networks of large numbers of neurons, although being biologically realistic models, thus generating accurate results, are computationally expensive, especially when the number of neurons is large. Moreover, the analytical treatment becomes unpractical due to its high dimensionality. As an alternative to this approach, the mean field models provide a macroscopic description of the average activity of large ensembles of neurons by means of a few differential equations, so they can be studied using techniques from dynamical systems theory. Examples of these models can be found in [26, 60].

The seminal Wilson-Cowan model [87, 52] provides a heuristic description of the dynamics for a neural network consisting of a single population of excitatory neurons and a single population of inhibitory neurons (E-I network). The model robustly produce oscillations via a Hopf or a Saddle-Node on an invariant curve (SNIC) bifurcation [9]. The underlying mechanism for generating oscillations is the E-I loop: when drive to excitatory population is strong enough, the excitatory population activates the inhibitory population that, on its turn, suppresses the excitatory activity. Once the inhibitory effect has vanished, if the stimulus remains, the excitatory neurons will fire again generating an oscillatory pattern [78]. In most of the problems considered along this manuscript, we will consider oscillations generated by means of a mechanism based on E-I interaction.

In this Chapter, we will review the typical bifurcations that give rise to oscillatory dynamics, namely the Hopf and the Saddle-Node in an invariant curve (SNIC) bifurcations. Moreover, we

will also introduce continuation techniques to compute bifurcation diagrams and we will apply them to the Wilson-Cowan model.

1.1 The Wilson-Cowan equations

We introduce a classical rate model, describing the average activity of two mutually coupled neuronal populations one excitatory (E) and other inhibitory (I), known as the Wilson-Cowan equations [87]:

$$\begin{aligned}\tau_e \frac{dE}{dt} &= -E + (1 - r_e E) S_e(c_1 E - c_2 I + P), \\ \tau_i \frac{dI}{dt} &= -I + (1 - r_i I) S_i(c_3 E - c_4 I + Q).\end{aligned}\tag{1.1}$$

whose dynamics and bifurcations will be reviewed in this Chapter.

The model describes the dynamics of the variables $E(t)$ and $I(t)$, corresponding to the fraction of neurons of the excitatory and the inhibitory populations respectively, which is emitting an action potential at time t . The coupling constants c_i determine the strength of the connexions between neuronal populations. The constants r_e and r_i represent the refractory time of the E and I population individual cells, respectively. Parameters P and Q are the (constant) external inputs which are injected to the E and I populations, respectively (see Fig. 1.1). Coupling constants c_i are positive, whereas external currents P and Q can be either positive or negative, depending whether its action is excitatory or inhibitory.

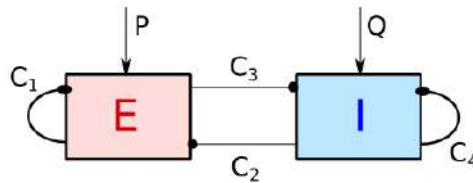


Figure 1.1: Schematic of a neuronal network modelled by the mean field model (1.1).

Assuming that a population $k = e, i$ is receiving an input x , the proportion of cells which will fire as a result of this input is modelled by the response function $S_k(x)$. The function $S_k(x)$ is a sigmoidal function defined as

$$S_k(x) = \frac{1}{1 + e^{-a_k(x - \theta_k)}}, \quad \text{with } k = e, i,\tag{1.2}$$

where the parameters θ_k and a_k are the position of the maximum slope and the value of this maximum slope, respectively. They are related through the relationship

$$\max_{x \in \mathbb{R}} [S'_k(x)] = S'_k(\theta_k) = \frac{a_k}{4}. \quad (1.3)$$

1.2 Dynamical Analysis

On the role of refractory-time constants r_e and r_i

Neurons have a refractory period r_k ($k = e, i$) during which they can not respond to external inputs. The factor $(1 - r_k K)$ in equations (1.1) represents the proportion of neurons of the population k which are able to be excited. In [68] it is shown how this term only rescales the parameters on $S_k(x)$ and its value does not change the qualitative behaviour of the system. Next, we will provide insight into the role of parameter r_k on the model dynamics. The nullclines $\dot{E} = 0$, $\dot{I} = 0$, of system (1.1) are given, respectively by:

$$I = g_i(E, P) = \frac{1}{c_2} [c_1 E - S_e^{-1} \left(\frac{E}{1 - r_e E} \right) + P], \quad (1.4)$$

$$E = f_e(I, Q) = \frac{1}{c_3} [S_i^{-1} \left(\frac{I}{1 - r_i I} \right) + c_4 I - Q], \quad (1.5)$$

where $S_k^{-1}(x)$ is the inverse of the response function (1.2) given by:

$$S_k^{-1}(x) = \frac{1}{a_k} \ln \left(\frac{x}{1 - x} \right) + \theta_k. \quad (1.6)$$

As the logarithm is defined between $(0, +\infty)$ the function $S_k^{-1}(x)$ has a restricted domain, ranging between $(0, 1)$. Since the inverse of the response function (see (1.6)) appearing in equations (1.4) and (1.5) has arguments of the form $\frac{k}{1 - r_k k}$, the values for k are restricted between $(k_{min}, k_{max}) = (0, \frac{1}{1 + r_k})$.

So, as the above expression for k_{max} shows, the values of r_e and r_i will bound the phase space, but as they appear in the argument of the function (1.6), their values will not affect qualitatively the shape of the nullclines and therefore, neither the number of critical points nor their stability. For this reason, we will perform our mathematical analysis considering refractory time-constants equal to zero. Thus, for the rest of the manuscript, when we work with the Wilson-Cowan equations, we

will consider the following system:

$$\begin{aligned}\tau_e \frac{dE}{dt} &= -E + S_e(c_1 E - c_2 I + P), \\ \tau_i \frac{dI}{dt} &= -I + S_i(c_3 E - c_4 I + Q).\end{aligned}\tag{1.7}$$

Nullclines

The E-nullcline is given by the equation

$$I = g_i(E, P),\tag{1.8}$$

where,

$$g_i(E, P) = \frac{1}{c_2} [c_1 E - S_e^{-1}(E) + P],\tag{1.9}$$

whereas the I-nullcline is given by

$$E = f_e(I, Q),\tag{1.10}$$

where,

$$f_e(I, Q) = \frac{1}{c_3} [S_i^{-1}(I) + c_4 I - Q].\tag{1.11}$$

Along this work we assume that constants c_2 and c_3 do not vanish in order to keep the coupling between E and I populations always present. From now on when referring to the derivatives of the functions (1.9) and (1.11), we will assume that parameters P and Q are fixed and therefore derivatives will be with respect to the variables E and I , respectively.

As the sigmoid's inverse is a function which increases monotonically, the function f_e defined in (1.11) is monotonically increasing as a function of I . By contrast, the shape for the g_i function in (1.9) is not so straightforward to foretell because of the sigmoid's negative sign. As the derivative of function g_i in (1.9) is negative for $E \rightarrow 0$ and $E \rightarrow 1$, g_i has vertical asymptotes at $E = 0$ and $E = 1$, if the maximum of the derivative of g_i is positive, then the derivative will be zero for two values of E . The necessary condition for this to happen comes from the fact that the derivative of $S_e^{-1}(E)$ has a minimum value and is written as:

$$c_1 > \frac{4}{a_e}.\tag{1.12}$$

As one can see in Fig. 1.2 (right), this change of the derivative's sign will create what is called in [87] a 'kink'. Moreover, these 'kinks' will always appear in pairs because of the symmetry with

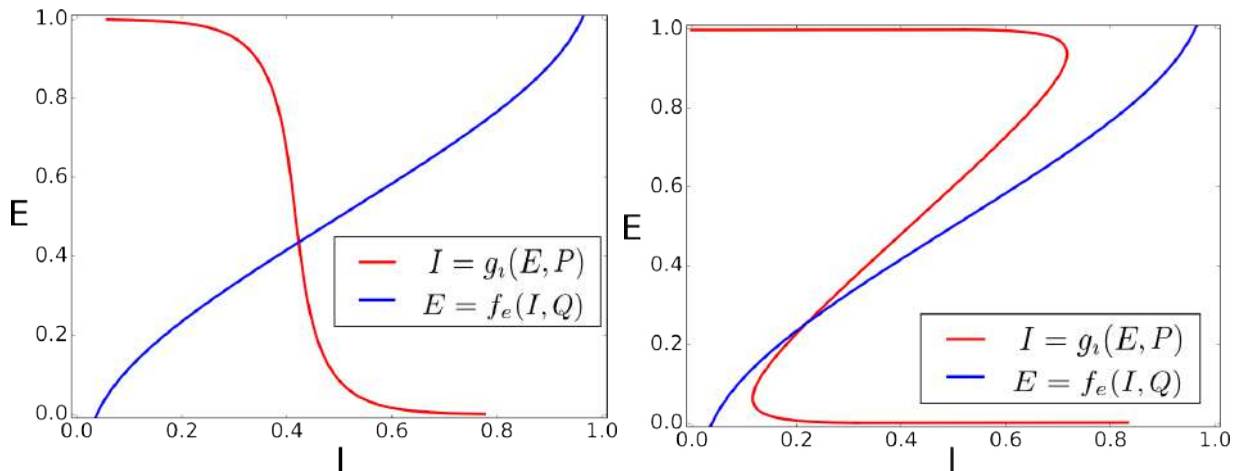


Figure 1.2: I-Nullcline given by equation $E = f_e(I, 0)$ (red curve) and E-Nullcline given by equation $I = g_i(E, P)$ (blue curve) for the Wilson-Cowan model (1.7). In order to show how the appearance of a kink in the E-nullcline depends on c_1 , the parameters for both images are the same except for c_1 and P which were $c_1 = 2$ and $P = 8$ for the left plot and $c_1 = 13$ and $P = 2.5$ for the right one. As equations (1.9) and (1.11) show, P and Q translate E and I nullclines along the I and E axes, respectively. Therefore, for some (P, Q) configurations, the E-nullcline can intersect several times the I-nullcline near its kinks (see right plot).

respect to the point of maximum slope in the derivative of the sigmoidal function (1.2). As fixed points correspond to the intersection of nullclines, the kinks may have important implications in the appearance and disappearance of critical points of system (1.7) and therefore in its dynamics (see Fig. 1.3).

Generation of Limit Cycles

As we are interested in oscillatory behaviour, we will review the work done in [87], which establishes conditions on the parameter set under which there will exist limit cycles. As we consider a 2D system and its phase space is bounded, the Poincaré-Bendixon theorem guarantees the existence of a limit cycle (and therefore oscillations) if the system has a unique unstable critical point.

Using linear system analysis we can see that a sufficient condition for the critical point to be unstable is to require the trace of the Jacobian matrix of system (1.7) given by

$$DX(E, I, P, Q) = \begin{pmatrix} \frac{-1+c_1S'_e(c_1E-c_2I+P)}{\tau_e} & -\frac{c_2S'_e(c_1E-c_2I+P)}{\tau_e} \\ \frac{c_3S'_i(c_3E-c_4I+Q)}{\tau_i} & \frac{-1-c_4S'_i(c_3E-c_4I+Q)}{\tau_i} \end{pmatrix} \quad (1.13)$$

to be positive for (E, I, P, Q) values which are also a solution of equations (1.8) and (1.10). As one can see, all the terms in the trace are negative, except for $c_1S'_e(c_1E - c_2I + P)$, which is positive. As a consequence, $S'_e(c_1E - c_2I + P)$ has to be large enough in order that (1.13) has a positive trace.

Furthermore, besides constants, the trace depends on the derivative of the response functions $S_e(x)$ and $S_i(x)$ defined in (1.3), which has a maximum. Therefore, a sufficient (but not necessary) condition for the trace to be positive is to choose P and Q so that the derivatives of the sigmoidal response functions $S_e(x)$, $S_i(x)$ in (1.13) are evaluated at their maximum values. Mathematically, this condition is written as:

$$c_1a_e - 4 > \frac{\tau_e}{\tau_i}(4 + c_4a_i). \quad (1.14)$$

As the terms on the right hand side of inequality (1.14) are strictly positive, the term $c_1a_e - 4$ must be positive too. Recalling condition (1.12), this implies that the E -nullcline will have kinks. As it was previously stated, the existence of 'kinks' for the E -nullcline allows for the possibility of having more than one equilibrium point. Therefore, we need to find extra conditions on parameters to ensure the existence of a single equilibrium point (for some pair of P , Q values). Using a geometric approach, we will see that we need to impose two requirements to ensure uniqueness.

The first one is to require that the minimum slope of the function $f_e(I, Q)$ in (1.11) is smaller than the inverse value of the maximum slope of the function $g_i(E, P)$ in (1.9). As $f_e(I, Q)$ has asymptotes at $I = 0$ and $I = 1$, if this condition is not satisfied, extra-crossings between both nullclines will appear (see Fig. 1.3). Mathematically, this condition is written as:

$$c_2c_3a_ea_i > (c_1a_e - 4)(4 + c_4a_i). \quad (1.15)$$

The second one is to impose that the distance between the images of E_1, E_2 which correspond to the values where the derivative of the function $g_i(E, P)$ is 0 (see Fig 1.4) must be less than the distance between the asymptotes of the function $f_e(I, Q)$. As the distance between both asymptotes is 1, if we define $I_2 = g_i(E_2, P)$ and $I_1 = g_i(E_1, P)$, we have to impose that $1 > I_2 - I_1$.

In order to express this condition in a more simplified way let us define the line $I = m(E)$ which passes through the point where the derivative of the function $g_i(E, P)$ is maximum, and it

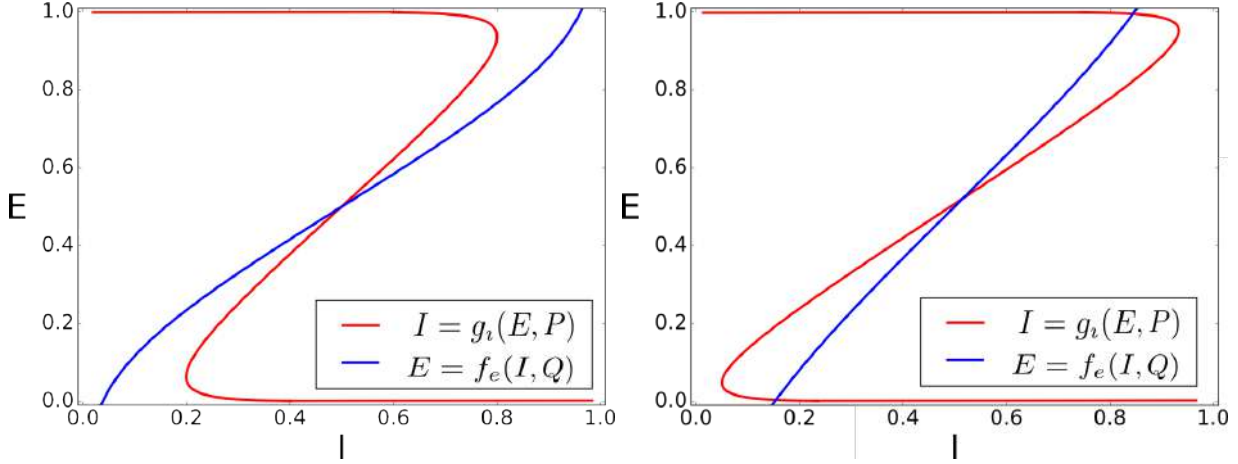


Figure 1.3: Nullclines for the Wilson-Cowan model showing condition (1.15) which requires that the minimum slope of the function $f_e(I, Q)$ is smaller than the inverse value of the maximum slope of the function $g_i(E, P)$. Left figure corresponds to a set of constants and P, Q values satisfying condition (1.15) whereas right figure corresponds to a set of constants which does not satisfy it.

has a slope value equal to that maximum value. Then it is straightforward to see that $|m(E_2, P) - m(E_1, P)| > |g_i(E_2, P) - g_i(E_1, P)|$ and thus all we need to impose is $1 > |m(E_2, P) - m(E_1, P)|$. As $m(E_2, P) - m(E_1, P) = \frac{c_1 a_e - 4}{c_2 a_e} (E_2 - E_1)$ and the distance $|E_2 - E_1|$ can not be bigger that 1, one can write the following sufficient condition:

$$\frac{c_1 a_e - 4}{c_2 a_e} < 1. \quad (1.16)$$

Conditions (1.14)-(1.15)-(1.16) guarantee the existence of a limit cycle for system (1.7) for appropriate (P, Q) values. Thus, the following set of parameters \mathcal{P} which satisfies the above mentioned conditions will be used for the rest of the manuscript when we work with the Wilson-Cowan equations (1.7):

$$\mathcal{P} = \{c_1 = 13, c_2 = 12, a_e = 1.3, \theta_e = 4, r_e = 0, \tau_e = 1, c_3 = 6, c_4 = 3, a_i = 2, \theta_i = 1.5, r_i = 0, \tau_i = 1\}. \quad (1.17)$$

1.3 Bifurcation Diagram

As we have shown in Section 1.2, parameters P and Q in system (1.7) translate nullclines given by equations (1.8) and (1.10), making the number and position of critical points vary. Therefore,

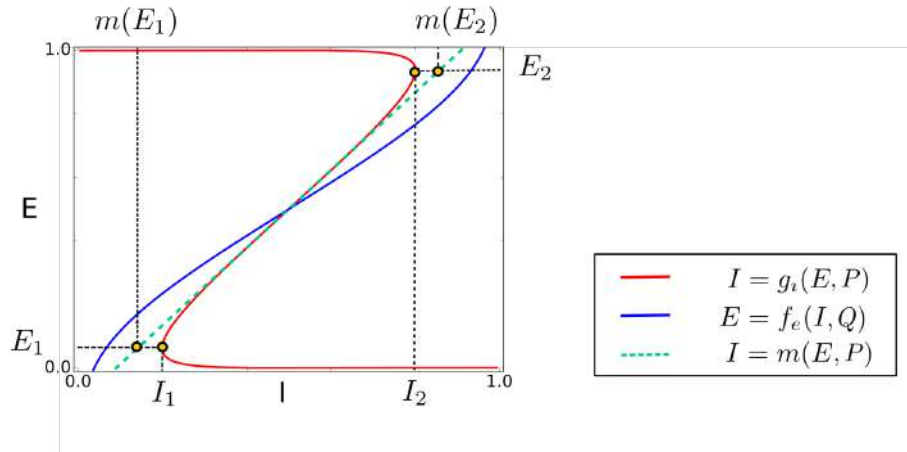


Figure 1.4: Nullclines for the Wilson-Cowan model (1.7) showing the strategy to prove a single crossing. The distance between kinks on the red curve must be smaller than the distance between the asymptotes of the blue curve. In order to establish a simple formulation for this condition, the central part of the E -nullcline will be approximated by a line (green dashed line). The image corresponds to the set of values \mathcal{P} given in (1.17) and $(P, Q) = (3.5, 0)$.

the Wilson-Cowan model will undergo different bifurcations when parameters P and Q are varied, that will yield the appearance of oscillations. Such oscillations are going to appear across Hopf, Saddle Node on Invariant Circle (SNIC) and homoclinic bifurcations [9, 48]. Next, we review them.

Andronov-Hopf bifurcations (Hopf bifurcations in the following) occur when an equilibrium point of focus type changes its stability, that is, the real part of its complex eigenvalues changes from negative (stable) to positive (unstable) or viceversa as the bifurcation parameter is varied. This change of stability is accompanied either by the appearance of a stable limit cycle (supercritical Hopf) or by the disappearance of an unstable limit cycle (subcritical Hopf) (see Fig. 1.5).

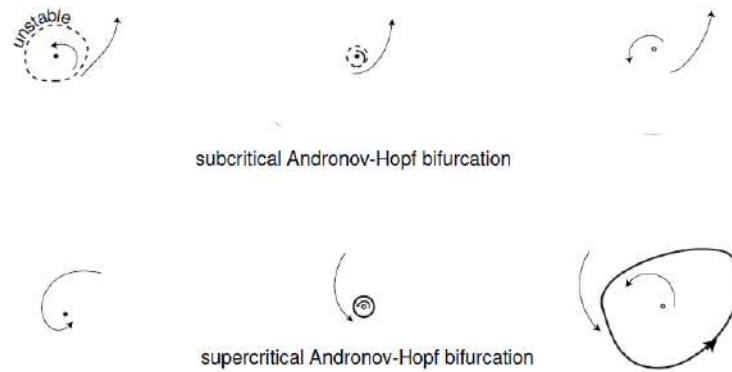


Figure 1.5: Subcritical and supercritical Andronov-Hopf bifurcation. Image adapted from [51].

Besides Hopf bifurcations we are interested in other bifurcations of fixed points. Although the Saddle-Node (SN) bifurcation is a bifurcation of fixed points, in some cases it can be associated to the emergence of an oscillatory behaviour. The system (1.7) that we are considering is planar and the dynamics is confined in a compact domain. Consider a situation in which we have 3 fixed points: an unstable focus, a saddle and a stable node. If the stable node and the saddle collide in a SN bifurcation, due to the Poincaré-Bendixon theorem a limit cycle appears. The bifurcation is then called a SNIC (Saddle Node on Invariant Circle) bifurcation (see Fig. 1.6). Before the SNIC bifurcation there exists a heteroclinic connection between the saddle and the attracting node. At the bifurcation, the saddle and the node collide and the connection becomes homoclinic. As a result, an invariant circle without fixed points appears after the bifurcation.

Another bifurcation involving limit cycles that occurs for the Wilson-Cowan model is the homoclinic bifurcation (see Fig. 1.7). The homoclinic bifurcation occurs when the stable and unstable manifolds of the saddle coincide and a limit cycle is born from this homoclinic connection. When comparing with the SNIC bifurcation, the main difference is the persistence of a saddle and a node after the appearance of the limit cycle.

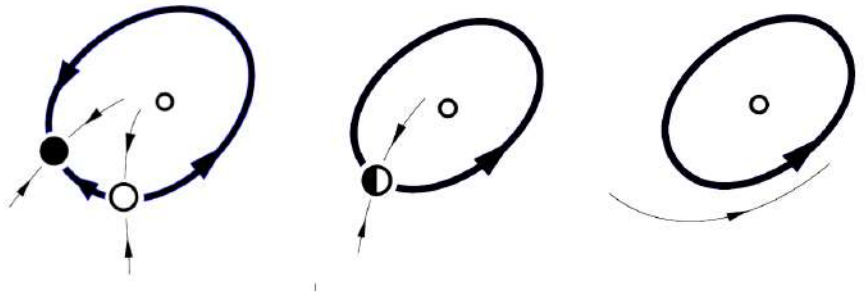


Figure 1.6: Saddle-Node on Invariant Circle (SNIC) bifurcation. Image from [51].

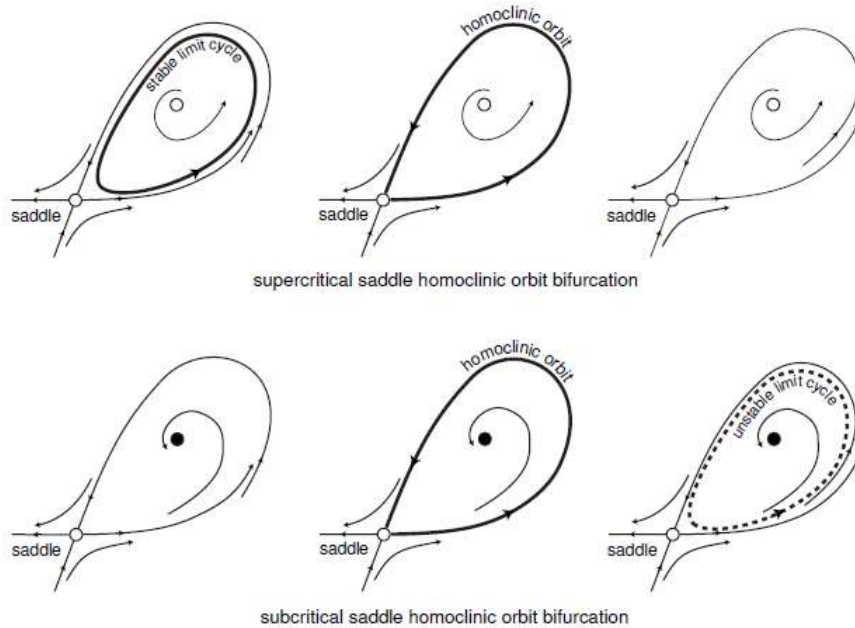


Figure 1.7: Homoclinic bifurcation. Image from [51].

We will only compute Hopf and Saddle-Node bifurcations, which are bifurcations of the critical points of the system. As we consider a 2D system, we have to look for points (E, I, P, Q) satisfying equations (1.8) and (1.10) and condition $Tr(DX(E, I, P, Q)) = 0$ for the Hopf bifurcation and $Det(DX(E, I, P, Q)) = 0$ for the Saddle Node bifurcation, where DX is the matrix defined in (1.13). Three equations define a curve on the (E, I, P, Q) space, which will be projected on the (P, Q) parameter space. We will refer to these curves as the Hopf and SN-curves respectively.

Continuation of Bifurcation Curves

Computing the Hopf and SN bifurcation curves presented in the previous Section 1.3, requires to solve a system $F(y) = 0$ of n equations and $n + 1$ unknowns. In these conditions we use a predictor-corrector method to compute the curve. The corrector step is based on a Newton method and Lagrange multipliers (see [2]). Start by considering the classical Newton's method: given an approximate solution y , one must look for Δy such that

$$F(y + \Delta y) = F(y) + D_y F(y) \cdot \Delta y + O(\|\Delta y\|^2) = 0. \quad (1.18)$$

Using only the linear order terms in (1.18), we are left with the following system of equations $D_y F(y) \Delta y = -F(y)$. The system has n equations and $n + 1$ unknowns. In order to obtain the extra equation needed to solve the system uniquely, we impose Δy to minimize $\|\Delta y\|^2$. The problem then becomes a Lagrange extreme conditioned problem that we can solve using the Lagrange multipliers method.

As we look for the minimum of $\|\Delta y\|^2$, with the restriction $D_y F(y) \Delta y + F(y) = 0$, we write the Lagrange function $L(\Delta y, \mu) = \|\Delta y\|^2 + \mu(D_y F(y) \Delta y + F(y)) = 0$ where μ is the Lagrange multiplier.

Once a solution y^* for system $F(y) = 0$ has been found, the implicit function theorem assures that, if $\text{Rank } D_y F(y^*) = n$, there exists a solution for $F(y) = 0$ in a neighbourhood of y^* . This ensures the existence of a curve of solutions for system $F(y) = 0$. Moreover, using a predictor method we can repeat the procedure and compute the next point of the curve.

The best estimate for the next point of the curve will be given by the tangent vector to the curve at the known point y^* . The assumption that system $F(y) = 0$ is regular enough allows us to define a parametrized curve by $c(t)$, where $c : \mathbb{R} \rightarrow \mathbb{R}^{n+1}$ such that $y^* = c(t_0)$ and $F(c(t)) = 0, \quad \forall t$. Therefore, using that $\left. \frac{dF(c(t))}{dt} \right|_{t=t_0} = 0$ and applying the chain rule we have

$$\left. \frac{dF(c(t))}{dt} \right|_{t=t_0} = D_y F(y^*) \cdot c'(t_0) = 0. \quad (1.19)$$

Thus, we can obtain the tangent vector $c'(t_0)$ to the curve at the point y^* as an element of the kernel of the matrix $D_y F(y^*)$. Let $v = \frac{c'(t_0)}{\|c'(t_0)\|}$ be the normalized vector, using the new estimate $y_{new} = y^* + h \cdot v$ (where $h \in \mathbb{R}$ is the continuation step) we can find a new solution for system $F(y) = 0$ by means of the extreme conditioned Newton's method described above. Using this procedure we have computed the Hopf and SN bifurcation curves depicted in Fig. 1.8.

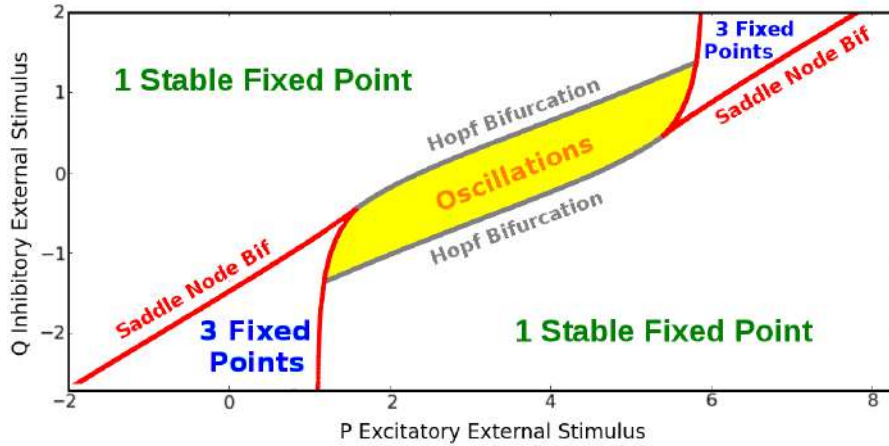


Figure 1.8: Bifurcation diagram for the Wilson-Cowan model (1.7) as a function of external stimuli P and Q for the set of parameters \mathcal{P} given in (1.17). Note that a simple rate model can show oscillations that emerge across different bifurcations (Hopf, SNIC and homoclinic (not shown, see [9])) which are qualitatively different.

1.4 Periodic orbits Γ_{HB} and Γ_{SN}

In this Chapter we have reviewed the bifurcation analysis of the Wilson-Cowan equations. The analysis performed allows us to choose the set of parameters \mathcal{P} in (1.17) for which the system (1.7) shows oscillations. As the bifurcation diagram in Fig. 1.8 shows, oscillations can appear through different types of bifurcations.

For the rest of the manuscript we introduce the notation Γ_{HB} and Γ_{SN} to denote the limit cycles of system (1.7) close to a Hopf or a SNIC bifurcation, respectively. In particular, these limit cycles correspond to the choice of parameters $(P, Q) = (2.5, 0)$ for Γ_{HB} and $(P, Q) = (1.4, -0.75)$ for Γ_{SN} . Fig. 1.9 shows the phase portraits of system (1.7) for the considered parameters. In all the qualitative and quantitative analysis that we will do in Chapters 2, 3 and 4, we will use these limit cycles. Of course, all the results obtained in these chapters apply for different models near these bifurcations.

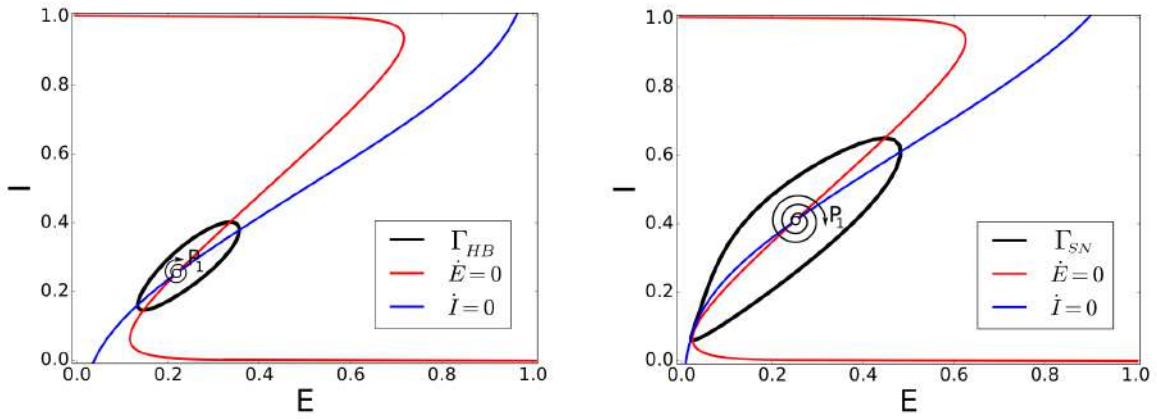


Figure 1.9: Limit cycles Γ_{HB} and Γ_{SN} and nullclines of system (1.7) for $(P, Q) = (2.5, 0)$ (left) and $(P, Q) = (1.4, -0.75)$ (right). Notice that in both cases there exists a unique equilibrium point labelled by P_1 , which is an unstable focus.

Chapter 2

Periodically forced oscillators beyond the weak coupling limit

Background oscillations, reflecting the excitability of neurons, are ubiquitous in the brain [10]. Although the role of oscillations is still unknown, several studies have conjectured that oscillations may play a role in neural communication. For instance, Communication Through Coherence (CTC) theory conjectures that oscillations provide a flexible mechanism of communication between brain areas. More precisely, when spikes sent by one population reach the other population in its peaks of excitability, then information transmission between two oscillating neuronal groups is more effective. In this context, two neuronal groups with underlying oscillatory activity communicate much effectively when they are properly phase-locked so that the windows for inputs and outputs are open at the same times.

Oscillations generated by the excitatory-inhibitory (E-I) interaction cause that the excitability of the excitatory population is not the same for all the phases of the cycle due to the inhibitory action [30]. Indeed, when the excitatory population receives an external input at the phase in which the inhibition is not present, the excitatory cells can respond effectively, while if the inhibition is present, the input might be ignored (see Fig. 2.1).

This mechanism is highly dependent on the existence of phase-locking between the emitting and receiving neuronal groups. A simplified framework for studying this mechanism is to consider the effect of an external oscillatory input onto a network model consisting of excitatory and inhibitory oscillating neural populations and study the phase-locked states. For such network we consider the simplest canonical model describing the mean firing rates of the excitatory and inhibitory populations: the Wilson-Cowan equations [87] which were profusely reviewed in the previous Chapter 1. The parameters of this model will be chosen so that the system shows oscillations.

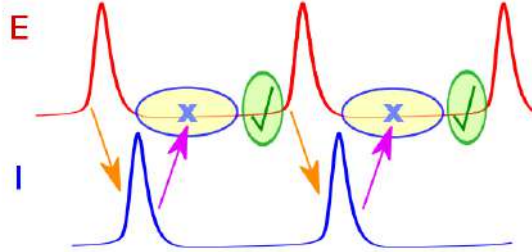


Figure 2.1: Oscillations arise from the interaction between the inhibition and the excitation. We illustrate how different phases of the oscillation may have different excitability properties due to the inhibition as suggested in [78]

In this Chapter, we want to understand the different mechanisms which give rise to synchronous activity between the E-I network and the external T' -periodic input. As we study a periodic perturbation, we consider the stroboscopic map (i.e. the time- T' map of the flow) and we look for fixed and periodic points of this map. As the autonomous system has an attracting periodic orbit we know that for small enough perturbations it persists as an attracting invariant curve of the map. To provide a full understanding of the dynamics beyond the appearance/breakdown of the invariant curve, we compute the fixed points of the map as well as their bifurcations.

The perturbed Wilson-Cowan equations have the following form:

$$\begin{aligned}\tau_e \frac{dE}{dt} &= -E + S_e(c_1 E - c_2 I + P + Ap(t)), \\ \tau_i \frac{dI}{dt} &= -I + S_i(c_3 E - c_4 I + Q),\end{aligned}\tag{2.1}$$

where A is the amplitude of the perturbation, and $p(t)$ is the T' -periodic function given by:

$$p(t) = 1 + \cos\left(\frac{2\pi t}{T'}\right),\tag{2.2}$$

modelling the activity of an external excitatory population. The analysis in this Chapter will be performed by using the set of parameters \mathcal{P} given in (1.17). We will consider two different dynamical regimes displayed by system (1.7) as the bifurcation parameters P and Q , are varied to study the effect of the perturbation on the limit cycle near different bifurcations. In particular, we will consider the limit cycles Γ_{HB} and Γ_{SN} defined in Chapter 1 (see Fig. 1.9). In order to study the effect of a periodic forcing, we introduce first the stroboscopic map (Section 2.1), as it is the most natural approach when considering periodic perturbations. Next, in Section 2.2 we will study its bifurcations which in turn separate synchronous from asynchronous dynamics and reveal the existence of bistable areas showing rich dynamics. A full description of the dynamics of the non-autonomous system (2.1) is given in Section 2.3.

2.1 The stroboscopic map

Consider a system of the form

$$\dot{x} = X(x) + Ap(x, t; A), \quad (2.3)$$

where p is a smooth T' -periodic function in t , that is: $p(x, t; A) = p(x, t + T'; A)$.

The stroboscopic map is defined by

$$\begin{aligned} F_A : \mathbb{R}^2 &\rightarrow \mathbb{R}^2, \\ x &\rightarrow F_A(x) = \phi_A(t_0 + T'; t_0, x), \end{aligned} \quad (2.4)$$

where $\phi_A(t; t_0, x)$ is the solution of (2.3) such that $\phi_A(t_0; t_0, x) = x$.

As it is well known, the fixed and periodic points and the invariant curves of the stroboscopic map (2.4) (which we will explain how to compute in the following Sections) will correspond to periodic and quasiperiodic solutions of system (2.3), respectively. For instance, if $\gamma(t) = \phi_A(t; t_0, x)$ is a solution of system (2.3) and $[F_A(x)]^q = x$, then by definition $\phi_A(t_0 + qT'; t_0, x) = x$ and therefore $\gamma(t)$ is a periodic orbit of system (2.3) with period qT' . Analogously, if $\gamma(t) = \phi_A(t; t_0, x)$ is a periodic orbit of period T of (2.3) with $\frac{T'}{T} = \frac{p}{q}$, $p, q \in \mathbb{N}$, then

$$[F_A(x)]^q = \phi_A(t_0 + qT'; t_0, x) = \phi_A(t_0 + pT; t_0, x) = x, \quad (2.5)$$

that is, fixed or periodic points of the map $F_A(x)$ correspond to periodic orbits of the system (2.3). Otherwise, if $T'/T \in \mathbb{R} \setminus \mathbb{Q}$, then the iterates of F_A fill densely an invariant curve.

The relationship (2.5) indicates that a $p:q$ phase locked state has been established between the population and the perturbation. In the perturbed Wilson-Cowan model (2.1) this means that the neuronal population variables E and I have completed p revolutions in the same time that the perturbation $p(t)$ has completed q revolutions. Later, we will see that depending on the amplitude A and the period T' of the perturbation, the system in (2.3) can display oscillations, which are either $p:q$ phase-locked (synchronous) or fill densely an invariant curve (asynchronous). Calculations performed along this Chapter assume that the initial time $t_0 = 0$.

2.2 Bifurcation Analysis for the fixed points of the Stroboscopic Map

As it was stated in the previous Section 2.1, the fixed points of map (2.4) correspond to T' -periodic periodic solutions of system (2.3), and thus 1:1 phase-locking between the periodic orbit

of the system and the perturbation. For this reason, computing the bifurcations of the fixed points of the stroboscopic map becomes relevant for our analysis, as they will separate synchronous from asynchronous regimes.

Consider a map F_α depending on a parameter $\alpha \in \mathbb{R}$ of the form:

$$\begin{aligned} F_\alpha : \mathbb{R}^n &\rightarrow \mathbb{R}^n \\ x &\rightarrow F_\alpha(x), \end{aligned} \quad (2.6)$$

if there exists $(\alpha_0, x_0) \in \mathbb{R} \times \mathbb{R}^n$ such that:

1. $F_{\alpha_0}(x_0) = x_0$,
2. $DF_{\alpha_0}(x_0)$ has eigenvalues λ_i with $|\lambda_i| \neq 1, i = 1, \dots, n$

then x_0 is a hyperbolic fixed point and it is known that, for α close to α_0 , there exists x_α fixed point of $F_\alpha(x_\alpha)$ of the same topological type of x_0 . Otherwise, when 2) fails we call α_0 a bifurcation value.

Thus, to compute the bifurcation values of fixed points of the map F_α we impose the existence of a fixed point together with a bifurcation condition $\Phi_{BIF} = 0$. Mathematically,

$$G_\alpha(x) = \begin{cases} F_\alpha(x) - x = 0 \\ \Phi_{BIF}(x) = 0. \end{cases} \quad (2.7)$$

We look for bifurcations of the fixed points of the map defined in (2.4). We will consider three bifurcations of fixed points: Saddle-Node (*SN*), Period Doubling (*PD*) and Neimark-Sacker (*NS*). At it is well known, SN and PD bifurcations occur generically when one of the real eigenvalues of the fixed point equals $+1$ or -1 , respectively, whereas a NS bifurcation occurs when the fixed point has a pair of complex eigenvalues whose modulus equals one. In a 2D map the conditions which must be satisfied at the bifurcation values are written as

$$\begin{aligned} \Phi_{SN} &= \det(DF_\alpha - Id) = 0, \\ \Phi_{PD} &= \det(DF_\alpha + Id) = 0, \\ \Phi_{NS} &= \det(DF_\alpha) - 1 = 0, \end{aligned}$$

where we denote by DF_α the Jacobian matrix of the map F_α evaluated at the fixed point, whose computation requires the solving of the variational equations of system (1.1) [75].

Using these techniques we compute the bifurcation diagrams for the stable fixed points of the stroboscopic map (2.4) as the amplitude and the frequency are varied for the system (2.1) with

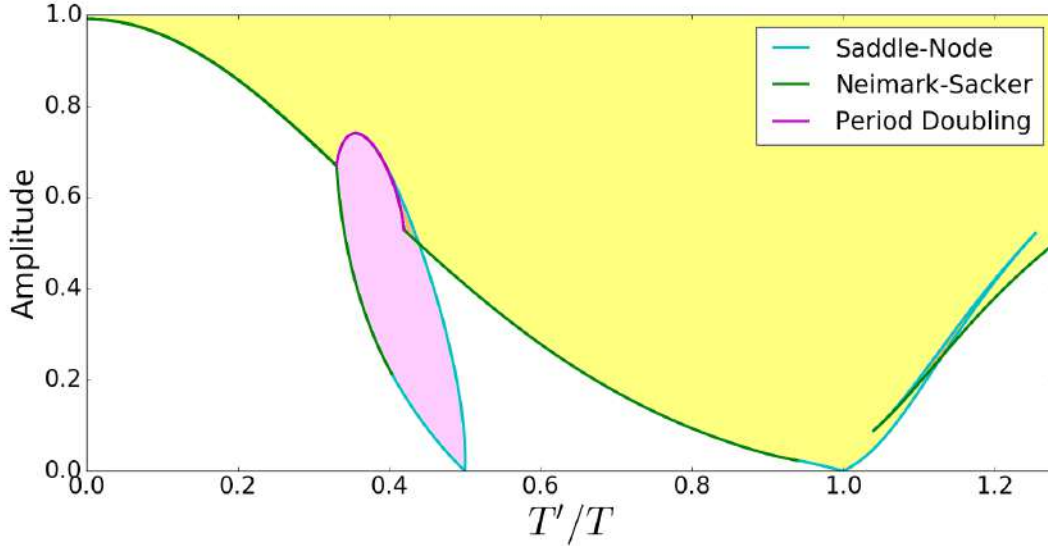


Figure 2.2: Bifurcation diagram for the fixed points of the stroboscopic map (2.4) as the frequency and the amplitude of the perturbation are varied. Solid lines correspond to bifurcations of stable fixed points whereas dashed ones correspond to bifurcations of unstable fixed points. The unperturbed case ($A = 0$) corresponds to the system (1.7) displaying a limit cycle Γ_{HB} .

parameters chosen so that the limit cycle Γ_{HB} or Γ_{SN} is close to a Hopf or a SNIC bifurcations, respectively. Results are shown in Figs. 2.2 and 2.3, respectively. In these Figures, there appear different coloured areas: the yellow and pink areas correspond to 1:1 and 1:2 phase locked states of the system (2.1), respectively. We recall that they correspond to fixed points (1:1) and 2-periodic-points (1:2) of the map F_A . The white areas, may contain other $p:q$ phase-locked states, as well as asynchronous states. Areas in orange contain more than one stable invariant for the map F_A .

As one can see, the diagram in Fig. 2.2 corresponding to the Γ_{HB} limit cycle near a Hopf bifurcation differs quantitatively from the diagram corresponding to Γ_{SN} limit cycle in Fig. 2.3. Indeed, one can observe that $p:q$ phase locked states are wider for Γ_{HB} (Fig. 2.2) than for Γ_{SN} (Fig. 2.3). This, as we will justify in Section 3.4.3 (see Fig. 3.8), is due to the different shape of the PRCs for the limit cycles arising from Hopf and SNIC bifurcations. Nevertheless, a detailed analysis of both figures, allows to perform a qualitative comparison of both diagrams. Thus, in both cases, the phase-locking areas are bounded by Saddle-Node bifurcation curves (for small values of A) and Neimark-Sacker bifurcation curves and Period-Doubling bifurcation curves for other values of the amplitude. For this reason, we will focus the analysis on the bifurcation diagram for Γ_{HB} in Fig. 2.2, as the numerical computations suggest the same dynamics is observed for Γ_{SN} in Fig. 2.3.

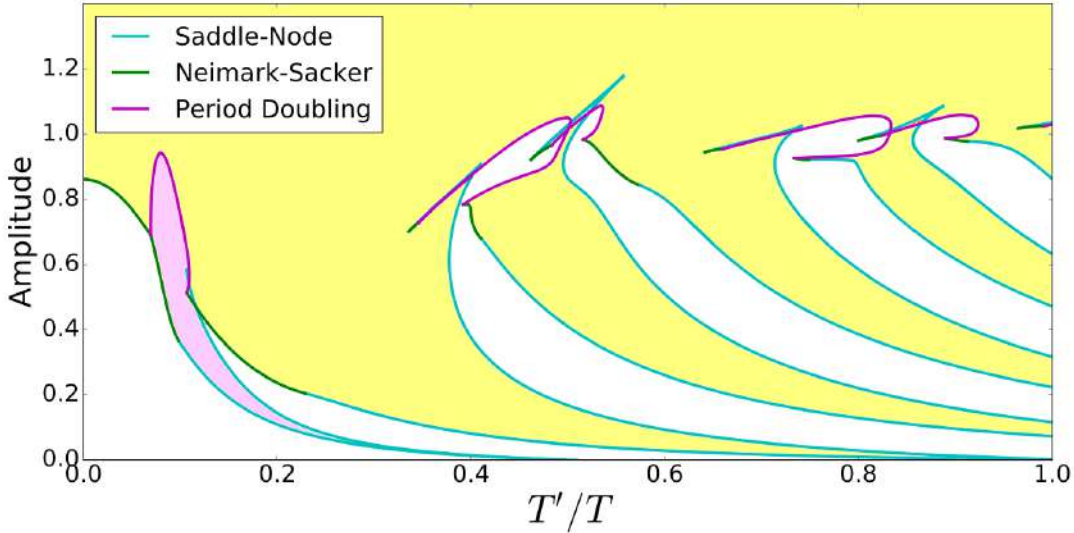


Figure 2.3: Bifurcation diagram for the stable points of the stroboscopic map (2.4) as the frequency and the amplitude of the perturbation are varied. The unperturbed case ($A = 0$) corresponds to the system (1.7) displaying a limit cycle Γ_{SN} .

2.3 Dynamics of the stroboscopic map F_A

In this Section we study in detail the bifurcation diagram in Fig. 2.2 corresponding to the stroboscopic map (2.4) as the amplitude and the frequency of the perturbation are varied. By choosing the set of parameters \mathcal{P} given in (1.17), $(P, Q) = (2.5, 0)$ and $A = 0$, the phase space for system (2.1) shows the limit cycle Γ_{HB} and the unstable focus P_1 (see Fig. 1.9 left). As both objects are normally hyperbolic we expect them to persist for amplitudes weak enough as an invariant curve Γ_A and a fixed point P_1 , respectively, for the corresponding stroboscopic map F_A in (2.4). The study that we perform in this Section focuses on 1:1 and 1:2 phase-locked states which occupy the largest regions of the parameter space.

Dynamics when crossing a Saddle-Node bifurcation

For values of T' such that $0.9388 < \frac{T'}{T} < 1.07$, the phase portrait for system (2.4) is shown in Fig. 2.4. In region A_1 , the attracting invariant curve Γ_A generated from the unperturbed limit cycle Γ_{HB} has no fixed points, and an unstable focus P_1 exists inside Γ_A . Once the saddle-node bifurcation (solid blue line) is crossed (region B), there appear two fixed points on the invariant curve Γ_A : a stable node P_2 and a saddle P_3 giving rise to a SNIC bifurcation. The invariant curve

consists of the union of the saddle P_3 , its unstable invariant manifolds, and the stable node P_2 . When increasing the amplitude (region C), P_1 becomes an unstable node (dashed gray line). If the amplitude is increased further, P_1 will coalesce with P_3 in a unstable saddle-node bifurcation (dashed blue line). This causes the disappearance of the invariant curve Γ_A and leaves the stable node P_2 as the unique fixed point (region D). As one may note it is possible to pass from area A_1 to area C, without passing through region B. When entering in the area A_2 the unstable focus P_1 becomes an unstable node before crossing the SN bifurcation curve.

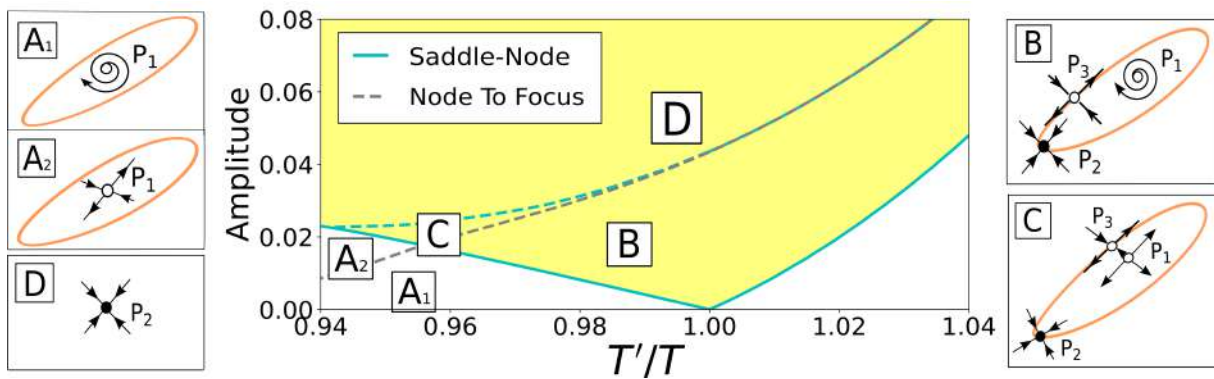


Figure 2.4: Dynamics when a Saddle-Node bifurcation is crossed.

Dynamics when crossing a Neimark-Sacker bifurcation

For values of T' such that $0.51 < \frac{T'}{T} < 0.9388$, the phase portrait for system (2.4) is shown in Fig. 2.5. For A small, the attracting invariant curve Γ_A has no fixed points of F_A , and an unstable focus P_1 exists inside Γ_A (region A). As the amplitude A is increased, this situation persists until it reaches the Neimark-Sacker bifurcation (green curve), where the curve Γ_A collapses to P_1 and disappears while P_1 becomes a stable focus (region B).

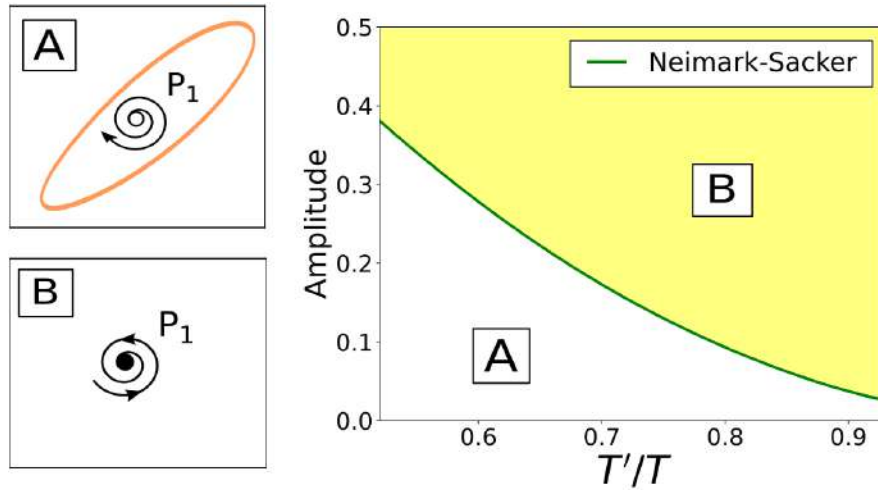


Figure 2.5: Dynamics when a Neimark-Sacker bifurcation is crossed.

Right hand side of the 1:2 Phase-Locking Area

For values of T' such that $0.48 < \frac{T'}{T} < 0.51$, the phase portrait for system (2.4) is shown in Fig. 2.6. For A small, the attracting invariant curve Γ_A has no fixed points of F_A , and an unstable focus P_1 exists inside Γ_A (region A). When the saddle-node bifurcation curve (blue curve) is crossed, there appear four fixed points on the invariant curve (Region B) for the map F_A^2 : two stable nodes (P_2 and P_4), and two saddles (P_3 and P_5). The invariant curve Γ_A consists of both saddles P_3 and P_5 and then unstable invariant manifolds and the two stable nodes P_2 and P_4 . As the amplitude is increased P_2, P_3, P_4 and P_5 pair-collide again on a saddle-node bifurcation (blue curve) and disappear leaving an attracting invariant curve without periodic points and the unstable fixed point P_1 (Region A). The amplitude of this invariant curve decreases as the amplitude A increases until it reaches a supercritical Neimark-Sacker bifurcation (green curve) for the map F_A leaving just a stable focus as the unique fixed point P_1 (Region C).

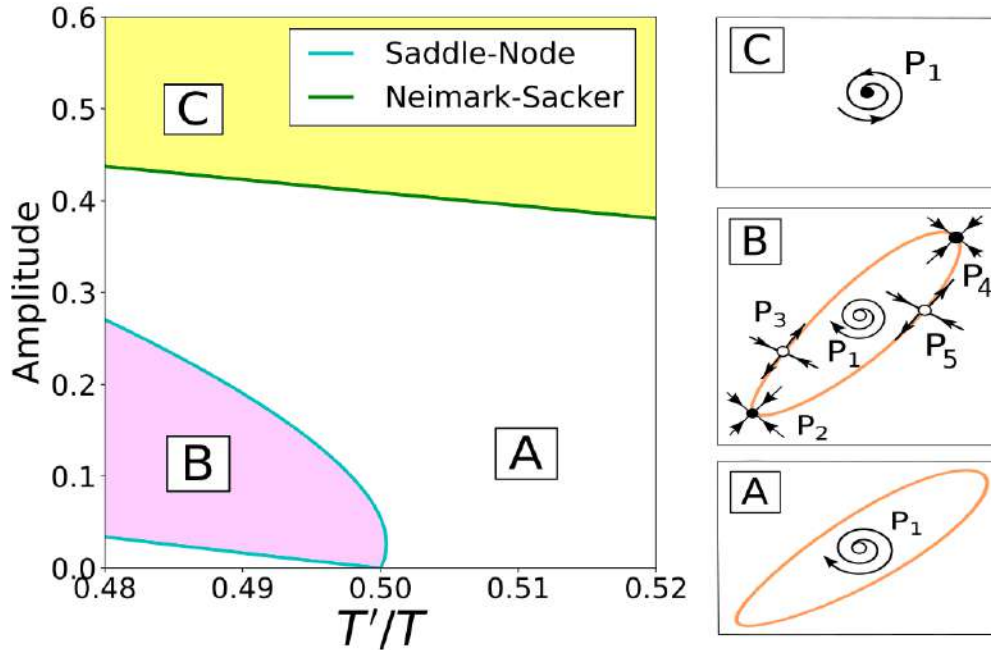


Figure 2.6: Dynamics generated on the right hand side of the 1:2 phase-locking area (see Fig. 2.2).

Central part of the 1:2 Phase-Locking Area

For values of T' such that $0.42 < \frac{T'}{T} < 0.48$, the phase portrait for system (2.4) is shown in Fig. 2.7. Once the saddle node bifurcation of F_A^2 is crossed (blue curve), there appear four fixed points on the invariant curve for the map $[F_A(x)]^2$: two stable nodes (P_2 and P_4), and two saddles (P_3 and P_5) (Region B). The invariant curve consists of the union of both saddles and their unstable invariant manifolds with the fixed points P_2 and P_4 . As amplitude A keeps increasing, very close to this saddle node bifurcation P_2 and P_4 become stable focuses (brown dashed curve), causing the invariant curve to disappear (Region C). In this area the only stable objects are the focuses P_2 and P_4 . As the amplitude is increased, this situation is maintained until P_2 and P_4 cross again the brown dashed curve and become stable nodes, causing the invariant curve to reappear as the union of the unstable invariant manifolds of P_3 and P_5 with the fixed points P_2 and P_4 and P_3 and P_5 (Region B').

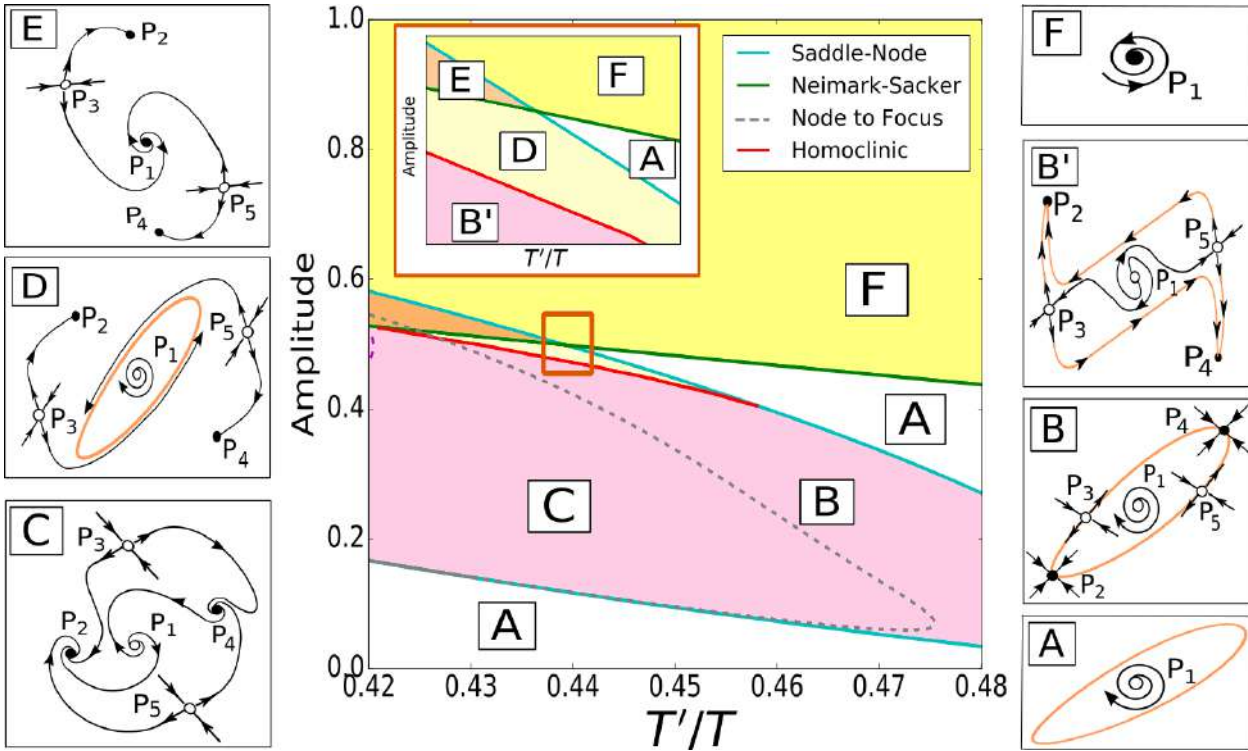


Figure 2.7: Dynamics on the central part of the 1:2 phase-locking area (see Fig. 2.2). For the sake of clarity we include a sketch of the bifurcations in the orange area.

As the amplitude is increased further, a homoclinic bifurcation is crossed (red curve) and a new invariant curve appears (Region D). Therefore, we have found a region where our system presents bistability between an attracting invariant curve and the fixed points P_2 and P_4 for F_A^2 . If the amplitude is increased further, a Neimark-Sacker bifurcation is crossed (green curve) making the invariant curve disappear and changing the stability of P_1 (Region E), leaving a situation where there exists coexistence between fixed points of F_A^2 (P_2, P_3, P_4, P_5) and F_A (P_1). This bistable situation between a 2-periodic orbit and a fixed point P_1 of $F_A(x)$ persists as the amplitude increases further until it reaches a Saddle-Node bifurcation (blue curve) for F_A^2 when the stable focus P_1 remains as the only fixed point (Region F).

For the sake of completeness we explain the method we have used to compute the homoclinic bifurcation curve. We integrate system (2.1) using an initial condition near the unstable focus P_1 . If an attracting invariant curve exists, this initial condition will tend to it for a large enough time of integration. Otherwise, the fixed points P_2 or P_4 will be the asymptotic solution. We consider then different values of the fraction $\frac{T'}{T}$, and vary the amplitude while checking which is the asymptotic solution. We delimit the bifurcation when we detect a qualitative change in the asymptotic solution.

Left hand side of the 1:2 Phase-Locking Area

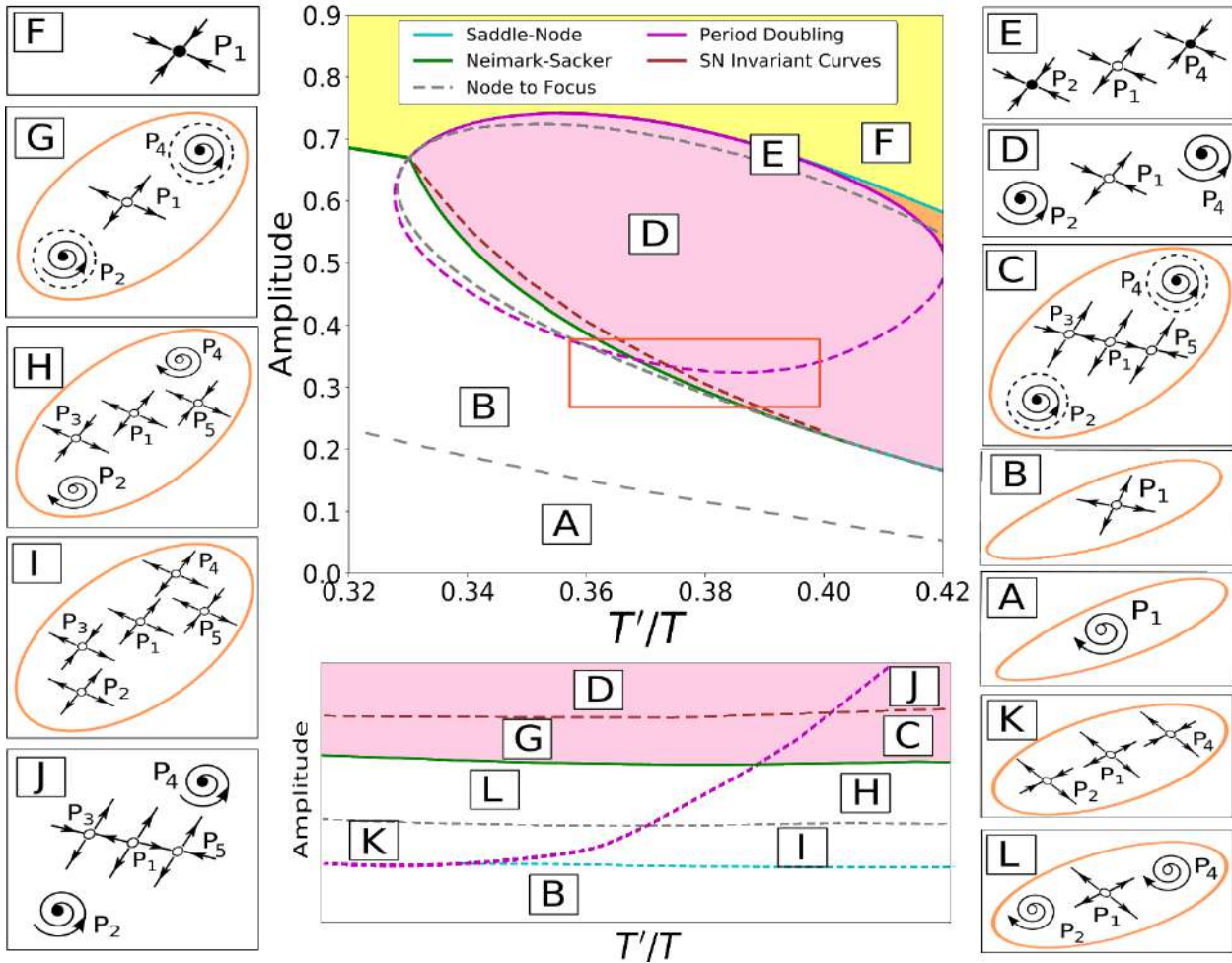


Figure 2.8: Dynamics on the left hand side of the 1:2 phase-locking area (see Fig. 2.2). For the sake of clarity we include a sketch of the bifurcations in the orange area.

For values of T' such that $0.32 < \frac{T'}{T} < 0.4$, the phase portrait is shown in Fig. 2.8. For A small a stable invariant curve and an unstable focus P_1 appear (Region A). When the amplitude increases, P_1 becomes an unstable node (dashed gray curve) (Region B). If the amplitude increases more, then one finds depending on the T' value considered, different bifurcation curves generating the appearance of unstable fixed points for F_A^2 . For $0.355 < \frac{T'}{T} < 0.4$, one finds that an unstable Saddle-Node bifurcation for F_A^2 is crossed (dashed blue curve) and two saddles (P_3 and P_5) and two unstable nodes (P_2 and P_4) appear as fixed points for the F_A^2 map (Region I). By contrast for 0.32

$< \frac{T'}{T} < 0.355$, one finds a period doubling bifurcation (dashed purple curve), from which there appear two unstable nodes (P_2 and P_4) (Region K). In both cases, a slightly increase of amplitude A causes the unstable node of F_A^2 to become an unstable focus (dashed gray line) (Regions H and K, respectively), which changes its stability at a subcritical Neimark-Sacker bifurcation (green curve). Thus an unstable invariant curve appears surrounding each of the stable focus (regions C and G, respectively), generating a situation of bistability between the invariant curve and the fixed points (P_2 and P_4). These invariant curves collide with the stable invariant curve collide in a saddle-node bifurcation of invariant curves, leaving the stable focus P_2 and P_4 as the unique attractors (brown-dashed curve) (regions D and J) respectively. Additionally there exists a tiny range of T'/T values for which, the one can see how unstable saddles (P_3 and P_5) disappear at a period doubling bifurcation.

So, for certain amplitude values and across different bifurcations, one ends up with the situation depicted in region D: the phase space is composed by a unstable node P_1 and two stable focus (P_2 and P_4) as fixed points for the map F_A^2 . Finally, for strong enough amplitudes, P_2 and P_4 , the stable focus for the map F_A^2 , become stable nodes (dashed gray line) (region E). Increasing the amplitude further, both points collapse at a period doubling bifurcation (solid purple line) where saddle P_1 becomes a stable node (region F).

Left hand side of the 1:1 Phase-Locking Area

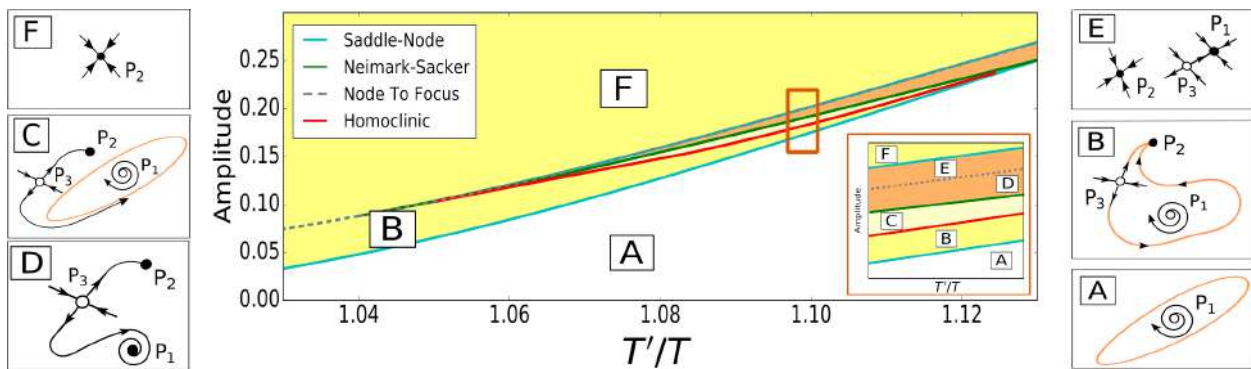


Figure 2.9: Dynamics on the left hand side of the 1:1 Phase-Locking Area (see Fig. 2.2). For the sake of clarity we include a sketch of bifurcations in the orange area.

For values of T' such that $1.04 < \frac{T'}{T} < 1.125$, the phase portrait for system (2.4) can be seen in Fig. 2.9. As Fig. 2.9 shows, the invariant curve Γ_A (Region A) evolves until crossing a Saddle-Node bifurcation (blue curve). From this bifurcation a stable node P_2 and a saddle P_3 are born and the invariant curve consists of the saddle P_2 and the union of its unstable invariant manifolds with

the stable node (Region B). Increasing the amplitude, dynamics over the invariant curve bifurcate through a homoclinic bifurcation (red curve) and there appears a stable invariant curve without fixed points, generating a bistable area where we have two attractors: the invariant curve and the fixed point P_2 (Region C). This invariant curve collapses at a Neimark-Sacker bifurcation (green curve), making the focus stable, and generating bistability between two fixed points (P_1 and P_2) (Region D). This situation persists until P_1 becomes a stable node (brown dashed line) (Region E) which coalesces with the saddle P_3 at a saddle node bifurcation (blue curve) and disappears leaving P_2 as the unique (stable) fixed point (Region F).

Right hand side of the 1:2 Phase-Locking Area

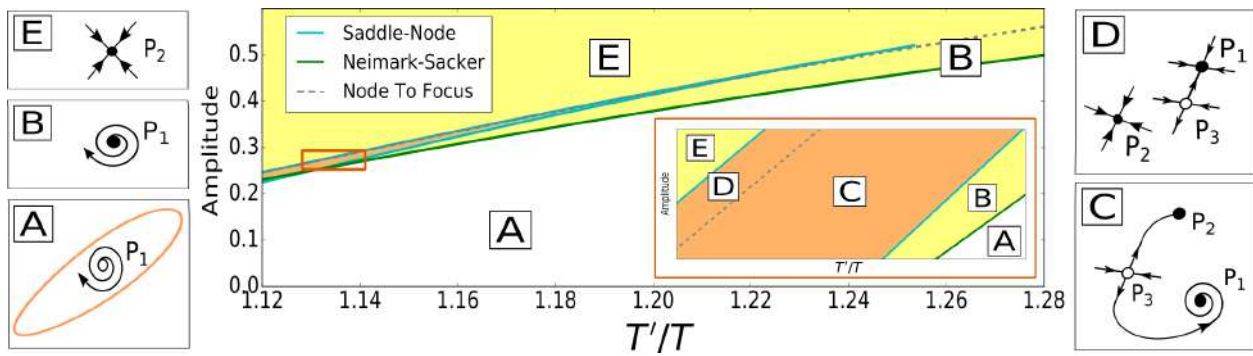


Figure 2.10: Dynamics on the right hand side of the 1:1 Phase-Locking Area. For the sake of clarity we include a sketch of bifurcations in the orange area.

For values of T' such that $1.125 < \frac{T'}{T} < 1.255$, the phase portrait for system (2.4) can be seen in Fig. 2.10. As the amplitude is increased, the invariant curve generated from the unperturbed limit cycle Γ (Region A) collapses at a Neimark-Sacker bifurcation (green curve), where the stability of the focus P_1 changes (Region B). If the amplitude is increased, a stable node P_2 and a saddle P_3 will appear at a Saddle-Node bifurcation (blue curve), generating a situation of bistability between the focus P_1 and the node P_2 (Region C). If the amplitude A increases further, P_1 will become a stable node (brown dashed line) (Region D) which will coalesce with P_3 at a Saddle-Node bifurcation, leaving node P_2 as the unique (stable) fixed point (Region E).

2.4 Discussion

In this Chapter we have performed a dynamical analysis of a periodic perturbation of the Wilson-Cowan equations. We have considered the stroboscopic map and performed a bifurcation analysis as a function of the perturbation parameters amplitude and frequency. We remark that the analysis performed does not have restrictions regarding the size of the amplitude or the value of the frequency. By computing the bifurcations of the stroboscopic map we obtained a diagram of the possible synchronous and asynchronous regions in the parameter space. We have focused in areas corresponding to 1:1 and 1:2 phase locking, and by performing a detailed dynamical analysis of the areas, we have found rich dynamics.

In general, our analysis revealed the existence in the parameter space of only one attracting object, either a fixed point for the map F (or F^2) or an invariant curve without fixed points on it, which correspond to stable synchronous or asynchronous regimes, respectively. In Fig. 2.11 we show the stable solutions corresponding to a synchronous and an asynchronous state. Notice that, the phase or time lag between the oscillations of the system and the perturbation is constant in the synchronous regime whereas it is not the case in the asynchronous regime.

Furthermore, the analysis in Section 2.3 revealed the existence of many different bistable areas. Namely,

- Bistability between a 2-periodic orbit and an invariant curve for the map F_A (panel D in Fig. 2.7 and panels C and G in Fig. 2.8).
- Bistability between a 2-periodic orbit and a fixed point of F_A (panel E in Fig. 2.7).
- Bistability between a fixed point and an invariant curve of the map F_A (panel C in Fig. 2.9).
- Bistability between two stable fixed points of the map F_A (panels D and E in Fig. 2.9 and panels C and D in Fig. 2.10).

These bistable areas can be interpreted in terms of the CTC framework. Bistability suggests that, for a given input, the population may operate in different regimes depending on the initial conditions (which in fact correspond to the initial phase between oscillators). More interestingly, the bistability areas that we have found can generate situations in which two different synchronous regimes are possible or co-existence of synchronous and asynchronous regimes.

In particular, as Fig. 2.12 illustrates, bistable situations between fixed points imply a defined phase locking relationship, suggesting that there can exist different encodings of the input by the receiving population depending on the initial phase difference. In this case, one of the solutions causes a larger variation in the activity of the E cells.

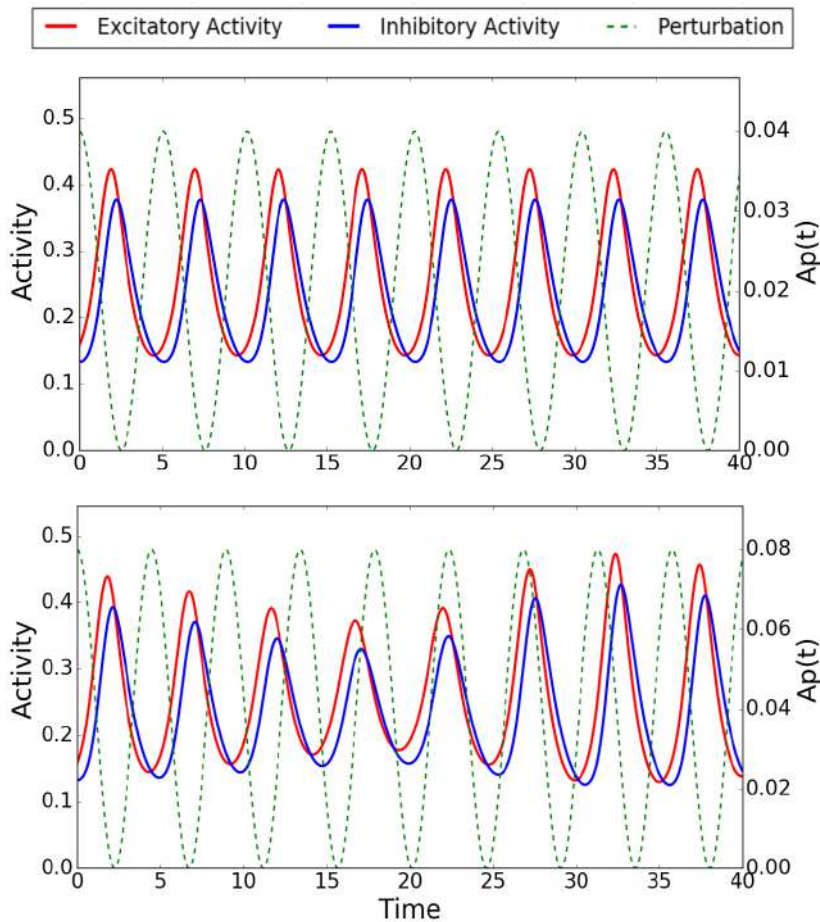


Figure 2.11: (Top) Synchronous solution of system (2.1) for $A = 0.02$ and $\frac{T'}{T} = 0.965$. (Bottom) Asynchronous solution of system (2.1) for $A = 0.04$ and $\frac{T'}{T} = 0.85$.

By contrast, as Fig. 2.13 illustrates, bistable situations between fixed points and attracting invariant curves, suggest that there might exist or not coherence between emitting and receiving neural groups depending on the initial condition. The absence of coherence (asynchronous regimes) prevents the communication between them.

Alongside, there are other results in this Chapter which can be related to the computational questions posed by the CTC theory, more precisely, the 1:2 phase-locking area. Indeed, one can interpret the 1:2 region as two identical inputs, $I_1(t)$ and $I_2(t)$, corresponding to different emitting neural populations, arriving to the receiving population separated by a half-period, so they are arriving in different phases of the oscillation (see Fig. 2.14 left). The effect of input $I_1(t)$ is to increase the firing rate of the population, while input $I_2(t)$ is mainly ignored (See Fig. 2.14 right). This observation opens the door to explore more thoroughly the effects of two emitting populations onto a receiving oscillatory population.

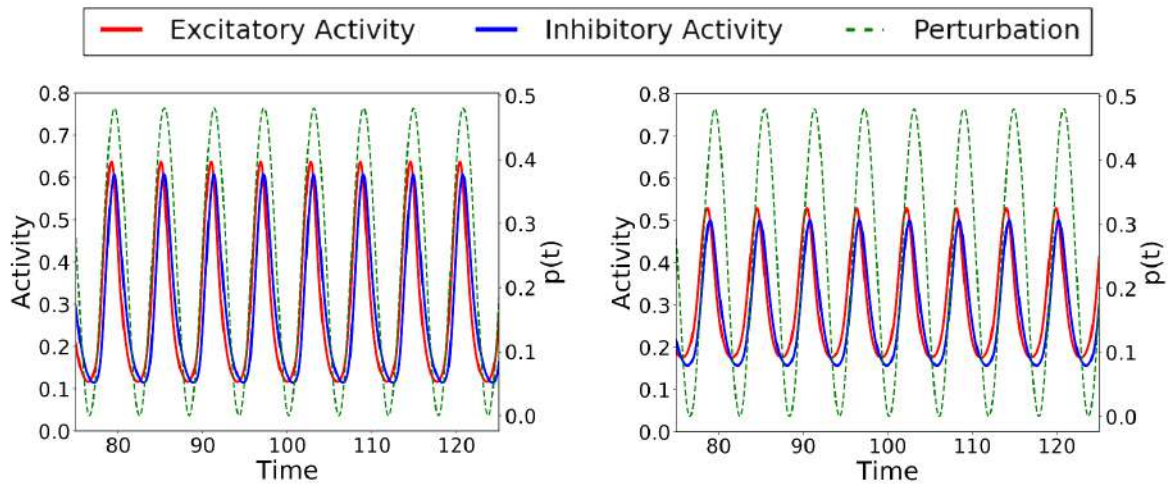


Figure 2.12: For a perturbation of $A = 0.24$ and $T'/T = 1.12$ system (2.1) shows bistability between two fixed points. This situation correspond to panel D in Fig. 2.10.

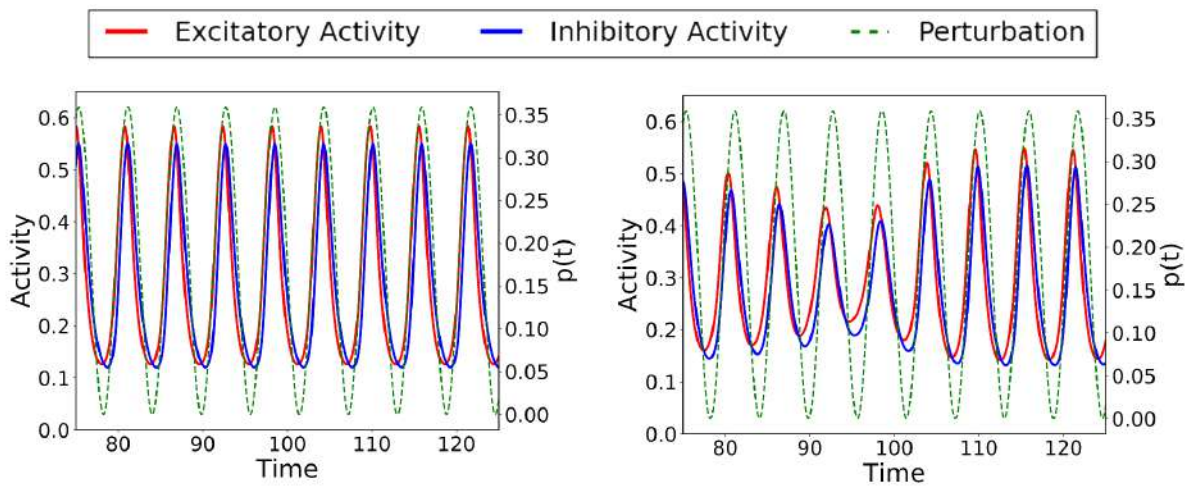


Figure 2.13: For a perturbation of $A = 0.1795$ and $T'/T = 1.1$ system (2.1) shows bistability between a fixed point and an invariant curve. This situation correspond to panel C in Fig. 2.9.

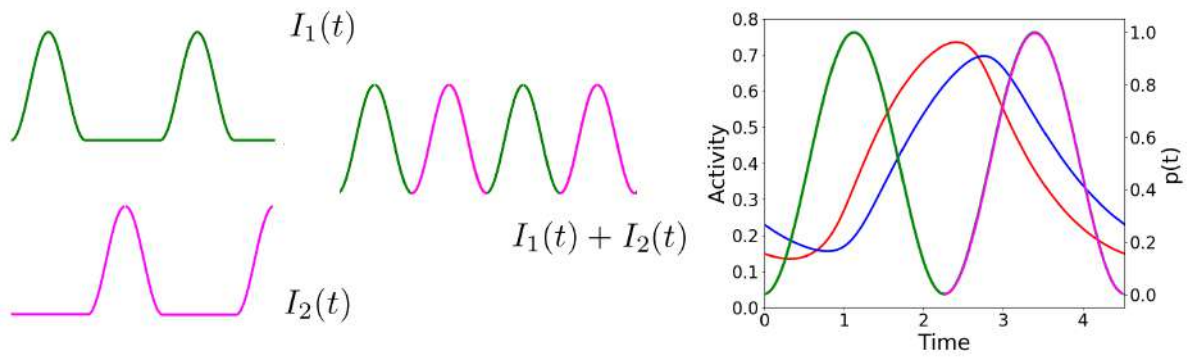


Figure 2.14: Left panel: 1:2 phase locked states can be thought as the sum of two identical inputs in anti-phase. Right panel: Time evolution of the activity of the E population (red) and the I population (blue) over one period under the forcing $p(t) = I_1(t) + I_2(t)$ described in the left panel.

Chapter 3

Neural Oscillations, phase and isochrons

In the previous Chapter, we have addressed a problem concerning the possible phase-locked states of a system due to a non-autonomous perturbation (a periodic forcing). To perform that study we used the stroboscopic map in terms of the original system variables. In this Chapter, we will motivate a change of variables which provides an alternative and complementary approach to the one performed previously. From the mathematical perspective, oscillations correspond to attracting limit cycles in the phase space whose dynamics can be described by a single variable: the phase. This phase variable will be the key concept of this Chapter.

Since perturbations displace trajectories away from the limit cycle, one may need to extend the phase variable out of the limit cycle. This extension can be done under generic conditions via the concepts of asymptotic phase and isochrons [37, 88]. An isochron is the sets of points in the basin of attraction of a limit cycle whose orbit approaches asymptotically the orbit of a given point on the limit cycle. We associate to these points the same phase as the base point on the limit cycle.

Isochron distribution is important because when the oscillator is perturbed with a transient external stimulus, the trajectory of each point is displaced away from the limit cycle and is sent to the isochron of a different point, thus causing a change in the phase of the oscillation. Phase displacements due to perturbations of the oscillator that act at different phases of the limit cycle are described by the so-called phase response curves (PRC) [24, 73]. PRCs constitute a useful tool to reduce the dynamics of the oscillator –which can appear in a system of higher dimension– to a single equation for the phase. This approach, based on the phase reduction, has been extensively used to study weakly perturbed nonlinear oscillators and predict synchronization properties in neuronal networks [16, 48].

Nevertheless, perturbations acting over an oscillation can occur during the transient state, in which trajectories have not relaxed yet to the limit cycle. Therefore, to predict correctly phase changes in the transient state, one needs to extend the PRC concept to a neighbourhood of the limit cycle. To that aim one needs to consider an extra variable: the amplitude variable (also known as isostable [84, 86]). This variable is transverse to the periodic orbit and controls the “distance” to the limit cycle [17, 82]. By using this variable one can define the phase response functions (PRFs) and the amplitude response functions (ARFs) which measure the change in phase and amplitude due to a perturbation acting over trajectories not necessarily on the limit cycle.

Therefore, the study of a given oscillatory system by means of the phase or phase-amplitude variables is of special interest. On one hand, it allows to interpret synchronization from a simple and more intuitive point of view since synchronization can easily be read from the relationship between phase variables. On the other hand, as we will show in this Chapter, it may allow to study a large dimensional system using a reduced set of equations.

In this Chapter we will review some of the main theory developed in the context of phase-amplitude variables (Sections 3.1 and 3.2) and how it can be used to describe the effects of perturbations over an oscillator (Section 3.3). Sections 3.4 and 3.5 will be devoted to study some models in neuroscience in 2 and 3 dimensions, respectively. The structure of Sections 3.4 and 3.5 will be similar: we start by computing a change of variables from the original system variables to phase amplitude variables that is valid on a neighbourhood of the limit cycle. Then, we will use this computation to obtain a local approximation of the isochrons and we use a numerical method to globalize them. Finally, we study the domains of applicability of some dimensional reductions when considering non autonomous perturbations.

Part of the work done in this Chapter has been published in [67].

3.1 Phase Variable and Isochrons

In this Section we introduce the phase variable. Start by considering an autonomous system of ODEs

$$\dot{x} = X(x), \quad x \in U \subseteq \mathbb{R}^d, \quad d \geq 2, \quad (3.1)$$

and let us denote its flow by $\phi_t(x)$.

Assume that X is an analytic vector field and that system (3.1) has a T -periodic hyperbolic limit

cycle Γ , parameterized by $\theta = t/T$ as

$$\begin{aligned} \gamma : \mathbb{T} := \mathbb{R}/\mathbb{Z} &\rightarrow \mathbb{R}^d \\ \theta &\mapsto \gamma(\theta), \end{aligned} \quad (3.2)$$

so that it has period 1, that is, $\gamma(\theta) = \gamma(\theta + 1)$ and $x(t) = \gamma(\frac{t}{T})$ satisfies (3.1). So, as one can see, the dynamics of (3.1) in Γ can be reduced to a single variable system

$$\dot{\theta} = \frac{1}{T}, \quad \theta \in \mathbb{T}. \quad (3.3)$$

As we study attracting limit cycles, it follows that any point in a neighbourhood Ω of the limit cycle Γ will tend to it as time tends to infinity. We will say that two points p and $q \in \Omega$ have the same asymptotic phase if

$$\lim_{t \rightarrow \infty} |\phi_t(q) - \phi_t(p)| = 0. \quad (3.4)$$

Therefore, we define the isochron \mathcal{I}_θ as the set of points having the same asymptotic phase θ [37], that is,

$$\mathcal{I}_\theta = \{x \in \Omega \mid |\phi_t(x) - \phi_t(\gamma(\theta))| = |\phi_t(x) - \gamma\left(\theta + \frac{t}{T}\right)| \rightarrow 0 \text{ as } t \rightarrow \infty\}. \quad (3.5)$$

When Γ is a normally hyperbolic attracting periodic orbit, isochrons are the leaves of the stable manifold \mathcal{M} of Γ , which coincides with its basin of attraction Ω .

3.2 Phase-Amplitude Variables, Isochrons and A-Curves

We look for a parameterization that allows us to extend the phase variable out of the limit cycle. To do so, we will look for a change of coordinates expressing the vector field X in (3.1) in the normal form for a d -dimensional vector field around an hyperbolic limit cycle. To that aim, we use the parameterization method introduced in [11, 12, 13] to obtain a parameterization of the limit cycle Γ and its stable invariant manifold \mathcal{M} (which in this case is the d -dimensional). The new coordinates will be the phase variable $\theta \in \mathbb{T}$ introduced in (3.1) and the amplitude variables $\sigma_1, \dots, \sigma_{d-1} \in \mathbb{R}$, corresponding to transverse directions to the limit cycle, whose dynamics is given by:

$$\dot{\theta} = \frac{1}{T}, \quad \dot{\sigma} = \Lambda \cdot \sigma, \quad \text{with} \quad \Lambda = \begin{pmatrix} \lambda_1 & & \\ & \ddots & \\ & & \lambda_{d-1} \end{pmatrix}, \quad (3.6)$$

where $\sigma = (\sigma_1, \dots, \sigma_{d-1}) \in \mathbb{R}^{d-1}$, and $\lambda_1, \dots, \lambda_{d-1}$ are the characteristic exponents of the limit cycle Γ . For simplicity we assume that the matrix Λ diagonalizes.

In this Chapter we will use the variational equations of system (3.1) along the solution $\gamma(\theta)$ as

$$\dot{\Phi} = DX(\gamma(t/T))\Phi, \quad \text{with } \Phi(0) = Id, \quad (3.7)$$

whose solution $\Phi(t)$ evaluated at $t = T$, $\Phi(T)$, is known as the Monodromy matrix. The eigenvalues of $\Phi(T)$, namely $\mu_i = e^{\lambda_i T}$, $i = 0, \dots, d-1$, are known as the Floquet multipliers of the limit cycle Γ and the values λ_i as the characteristic exponents. The index $i = 0$ will be assigned from now on to the trivial multiplier $\mu_0 = 1$, so $\lambda_0 = 0$.

From [13], we know that there exists an analytic map

$$\begin{aligned} K : \mathbb{T} \times \mathbb{R}^{d-1} &\rightarrow \mathbb{R}^d \\ (\theta, \sigma) &\rightarrow K(\theta, \sigma), \end{aligned} \quad (3.8)$$

such that the flow of the vector field X in (3.1) on $\mathcal{M} \subset \mathbb{R}^d$ expressed in the new variables (θ, σ) satisfies

$$\phi_t(K(\theta, \sigma)) = K\left(\theta + \frac{t}{T}, e^{\Lambda t} \sigma\right). \quad (3.9)$$

That is, the dynamics for θ consists on a rigid rotation, whereas the dynamics for σ_i consists of a contraction whose rate is given by λ_i . Furthermore, since $\Phi_t(K(\theta, \sigma))$ is a solution of system (3.1), the parameterization $K(\theta, \sigma)$ satisfies the following invariance equation

$$\frac{1}{T} \frac{\partial}{\partial \theta} K(\theta, \sigma) + \sum_{i=1}^{d-1} \lambda_i \sigma_i \frac{\partial}{\partial \sigma_i} K(\theta, \sigma) = X(K(\theta, \sigma)). \quad (3.10)$$

Once it has been found, we can use the map K to define a scalar function $\Theta(x)$ such that it assigns a phase to any point in a neighbourhood Ω of the limit cycle Γ :

$$\begin{aligned} \Theta : \Omega \subset \mathbb{R}^d &\rightarrow \mathbb{T} = [0, 1), \\ x &\mapsto \Theta(x) = \theta \quad \text{if } x \in \mathcal{I}_\theta. \end{aligned} \quad (3.11)$$

Analogously, $\Theta(x) = \theta$ if $\exists \sigma \in \mathbb{R}$ such that $x = K(\theta, \sigma)$. This function $\Theta(x)$ satisfies: $\Theta(\phi_t(x)) = \Theta(x) + \frac{t}{T}$. Isochrons \mathcal{I}_θ given in (3.5) will be the level curves of $\Theta(x)$:

$$\mathcal{I}_\theta = \{x \in \Omega \mid \Theta(x) = \theta\}. \quad (3.12)$$

Analogously, we can define a function Σ that assigns a value for the amplitude variable to any point $x \in \Omega$:

$$\begin{aligned} \Sigma_i : \Omega \subset \mathbb{R}^d &\rightarrow \mathbb{R}, \\ x &\mapsto \Sigma_i(x) = \sigma_i, \end{aligned} \quad (3.13)$$

where $\Sigma(x) = \sigma$ if $\exists \theta \in \mathbb{T}$ such that $x = K(\theta, \sigma)$. This function $\Sigma(x)$ satisfies: $\Sigma(\phi_t(x)) = \Sigma(x)e^{\frac{\lambda t}{T}}$. The level curves of Σ will be called, *A-curves* in [17] and are referred to *isostables* in [56, 57].

$$\mathcal{A}_c^i = \{x \in \Omega \mid \Sigma_i(x) = c\}. \quad (3.14)$$

From its definition, for $x \in \Omega$, one has $K^{-1}(x) = (\Theta(x), \Sigma(x))$.

3.3 Non Autonomous Perturbation

In this Section we consider perturbed systems of the form

$$\dot{x} = X_A(x, t) = X(x) + Ap(x, t; A), \quad (3.15)$$

and we discuss how they can be written in terms of the phase amplitude variables.

3.3.1 Phase Reduction Approach

When considering perturbations over trajectories on a limit cycle, the classical approach is using the phase reduction [89]. This approach assumes that, for weak enough perturbations, the dynamics can be described by the phase variable defined on the oscillator.

Let us start by considering that the perturbation acting over a T -periodic limit cycle is an instantaneous pulse,

$$p(x, t; A) = \delta(t - t_s), \quad (3.16)$$

where $\delta(t)$ is the Dirac delta function. The perturbation will move trajectories from one isochron to another, causing a phase shift. The phase shift will depend on the amplitude of the pulse and on the phase at which it was applied. Thus, one can define the so called Phase Response Curves (PRCs). They are calculated by applying the same pulse to the limit cycle at different phases and registering how much the phase is advanced (or delayed) (See Fig. 3.1). Let $x = \gamma(\theta)$ be a point on the limit cycle. Note that $\Theta(x) = \theta$ by definition. If we consider an arbitrary pulsatile perturbation, it is clear that it will move x to $x_{new} = x + \Delta x$. Thus, the PRC is defined as

$$PRC(A, \theta) = \theta_{new} - \theta, \quad (3.17)$$

where $\theta_{new} = \Theta(x_{new})$.

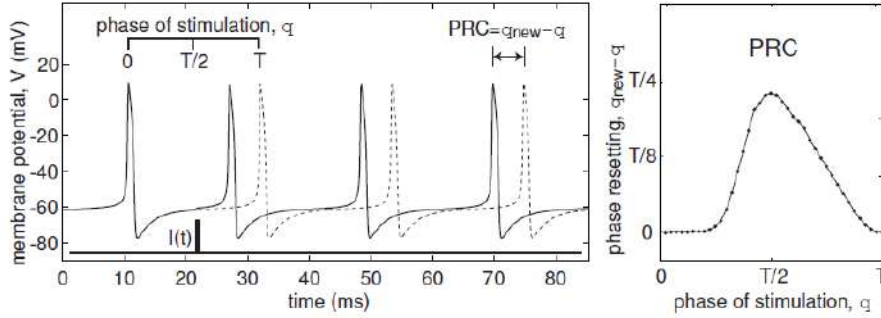


Figure 3.1: The phase of a neuronal oscillator changes due a pulsatile perturbation. The dashed voltage trace is the free-running trajectory, while the solid line shows the perturbed trajectory. PRCs show the phase shift as a function of the phase of perturbation. Picture from [51].

The expression for the PRCs given in (3.17) is a general expression. One can consider the case in which the perturbation is small, and derive an approximate expression for it. The new phase is

$$\theta_{new} = \Theta(x + \Delta x) = \Theta(x) + \nabla\Theta(x) \cdot \Delta x + O(|\Delta x|^2), \quad (3.18)$$

and therefore, for small amplitude pulse-like perturbations

$$\theta_{new} - \theta = PRC(\Delta x, \theta) \simeq \nabla\Theta(\gamma(\theta)) \cdot \Delta x. \quad (3.19)$$

Thus, for small Δx , one can relate the PRCs and the phase function Θ introduced in (3.11) by means of $\nabla\Theta(\gamma(\theta))$, which is usually known as the Infinitesimal Phase Response Curve (iPRC). Although it has d components, usually one just considers the x -component, as it usually corresponds to the voltage of the neuron, the physical magnitude which is usually perturbed.

There are some methods to calculate the iPRC $\nabla\Theta(\gamma(\theta))$. The classical one is the so-called adjoint method [25], that we briefly review here. Let $\gamma(t/T)$ be the T -periodic solution of the system (3.1), then $\nabla\Theta(\gamma(t/T))$ is a T -periodic solution of the system:

$$\frac{dQ}{dt} = -DX^T(\gamma(t/T))Q, \quad (3.20)$$

satisfying the normalization condition $\langle Q(t), X(\gamma(t/T)) \rangle = \frac{1}{T}$. In next Section we provide an alternative method to compute iPRC in terms of the parameterization $K(\theta, \sigma)$ defined in (3.8).

Applications of the iPRC and PRC

The PRC can be used to study the dynamical effect of a periodic train of pulses of period T_s onto an oscillator. The stroboscopic map, also called the Poincaré Phase Map, describing the phase

at the impact times, has the following expression as a function of the PRC:

$$\theta_{n+1} = f(\theta_n) = \theta_n + PRC(A, \theta_n) + \frac{T_s}{T}. \quad (3.21)$$

For weak amplitude stimulus it can be approximated by

$$\theta_{n+1} = f(\theta_n) \approx \theta_n + A \cdot iPRC(\theta_n) + \frac{T_s}{T}. \quad (3.22)$$

If we consider the case of a general continuous perturbation, the phase dynamics for the unperturbed system (3.15) (case $A = 0$) is given by the equation

$$\frac{d\Theta(x)}{dt} = \nabla\Theta(x) \cdot \frac{dx}{dt} = \nabla\Theta(x) \cdot X(x), \quad (3.23)$$

and as phase dynamics satisfies $\dot{\theta} = \frac{1}{T}$, we have

$$\nabla\Theta(x) \cdot X(x) = \frac{1}{T} \quad \text{for } x = \gamma(\theta). \quad (3.24)$$

Then, for $A \neq 0$, we have (see [53])

$$\dot{\theta} = \nabla\Theta(x) \cdot X_A(x, t) = \nabla\Theta(x) \cdot \{X(x) + Ap(x, t; A)\} = \frac{1}{T} + A\nabla\Theta(x) \cdot p(x, t; A), \quad (3.25)$$

which provides an equation that describes the effects of a perturbation $p(x, t; A)$ on the phase. Recall that $\nabla\Theta(\gamma(\theta))$ is the iPRC.

3.3.2 Phase-Amplitude Approach and Phase-Amplitude Response Functions

The phase approach assumes that during the interval in which the perturbation is acting, the trajectories are close to the limit cycle. This approach is suitable for continuous perturbations of weak amplitude or trains of pulses whose interpulse interval is large enough. It turns out that this will not be the case for a general perturbation $Ap(x, t; A)$ in (3.15), specially as the amplitude A is increased. This makes clear the interest of considering the phase-amplitude approach to study the dynamics in a neighbourhood $\Omega \in \mathcal{M}$. Next, we will explain how to compute the perturbed dynamics in this framework.

Let us start by considering a pulsatile perturbation acting over a point $x = K(\theta, \sigma) \in \Omega$ and thus displacing it from x to $x + \Delta x$. Therefore the new phase θ_{new} and the new amplitude variables σ_{new} are given by:

$$\begin{aligned}\theta_{new} &= \Theta(x) + PRF(A, \theta, \sigma), \\ \sigma_{new} &= \Sigma(x) + ARF(A, \theta, \sigma),\end{aligned}\tag{3.26}$$

where, following [17, 39], we have introduced the Phase Response Functions (PRFs) and the Amplitude Response Functions (ARFs). Analogously to the PRC concept for the phase reduction in (3.17), they quantify how the phase and the amplitude change due to the effect of the perturbation at a given point $x = K(\theta, \sigma) \in \Omega$, respectively. Notice that PRC is just the PRF restricted to the limit cycle ($\sigma = 0$). Analogously, one can define the Amplitude Response Curves (ARCs) as:

$$ARC(A, \theta) = ARF(A, \theta, \sigma)|_{\Gamma}.\tag{3.27}$$

For the case of a pulse of weak amplitude we have

$$\begin{aligned}\theta_{new} &= \Theta(x + \Delta x) = \Theta(x) + \nabla\Theta(x) \cdot \Delta x + O(|\Delta x|^2), \\ \sigma_{new} &= \Sigma(x + \Delta x) = \Sigma(x) + \nabla\Sigma(x) \cdot \Delta x + O(|\Delta x|^2),\end{aligned}\tag{3.28}$$

for $x \in \Omega$. Thus, one can define, analogously to the iPRCs in (3.19), the iPRFs and the iARFs as $\nabla\Theta(x)$ and $\nabla\Sigma(x)$, respectively.

Analogously to the adjoint equation for the iPRC given in (3.20), one can compute the iPRF and the iARF using the adjoint methods. The iPRF $\nabla\Theta(x)$ satisfies the following adjoint equation

$$\frac{dQ}{dt} = -DX^T(\phi(x, t))Q,\tag{3.29}$$

with the normalization condition $\langle Q(t), X(\phi(x, t)) \rangle = \frac{1}{T}$.

Analogously, $Q = \nabla\Sigma_i(x)$ satisfies the following adjoint equation, derived in [17, 84]:

$$\frac{dQ}{dt} = (\lambda_i - DX^T(\phi(x, t)))Q,\tag{3.30}$$

with the normalization condition $\langle Q(t), v_i \rangle = 1$, where v_i is the eigenvector associated to the i -th multiplier of the Monodromy matrix (see Eq. (3.7)).

An alternative method to compute the iPRF, $\nabla\Theta$ and the iARF $\nabla\Sigma$ can be found in [17]. By using $K(\Theta(x), \Sigma_1(x), \dots, \Sigma_{d-1}(x)) = x$, where K is the parameterization in (3.37), and taking derivatives, we have

$$\begin{bmatrix} 1 & & & \\ & \ddots & & \\ & & & 1 \end{bmatrix} = [DK(\theta, \sigma)] \begin{bmatrix} \nabla\Theta(x) \\ \nabla\Sigma_1(x) \\ \vdots \\ \nabla\Sigma_{d-1}(x) \end{bmatrix},$$

and therefore

$$\begin{bmatrix} \nabla\Theta(x) \\ \nabla\Sigma_1(x) \\ \vdots \\ \nabla\Sigma_{d-1}(x) \end{bmatrix} = [DK(\theta, \sigma)]^{-1}, \quad (3.31)$$

for $x = K(\theta, \sigma) \in \Omega$:

Applications of the PRF and the ARF

For perturbations that are pulsatile and T_s -periodic, the stroboscopic map at time T_s can be written explicitly as (see [17]):

$$\begin{aligned} \theta_{k+1} &= \theta_k + PRF(A, \theta_k, \sigma_k) + \frac{T_s}{T}, & (\text{mod } 1) \\ \sigma_{k+1} &= (\sigma_k + ARF(A, \theta_k, \sigma_k))e^{\Lambda T_s}, \end{aligned} \quad (3.32)$$

which in the case of weak enough perturbations can be approximated by

$$\begin{aligned} \theta_{k+1} &\approx \theta_k + A\nabla\Theta(K(\theta_k, \sigma_k)) + \frac{T_s}{T}, & (\text{mod } 1) \\ \sigma_{k+1} &\approx (\sigma_k + A\nabla\Sigma(K(\theta_k, \sigma_k)))e^{\Lambda T_s}. \end{aligned} \quad (3.33)$$

For the general case of $p(t)$ being a continuous perturbation, the phase-amplitude approach describes the perturbed dynamics in the following way:

$$\begin{aligned} \dot{\theta} &= \nabla\Theta(x) \cdot X_A(x, t) = \nabla\Theta(x) \cdot \{X(x) + Ap(x, t; A)\} = \frac{1}{T} + A\nabla\Theta(x) \cdot p(x, t; A), \\ \dot{\sigma}_i &= \nabla\Sigma_i(x) \cdot X_A(x, t) = \nabla\Sigma_i(x) \cdot \{X(x) + Ap(x, t; A)\} = \lambda_i\sigma_i + A\nabla\Sigma_i(x) \cdot p(x, t; A), \end{aligned} \quad (3.34)$$

for $i = 1, \dots, d-1$ and $x = K(\theta, \sigma)$.

3.4 The 2D case

In this Section we apply the general framework described in Sections 3.1, 3.2 and 3.3 to a 2D planar system: the Wilson-Cowan equations. Methodology to obtain the parameterization $K(\theta, \sigma)$ in (3.8) near a limit cycle Γ for a 2D planar system was studied in [39]. Next, we review the methods introduced in [39] for computing numerically $K(\theta, \sigma)$. Then, we will use $K(\theta, \sigma)$ to globalize the isochrons \mathcal{I}_θ and the A-curves \mathcal{A}_σ for the limit cycles of the Wilson-Cowan equations

(1.7), Γ_{HB} and Γ_{SN} , which arise from Hopf and SNIC bifurcations, respectively. Our main goal, is to apply a T' -periodic non-autonomous perturbation to system (1.7) and study the perturbed dynamics in terms of phase amplitude variables and the phase reduction.

3.4.1 Numerical computation of $K(\theta, \sigma)$

We consider system (3.1) for $d = 2$, and we impose that the equations in phase-amplitude variables are

$$\begin{aligned}\dot{\theta} &= \frac{1}{T}, \\ \dot{\sigma} &= \frac{\lambda\sigma}{T},\end{aligned}\tag{3.35}$$

where T is the period of the limit cycle Γ and λ is the characteristic exponent of Γ ; since the limit cycle is hyperbolic stable, we will have that $\lambda < 0$.

Remark 3.4.1. Notice that in (3.35) in order to avoid stodgy notation, we have defined $\sigma_1 = \sigma$ and $\lambda_1 = \lambda$. In general in the 2D case we avoid the i subscripts. We also will follow the notation introduced in [39] so dynamics for σ is divided by T . The only change is that one has to replace λ by $\frac{\lambda}{T}$ in previous equations.

Therefore we will use that the parameterization K in (3.8) satisfies the following invariance equation

$$\left(\frac{1}{T}\partial_\theta + \frac{\lambda\sigma}{T}\partial_\sigma\right)K(\theta, \sigma) = X(K(\theta, \sigma)),\tag{3.36}$$

to solve it and obtain an expression for $K(\theta, \sigma)$.

In order to solve the invariance equation (3.36), we write $K(\theta, \sigma)$ in Fourier-Taylor series:

$$K(\theta, \sigma) = \sum_{n=0}^{\infty} K_n(\theta)\sigma^n,\tag{3.37}$$

where $K_n(\theta)$ are 1-periodic real functions in θ :

$$K_n(\theta) = a_0^n + \sum_{k>0} a_k^n \cos(2\pi k\theta) + b_k^n \sin(2\pi k\theta).\tag{3.38}$$

Substituting (3.37) in (3.36) and matching similar coefficients in σ^n , we are left with the following equations for K_n $n \geq 0$:

$$\begin{aligned} \frac{1}{T} \frac{d}{d\theta} K_0 &= X(K_0), & \text{for } n = 0 \\ \frac{1}{T} \frac{d}{d\theta} K_1 + \frac{\lambda}{T} K_1 &= DX(K_0)K_1, & \text{for } n = 1 \\ \frac{1}{T} \frac{d}{d\theta} K_n + \frac{n\lambda}{T} K_n &= DX(K_0)K_n + R_n, & \text{for } n \geq 2 \end{aligned}$$

where R_n is the n^{th} order term of the Taylor expansion of $X \left(\sum_{l=0}^{n-1} K_l(\theta) \sigma^l \right)$. Notice that R_n is an explicit polynomial depending on the functions $K_0, K_1 \dots K_{n-1}$, whose coefficients are the derivatives of X evaluated at K_0 , which will be numerically computed using automatic differentiation techniques [41]. Automatic differentiation (see [36] and [42]) consists in a set of algorithms for computing the derivatives of arbitrary order of a multivariate function evaluated at a fixed value. By writing the vector field X as a combination of algebraic operations and elementary functions (exp, log, sin, cos, ...) and using the chain rule we compute efficiently the terms in R_n .

The numerical implementation requires to choose some values $N, L > 0$ and truncate the power series at order L and the corresponding Fourier series at order N . As a consequence, we can only compute a local approximate solution \bar{K} of the invariance equation (3.36). Given a fixed tolerance E , the approximate solution \bar{K} , will have a domain of accuracy $\Omega_{loc}(E)$ defined as:

$$\Omega_{loc}(E) := \{(\theta, \sigma) \in \mathbb{T} \times \mathbb{R} \mid \| D\bar{K}(\theta, \sigma)\mathcal{X}(\theta, \sigma) - X(\bar{K}(\theta, \sigma)) \| < E\}, \quad (3.39)$$

where $\mathcal{X}(\theta, \sigma) = \left(\frac{1}{T}, \frac{\lambda}{T}\sigma \right)^\top$.

Table 3.1 shows the numerical values at which we have truncated the series for the two dynamical regimes exhibited by system (1.7). Notice the difference on the number of Fourier coefficients used in the computations for each case. As it is discussed in [39], the periodic orbit Γ_{SN} needs a larger number of points to discretize it properly due to the inhomogeneous dynamics over the limit cycle. Fig. 3.2 shows the limit cycles and the error in the set $\Omega_{loc}(E)$ with $E = 10^{-3}$ for the two cases studied.

P	Q	Dynamic Regime	T	λ	L	N
2.5	0	Γ_{HB}	5.26	0.825	15	$2^8 = 256$
1.4	-0.75	Γ_{SN}	23.54	16.95	5	$2^{11} = 2048$

Table 3.1: Parameter values for the limit cycles of system (1.7), Γ_{HB} and Γ_{SN} arising from Hopf and SNIC bifurcations, respectively. T and λ are the computed period and the characteristic exponent respectively of the periodic orbit Γ . L and N represent the truncation order of the Taylor and the Fourier series, respectively.

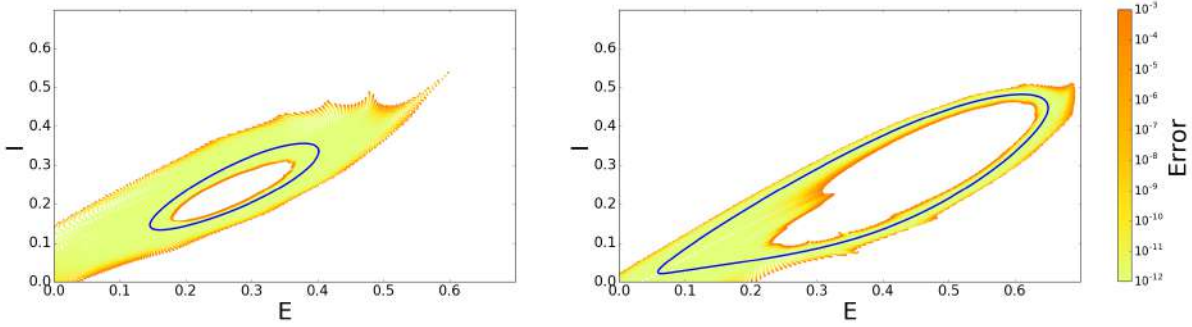


Figure 3.2: Limit cycles Γ_{HB} (left) and Γ_{SN} (right) (blue curves) and error of the computed local parameterizations for the Wilson-Cowan equations (1.7)

3.4.2 Globalizing \mathcal{I}_θ , \mathcal{A}_σ and $K(\theta, \sigma)$

Once we have computed $K(\theta, \sigma)$ for $\theta, \sigma \in \Omega_{loc}(E)$, we can obtain the local isochrons \mathcal{I}_θ and the A-curves \mathcal{A}_σ by fixing the parameters θ and σ , respectively.

In this Section we propose a method to globalize simultaneously the isochrons \mathcal{I}_θ , and the A-curves \mathcal{A}_σ . Start by considering a value of $\sigma = \sigma^*$ such that the corresponding A-curve, \mathcal{A}_{σ^*} defined in (3.14) is contained in $\Omega_{loc}(E)$ defined in (3.39) for E small enough. We parameterize \mathcal{A}_{σ^*} by $K_{\sigma^*} := K(\cdot, \sigma^*)$. We will extend the local isochron $\mathcal{I}_{\theta^*_{loc}} = \{x \in \Omega \mid x = K(\theta^*, \sigma) \text{ for } \sigma \leq \sigma^*\}$. Consider the point on the A-curve \mathcal{A}_{σ^*} given by $K(\theta^* + \frac{\Delta t}{T}, \sigma^*)$. It is straightforward to see that the point $\phi_{-\Delta t}(K(\theta^* + \frac{\Delta t}{T}, \sigma^*)) = K(\theta^*, \sigma^* e^{-\frac{\lambda \Delta t}{T}})$ will belong to the isochron \mathcal{I}_{θ^*} (see Fig. 3.3). Therefore, varying Δt and repeating the procedure described above one can globalize the isochron \mathcal{I}_{θ^*} and furthermore, its parametrization by σ . More precisely we obtain $x_j \in \mathcal{I}_{\theta^*}$ and σ_j for $j = 0, \dots, M$ such that $x_j = K(\theta^*, \sigma_j)$ for $\sigma_j = \sigma^* e^{-\frac{j \lambda \Delta t}{T}}$ for $j = 0, \dots, M$. By repeating the same procedure for θ in \mathbb{T} one can globalize the isochron \mathcal{I}_{θ^*} .

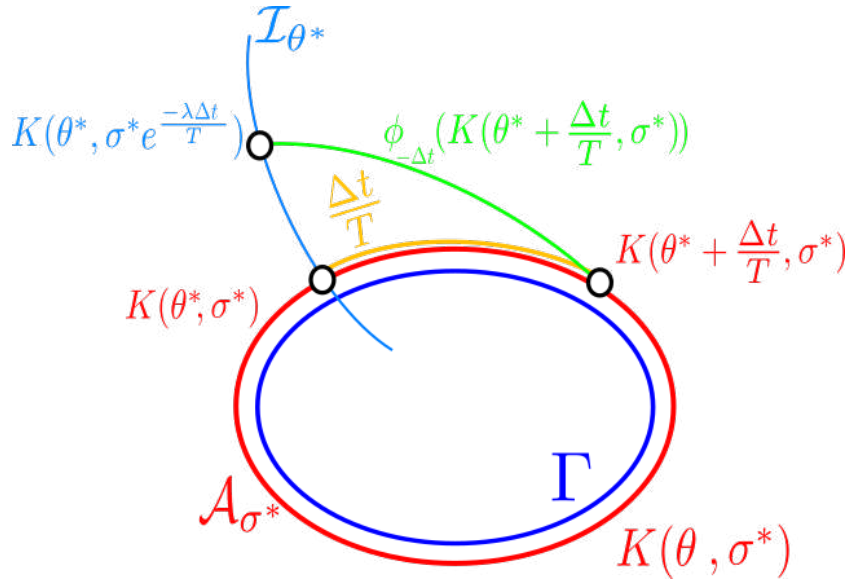


Figure 3.3: Sketch for the globalization method.

Moreover, if the isochrons are globalized using the same set of discrete values σ , one can easily obtain the A-curves \mathcal{A}_{σ_j} where $\sigma_j = \sigma^* e^{-\frac{j\lambda\Delta t}{T}}$. It is important to remark that this method is a different from the one introduced in [39]. The one presented in this Section considers the use of the A-curves to globalize the isochrons. As the A-curve \mathcal{A}_{σ^*} used to globalize is discrete, we make use of interpolation. Although this interpolation introduces certain errors, thus making it less precise than the method in [39] which relies only on the computed local isochrons, it has the advantage of having better control of its parameterization by σ .

The numerical method preserves the main numerical controls used in [39]. In particular, by means of changing Δt it is possible to control the distance $\|\Delta x\|$ between points of the same isochron. This allows us to ensure that the distance between points globalizing a given isochron is always smaller than a certain value. Alternative strategies to compute isochrons can be found in [55, 56, 65].

As one can see the globalization of \mathcal{I}_{θ} and \mathcal{A}_{σ} allows a better knowledge of the attracting dynamics near the limit cycle. By globalizing the isochrons one can see the phase distribution around the limit cycle. Moreover, by globalizing the A-curves one can see how different is the contraction towards the limit cycle.

In Figures 3.4, 3.5, 3.6, 3.7, we show, as an example of application of the techniques in [39] and the globalization methods introduced in this Section, the numerical computation of the isochrons \mathcal{I}_{θ} and the A-curves \mathcal{A}_{σ} for system (1.7) with limit cycles Γ_{HB} and Γ_{SN} .

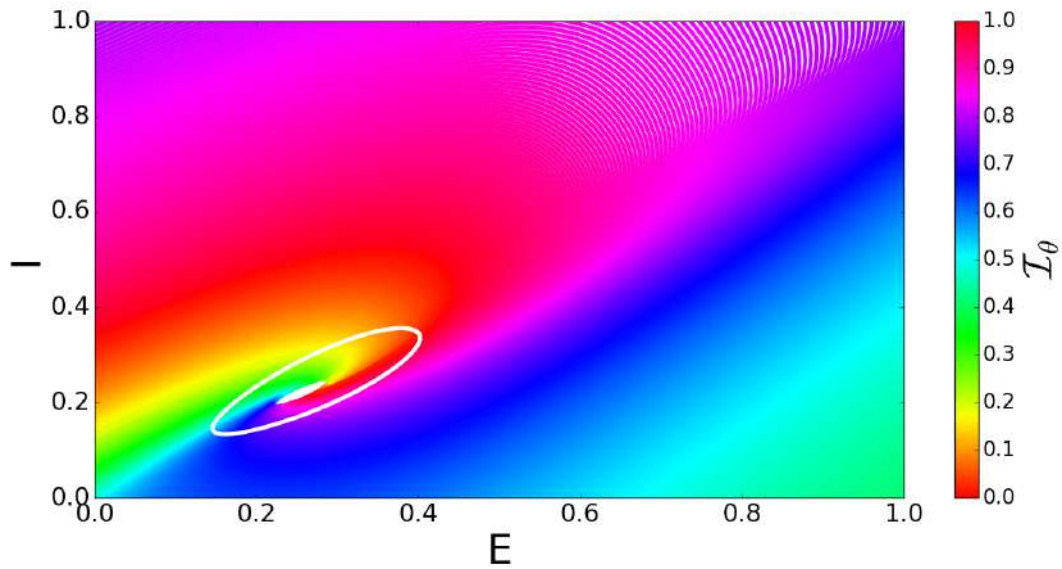


Figure 3.4: Isochrons \mathcal{I}_θ for Γ_{HB} .

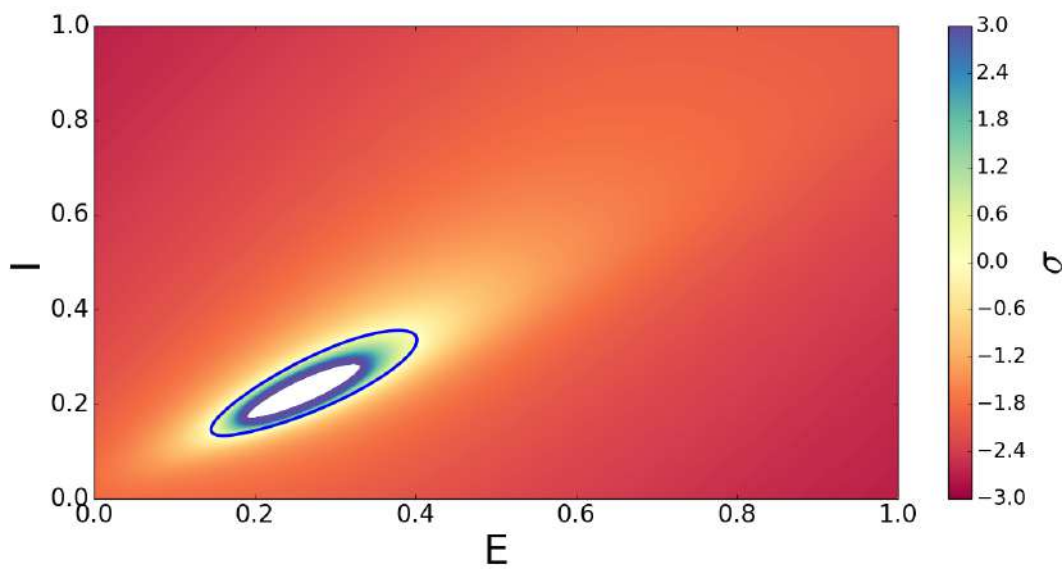


Figure 3.5: A-curves \mathcal{A}_σ for Γ_{HB} .

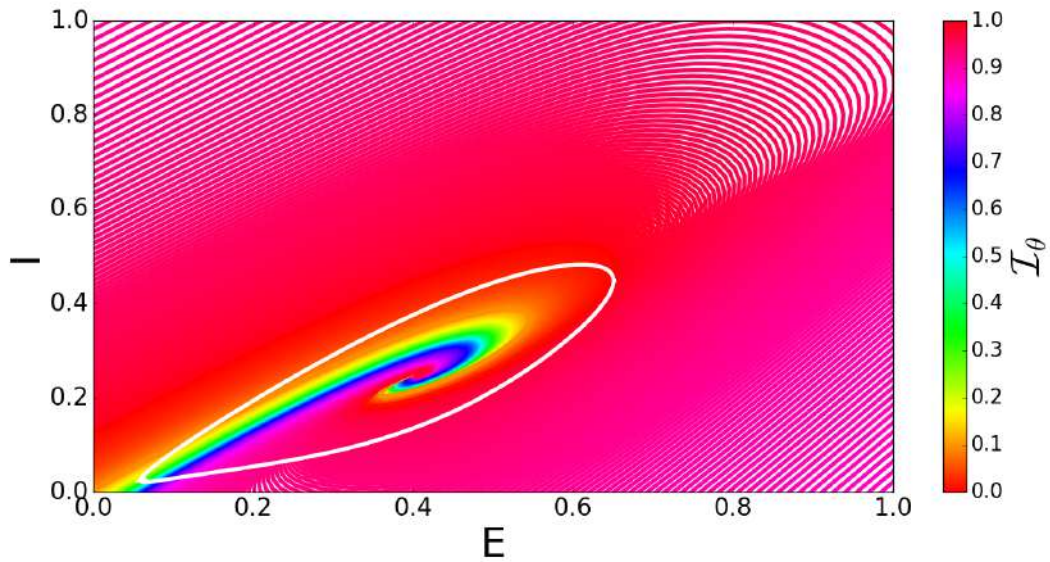


Figure 3.6: Isochrons \mathcal{I}_θ for Γ_{SN} .

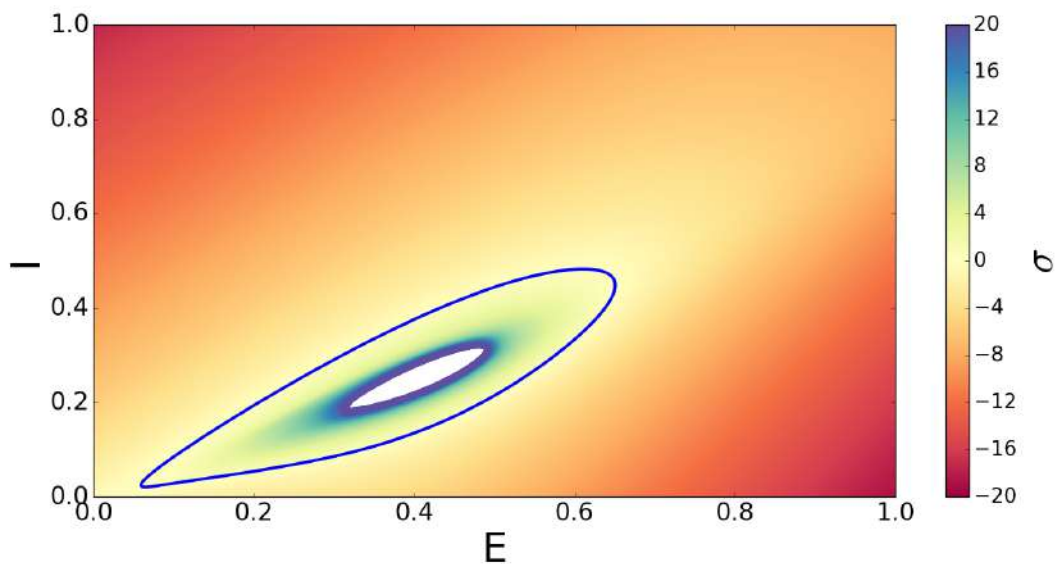


Figure 3.7: A-curves \mathcal{A}_σ for Γ_{SN} .

Notice that the distribution of isochrons is quite regular for the Hopf case (see Fig. 3.4), whereas it is inhomogeneous in the SNIC case (see Fig. 3.6). Concerning the A-curves, the attraction of

both limit cycles is homogeneously distributed (see Figs. 3.5 and 3.7) although it is larger for Γ_{SN} than for Γ_{HB} .

3.4.3 Study of perturbations: the rotation number

This Section is devoted to use the rotation number to understand the dynamics near a limit cycle after a periodic perturbation. We will show that the use of phase-amplitude variables is more accurate than the classical phase reduction. We will consider the dynamics generated by the periodic perturbation

$$p(t) = 1 + \cos\left(\frac{2\pi t}{T'}\right), \quad (3.40)$$

as the frequency $1/T'$ and the amplitude of the perturbation are varied. To that aim, we will use the phase variable to compute a rotation number ρ . Whereas the comparison between the phase and the phase-amplitude approach will allow us to assess the range of applicability of the phase reduction, we will also assess the range of applicability of the phase-amplitude variables by computing ρ in the natural variables of the system as described below.

As we want to link the results from this analysis with the work in previous Chapter 2, we will also consider the perturbed Wilson-Cowan equations in (2.1). Nevertheless, as the derivation of the study of perturbations (see Section 3.3), was done for systems of the form

$$\dot{x} = X_A(x, t) = X(x) + Ap(x, t; A), \quad (3.41)$$

we consider the system (2.1) in the following form:

$$\begin{aligned} \tau_e \frac{dE}{dt} &= -E + S_e(c_1 E - c_2 I + P + Ap(t)) \\ &= -E + S_e(c_1 E - c_2 I + P) + Ap(t) S_e'(c_1 E - c_2 I + P) + \mathcal{O}(A^2) \\ \tau_i \frac{dI}{dt} &= -I + S_i(c_3 E - c_4 I + Q), \end{aligned} \quad (3.42)$$

where $p(t)$ is given in (3.40).

The rotation number

The rotation number is defined for any continuous orientation preserving map of the circle

$$\begin{aligned} f : \mathbb{T} &\rightarrow \mathbb{T} \\ \phi &\mapsto f(\phi) \end{aligned}$$

as

$$\rho = \lim_{n \rightarrow \infty} \frac{\phi_n - \phi_0}{n}, \quad \phi_n = f^n(\phi_0). \quad (3.43)$$

As it is well known, ρ exists and is independent of the point ϕ_0 (see [4]). Moreover, if $\rho = \frac{p}{q} \in \mathbb{Q}$, the map f has at least one periodic orbit of period q . On the other hand, under some regularity assumptions, if $\rho \in \mathbb{R} \setminus \mathbb{Q}$, by Denjoy theorem, the map f is conjugated to a rotation of angle ρ and the orbit of every point θ fills densely \mathbb{T} .

When computing ρ numerically, the limit to infinity is substituted by a large enough number of iterations but the convergence to ρ is very slow. We use the methods presented in [74], which refine the computation of rotation numbers saving computational effort and accelerating the convergence of the method.

When no perturbation acts ($A = 0$) in system (3.42) the phase portrait is described by the stroboscopic map F_0 given in (2.4) and is the same as the one generated by the unperturbed system. In particular, if Γ is a limit cycle for (3.42) for $A = 0$, we have $F_0(\Gamma) \subseteq \Gamma, \forall T'$, that is, Γ is an attracting invariant curve for the map (2.4). As we saw in Chapter 2, when applying a T' -periodic continuous perturbation, as Γ is normally hyperbolic, it will continue existing for small amplitude perturbations, and it can be studied as an invariant object for the stroboscopic map F_A when $A \neq 0$. In particular, the attracting limit cycle Γ will become an attracting invariant curve Γ_A over which we can define and compute the rotation number ρ . Notice that $\Gamma = \Gamma_0$.

To compute the rotation number using the original variables of system (3.42), we will take $f_A := F_A|_{\Gamma_A}$ and proceed as follows: given a point $x \in \Gamma_A$, define the angle φ between the segment from $P_1(A)$ to x and the positive E -axis. Then, given a point $x_0 \in \Gamma_A$ for $x_n = F_A^n(x_0)$ being φ_n its angle, one can compute the rotation number in (3.43) using φ_n .

Alternatively to this method, we may have used the parameterization method that we explain in detail in Chapter 4. This method provides a parameterization K_A for the invariant curve $\Gamma_A = \{x = K_A(\theta), \theta \in \mathbb{T}\}$ satisfying the invariance equation $F_A(K_A(\theta)) = K_A(f_A(\theta))$. Using methodology described in Section 4.3.1, we can obtain unknowns K_A and f_A . As f_A gives the dynamics on the curve Γ_A we can use it to compute the rotation number in (3.43).

To compute the rotation number in the variables (θ, σ) , we define the stroboscopic map in these variables:

$$\begin{aligned} \mathcal{F}_A : \mathbb{T} \times \mathbb{R} &\rightarrow \mathbb{T} \times \mathbb{R} \\ (\theta, \sigma) &\mapsto \Psi_A(T', 0, \theta, \sigma), \end{aligned} \quad (3.44)$$

where $\Psi_A(t, t_0, \theta, \sigma)$ is the solution of (3.34), which in the 2D case becomes

$$\begin{aligned}\dot{\theta} &= \nabla\Theta(x) \cdot X_A(x, t) = \nabla\Theta(x) \cdot \{X(x) + Ap(x, t; A)\} = \frac{1}{T} + A\nabla\Theta(x) \cdot p(x, t; A), \\ \dot{\sigma} &= \nabla\Sigma(x) \cdot X_A(x, t) = \nabla\Sigma(x) \cdot \{X(x) + Ap(x, t; A)\} = \frac{\lambda\sigma}{T} + A\nabla\Sigma(x) \cdot p(x, t; A),\end{aligned}\tag{3.45}$$

with initial condition $\Psi_A(0, 0, \theta, \sigma) = (\theta, \sigma)$.

Thus, one has that $\tilde{\Gamma}_0 = \{(\theta, 0), \theta \in \mathbb{T}\}$ is an invariant circle of (3.34) when $A = 0$. Moreover as $\lambda < 0$ it is an attracting invariant curve. Therefore, for small perturbations an invariant circle exists $\tilde{\Gamma}_A = \{(\theta, \sigma), S = \sigma(\theta; A)\}$ where $S(\theta; A) = \mathcal{O}(A)$. Defining $f_A := \mathcal{F}_A|_{\tilde{\Gamma}_A}$ and taking $(\theta_0, \sigma_0) \in \tilde{\Gamma}_A$ and computing its orbit $(\theta_n, \sigma_n) = \mathcal{F}_A^n(\theta_0, \sigma_0)$ we can define a circle map from which we can compute the rotation number, defined as

$$\rho = \lim_{n \rightarrow \infty} \frac{\theta_n - \theta_0}{n},\tag{3.46}$$

where θ_n is the θ component of $\mathcal{F}_A^n(\theta_0, \sigma_0)$. Moreover, as $\tilde{\Gamma}_A$ is attracting and close to $\tilde{\Gamma}_0$, one can take (θ_0, σ_0) with σ_0 small (even $\sigma_0 = 0$) and the method will also converge to ρ . We remark that this method is different from the one used in the phase approach, which consists in considering $\sigma = 0$ in all iterates $(\theta_n, \sigma_n) = \mathcal{F}_A(\theta_{n-1}, 0)$.

As a final remark, notice that the computation of the rotation number ρ either in the phase amplitude framework or the phase reduction, requires the computation of $\nabla\Theta(x)$ and $\nabla\Sigma(x)$. Instead of the adjoint methods (see Eqs. (3.20) and (3.30)), as we have computed the parameterization $K(\theta, \sigma)$, we will compute them using (3.31), which is explicitly derived in [17] for the 2D case

$$\begin{bmatrix} \nabla\Theta(x_1, x_2) \\ \nabla\Sigma(x_1, x_2) \end{bmatrix} = [DK(\theta, \sigma)]^{-1} = \frac{1}{\det(DK)} \begin{bmatrix} \partial_\sigma K_{x_2}(\theta, \sigma) & -\partial_\sigma K_{x_1}(\theta, \sigma) \\ -\partial_\theta K_{x_2}(\theta, \sigma) & \partial_\theta K_{x_1}(\theta, \sigma) \end{bmatrix},\tag{3.47}$$

for $(x_1, x_2) = K(\theta, \sigma)$.

For the phase reduction, we just need to compute $\nabla\Theta(x)$ restricted to the limit cycle. Following [39, 17], one can use the parameterization $x = K(\theta, \sigma)$ defined in (3.37) to obtain:

$$\nabla\Theta(\gamma(\theta)) = \frac{K_1^\perp(\theta)}{T \langle K_1^\perp(\theta), X(\gamma(\theta)) \rangle}.\tag{3.48}$$

where $K_1^\perp(\theta) = J \cdot K_1(\theta)$ for $J = \begin{pmatrix} 0 & -1 \\ 1 & 0 \end{pmatrix}$ and $K_1(\theta) = \partial_\sigma K(\theta, \sigma)|_{\sigma=0}$.

In Fig. 3.8 we show the iPRC for Γ_{HB} and Γ_{SN} computing used the expression (3.48). Notice that, a perturbation onto Γ_{HB} can advance or delay the phase depending on the phase at which

the perturbation is applied. By contrast, a perturbation onto Γ_{SN} mainly advances or delays the phase for the whole phase interval. Following the criteria established in [40] iPRC for Γ_{SN} is of Type 1, whereas the iPRC for Γ_{HB} is of Type 2. Using these results one can interpret the shape of bifurcation diagrams in Figs.2.2 and 2.3 for Γ_{HB} and Γ_{SN} for weak enough perturbations. As iPRC for Γ_{HB} can either advance or delay its phase it is possible for the oscillator to synchronize with frequencies lower or higher than the resonant one. By contrast as iPRC for Γ_{SN} shows, this oscillator only can advance its phase, so it can only synchronize with inputs of higher frequencies.

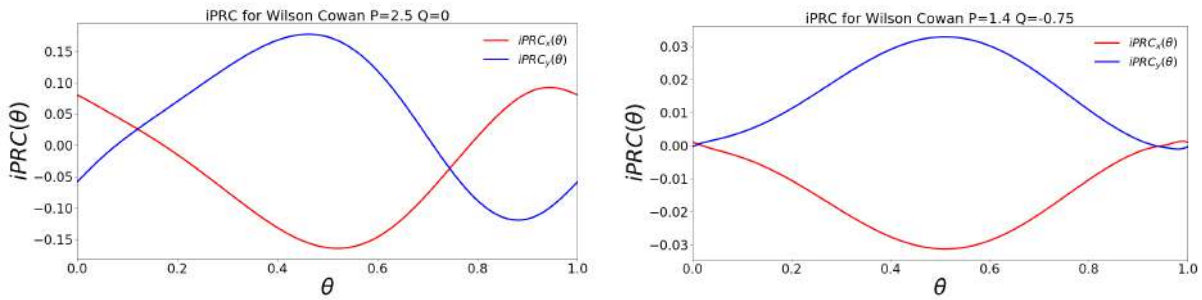


Figure 3.8: Infinitesimal phase response curves (iPRCs) for Γ_{HB} and Γ_{SN} (left and right panels, respectively) of system (1.7).

Computing the rotation Number for Γ_{HB} and Γ_{SN}

In this Section we present computations of the rotation number for system (3.42) using the original variables of the system (2.1) and the phase and phase-amplitude variables (see Figs. 3.9 and 3.10). We recall that when $A = 0$, by considering the set of parameters \mathcal{P} in (1.17), and choosing $(P, Q) = (2.5, 0)$ and $(P, Q) = (1.4, -0.75)$ the phase space of system (3.42) will consist on an unstable focus (P_1) and the limit cycles Γ_{HB} and Γ_{SN} , respectively (see Fig. 1.9).

Figs. 3.9 and 3.10 for Γ_{HB} and Γ_{SN} respectively, show the classical Devil's Staircase [4] for the rotation number ρ as a function of $\frac{T'}{T}$. The function shows intervals on the x -axis (showing the ratio $\frac{T'}{T}$) for which the rotation number ρ is constant. That is, there exists a solution of (3.42) which is phase-locked to the periodic perturbation. For small positive amplitudes, the largest intervals correspond to the phase locked states 1:1 ($\rho = 1$) and 1:2 ($\rho = \frac{1}{2}$). The phase-locked intervals widen as the amplitude is increased. As it was expected, the precision of the computations of the rotation number ρ using the phase approach is worse as the amplitude A of the forcing is increased. By contrast, as the amplitude A of the forcing is increased the phase-amplitude description in general provides an accurate description of ρ .

Interestingly, for the Γ_{HB} case, the rotation number displays a discontinuity at some values of

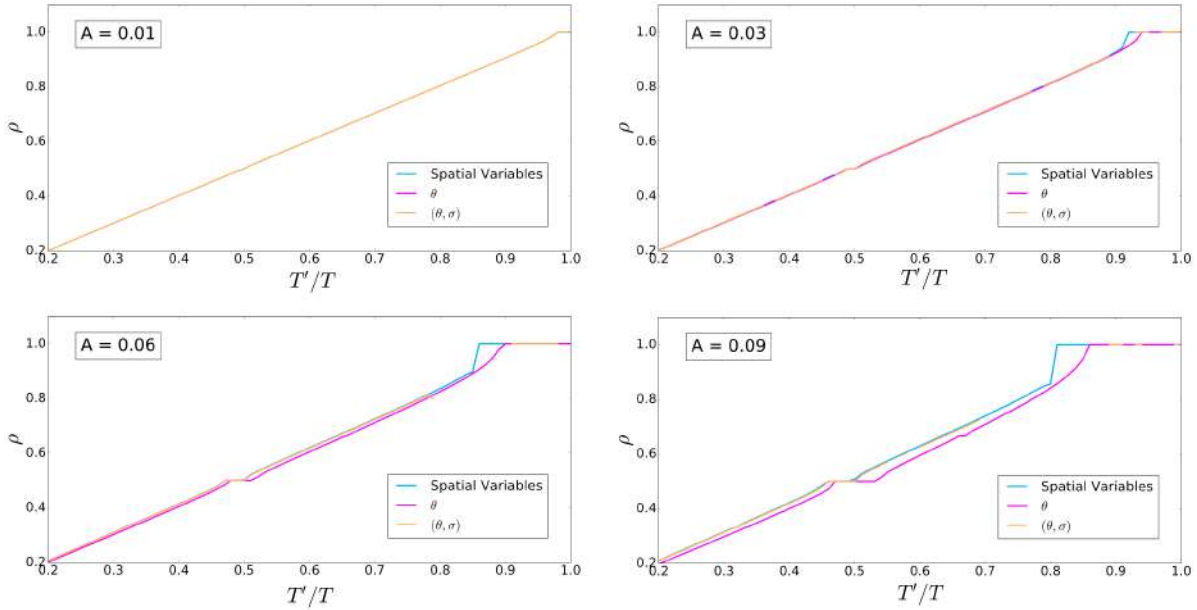


Figure 3.9: Rotation number for the perturbed Wilson-Cowan model near a Hopf bifurcation Γ_{HB} . For different amplitudes we show the rotation number using the phase, the phase-amplitude, and the spatial variables.

T' jumping suddenly to $\rho = 1$ as the amplitude is increased. As the rotation number is defined over an invariant curve of the stroboscopic map F_A , this discontinuity may indicate its breakdown for non-weak amplitudes. These discontinuities can be explained computing the bifurcation diagrams for the fixed points of the stroboscopic map F_A , using the procedure described in Chapter 2. As left panel in Fig. 3.11 shows, near the point $(A, \frac{T'}{T}) \approx (0.023, 0.9388)$ emanate two bifurcation curves. Namely, a Saddle-Node (SN) and Neimark-Sacker (NS) bifurcations. As it is widely known, SN bifurcations imply the birth/disappearance of two fixed points (a saddle and a node) over an invariant curve. By contrast Neimark-Sacker (NS) bifurcations, coinciding with the amplitude values for which ρ shows discontinuities, imply the appearance/disappearance of the invariant curve.

Furthermore, the crossing of NS bifurcation has implications in numerics. For values of T' near this discontinuity the numerical computation of ρ in the phase-amplitude variables fails. This is because near a Neimark-Sacker bifurcation the invariant curve shrinks and collapses around an unstable focus. As we are considering small amplitude values, this fixed unstable focus may be located nearby the focus P_1 for the unperturbed system. This causes two numerical drawbacks which we illustrate using Fig. 3.14. First, is that near this point the error of the parameterization $K(\theta, \sigma)$ is large. Second, drawback is due to the fact that near this focus, the distribution of isochrons and

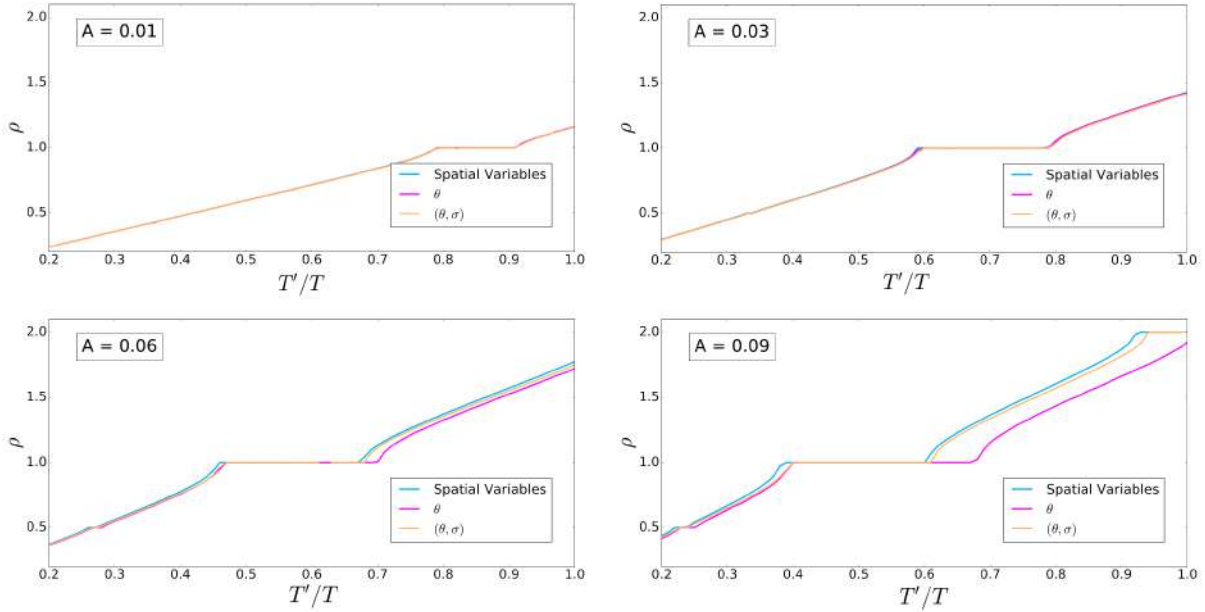


Figure 3.10: Rotation number for the perturbed Wilson-Cowan model near a Hopf bifurcation Γ_{SN} . For different amplitudes we show the rotation number using the phase, the phase-amplitude, and the spatial variables.

A-Curves tends to pack, so $\nabla\Theta(x)$ and $\nabla\Sigma(x)$ have large values and enhance numerical errors.

As bifurcation digram for the stroboscopic map F_A in the right panel of Fig. 3.11 shows, there are no Neimark-Sacker bifurcations for the amplitude values of the perturbations considered over Γ_{SN} . Because of this, there are no discontinuities or numerical gaps for the computed values of the rotation number ρ in this case. Nevertheless, as Fig. 3.10 shows, for high values of frequency and amplitude, the error of the numerical computation of ρ for phase amplitude variables is bigger than the one computed for the Γ_{HB} case. In Fig. 3.15, we observe that the invariant curve of the map F_A lies outside the area $\Omega_{loc}(E)$ in (3.39) where the error of the parameterization $\bar{K}(\theta, \sigma)$ for Γ_{SN} is high (bigger than 10^{-3}) and thus cause the numerical errors.

In Figs. 3.12 and 3.13 we illustrate the Saddle-Node and Neimark-Sacker bifurcations by computing the invariant curve by the parameterization method explained in Section 4.3.1, obtaining a parameterization $K_A(\theta)$ of the invariant curve such that $F_A(K_A(\theta)) = K_A(f_A(\theta))$. The SN bifurcation in Fig. 3.12 $f_A(\theta)$ is tangent to the identity line. Fig. 3.13 show the disappearance of the invariant curve at the NS bifurcation.

As a first conclusion, as we expected, for the case of periodic continuous perturbations the

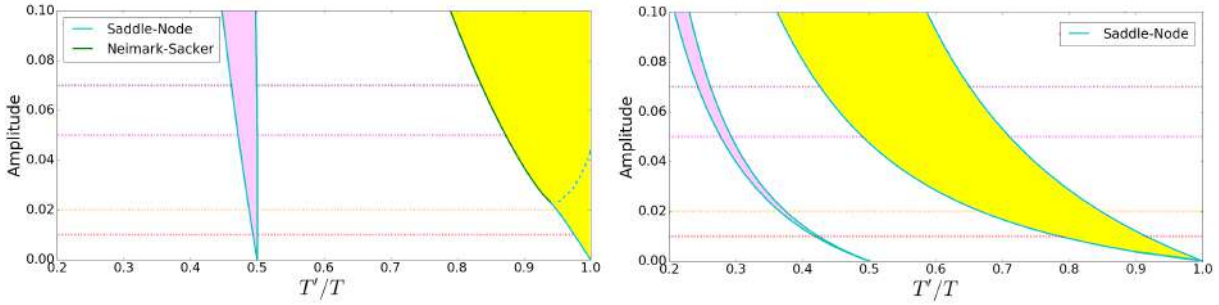


Figure 3.11: Bifurcation diagrams for the stroboscopic map F_A of the perturbed Wilson-Cowan system (2.1) with limit cycles Γ_{HB} (left) and Γ_{SN} (right). Saddle-Node and Neimark-Sacker bifurcations (cyan and green curves respectively) were found. Constant amplitudes for which rotation numbers in Figs. 3.9 and 3.10 were computed are drawn respecting the same colour code. Inside the yellow area there exists a stable fixed point for the map F_A corresponding to a 1:1 phase locking with the external input, whereas inside the violet area there exists a 2-periodic orbit of the map F_A corresponding to a 1:2 phase locking relationship with the external input.

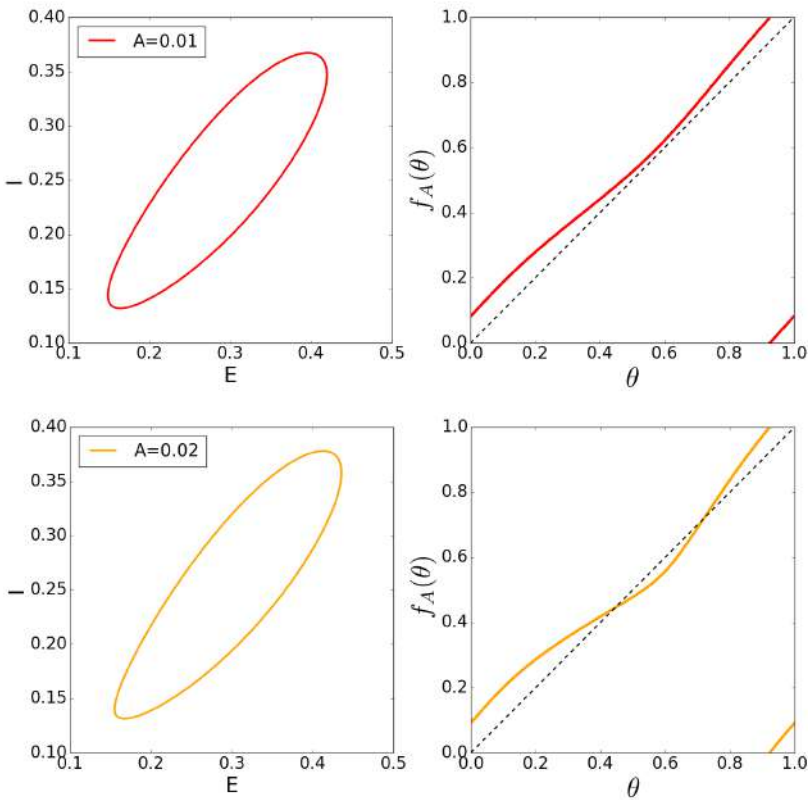


Figure 3.12: For different values of the Amplitude and a fixed value of $\frac{T'}{T} = 0.965$ for perturbations over Γ_{HB} we show: (Left) Invariant curve Γ_A for the stroboscopic map. (Right) Dynamics $f_A(\theta)$ over the invariant curve. For $\frac{T'}{T} = 0.965$ there is Saddle-Node bifurcation for $A_{SN} \approx 0.014$. For $A = 0.01 < A_{SN}$, there exists an invariant curve Γ_A whose dynamics have no crossings with the identity line. By contrast for $A = 0.02 > A_{SN}$, two crossings appear between f_A and the identity line, indicating the presence of two fixed points over Γ_A . Computations of Γ_A and f_A were done and using the algorithms introduced in Section 4.3.1.

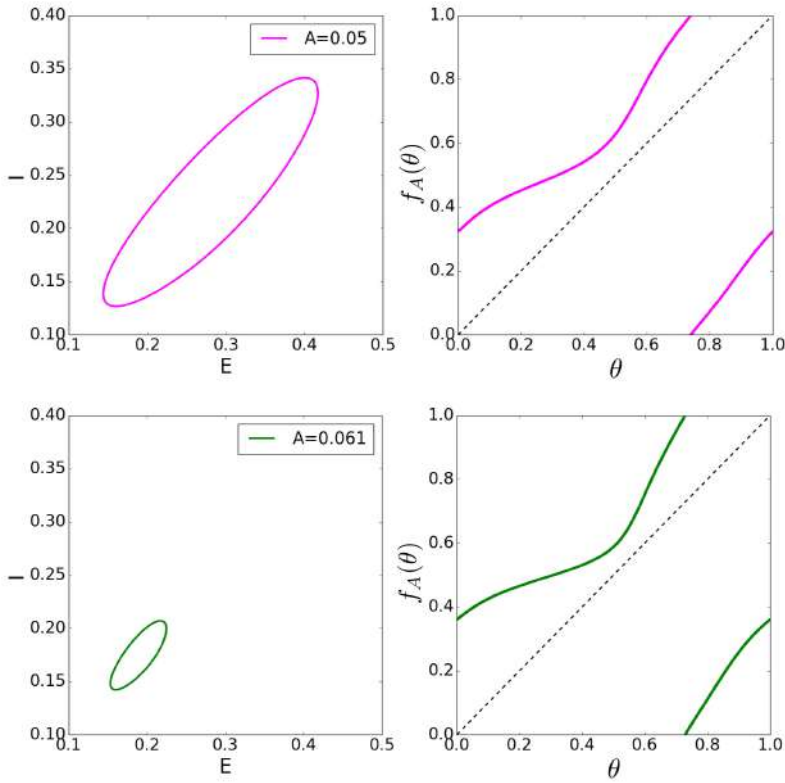


Figure 3.13: For different values of the Amplitude and a fixed value of $\frac{T'}{T} = 0.85$ for perturbations over Γ_{HB} we show: (Left) Invariant curve Γ_A for the stroboscopic map. (Right) Dynamics $f_A(\theta)$ over the invariant curve. For $\frac{T'}{T} = 0.85$ there is Neimark-Sacker bifurcation for $A_{NS} \approx 0.062$. For $A = 0.05 < A_{NS}$, there exists an invariant curve Γ_A whose dynamics have no crossings with the identity line. Notice how Γ_A shrinks for amplitude values $A = 0.061 < A_{NS}$ near the bifurcation. Computations of Γ_A and f_A were done and using the algorithms introduced in Section 4.3.1.

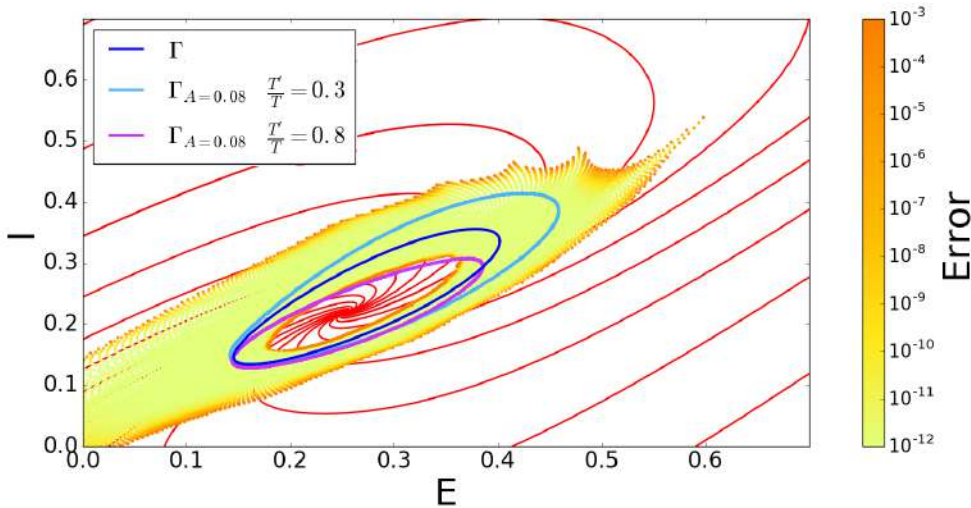


Figure 3.14: Limit cycle Γ_{HB} , their isochrons and the error of the parameterization K . We show two invariant curves of the stroboscopic map for different values of amplitude and frequency of the perturbation.

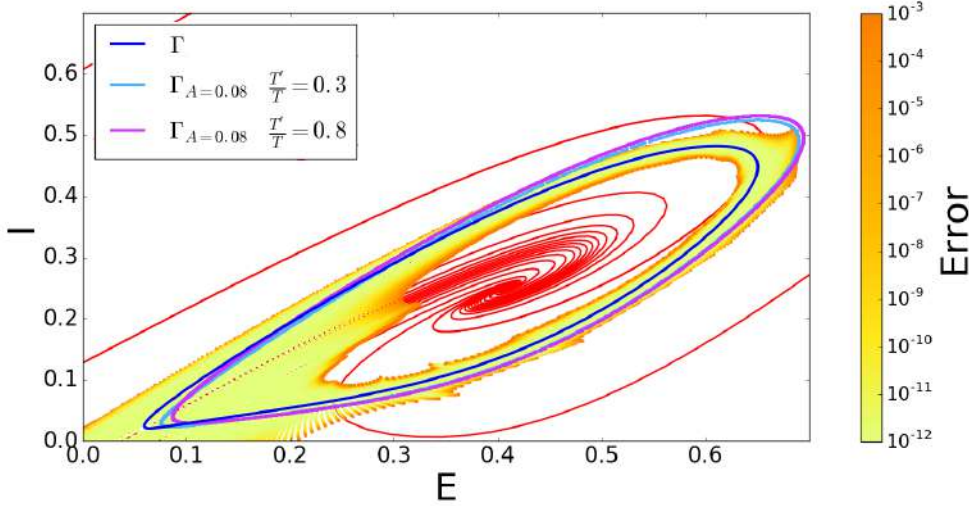


Figure 3.15: Limit cycle Γ_{SN} , their isochrons and the error of the parameterization K . We show two invariant curves of the stroboscopic map F_A corresponding to two values of the amplitude and frequency of the perturbation.

phase approach is also restricted to very small values of the amplitude. This domain of applicability can be enlarged by means of the phase-amplitude variables. Nevertheless, the study that we have performed also focused in how the computations in terms of the phase-amplitude variables respond to different bifurcations. We have seen how near Neimark-Sacker bifurcations, numerical calculations fail as the invariant curve shrinks near the focus of the unperturbed system, an area in which $\nabla\Theta$ and $\nabla\Sigma$ are large. We also have related errors in computations with the errors of the parameterization $K(\theta, \sigma)$. Thus, we aimed not just to illustrate how phase-amplitude variables enlarge the phase approach, but also to illustrate some numerical drawbacks.

3.5 The 3D case

In this Section we apply the general framework described in the previous Sections 3.1, 3.2 and 3.3 to a 3D system. The methodology to obtain the map $K(\theta, \sigma) = K(\theta, \sigma_1, \sigma_2)$ introduced in (3.8) near a limit cycle Γ for a 3D system was studied in [18]. Although this work considers a more general situation (systems having stable and unstable manifolds), next we review the methods introduced in [18] for computing numerically $K(\theta, \sigma)$ in the context of a 3D normally hyperbolic attracting periodic orbit. Next, we will use $K(\theta, \sigma)$ to propose some strategies to globalize the isochrons \mathcal{I}_θ and the A-surfaces \mathcal{A}_σ . We will apply these methods to compute the isochrons for single neuron and neural population models. Finally, we will consider the study of perturbations

by using the phase amplitude variables with the aim of exploring also some useful reductions.

The dynamics of system (3.1) for $d = 3$, in terms of the phase amplitude variables will be given by

$$\dot{\theta} = \frac{1}{T}, \quad \dot{\sigma} = \Lambda \cdot \sigma, \quad \text{with} \quad \Lambda = \begin{pmatrix} \lambda_1 & 0 \\ 0 & \lambda_2 \end{pmatrix}, \quad (3.49)$$

where $\sigma = (\sigma_1, \sigma_2) \in \mathbb{R}^2$, and λ_1 and λ_2 are the characteristic exponents of Γ .

Therefore we will use that the parameterization K in (3.8) satisfies the following invariance equation

$$\frac{1}{T} \frac{\partial}{\partial \theta} K(\theta, \sigma) + \sum_{i=1}^2 \lambda_i \sigma_i \frac{\partial}{\partial \sigma_i} K(\theta, \sigma) = X(K(\theta, \sigma)), \quad (3.50)$$

to solve it and obtain $K(\theta, \sigma)$.

3.5.1 A formal solution for the invariance equation

Similarly to the 2D case in Section 3.4.1, we will solve Eq. (3.50) for $K(\theta, \sigma)$ by assuming that $K(\theta, \sigma)$ can be expressed in Taylor series in σ :

$$K(\theta, \sigma) = \sum_{m=0}^{\infty} \sum_{\alpha=0}^m K_{\alpha, m-\alpha}(\theta) \sigma_1^\alpha \sigma_2^{m-\alpha}. \quad (3.51)$$

To compute the function K , we substitute (3.51) into the invariance equation (3.10) and expand the vector field $X(K(\theta, \sigma))$ in Taylor series with respect σ around $\sigma = 0$. Then one just has to collect terms with the same power of σ and solve the resulting equations.

For $m = 0$ the term $K_0(\theta) := K_{00}(\theta)$ satisfies the equation

$$\frac{1}{T} \frac{d}{d\theta} K_0(\theta) = X(K_0(\theta)). \quad (3.52)$$

Clearly, the solution of (3.52) is the limit cycle itself, that is $K_0(\theta) = \gamma(\theta)$.

For $m = 1$, the equations for $K_{10}(\theta)$ and $K_{01}(\theta)$ are

$$\begin{aligned} \frac{1}{T} \frac{d}{d\theta} K_{10}(\theta) + \lambda_1 K_{10}(\theta) &= DX(K_0(\theta)) K_{10}(\theta), \\ \frac{1}{T} \frac{d}{d\theta} K_{01}(\theta) + \lambda_2 K_{01}(\theta) &= DX(K_0(\theta)) K_{01}(\theta), \end{aligned} \quad (3.53)$$

respectively. The solutions for these equations are given by

$$K_{10}(\theta) = \Phi(\theta T)e^{-\lambda_1\theta T}v_1, \quad K_{01}(\theta) = \Phi(\theta T)e^{-\lambda_2\theta T}v_2, \quad (3.54)$$

where $\Phi(\theta T) = \Phi(t)$ is the solution of the variational equations (3.7) and v_i is the eigenvector of the Monodromy matrix $\Phi(T)$ associated to the i -th Floquet multiplier μ_i , for $i = 1, 2$ (discarding the trivial eigenvalue $\mu_0 = 1$).

Finally, for $m \geq 2$, the terms $K_{\alpha, m-\alpha}(\theta)$, $\alpha = 0, \dots, m$, satisfy the so-called *homological equations*

$$\frac{1}{T} \frac{dK_{\alpha, m-\alpha}(\theta)}{d\theta} + (\alpha\lambda_1 + (m-\alpha)\lambda_2)K_{\alpha, m-\alpha}(\theta) = DX(K_0(\theta))K_{\alpha, m-\alpha}(\theta) + B_{\alpha, m-\alpha}(\theta), \quad (3.55)$$

where $B_{\alpha, m-\alpha}(\theta)$ is the coefficient of the term $\sigma_1^\alpha \sigma_2^{m-\alpha}$ in the Taylor expansion of

$$X \left(\sum_{n=0}^{m-1} \sum_{\alpha=0}^n K_{\alpha, n-\alpha}(\theta) \sigma_1^\alpha \sigma_2^{n-\alpha} \right). \quad (3.56)$$

Notice that $B_{\alpha, m-\alpha}(\theta)$ is an explicit polynomial depending on the terms $K_{\alpha, n-\alpha}(\theta)$ for $n < m$ and whose coefficients are the derivatives of X evaluated at K_0 . They can be numerically computed using automatic differentiation techniques [42].

Notice that equations (3.55) can be solved assuming that $K_{\alpha, m-\alpha}(\theta)$ can be written in Fourier series so its coefficients are the unknowns. The resulting system of equations for the Fourier coefficients is linear, but it involves a large dimensional matrix which can make calculations tedious. To avoid this numerical drawback, in the next Section, we review the method proposed in [18] to solve the homological equation (3.55) in a faster way using the Floquet normal form.

Reducibility of the homological equations via Floquet normal form

By Floquet theory [29], the solution $\Phi(t)$ of system (3.7) can be written as

$$\Phi(t) = Q(t)e^{tR}, \quad (3.57)$$

where $Q(t)$ is a T -periodic matrix and R is a constant matrix.

As (3.57) is a solution of (3.7), it satisfies

$$\frac{1}{T} \left(\frac{dQ(\theta)}{d\theta} + Q(\theta)TR \right) = DX(\gamma(\theta))Q(\theta), \quad (3.58)$$

where $Q(\theta) = \mathcal{Q}(\theta T)$.

Then, writing $K_{\alpha, m-\alpha}(\theta)$ in (3.55) as

$$K_{\alpha, m-\alpha}(\theta) = Q(\theta)w(\theta), \quad (3.59)$$

and substituting it in (3.55), one has

$$\frac{1}{T} \left(\frac{dQ(\theta)}{d\theta} w(\theta) + Q(\theta) \frac{dw(\theta)}{d\theta} \right) + \Sigma Q(\theta)w(\theta) = DX(K_0(\theta))Q(\theta)w(\theta) + B_{\alpha, m-\alpha}(\theta), \quad (3.60)$$

where we have introduced the constant matrix $\Sigma := (\alpha\lambda_1 + (m - \alpha)\lambda_2) \cdot Id$.

Then, using (3.58) in equation (3.60), we obtain

$$\frac{1}{T} \left(-Q(\theta)TRw(\theta) + Q(\theta) \frac{dw(\theta)}{d\theta} \right) + \Sigma Q(\theta)w(\theta) = B_{\alpha, m-\alpha}(\theta), \quad (3.61)$$

and multiplying both sides by $Q^{-1}(\theta)$ we have

$$\frac{1}{T} \frac{dw(\theta)}{d\theta} = (-\Sigma + R)w(\theta) + Q^{-1}(\theta)B_{\alpha, m-\alpha}(\theta). \quad (3.62)$$

Finally, we assume that the matrix R in (3.57) can be diagonalized

$$J = C^{-1}RC = \begin{pmatrix} \lambda_0 & 0 & 0 \\ 0 & \lambda_1 & 0 \\ 0 & 0 & \lambda_2 \end{pmatrix}, \quad (3.63)$$

so by expressing $w(\theta) = Cu(\theta)$ and multiplying both sides by C^{-1} , expression (3.62) reads as

$$\frac{1}{T} \frac{du(\theta)}{d\theta} = (-\Sigma + J)u(\theta) + A_{\alpha, m-\alpha}(\theta), \quad (3.64)$$

where $A_{\alpha, m-\alpha}(\theta) = C^{-1}Q^{-1}(\theta)B_{\alpha, m-\alpha}(\theta)$.

Finally, we write $u(\theta)$ and $A_{\alpha, m-\alpha}(\theta)$ in Fourier series

$$u(\theta) = \sum_{k=-\infty}^{\infty} u_k e^{2\pi i k \theta}, \quad A_{\alpha, m-\alpha}(\theta) = \sum_{k=-\infty}^{\infty} A_k e^{2\pi i k \theta} \quad (A_k, u_k \in \mathbb{C}^2), \quad (3.65)$$

and substitute expressions (3.65) in Eq. (3.64). We obtain a linear system for the Fourier coefficients u_k which is diagonal and can be solved component wise, thus obtaining the following expression for the Fourier coefficients:

$$u_k^{(j)} = \frac{1}{\frac{2\pi i k}{T} + \alpha\lambda_1 + (m - \alpha)\lambda_2 - \lambda_{j-1}} A_k^{(j)}, \quad (3.66)$$

for $j = 1, 2, 3$. Finally, the solution $K_{\alpha, m-\alpha}(\theta)$ is given by

$$K_{\alpha, m-\alpha}(\theta) = Q(\theta)Cu(\theta). \quad (3.67)$$

Remark 3.5.1. The Fourier coefficients $u_k^{(j)}$ in (3.66) are formally well defined to all orders provided there are no resonances, that is $\frac{2\pi ik}{T} + \alpha\lambda_1 + (m-\alpha)\lambda_2 - \lambda_{j-1} \neq 0$ (for $j = 1, 2, 3$).

Computation of the Floquet normal form

By Floquet theory [29], the monodromy matrix satisfies

$$M = \Phi(T) = Q(T)e^{TR} = Q(0)e^{TR} = \Phi(0)e^{TR} = e^{TR}, \quad (3.68)$$

where we have used $\Phi(0) = Id$ and $Q(T)$ is a T-periodic matrix.

Then, if there exists a matrix C such that

$$\Phi(T) = CDC^{-1} \quad \text{where} \quad D = \text{diag}(1, \mu_1, \mu_2), \quad (3.69)$$

one can find the matrix R in (3.57) as

$$R = \frac{1}{T}C \begin{pmatrix} 0 & & \\ & \ln(\mu_1) & \\ & & \ln(\mu_2) \end{pmatrix} C^{-1} = CJC^{-1}, \quad (3.70)$$

where J is given in (3.63), with $\lambda_0 = 0$, $\lambda_i = \ln(\mu_i)/T$ $i = 1, 2$. Therefore the matrix Q in (3.57) is given by

$$Q(t) = \Phi(t)e^{-tR} = \Phi(t)C \begin{pmatrix} 1 & & \\ & e^{\frac{-t}{T} \ln(\mu_1)} & \\ & & e^{\frac{-t}{T} \ln(\mu_2)} \end{pmatrix} C^{-1} = \Phi(t)C \begin{pmatrix} 1 & & \\ & e^{-t\lambda_1} & \\ & & e^{-t\lambda_2} \end{pmatrix} C^{-1}. \quad (3.71)$$

We recall that μ_1 and μ_2 are usually called Floquet multipliers and λ_1 and λ_2 the Floquet exponents.

3.5.2 Numerical Implementation

For numerical proposes we will truncate the power series at order L and the Fourier expansion at order N . Thus, we compute an approximate solution \bar{K} for the invariance equation (3.50), given by,

$$\bar{K}(\theta, \sigma) = \sum_{m=0}^L \sum_{\alpha=0}^m \bar{K}_{\alpha, m-\alpha}(\theta) \sigma_1^\alpha \sigma_2^{m-\alpha}, \quad \text{where} \quad \bar{K}_{\alpha, m-\alpha}(\theta) = \sum_{k=-N/2}^{N/2} c_k e^{2\pi i k \theta}. \quad (3.72)$$

Because of the truncation, the approximation \bar{K} will have an error E given by

$$E(\theta, \sigma) = \frac{1}{T} \frac{\partial}{\partial \theta} \bar{K}(\theta, \sigma) + \sum_{i=1}^2 \lambda_i \sigma_i \frac{\partial}{\partial \sigma_i} \bar{K}(\theta, \sigma) - X(\bar{K}(\theta, \sigma)). \quad (3.73)$$

Therefore, for a given error tolerance $E > 0$, the approximate solution will have a domain of accuracy $\Omega_{loc}(E)$ defined as

$$\Omega_{loc}(E) := \{(\theta, \sigma) \in \mathbb{T} \times \mathbb{R}^2 \mid \|E(\theta, \sigma)\| < E\}, \quad (3.74)$$

where $\|\cdot\|$ is the euclidean norm in \mathbb{R}^3 .

Next Sections are devoted to explain how to compute the approximate solution \bar{K} of (3.10). Moreover, we explain how to use the local approximation \bar{K} which is valid in the domain $\Omega_{loc}(E)$ in (3.74) to globalize the isochrons \mathcal{I}_θ to a larger domain. From now on, to avoid stodgy notation, we skip the bar in \bar{K} .

Numerical Computation of $K(\theta, \sigma)$

In this Section we discuss how to numerically solve Eqs. (3.52), (3.53) and (3.55).

First, we compute the periodic solution $\Gamma = \{\gamma(t/T), \theta \in [0, 1)\}$. To do so, we construct a Poincaré Section and use a Newton method to find a fixed point of the corresponding Poincaré map. By doing this, we find a point $x_0 \in \Gamma$ and the value T of the period.

We integrate system (3.1) with initial condition $x(0) = x_0$ and system (3.7) altogether for a time T to obtain $\gamma(t/T) = K_0(\theta)$ and $\Phi(\theta T)$ for $\theta \in [0, 1)$. We store them for equidistant values of θ ; that is $\theta_i = i/N$ for $i = 0, \dots, N-1$ which is equivalent to store the coefficients of the Fourier series up to order N . Indeed, we can switch between them by means of a FFT algorithm.

We consider the monodromy matrix $\Phi(T)$ and obtain its eigenvalues μ_i , called Floquet multipliers, and the Floquet exponents $\lambda_i = \frac{1}{T} \ln(\mu_i)$ and its associate eigenvectors v_i for $i = 1, 2$ to compute K_{10} and K_{01} according to the formulas in (3.54).

We use the scheme described in Section 3.5.1 to compute $K_{\alpha, m-\alpha}$ for $m \geq 2$ and $\alpha = 0, \dots, m$. So, we compute first the matrices Q and R in (3.57) (see Section 3.5.1). To obtain the functions $B_{\alpha, m-\alpha}$ we need to compute the Taylor expansion of $X(f((\sigma_1, \sigma_2)))$, where $f((\sigma_1, \sigma_2))$ is a Taylor polynomial in σ_1, σ_2 up to order $m-1$. As X consists of a combination of elementary functions, we can use automatic differentiation to compute the coefficients $B_{\alpha, m-\alpha}$ of the Taylor expansion

of X up to arbitrary order. Finally, we use formula (3.66) to obtain the Fourier coefficients of $K_{\alpha, m-\alpha}$.

To decide how many Fourier coefficients N we have to consider, we use a similar criteria to the one given in [39]. Namely, we pick a value N such that the norm of the series with the last 10% coefficients is smaller than a given tolerance E_{tail} , that is

$$|K_{\alpha, m-\alpha}^{tail}| = 2 \sum_{k=0.9N/2}^{N/2} |c_k| < E_{tail}. \quad (3.75)$$

To check the accuracy of the solutions $K_{\alpha, m-\alpha}$ obtained, we substitute them in the corresponding equation (Eq. (3.52) for $m = 0$, Eq. (3.53) for $m = 1$ and Eq. (3.55) for $m \geq 2$) for discrete values of θ , that is, $\theta_i = i/N$ for $i = 0, \dots, N-1$. For each value θ_i , this substitution provides an evaluation of the error $E_{\alpha, m-\alpha}(\theta_i)$. Finally, we compute the discrete ℓ_1 norm of $\{E_{\alpha, m-\alpha}(\theta_i)\}_{i=0}^{N-1}$ to get the accuracy; that is,

$$\|E_{\alpha, m-\alpha}\|_1 = \frac{1}{N} \sum_{i=0}^{N-1} |E_{\alpha, m-\alpha}(\theta_i)|. \quad (3.76)$$

3.5.3 Globalizing \mathcal{I}_θ , \mathcal{A}_σ and $K(\theta, \sigma)$

In this Section we explain how to globalize the isochrons \mathcal{I}_θ and the A-surfaces A_σ^i using the approximation given by \bar{K} in $\Omega_{loc}(E)$ (see Eq. (3.74)). The strategy used in what follows, adapted from [75] and depicted in Fig. 3.16, proposes a method to globalize isochrons with a homogeneous distribution of points. From now on, we will assume $|\lambda_1| > |\lambda_2|$.

We perform the following steps:

- Look for a point x_0^0 such that: $x_0^0 = K(\theta, 0, \sigma_2^0)$, satisfying $x_0^0 \in \Omega_{loc}^\theta = \Omega_{loc} \cap \{\theta\}$ (see Eq. (3.74)). Observe that Ω_{loc}^θ is the local approximation of the isochron \mathcal{I}_θ . Integrate it backwards by the flow a time nT , thus getting the point $x_0^1 = \phi_{-nT}(x_0^0)$. Check that the euclidean distance Δx between x_0^0 and x_0^1 is lower than a threshold Δx_{max} . If it is not, try either a lower value of n or choose a point x_0^0 closer to the limit cycle Γ and repeat the computation.
- Once we obtain the point x_0^1 , notice that it satisfies $\Sigma_1(x_0^1) = 0$, and $\Sigma_2(x_0^1) = \sigma_2^0 e^{-\lambda_2 nT} := c$. As $x_0^1 \in \mathcal{I}_\theta$ (the isochron of phase θ), we have obtained a new point on the isochron \mathcal{I}_θ with $\sigma_2 = c$.

- Then, the strategy is to fix the constant value c for σ_2 and vary σ_1 , thus extending the isochron along the curve $\Sigma_2(x) = c$. To do so, consider a σ_1 value such that the point $x_1^0 = K(\theta, \sigma_1^1, \sigma_2^0) \in \Omega_{loc}^\theta$ and integrate backwards by the flow ϕ_t . If the point $x_1^1 = \phi_{-nT}(x_1^0)$ is at a distance from x_0^1 smaller than the tolerance Δx_{max} we add it to the isochron. If not, take a point x_1^0 closer to x_0^0 and repeat the computations.
- Continue extending the isochron \mathcal{I}_θ by repeating the previous step for values of σ_1 such that the point $x_{k+1}^0 = K(\theta, \sigma_1^{k+1}, \sigma_2^0) \in \Omega_{loc}^\theta$. When integrated backwards by the flow, $x_{k+1}^1 = \phi_{-nT}(x_{k+1}^0)$ is at a distance from x_k^1 smaller than Δx_{max} .
- It might happen that the next σ_1 value to continue extending the isochron lies outside the accuracy domain Ω_{loc}^θ , that is $x_{k+1}^0 = K(\theta, \sigma_1^{k+1}, \sigma_2^0) \notin \Omega_{loc}^\theta$. Then, if we denote by $x_k^0 = K(\theta, \sigma_1^k, \sigma_2^0) \in \Omega_{loc}^\theta$ the last point used to globalize the isochron \mathcal{I}_θ , we need to look for the $\Delta\theta$ value such that the point $x_k^0 = K(\theta + \Delta\theta, \sigma_1^k e^{-\lambda_1 \Delta\theta T}, \sigma_2^0 e^{-\lambda_2 \Delta\theta T}) \in \Omega_{loc}^{\theta + \Delta\theta}$. Then, one just has to continue varying σ_1 and continue extending the isochron by integrating backwards a time $(n + \Delta\theta)T$.
- Once we have globalized the isochron \mathcal{I}_θ along $\Sigma_2(x) = c$, continue globalizing the isochron by repeating the same procedure for a different value c . Look for a new $x_0^0 \in \Omega_{loc}^\theta$ such that the point $x_0^{k+1} = \phi_{-nT}(x_0^0)$ is at a distance of x_0^k lower than Δx_{max} . Then repeat the previous steps.

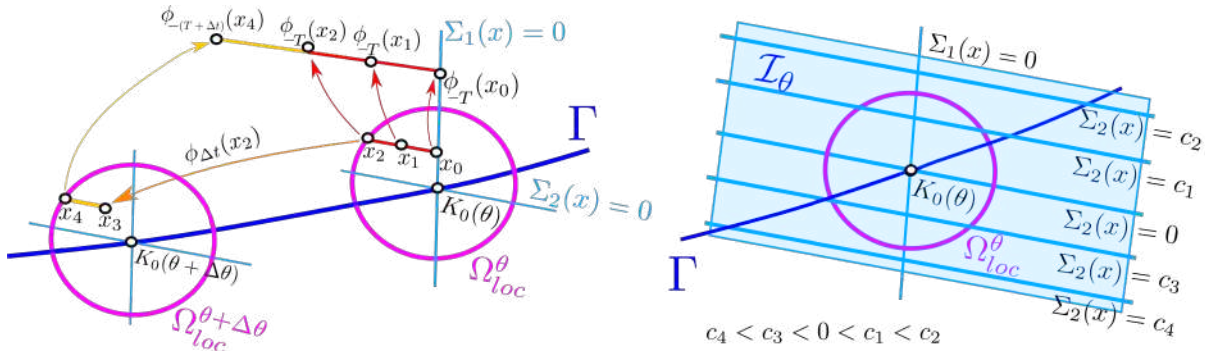


Figure 3.16: Sketch of the method. As we want to globalize points on the Isochron \mathcal{I}_θ having a σ_2 constant value ($\Sigma_2(x) = c, c \in \mathbb{R}$), one just has to look for points $x = K(\theta, \sigma_1, c) \in \Omega_{loc}^\theta$ and vary σ_1 to extend the isochron along the curves $\Sigma_2(x) = c$. If the required value to continue extending the isochron lies outside the local domain Ω_{loc}^θ we use neighbouring local approximations to continue extending the isochron.

It is important to remark that this method requires a good numerical precision to extend the isochrons to a larger domain. The reason is that the globalization starts at a point $x_0^0 = K(\theta, 0, \sigma_2^0)$

but numerically it corresponds to a value $K(\theta, E_1, \sigma_2^0)$, where E_1 is a small error. Since $|\lambda_1| > |\lambda_2|$, this error dramatically grows as we integrate backwards in time

$$\phi_{-t}(x_0^0) = K(\theta + t/T, E_1 e^{\lambda_1 t}, \sigma_2 e^{\lambda_2 t}), \quad (3.77)$$

and thus generates isochrons not accurate enough and the homogeneous coverage of the space, specially for points near the manifold $\Sigma_1(x) = 0$, is not possible.

Concerning the computation of A-surfaces in the 3D case, the method described previously provides the A-surfaces \mathcal{A}_σ^2 defined in (3.14).

Moreover, the slow manifold

$$\mathcal{S} = \{x \in \Omega \mid \Sigma_1(x) = 0\}, \quad (3.78)$$

can also be computed using the method described in Section 3.5.3. This manifold is important because the orbits approach the limit cycle along this manifold.

Numerical Examples

In this Section we will apply the methodology described in the previous Sections to different models in neuroscience, both for single neuron and neural populations.

- A single neuron model introduced in [72] that we refer to as *RT*:

$$\begin{aligned} C_m \dot{V} &= -I_L(V) - I_{Na}(V, h) - I_K(V, h) - I_T(V, r) + I_{app}, \\ \dot{h} &= \frac{h_\infty(V) - h}{\tau_h(V)}, \\ \dot{r} &= \frac{r_\infty(V) - r}{\tau_r(V)}, \end{aligned} \quad (3.79)$$

where V describes the membrane potential and h and r are the gating variables.

For the single neuron model (3.79) we have used the following functions

$$\begin{aligned}
I_L &= g_L(V - V_L), & I_{Na} &= g_{Na}m_\infty^3h(V - V_{Na}), \\
I_K &= g_K(.75(1 - h))^4(V - V_K), & I_T &= g_Tp_\infty^2r(V - V_T), \\
h_\infty(V) &= \frac{1}{1 + \exp((v + 41)/4)}, & r_\infty(V) &= \frac{1}{1 + \exp((v + 84)/4)}, \\
m_\infty(V) &= \frac{1}{1 + \exp(-(v + 37)/7)}, & p_\infty(V) &= \frac{1}{1 + \exp(-(v + 60)/6.2)}, \\
\tau_r(V) &= 28 + \exp(-(v + 25)/10.5), & \tau_h(V) &= 1/(a_h(V) + b_h(V)), \\
a_h(V) &= 0.128 \exp(-(v + 46)/18), & b_h(V) &= \frac{4}{1 + \exp(-(v + 23)/5)},
\end{aligned}$$

and the following set of parameters

$$\mathcal{P}_{RT} = \{C_m = 1, g_L = 0.05, V_L = -70, g_{Na} = 3, V_{Na} = 50, \\
g_K = 5, V_K = -90, g_T = 5, V_T = 0\}.$$

- A reduced Hodgkin-Huxley-like system that we refer to as *HH*:

$$\begin{aligned}
C_m \dot{V} &= -I_L(V) - I_{Na}(V, h) - I_K(V, n) + I_{app}, \\
\dot{n} &= \frac{n_\infty(V) - n}{\tau_n(V)}, \\
\dot{h} &= \frac{h_\infty(V) - h}{\tau_h(V)},
\end{aligned} \tag{3.80}$$

where V describes the membrane potential and n and h are the gating variables.

For the HH model (3.80) we have used the following functions

$$\begin{aligned}
I_L &= g_L(V - V_L), & I_{Na} &= g_{Na}m_\infty^3h(V - V_{Na}), & I_K &= g_Kn^4(V - V_K), \\
n_\infty(V) &= \frac{1}{1 + \exp(-(v + 53)/15)}, & h_\infty(V) &= \frac{1}{1 + \exp((v + 62)/7)}, \\
\tau_h(V) &= 7.4 \exp(-((67 + V)/20)^2) + 1.2, & \tau_n(V) &= 4.7 \exp(-((79 + V)/50)^2) + 1.1,
\end{aligned}$$

and the following set of parameters

$$\mathcal{P}_{HH} = \{C_m = 1, g_L = 0.1, V_L = -75.6, g_{Na} = 30, V_{Na} = 55, g_K = 9, V_K = -77\}.$$

- An extension of the Wilson-Cowan equations including synaptic dynamics that we refer to as WC_{Syn} :

$$\begin{aligned}
\tau_e \dot{E} &= -E + \delta_E(c_1E - c_2S + P), \\
\tau_i \dot{I} &= -I + \delta_I(c_3E - c_4S + Q), \\
\dot{s} &= -\frac{s}{\tau_d} + \frac{I}{\tau_r},
\end{aligned} \tag{3.81}$$

where E and I are the mean firing rates of excitatory and inhibitory populations, whereas s describes the synaptic dynamics.

For the extension of the Wilson-Cowan equations (3.81) we have used the following functions

$$\delta_E(x) = \frac{1}{1 + \exp(-a_E(v - \theta_E))}, \quad \delta_I(x) = \frac{1}{1 + \exp(-a_I(v - \theta_I))},$$

for the following parameters

$$\mathcal{P}_{WC} = \{P = 4.5, \tau_e = 3, a = 8, b = 16, a_E = 3, \theta_E = 4, Q = 0, \\ d = 3, \tau_i = 3, c = 7, a_I = 2, \theta_I = 3, \tau_r = 1, \tau_d = 6\}.$$

- A model for the mean field activity of a population of heterogeneous quadratic integrate-and-fire neurons [19] that we refer to as *QIF – FRE*:

$$\begin{aligned} \tau_m \dot{R} &= -\frac{\Delta}{\pi\tau_m} + 2RV, \\ \tau_m \dot{V} &= V^2 - (\pi\tau_m R)^2 - J\tau_m S + \Theta, \\ \tau_d \dot{S} &= -S + R, \end{aligned} \tag{3.82}$$

where R is the mean firing rate of the population, V is the mean membrane potential and S is the synaptic activation.

For the QIF-FRE model (3.82) we used the following parameters

$$\mathcal{P}_{QF} = \{\tau_m = 10, \Delta = 0.3, J = 21, \Theta = 4, \tau_d = 5\}.$$

Numerical computation

For the four cases considered, we study the dynamics in a neighbourhood of a T -periodic hyperbolic attracting limit cycle Γ , which surrounds an unstable fixed point. We set the zero phase value at the maximum of the voltage value V (in the WC_{Syn} model it will be the maximum of the E variable). Each limit cycle Γ has two characteristic exponents, λ_1 and λ_2 . The computation of the periodic orbits has been performed using a Runge-Kutta method with a tolerance of 10^{-14} . In the neighbourhood of Γ we have performed a Taylor expansion as in (3.72) up to order L and we have considered $N + 1$ Fourier coefficients for the coefficient $K_{\alpha, m-\alpha}$. Using this coefficients we have computed the residuals defined in (3.75) which are smaller than E_{tail} . The local approximation for the isochrons defined in (3.74) is computed with an error smaller than E_{loc} , while the globalization of the manifold, has been performed using the method in Section 3.5.3 and using a Runge-Kutta method with a tolerance of 10^{-14} . In the globalization we require a distance of order $\Delta x_{max} < 0.01$. Table 3.2 lists for each model the values of the parameters described above.

Model	Figure	$T \approx$	$\lambda_1 \approx$	$\lambda_2 \approx$	$L =$	$N =$	E_{tail}	E_{loc}
<i>RT</i>	3.17	8.395	-0.368	-0.022	15	2048	10^{-10}	10^{-8}
<i>HH</i>	3.18	7.586	-1.73	-0.2	5	2048	10^{-10}	10^{-6}
<i>WC_{Syn}</i>	3.19	24.43	-0.445	-0.246	10	2048	10^{-10}	10^{-8}
<i>QIF – FRE</i>	3.20	27.58	-0.408	-0.06	10	2048	10^{-10}	10^{-8}

Table 3.2: Numerical values for the different models considered; T = period of the periodic orbit Γ ; λ_1, λ_2 characteristic exponents associated to Γ ; L order of the Taylor expansion; $N + 1$ number of Fourier coefficients; tolerance E_{tail} defined in (3.75); maximal error E_{loc} when computing local approximation of the isochrons.

For each model, we present a Figure (Figs. 3.17 to 3.20) having different panels, that we describe and compare below. In the four figures, panel A shows the variables of each model during a period. Panel B shows the xyz coordinates over a period for K_{10} and K_{01} . Notice since the attraction to the limit cycle is not homogeneous along the cycle the functions K_{10} and K_{01} show dramatic changes along a period, specially for the *RT* and *HH* models (see Figs. 3.17 and 3.18). Panel C shows the isochrons using the local approximation for $K(\theta, \sigma_1, \sigma_2)$. Notice that for the phases for which K_{01} or K_{10} is close to zero show smaller domains of accuracy for their local approximations of $K(\theta, \sigma_1, \sigma_2)$ noticeable by the size of the isochrons. This difference in size can be easily seen comparing panel C for *HH* equations (Fig. 3.18) and *WC_{Syn}* (Fig.3.19) and their respective values of K_{01} and K_{10} . Panel D shows the slow manifold. Finally, panel E shows the global of the isochrons. Notice that they are not homogeneously distributed along the cycle. The isochron computation has been restricted to values that are biophysically plausible. Namely, for the *HH* model, the gating variables n and h are allowed to vary between 0 and 1. The same criterion was applied to the gating variables h and r in *RT* model. For the *WC_{Syn}* model, the three variables E, I and s are restricted between 0 and 1. Finally, for *QIF – FRE* model, R and S variables can not be negative.

3.5.4 A 3 dimensional study of perturbations

As we discussed in Section 3.3, the extension of the phase function to a neighbourhood Ω of an attracting limit cycle Γ by means of the amplitude variables σ_1 and σ_2 , is specially useful to account for an accurate description of the dynamics far from the limit cycle Γ . Using our method, by means of the parameterization $K(\theta, \sigma)$ in Ω and allows us to define the functions Θ, Σ_1 and

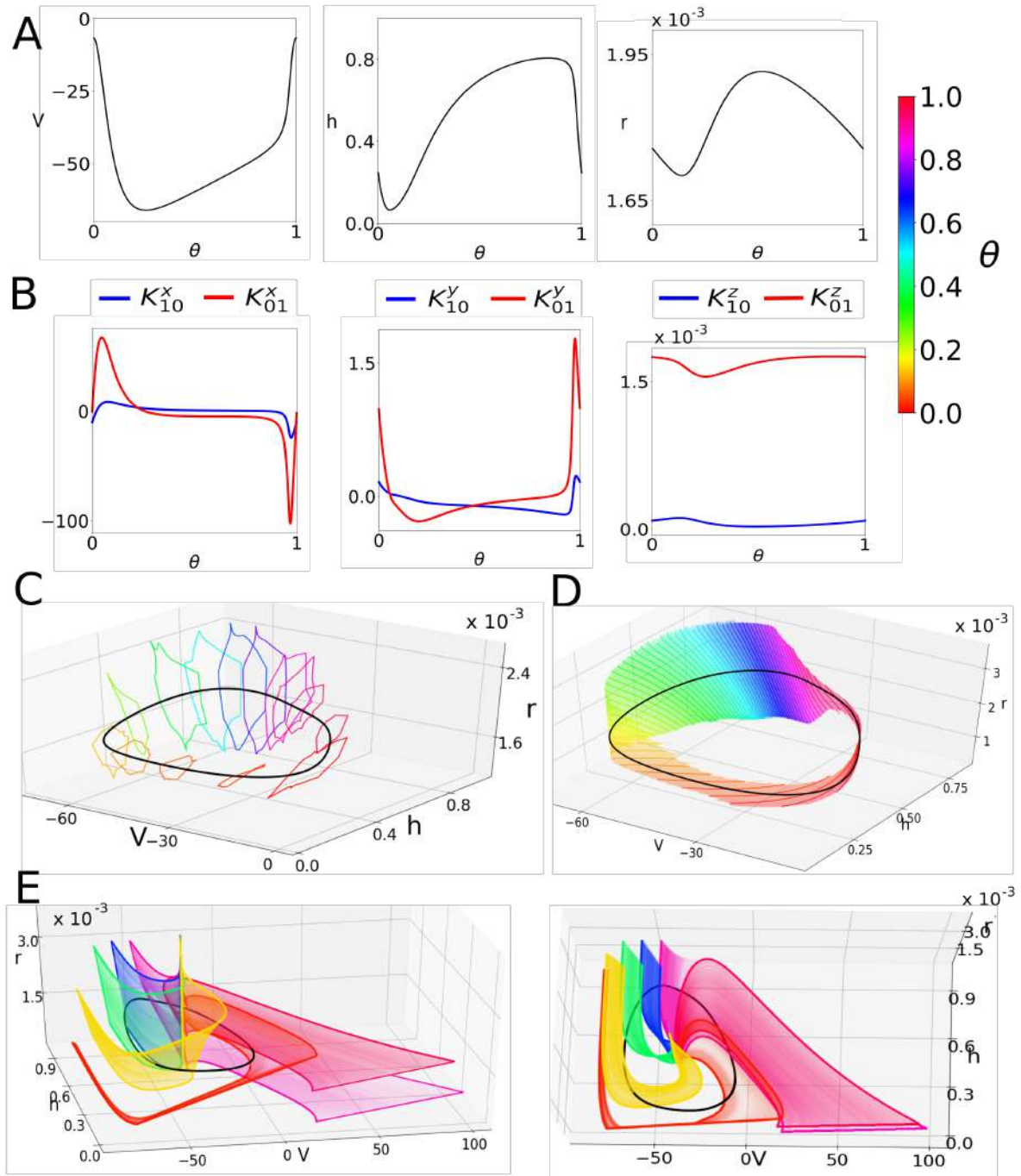


Figure 3.17: For RT model (3.79) we show: (A) the coordinates of V , h , and r of the periodic orbit as functions of the phase θ . (B) The coordinates of V , h , and r of K_{10} and K_{01} as functions of the phase θ . (C) Domain of accuracy for the local approximation of $K(\theta, \sigma_1, \sigma_2)$. (D) Slow attractive manifold of Γ , corresponding to $\sigma_1 = 0$. (E) Two perspectives of the globalized isochrons \mathcal{I}_θ . Here xyz refer to V , h and r , respectively.

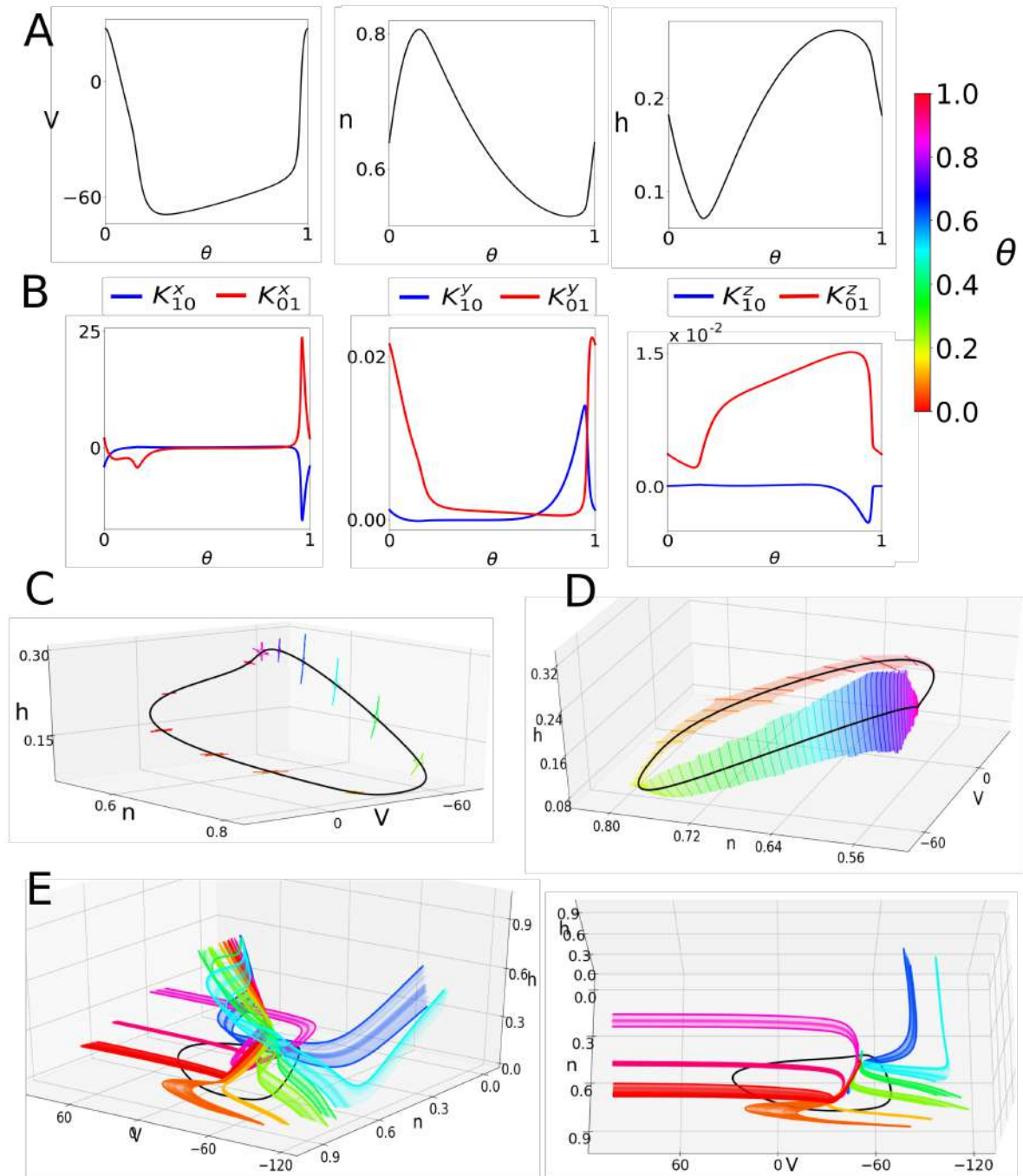


Figure 3.18: For HH equations (3.80) we show: (A) the coordinates of V , n , and h of the periodic orbit as functions of the phase θ . (B) The coordinates of V , n , and h of K_{10} and K_{01} as functions of the phase θ . (C) Domain of accuracy for the local approximation of $K(\theta, \sigma_1, \sigma_2)$. (D) Slow attractive manifold of Γ , corresponding to $\sigma_1 = 0$. (E) Two perspectives of the globalized isochrons \mathcal{I}_θ . Here xyz refer to V , n and h , respectively.

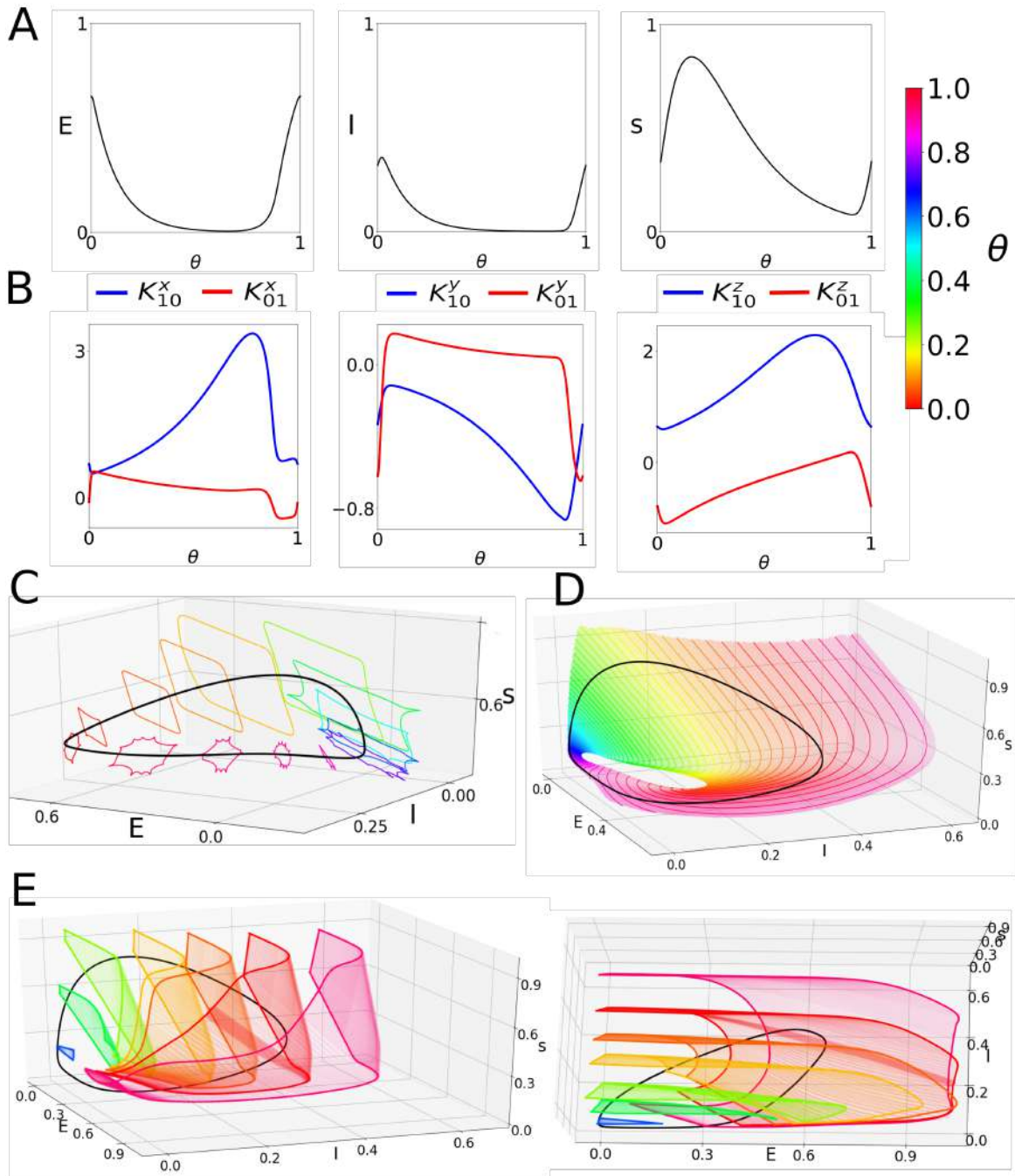


Figure 3.19: For the WC_{Sym} equations (3.81) we show: (A) the coordinates of E, I , and s of the periodic orbit as functions of the phase θ . (B) The coordinates of E, I , and s of K_{10} and K_{01} as functions of the phase θ . (C) Domain of accuracy for the local approximation of $K(\theta, \sigma_1, \sigma_2)$. (D) Slow attractive manifold of Γ , corresponding to $\sigma_1 = 0$. (E) Two perspectives of the globalized isochrons \mathcal{I}_θ . Here xyz refer to E, I and s , respectively.

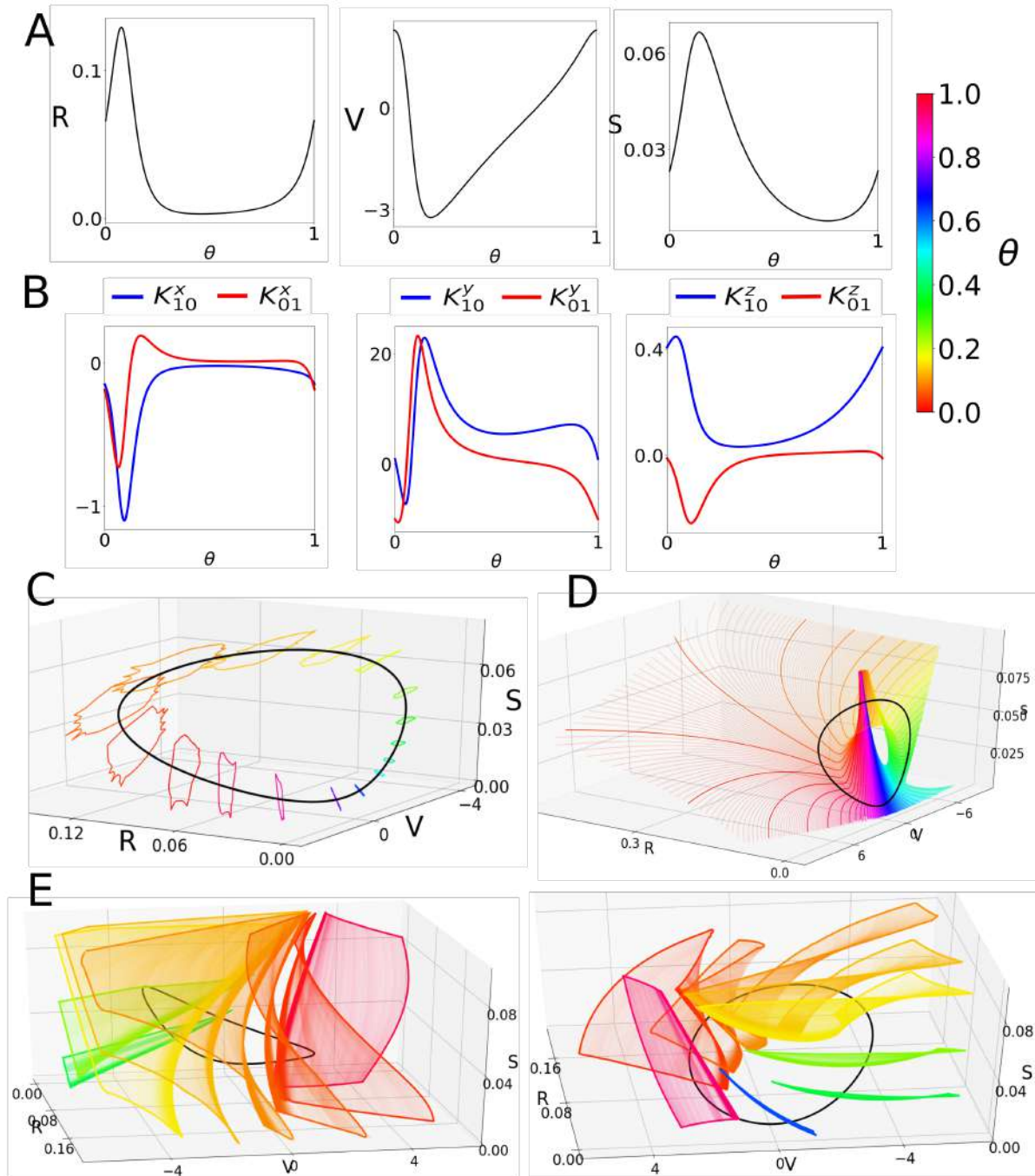


Figure 3.20: For the QIF-FRE model (3.82) we show: (A) the coordinates of R, V , and s of the periodic orbit as functions of the phase θ . (B) The coordinates of R, V , and s of K_{10} and K_{01} as functions of the phase θ . (C) Domain of accuracy for the local approximation of $K(\theta, \sigma_1, \sigma_2)$. (D) Slow attractive manifold of Γ , corresponding to $\sigma_1 = 0$. (E) Two perspectives of the globalized isochrons \mathcal{I}_θ . Here xyz refer to R, V and s , respectively.

Σ_2 (see Eqs. (3.11), (3.13)) which provide a description of the effects of a perturbation onto the oscillation.

Following the general derivation in Section 3.3, for the 3D case ($d = 3$), a perturbed system of the form

$$\dot{x} = X_A(x, t) = X(x) + Ap(x, t; A), \quad (3.83)$$

can be written in terms of the phase-amplitude variables as

$$\begin{aligned} \dot{\theta} &= \frac{1}{T} + A\nabla\Theta(K(\theta, \sigma)) \cdot p(t), \\ \dot{\sigma}_i &= \lambda_i\sigma_i + A\nabla\Sigma_i(K(\theta, \sigma)) \cdot p(t), \quad i = 1, 2, \end{aligned} \quad (3.84)$$

with $\theta \in \mathbb{T}$, $\sigma = (\sigma_1, \sigma_2) \in \mathbb{R}^2$. We recall (see (3.34)), that the functions $\nabla\Theta$ and $\nabla\Sigma_i$ are the first order approximation of the phase response functions (PRF) and the amplitude response functions (ARF), respectively.

We also recall that if $p(t)$ is a T_s -periodic pulsatile perturbation, dynamics can be described by the following stroboscopic map

$$\begin{aligned} \theta^{k+1} &= \theta^k + A\nabla\Theta(K(\theta^k, \sigma^k)) \cdot \vec{v} + \frac{T_s}{T}, \quad (\text{mod } 1) \quad k \in \mathbb{N} \\ \sigma_i^{k+1} &= (\sigma_i^k + A\nabla\Sigma_i(K(\theta^k, \sigma^k)) \cdot \vec{v})e^{\lambda_i T_s} \quad i = 1, 2, \end{aligned} \quad (3.85)$$

where v is a 3D vector representing the direction of the pulsatile perturbation.

Analogously to (3.31), we can compute the PRF and the ARFs in the 3D case using that $K(\Theta(x), \Sigma_1(x), \Sigma_2(x)) = x$; thus differentiating we have for $x = (x_1, x_2, x_3) \in \Omega$:

$$\begin{bmatrix} 1 & 0 & 0 \\ 0 & 1 & 0 \\ 0 & 0 & 1 \end{bmatrix} = [DK(\theta, \sigma)] \begin{bmatrix} \nabla\Theta(x) \\ \nabla\Sigma_1(x) \\ \nabla\Sigma_2(x) \end{bmatrix}$$

therefore

$$\begin{bmatrix} \nabla\Theta(x) \\ \nabla\Sigma_1(x) \\ \nabla\Sigma_2(x) \end{bmatrix} = [DK(\theta, \sigma)]^{-1} = \begin{bmatrix} \partial_\theta K_{x_1}(\theta, \sigma) & \partial_{\sigma_1} K_{x_1}(\theta, \sigma) & \partial_{\sigma_2} K_{x_1}(\theta, \sigma) \\ \partial_\theta K_{x_2}(\theta, \sigma) & \partial_{\sigma_1} K_{x_2}(\theta, \sigma) & \partial_{\sigma_2} K_{x_2}(\theta, \sigma) \\ \partial_\theta K_{x_3}(\theta, \sigma) & \partial_{\sigma_1} K_{x_3}(\theta, \sigma) & \partial_{\sigma_2} K_{x_3}(\theta, \sigma) \end{bmatrix}^{-1} \quad (3.86)$$

where K_{x_i} $i = 1, 2, 3$ denotes the i -th component of the parameterization $K(\theta, \sigma)$.

Slow manifold reduction

As discussed in Section 3.4.3, the phase approach was limited to very weak perturbations. For an accurate description of the perturbed dynamics it was necessary to consider the amplitude variable σ . In the 3D case, apart from the phase reduction (see Section 3.3.1), we can explore the slow manifold reduction. This reduction is based on the fact that the amplitude variables σ_1 and σ_2 , decay to zero at a rate that depends on its associated Floquet multiplier. If we have $|\lambda_1| \gg |\lambda_2|$, we can assume that $\sigma_1 = 0$ and the dynamics occurs on the slow manifold \mathcal{S} defined in (3.78).

In the slow manifold, the dynamics is given by

$$\begin{aligned}\dot{\theta} &= \frac{1}{T} + A\nabla\Theta(K(\theta, 0, \sigma_2)) \cdot p(t) \\ \dot{\sigma}_2 &= \lambda_2\sigma_2 + A\nabla\Sigma_2(K(\theta, 0, \sigma_2)) \cdot p(t),\end{aligned}\tag{3.87}$$

and similarly the stroboscopic map in (3.32) writes as

$$\begin{aligned}\theta^{k+1} &= \theta^k + A\nabla\Theta(K(\theta^k, 0, \sigma_2^k)) \cdot \vec{v} + \frac{T_s}{T}, \quad (\text{mod } 1) \quad k \in \mathbb{N} \\ \sigma_2^{k+1} &= (\sigma_2^k + A\nabla\Sigma_2(K(\theta^k, 0, \sigma_2^k)) \cdot \vec{v})e^{\lambda T_s}.\end{aligned}\tag{3.88}$$

3.5.5 Preliminary study of perturbations

We study the perturbed dynamics by means of the phase reduction, the slow manifold reduction and using the full phase-amplitude variables for a particular example. We consider a train of n pulses of size ϵ separated by a time T_s (see Fig. 3.21). Each train of pulses is separated by a time T_p . We expect for this perturbation the dynamics to occur near but not on the limit cycle.

We consider a pulse of amplitude weak enough so the dynamics can be described by the following map

$$F(x) := \varphi_{T_p} \circ \underbrace{f \circ \dots \circ f}_n(x),\tag{3.89}$$

where $f(x) := \varphi_{T_s}(x + \epsilon)$.

As an example of application, we will apply the perturbation (3.89) described above to the limit cycle of the RT model (3.79). In particular, we will consider a train of $n = 50$ pulses of amplitude $\epsilon = -0.15$, separated by a time interval $T_s = 0.01$. The interval between input trains will be set to $T_p = T = 8.395$, where T is the period of the unperturbed limit cycle.

The phase-amplitude variables coincide with the description of the state variables at multiples of the period (see Fig. 3.22A). In Fig. 3.22B we show the phase coordinate for several iterates using

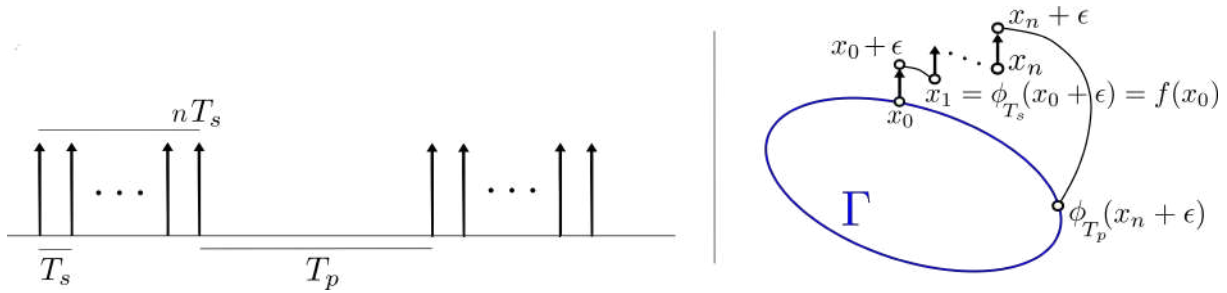


Figure 3.21: We will consider a train of n pulses of size ϵ separated by a time T_s . Each train of pulses will be separated by a time T_p (left panel). By using this perturbation, we expect the dynamics to occur near but not on the limit cycle (right panel).

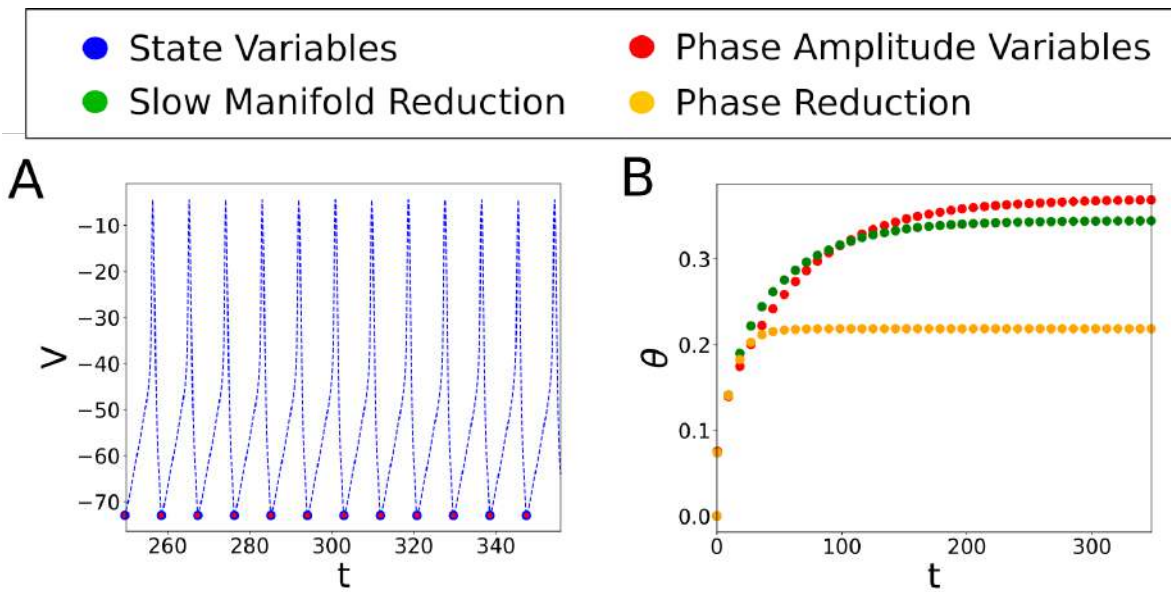


Figure 3.22: For the map (3.89) applied to the RT model (3.79) we show: (A) the voltage coordinate provided by the dynamics of the full system in the state variables (blue) and the dynamics of the full system in the phase-amplitude variables (red). The dashed curve represents the evolution of the voltage provided by the original system. (B) Phase coordinate for several iterates using the dynamics provided by the phase reduction (yellow), the slow manifold reduction (green) and the full system in phase-amplitude variables (red).

the dynamics provided by the phase reduction, the slow manifold reduction and the full system in phase-amplitude variables. Dynamics seems to tend to a fixed point which is specially different for the phase reduction.

3.6 Discussion

In this Chapter we extend the relationship between the parameterization method and the phase reduction framework initiated in [17, 39, 49] where it was applied to pulsatile perturbations of 2D systems. Here we extend these results to continuous time dependent perturbations and beyond the 2D case.

For the 2D case we have applied the methods in [39] to obtain the parameterization $K(\theta, \sigma)$ of the Wilson-Cowan equations and use it to compute its iPRCs, isochrons and A-Curves. The calculation of these objects near two different bifurcations, namely a Hopf and a SNIC, allowed us to understand how a given oscillator may respond differently to the same perturbation and to relate this response with some features which can be easily seen when looking either to the iPRCs (that is if are of type I or II) or how packed is their isochron distribution. Then, we have studied the domain of applicability of phase and phase-amplitude variables when forcing the Wilson-Cowan equations with a T -periodic continuous perturbation.

The main achievement of this Chapter is the efficient extension of the method in [39, 49] to the computation of isochrons for a d -dimensional dynamical system, $d \geq 2$ with the Floquet normal form (see [18]) which provides powerful and fast methods to compute the parameterization $K(\theta, \sigma)$.

The parameterization $K(\theta, \sigma)$ provided an accurate computation of the isochrons and A-surfaces of a given limit cycle. We remark that several features require an accurate numerical precision in order to globalize the global isochrons to a larger domain. Namely, when the ratio $\lambda_{max}/\lambda_{min}$ is large or the domain for the local approximation is small. Both features are typically a consequence of the slow-fast dynamics.

The parameterization $K(\theta, \sigma)$ can also be used to compute iPRFs and iARFs of limit cycles of d -dimensional systems. Furthermore, it allows to compute in phase-amplitude variables the effect of discrete and continuous perturbations with high accuracy. We have carried out an initial exploration of how the slow manifold reduction can explain the effect of perturbations for the case $d > 2$. Thus, the work performed in this Chapter opens the door for further studies and applications in the context of optimal control strategies for periodic dynamics.

Chapter 4

Computation of PRCs by means of the parameterization method

The goal of this Chapter will be to present a methodology, merging concepts introduced in previous Chapters 2 and 3, such as the invariant curves for the stroboscopic map Γ_A , the phase-amplitude variables and the isochrons, to compute the PRCs for perturbations of large amplitude and not necessarily pulsatile.

In general, PRCs can be measured, both experimentally and numerically, in individual neurons and in neuronal populations, and for arbitrary stimuli, assuming that there is enough time to allow the perturbed trajectory to relax back to the limit cycle. As we have seen in previous Chapter, for perturbations that are infinitesimally small in duration (pulsatile) and amplitude, one obtains the so called infinitesimal PRC (iPRC). The iPRC corresponds to the first order approximation of the PRC with respect to the amplitude and it can be easily computed by means of solving the Adjoint equation [25]. Perturbations of small amplitude but longer duration are assumed to sum linearly, thus the phase resetting experienced by the oscillator is obtained by convolving the input waveform with the iPRC. Of course, this approximation fails when the perturbation is strong.

There exists different alternatives to the Adjoint method for the computation of PRCs [51, 35]. The underlying idea for the method we present here is to construct a particular periodic perturbation consisting of the repetition of the transient stimulus followed by a resting period when no perturbation acts. For this periodic system we consider the corresponding stroboscopic map and we prove that, under certain conditions, the map has an invariant curve. The core mathematical result of this Chapter is Theorem 4.2.2, which gives the existence of the invariant curve and provides the relationship between the PRC and the internal dynamics of the curve. The proof of the Theorem relies on using the coordinate system given by the previously defined phase and the amplitude

variables (see Chapter 3). In these variables, the map is contracting in the amplitude direction and one can apply results about the existence of invariant curves from [62, 63]. In fact, working in the original variables, one could also use theorems on the persistence of normally hyperbolic invariant manifolds with a posteriori format [7, 43]. That is, one formulates a functional equation for the parameterization of the invariant curve and its internal dynamics. Then, if there exists an approximate solution of this invariance equation, which satisfies some explicit nondegeneracy conditions, there is a true solution nearby.

Furthermore, these *a posteriori* theorems provide a numerical algorithm to compute the invariant curve and its internal dynamics based on a 'quasi-Newton' method. We will implement this algorithm and compute the PRC using the result in Theorem 4.2.2. We also present an extension of the algorithm to compute the PRC for those cases in which the invariant curve of the stroboscopic map does not exist (possibly because it loses its normal hyperbolic properties). In this case, it is possible to write an invariance equation which can be solved approximately using similar algorithms and still obtain the PRC. Our methods can also be used to find the ARC.

We apply our methodology to some representative examples in the literature, namely the Morris-Lecar model and the Wilson-Cowan equations, with a sinusoidal type of stimulus. As the amplitude is increased, we detect the breakdown of the curve, which we can relate with the geometry of the isochrons. Moreover, we compute the PRC beyond the breakdown of the invariant curve with a modified version of the algorithms. We compare the results for the PRC using our methodology with the one obtained using the standard approach, showing a good agreement. This accuracy is maintained for all the amplitudes, including the transition from type 0 to type 1 PRC [32, 33], which occurs when the perturbation sends points of the limit cycle to the phaseless sets.

The Chapter is organized as follows: in Section 4.1 we set the mathematical formalism. In Section 4.2.1 we state the main result: Theorem 4.2.2. In Section 4.3 we describe the numerical algorithms based on Theorem 4.2.2 and present an extension for the case when the invariant curve does not exist but the PRC can still be computed. In Section 4.4 we present numerical results for some representative examples. We finish with a discussion in Section 4.5.

Results in this Chapter have been submitted for publication [50].

4.1 Mathematical Formalism

Let us consider a smooth system of ODEs given by

$$\dot{x} = X(x) + Ap(t; A), \quad x \in \mathbb{R}^n \quad (4.1)$$

where $p(t; A)$ is a function with compact support satisfying $p(t; A) = 0$ everywhere except for $0 \leq t \leq T_{pert}$ and $\max_{t \in \mathbb{R}} |p(t; A)| = 1$, therefore A determines the amplitude of the perturbation.

We assume that when $A = 0$ (i.e the unperturbed case) system (4.1) has a hyperbolic attracting limit cycle Γ_0 of period T

$$\Gamma_0 := \{\gamma_0(t), t \in [0, T)\},$$

being γ_0 a T -periodic solution of (4.1).

In the following we will denote by $\psi_A(t; t_0, x)$ the general solution of system (4.1). As system (4.1) is autonomous for $A = 0$, we know that $\psi_0(t; t_0, x) = \phi_0(t - t_0; x)$, where $\phi_0(t; x)$ is the flow of the unperturbed system. Moreover, abusing of notation we will denote by $\phi_A(t; x) = \psi_A(t; 0, x)$.

For the unperturbed case, we can define a parameterization K_0 for Γ_0 by means of the phase variable $\theta = \frac{t}{T}$, that is,

$$K_0 : \mathbb{T} := [0, 1) \rightarrow \mathbb{R}^n, \quad (4.2)$$

such that $K_0(\theta) = \gamma_0(\theta T)$. Thus, the dynamics for θ satisfies

$$\dot{\theta} = 1/T \quad \text{with solution} \quad \Psi_0(t; \theta_0) = \theta_0 + \frac{t}{T}. \quad (4.3)$$

Observe that $\phi_0(t; K_0(\theta)) = K_0(\theta + \frac{t}{T}) = K_0(\Psi_0(t; \theta))$.

Consider a point x in the basin of attraction \mathcal{M} (stable manifold) of the limit cycle Γ_0 . Since Γ_0 is a Normally Hyperbolic Invariant Manifold (NHIM), by NHIM theory (see [27, 37, 46]), there exists a unique point on the limit cycle, $K_0(\theta) \in \Gamma_0$, such that

$$d(\phi_0(t; x), \phi_0(t; K_0(\theta))) \leq Ce^{-\lambda t} \quad \text{for } t \geq 0, \quad (4.4)$$

where $-\lambda < 0$ is the maximal Lyapunov exponent of Γ_0 . Analogously to Chapter 3, this property allows us to assign a phase θ to any point $x \in \mathcal{M}$. Indeed, the phase function is defined as (see [37]):

$$\begin{aligned} \Theta : \mathcal{M} \subset \mathbb{R}^n &\rightarrow \mathbb{T}, \\ x &\mapsto \Theta(x) = \theta, \end{aligned} \quad (4.5)$$

such that equation (4.4) is satisfied. The sets of points with the same asymptotic phase are called isochrons [88] (previously defined in Eq. (3.5)). The sets of points where the asymptotic phase is not defined are called phaseless sets [37]. Clearly, for an attracting Normally Hyperbolic Invariant Manifold the phaseless sets are contained in $\mathbb{R}^n \setminus \mathcal{M}$.

In this context, the definition of the PRC (see [24]) for the general perturbation $Ap(t; A)$ in (4.1) is defined as

$$PRC(\theta, A) = \Theta(\phi_A(T_{pert}, K_0(\theta))) - \Theta(\phi_0(T_{pert}, K_0(\theta))), \quad (4.6)$$

if $\phi_A(T_{pert}, K_0(\theta)) \in \mathcal{M}$.

In the sequel, abusing notation, we will denote by \mathcal{M} a bounded neighbourhood of the periodic orbit Γ_0 such that $\bar{\mathcal{M}}$ is contained in the basin of attraction of Γ_0 .

If we denote by

$$x_{pert} := \phi_A(T_{pert}; K_0(\theta)), \quad \theta_{pert} := \Theta(x_{pert}), \quad (4.7)$$

from (4.3) and (4.6) we have that

$$PRC(\theta, A) = \theta_{pert} - \left(\theta + \frac{T_{pert}}{T} \right). \quad (4.8)$$

Moreover, since $\phi_A(T_{pert} + t; K_0(\theta)) = \phi_0(t; x_{pert})$ and by the definition of phase function given in (4.5) we have that

$$PRC(\theta, A) = \Theta(\phi_A(T_{pert} + t; K_0(\theta))) - \Theta(\phi_0(T_{pert} + t; K_0(\theta))), \quad (4.9)$$

for all $t \geq 0$.

The standard method to compute the PRC

In order to compute the PRC either experimentally or numerically, usually one finds the time $t_1 \gg T_{pert}$ at which some x_i -coordinate of the perturbed trajectory $\phi_A(t; K_0(\theta))$ reaches the maximum after the perturbation is turned off and compares this value with the time t_0 which is closest to t_1 at which the unperturbed trajectory $\phi_0(t; K_0(\theta))$ reaches this maximum (see Figure 4.1). Then, the PRC is given approximately by

$$\Delta\theta = \frac{t_1 - t_0}{T}. \quad (4.10)$$

This approach (that we will refer to as the *standard method*) provides a good approximation of the PRC if the time to relax back to the oscillator Γ_0 is short either because there is a strong contraction (the maximal Lyapunov exponent $-\lambda$ in (4.4) is sufficiently negative) or the perturbation is weak ($A \ll 1$ in (4.1)). Otherwise, one should wait several periods (kT , $k \in \mathbb{N}$ sufficiently large) before computing the phase difference.

In the next Sections we present theoretical and numerical results based on the parameterization method to compute the PRC.

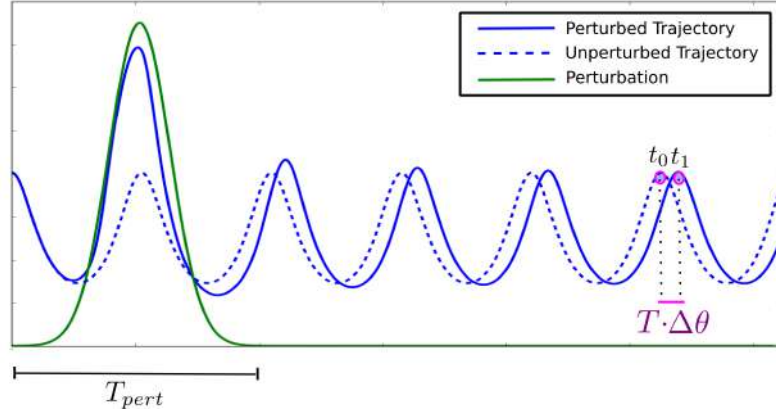


Figure 4.1: After the perturbation is turned off ($t > T_{pert}$), the trajectories relax back to the limit cycle and a phase shift $\Delta\theta$ is experienced.

4.2 Computation of the PRC by means of the parameterization method. Theoretical results

4.2.1 Stroboscopic approach

The perturbation $p(t; A)$ in (4.1) is not periodic. However, we will introduce a periodic perturbation $\bar{p}(t; A)$ of period $T' := T_{pert} + T_{rel}$, with $T_{rel} \gg T_{pert}$ which coincides with $p(t; A)$ for $0 \leq t \leq T'$. Then, we consider the T' -periodic system

$$\dot{x} = X(x) + A\bar{p}(t; A), \quad x \in \mathbb{R}^n \quad (4.11)$$

whose solutions coincide with the solutions of (4.1) for $0 \leq t \leq T'$. Since $\bar{p}(t; A)$ is periodic, we can define the stroboscopic map given by the flow of (4.11) at time T' starting at $t = 0$, i.e.

$$\begin{aligned} F_A : \mathbb{R}^n &\rightarrow \mathbb{R}^n, \\ x &\rightarrow F_A(x) = \phi_A(T'; x) = \phi_A(T_{pert} + T_{rel}; x). \end{aligned} \quad (4.12)$$

Using this approach the formula for the PRC given in (4.9) for $t = T_{rel}$ writes as

$$PRC(\theta, A) = \Theta(F_A(K_0(\theta))) - \Theta(F_0(K_0(\theta))). \quad (4.13)$$

Note that for $A = 0$, one has

$$F_0(K_0(\theta)) = \phi_0(T'; K_0(\theta)) = K_0(\theta + T'/T), \quad (4.14)$$

therefore

$$\Gamma_0 = \{K_0(\theta), \theta \in [0, 1]\} \quad (4.15)$$

is an invariant curve of the map F_0 . Moreover, for any $x \in \mathcal{M}$, by (4.4) we have

$$|F_0(x) - F_0(K_0(\theta))| \leq Ce^{-\lambda T'},$$

where $\theta = \Theta(x)$. Therefore, Γ_0 is a normally hyperbolic attracting invariant curve of the map F_0 .

Let us recall here, following [27, 28, 46], the definition of normally hyperbolic attracting invariant curve adapted to our problem.

Definition 4.2.1. *Let $F : M \rightarrow M$ a C^r map on a C^r -differentiable manifold M . Assume that there exists a manifold $\Gamma \subseteq M$ that is invariant for F . We say that $\Gamma \subset M$ is a hyperbolic attracting manifold if there exist a splitting of the tangent bundle of TM into DF -invariant sub-bundles, i.e.,*

$$TM = E^s \oplus T\Gamma,$$

and constants $C > 0$ and

$$0 < \lambda_+ < \eta^{-1} \leq 1, \quad (4.16)$$

such that for all $x \in \Gamma$ we have

$$\begin{aligned} v \in E_x^s &\Leftrightarrow \|DF^k(x)v\| \leq C\lambda_+^k \|v\|, \text{ for all } k \geq 0, \\ v \in T_x\Gamma &\Leftrightarrow \|DF^k(x)v\| \leq C\eta^{|k|} \|v\|, \text{ for all } k \in \mathbb{Z}. \end{aligned} \quad (4.17)$$

For our problem, following [39, 49], we can differentiate the invariance equation (4.14) of Γ_0 obtaining:

$$DF_0(K_0(\theta))DK_0(\theta) = DK_0\left(\theta + \frac{T'}{T}\right), \quad (4.18)$$

and for $n = 2$ in [39, 49] it is shown that there exists $N(\theta)$ such that

$$DF_0(K_0(\theta))N(\theta) = e^{-\lambda T'}N\left(\theta + \frac{T'}{T}\right). \quad (4.19)$$

Therefore, for any $x = K_0(\theta) \in \Gamma_0$, there is a splitting $\mathbb{R}^2 = \langle DK_0(\theta) \rangle \oplus \langle N(\theta) \rangle$ and rates $\lambda_+ = e^{-\lambda T'}$ and $\eta = 1$, thus showing that Γ_0 is a normally hyperbolic attracting manifold.

This can be generalized to $n \geq 2$ (see Remark 4.2.4) using the information of the variational equations along the periodic orbit Γ_0 .

Next, we present the main result of this Chapter which provides the existence of an invariant curve Γ_A of the stroboscopic map F_A of system (4.11) which is $\mathcal{O}(Ae^{-\lambda T_{rel}})$ -close to Γ_0 and relates its internal dynamics with the PRC of Γ_0 in system (4.1) (see Fig. 4.2). The proof of this Theorem is postponed to Section 4.2.2.

Theorem 4.2.2. *Consider the stroboscopic map F_A of the T' -periodic system (4.11) defined in (4.12) with $T' = T_{pert} + T_{rel}$ and let Γ_0 be the normally hyperbolic attracting invariant curve of the map F_0 , parameterized by K_0 such that*

$$F_0 \circ K_0 = K_0 \circ f_0,$$

where $f_0(\theta) = \theta + T'/T$.

Take $A > 0$. If A is small or $A = \mathcal{O}(1)$ and the following hypothesis are satisfied:

H1 $\phi_A(T_{pert}; x) \in \mathcal{M}$ for any $x \in \Gamma_0$,

H2 The function $PRC(\theta, A) + \theta$ is a monotone function,

H3 T_{rel} is sufficiently large,

then, there exists an invariant curve Γ_A of the map F_A . Moreover, there exists a parameterization K_A of Γ_A and a periodic function f_A such that

$$F_A(K_A(\theta)) = K_A(f_A(\theta)), \tag{4.20}$$

$$K_A(\theta) = K_0(\theta) + \mathcal{O}(Ae^{-\lambda T_{rel}}),$$

$$PRC(\theta, A) = f_A(\theta) - f_0(\theta) + \mathcal{O}(Ae^{-\lambda T_{rel}}).$$

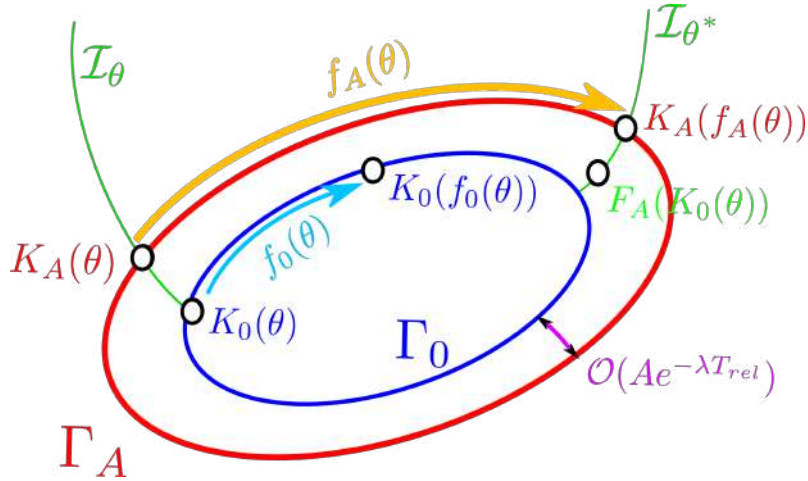


Figure 4.2: Sketch of the results of Theorem 4.2.2. The perturbation acting on a point $K_0(\theta) \in \Gamma_0$ for a time $T' = T_{pert} + T_{rel}$ displaces it to a point $F_A(K_0(\theta))$. In Theorem 4.2.2 we show that the phase difference between the perturbed and unperturbed trajectories is given up to an error $\mathcal{O}(Ae^{-\lambda T_{rel}})$ by the difference between the internal dynamics $f_A(\theta)$ on Γ_A and $f_0(\theta)$ on Γ_0 . For the sake of clarity we have located points $K_0(\theta)$ and $K_A(\theta)$ (resp. $F_A(K_0(\theta))$ and $K_A(f_A(\theta))$) on the same isochron \mathcal{I}_θ (resp. \mathcal{I}_{θ^*} , where $\theta^* := f_A(\theta)$) although they are $\mathcal{O}(Ae^{-\lambda T_{rel}})$ -close.

4.2.2 Proof of Theorem 4.2.2

The case A small

In this Section we will prove Theorem 4.2.2 for A small. We first prove the following lemma which shows that the map F_A has an invariant curve Γ_A which is $\mathcal{O}(Ae^{-\lambda T_{rel}})$ close to Γ_0 .

Lemma 4.2.3. *Consider the stroboscopic map F_A of the T' -periodic system (4.11) defined in (4.12) and let Γ_0 be the normally hyperbolic invariant curve of the map F_0 , parameterized by K_0 (see (4.2)). Then, for A small enough there exists an invariant curve Γ_A of the map F_A . Moreover, there exist a parameterization $K_A : \mathbb{T} \rightarrow \mathbb{R}^n$ and a periodic function $f_A : \mathbb{T} \rightarrow \mathbb{T}$ satisfying the invariance equation*

$$F_A(K_A(\theta)) = K_A(f_A(\theta)),$$

such that $K_A(\theta)$ satisfies

$$|K_A(\theta) - K_0(\theta)| = \mathcal{O}(Ae^{-\lambda T_{rel}}), \quad (4.21)$$

where $-\lambda < 0$ is the maximal Lyapunov exponent of Γ_0 .

Proof. When $n = 2$, since, by (4.18) and (4.19), Γ_0 is a normally hyperbolic attracting invariant manifold of F_0 , the existence of the invariant curve for A small enough follows from Fenichel's Theorem [27, 28]. We will perform the rest of the proof for $n = 2$ but it can be easily generalized to arbitrary n (see Remark 4.2.4). Using results in [39] (see [13, 18] for higher dimensions), we can describe a point $(x, y) \in \mathcal{M}$ in terms of the so called phase-amplitude variables (more details about this change were given in Chapter 3). More precisely, consider the change of coordinates

$$\begin{aligned} K : \Omega \subset \mathbb{T} \times \mathbb{R} &\rightarrow \mathcal{M} \subset \mathbb{R}^2 \\ (\theta, \sigma) &\rightarrow K(\theta, \sigma) = (x, y), \end{aligned} \quad (4.22)$$

where $\Omega := \mathbb{T} \times U$ and $U \subset \mathbb{R}$, such that system (4.11) for $A = 0$, expressed in the variables (θ, σ) , has the following form

$$\begin{aligned} \dot{\theta} &= \frac{1}{T}, \\ \dot{\sigma} &= -\lambda\sigma. \end{aligned} \quad (4.23)$$

Moreover, system (4.11) for $A \neq 0$ small enough, expressed in the variables (θ, σ) , writes as the T' -periodic system

$$\begin{aligned} \dot{\theta} &= \frac{1}{T} + \mathcal{O}(A), \\ \dot{\sigma} &= -\lambda\sigma + \mathcal{O}(A), \end{aligned} \quad (4.24)$$

and we will denote by $\Psi_A(t; t_0, \theta, \sigma)$ the general solution of (4.24).

Consider now the stroboscopic map F_A in the variables (θ, σ) , i.e. $\tilde{F}_A : \Omega \rightarrow \Omega$, such that $\tilde{F}_A = K^{-1} \circ F_A \circ K$. We have

$$\tilde{F}_A(\theta, \sigma) = \Psi_A(T'; 0, \theta, \sigma) = \left(\theta_{pert} + \frac{T_{rel}}{T}, \sigma_{pert} e^{-\lambda T_{rel}} \right), \quad (4.25)$$

where $K(\theta_{pert}, \sigma_{pert}) = \phi_A(T_{pert}, K(\theta, \sigma)) \in \mathcal{M}$. Therefore, for A small enough we have

$$(\theta_{pert}, \sigma_{pert}) = \Psi_A(T_{pert}; 0, \theta, \sigma) = \left(\theta + \frac{T_{pert}}{T} + \mathcal{O}(A), \sigma e^{-\lambda T_{pert}} + \mathcal{O}(A) \right).$$

In conclusion,

$$\tilde{F}_A(\theta, \sigma) = \left(\theta + \frac{T'}{T} + \mathcal{O}(A), \sigma e^{-\lambda T'} + \mathcal{O}(A e^{-\lambda T_{rel}}) \right) = \tilde{F}_0 + \mathcal{O}(A). \quad (4.26)$$

The unperturbed invariant curve Γ_0 for \tilde{F}_0 in the variables (θ, σ) is given by

$$\tilde{\Gamma}_0 = \{(\theta, \sigma) \mid \theta \in \mathbb{T}, \sigma = 0\}.$$

Therefore, by Fenichel's Theorem, for $A \neq 0$ small enough, there exists a function

$$\begin{aligned} S_A : \mathbb{T} &\rightarrow \mathbb{R} \\ \theta &\rightarrow S_A(\theta), \end{aligned} \quad (4.27)$$

such that $S_A(\theta) = \mathcal{O}(A)$ and the perturbed invariant curve for \tilde{F}_A is given by

$$\tilde{\Gamma}_A = \{(\theta, \sigma) \mid \theta \in \mathbb{T}, \sigma = S_A(\theta)\}. \quad (4.28)$$

Analogously, $\tilde{K}_A(\theta) = (\theta, S_A(\theta))$ is a parameterization of the invariant curve $\tilde{\Gamma}_A$. Hence, using the invariance property, we have

$$\begin{aligned} \tilde{F}_A(\tilde{K}_A(\theta)) &= \tilde{F}_A(\theta, S_A(\theta)) \\ &= (\tilde{F}_A^1(\theta, S_A(\theta)), \tilde{F}_A^2(\theta, S_A(\theta))) \\ &= (\tilde{F}_A^1(\theta, S_A(\theta)), S_A(\tilde{F}_A^1(\theta, S_A(\theta)))) \\ &= \tilde{K}_A(\tilde{F}_A^1(\theta, S_A(\theta))) \\ &:= \tilde{K}_A(f_A(\theta)), \end{aligned}$$

where the internal dynamics is given by

$$f_A(\theta) = \tilde{F}_A^1(\theta, S_A(\theta)),$$

and \tilde{F}_A^1 and \tilde{F}_A^2 correspond to the θ and σ component of \tilde{F}_A , respectively.

Using the invariance property of $\tilde{\Gamma}_A$ and the expression (4.26) for the stroboscopic map \tilde{F}_A , we obtain:

$$S_A \left(\theta + \frac{T'}{T} + \mathcal{O}(A) \right) = S_A(\theta) e^{-\lambda T'} + \mathcal{O}(A e^{-\lambda T_{rel}}), \quad \forall \theta \in \mathbb{T}.$$

Therefore, since $S_A(\theta) = \mathcal{O}(A)$ and $T' = T_{pert} + T_{rel}$ we get an improved bound for S_A

$$S_A = \mathcal{O}(A e^{-\lambda T_{rel}}).$$

Returning to the original variables (x, y) using the change of variables given in (4.22) and assuming $(x, y) \in \Gamma_A \subset \mathcal{M}$, if A is small enough, one has

$$(x, y) = K(\theta, \sigma) = K(\theta, S_A(\theta)) = K \circ \tilde{K}_A(\theta) =: K_A(\theta). \quad (4.29)$$

Thus, the invariant curve can be parameterized by K_A and

$$F_A(K_A(\theta)) = F_A \circ K \circ \tilde{K}_A(\theta) = K \circ \tilde{F}_A \circ \tilde{K}_A(\theta) = K \circ \tilde{K}_A(f_A(\theta)) = K_A(f_A(\theta)),$$

that is, the internal dynamics over the invariant curve Γ_A is the same for both parameterizations. Therefore,

$$\begin{aligned} |K_A(\theta) - K_0(\theta)| &= |K \circ \tilde{K}_A(\theta) - K \circ \tilde{K}_0(\theta)| \\ &\leq \sup_{(\theta, \sigma) \in \tilde{\Omega}} |DK(\theta, \sigma)| |\tilde{K}_A(\theta) - \tilde{K}_0(\theta)| \\ &\leq \bar{C} |S_A(\theta)| \leq C A e^{-\lambda T_{rel}}, \end{aligned} \quad (4.30)$$

where C is a constant independent of T_{rel} and A . \square

Remark 4.2.4. Notice that the proof can be generalized to any n , just considering $\sigma = (\sigma_1, \dots, \sigma_{n-1}) \in \mathbb{R}^{n-1}$ and

$$\dot{\sigma} = \Lambda\sigma,$$

where Λ is the real canonical form of the projection onto the stable subspace of the monodromy matrix of the first variational equation along the periodic orbit:

$$\dot{x} = DX(\gamma(t))x.$$

The proof can be derived analogously using that $\sigma(t) = \sigma(0)e^{\Lambda t}$ and $|\sigma_0 e^{\Lambda t}| < |\sigma_0|e^{-\lambda t}$, where $-\lambda < 0$ is the maximal Lyapunov exponent of Γ_0 .

End of the Proof of Theorem 4.2.2 for A small

To finish the proof of Theorem 4.2.2 we need to show that the internal dynamics f_A in Γ_A is close to the PRC of Γ_0 under system (4.1).

Consider the parameterization K_A of the invariant curve Γ_A given in Lemma 4.2.3, we have

$$K_A(f_A(\theta)) = F_A(K_A(\theta)) = F_A(K_0(\theta)) + F_A(K_A(\theta)) - F_A(K_0(\theta)).$$

Assuming that $\sup_{x \in \bar{\mathcal{M}}} |DF_A| \leq C$ and using that $|K_A(\theta) - K_0(\theta)| = \mathcal{O}(Ae^{-\lambda T_{rel}})$ (see Lemma 4.2.3), we have

$$F_A(K_0(\theta)) = K_A(f_A(\theta)) + \mathcal{O}(Ae^{-\lambda T_{rel}}). \quad (4.31)$$

Moreover, using the formula for the PRC given in (4.13), we have

$$\begin{aligned} PRC(A, \theta) &= \Theta[F_A(K_0(\theta))] - \Theta[F_0(K_0(\theta))] \\ &= \Theta[K_A(f_A(\theta)) + \mathcal{O}(Ae^{-\lambda T_{rel}})] - \Theta[K_0(f_0(\theta))] \\ &= \Theta[K_A(f_A(\theta))] - \Theta[K_0(f_0(\theta))] \\ &+ \Theta[K_A(f_A(\theta)) + \mathcal{O}(Ae^{-\lambda T_{rel}})] - \Theta[K_A(f_A(\theta))] \\ &= f_A(\theta) - f_0(\theta) + \Theta[K_A(f_A(\theta)) + \mathcal{O}(Ae^{-\lambda T_{rel}})] - \Theta[K_A(f_A(\theta))]. \end{aligned} \quad (4.32)$$

Now using that $\sup_{x \in \bar{\mathcal{M}}} |\nabla\Theta| \leq C$ we have

$$PRC(A, \theta) = f_A(\theta) - f_0(\theta) + \mathcal{O}(Ae^{-\lambda T_{rel}}).$$

The case $A = \mathcal{O}(1)$

To prove Theorem 4.2.2 for $A = \mathcal{O}(1)$ one could use the results in [7], which state that if a map has an approximately invariant manifold which is approximately normally hyperbolic, then the map has a true invariant manifold nearby.

Due to the strong attracting properties of the invariant curve Γ_0 , it is straightforward to see that Γ_0 is approximately invariant for the map F_A , even if $A = \mathcal{O}(1)$.

Consider the intermediate map

$$F_{pert}(x) = \phi_A(T_{pert}; x), \quad (4.33)$$

we will use the hypothesis **H1** that states that F_{pert} maps the curve Γ_0 into its basin of attraction \mathcal{M} . Then, given a point $x = K_0(\theta) \in \Gamma_0$, if $x_{pert} = F_{pert}(x) = \phi_A(T_{pert}; x) \in \mathcal{M}$, (see (4.7)), by equation (4.4), there exists a point $K_0(\theta_{pert}) \in \Gamma_0$ such that, for $t \geq 0$

$$\left| F_A(K_0(\theta)) - K_0\left(\theta_{pert} + \frac{T_{rel}}{T}\right) \right| = |\phi_0(T_{rel}; x_{pert}) - \phi_0(T_{rel}, K_0(\theta_{pert}))| \leq Ce^{-\lambda T_{rel}}. \quad (4.34)$$

Using the formula for the PRC given in (4.8) we have that

$$\theta_{pert} + \frac{T_{rel}}{T} = PRC(\theta, A) + \theta + \frac{T_{pert}}{T} + \frac{T_{rel}}{T} = PRC(\theta, A) + f_0(\theta), \quad (4.35)$$

where $f_0(\theta) = \theta + T'/T$. Hence, defining

$$\bar{f}_A(\theta) := PRC(\theta, A) + f_0(\theta), \quad (4.36)$$

expression (4.34) reads as

$$|F_A(K_0(\theta)) - K_0(\bar{f}_A(\theta))| \leq Ce^{-\lambda T_{rel}}. \quad (4.37)$$

In other words, the curve Γ_0 with inner dynamics \bar{f}_A is approximately invariant with respect to F_A with an error $\mathcal{O}(e^{-\lambda T_{rel}})$ that can be made as small as we want taking T_{rel} large enough. To apply the results in [7] one needs to show that Γ_0 is approximately normally hyperbolic for F_A . That is, for each point $x \in \Gamma_0$ there exists a decomposition $\Gamma_{0,x} = \Gamma_{0,x}^c \oplus \Gamma_{0,x}^s$, with $\Gamma_{0,x}^c$ an approximation of the tangent space to Γ_0 at x and such that

- This splitting is approximately invariant under the linearized map, DF_A ,
- $DF_A(x)|_{\Gamma_{0,x}^s}$ expands and does so at a greater rate than does $DF_A(x)|_{\Gamma_{0,x}^c}$.

Again, we will work in the 2-dimensional case, but results can be generalized to arbitrary dimension (see Remark 4.2.4). Using the change of variables K introduced in (4.22) the map F_A satisfies (see equation (4.25))

$$F_A(K(\theta, \sigma)) = K\left(\theta_{pert} + \frac{T_{rel}}{T}, \sigma_{pert} e^{-\lambda T_{rel}}\right), \quad (4.38)$$

where $K(\theta_{pert}, \sigma_{pert}) = F_{pert}(K(\theta, \sigma))$ (see (4.33)). Notice that θ_{pert} and σ_{pert} are correctly defined as long as $F_{pert}(K(\theta, \sigma)) \in \mathcal{M}$, which is satisfied for points $(\theta, 0)$ on the invariant curve Γ_0 by hypothesis **H1** and therefore in a small neighbourhood of Γ_0 . Taking derivatives with respect to θ and σ in expression (4.38) we have

$$\begin{aligned} DF_A(K(\theta, \sigma))D_\theta K(\theta, \sigma) &= D_\theta K\left(\theta_{pert} + \frac{T_{rel}}{T}, \sigma_{pert}e^{-\lambda T_{rel}}\right)\frac{d\theta_{pert}}{d\theta} \\ &\quad + D_\sigma K\left(\theta_{pert} + \frac{T_{rel}}{T}, \sigma_{pert}e^{-\lambda T_{rel}}\right)e^{-\lambda T_{rel}}\frac{d\sigma_{pert}}{d\theta}, \\ DF_A(K(\theta, \sigma))D_\sigma K(\theta, \sigma) &= D_\theta K\left(\theta_{pert} + \frac{T_{rel}}{T}, \sigma_{pert}e^{-\lambda T_{rel}}\right)\frac{d\theta_{pert}}{d\sigma} \\ &\quad + D_\sigma K\left(\theta_{pert} + \frac{T_{rel}}{T}, \sigma_{pert}e^{-\lambda T_{rel}}\right)e^{-\lambda T_{rel}}\frac{d\sigma_{pert}}{d\sigma}. \end{aligned} \quad (4.39)$$

and evaluating on points $(\theta, 0)$, we have

$$\begin{aligned} DF_A(K_0(\theta))DK_0(\theta) &= D_\theta K(\bar{f}_A(\theta), \sigma_{pert}(\theta, 0)e^{-\lambda T_{rel}})\frac{d\theta_{pert}}{d\theta}(\theta, 0) \\ &\quad + D_\sigma K(\bar{f}_A(\theta), \sigma_{pert}(\theta, 0)e^{-\lambda T_{rel}})e^{-\lambda T_{rel}}\frac{d\sigma_{pert}}{d\theta}(\theta, 0), \\ DF_A(K_0(\theta))K_1(\theta) &= D_\theta K(\bar{f}_A(\theta), \sigma_{pert}(\theta, 0)e^{-\lambda T_{rel}})\frac{d\theta_{pert}}{d\sigma}(\theta, 0) \\ &\quad + D_\sigma K(\bar{f}_A(\theta), \sigma_{pert}(\theta, 0)e^{-\lambda T_{rel}})e^{-\lambda T_{rel}}\frac{d\sigma_{pert}}{d\sigma}(\theta, 0), \end{aligned} \quad (4.40)$$

where \bar{f}_A is defined in (4.36) (see also (4.35)) and

$$K_1(\theta) := D_\sigma K(\theta, \sigma)|_{\sigma=0}. \quad (4.41)$$

Now, we Taylor expand the function $K(\theta, \sigma)$ around $\sigma = 0$, and obtain

$$\begin{aligned} DF_A(K_0(\theta))DK_0(\theta) &= [DK_0(\bar{f}_A(\theta)) + e^{-\lambda T_{rel}}\sigma_{pert}(\theta, 0)DK_1(\bar{f}_A(\theta))] \frac{d\theta_{pert}}{d\theta}(\theta, 0) \\ &\quad + K_1(\bar{f}_A(\theta))e^{-\lambda T_{rel}}\frac{d\sigma_{pert}}{d\theta}(\theta, 0) + \mathcal{O}(e^{-2\lambda T_{rel}}), \\ DF_A(K_0(\theta))K_1(\theta) &= [DK_0(\bar{f}_A(\theta)) + e^{-\lambda T_{rel}}\sigma_{pert}(\theta, 0)DK_1(\bar{f}_A(\theta))] \frac{d\theta_{pert}}{d\sigma}(\theta, 0) \\ &\quad + K_1(\bar{f}_A(\theta))e^{-\lambda T_{rel}}\frac{d\sigma_{pert}}{d\sigma} + \mathcal{O}(e^{-2\lambda T_{rel}}). \end{aligned} \quad (4.42)$$

Moreover, as the functions $\theta_{pert}(\theta, \sigma)$ and $\sigma_{pert}(\theta, \sigma)$ are smooth functions at the points $(\theta, 0)$ we can ensure that the error terms are uniform with respect to $\theta \in \mathbb{T}$. Let us now define

$$Z(\theta) = \frac{d\theta_{pert}}{d\sigma}(\theta, 0)DK_0(\theta) - \frac{d\theta_{pert}}{d\theta}(\theta, 0)K_1(\theta),$$

straightforward computations give

$$DF_A(K_0(\theta))Z(\theta) = \mathcal{O}(e^{-\lambda T_{rel}})$$

Therefore calling $\varepsilon = e^{-\lambda T_{rel}}$, we have

$$\begin{aligned} DF_A(K_0(\theta))DK_0(\theta) &= \Lambda_T(\theta)DK_0(\bar{f}_A(\theta)) + \mathcal{O}(\varepsilon), \\ DF_A(K_0(\theta))Z(\theta) &= \mathcal{O}(\varepsilon), \end{aligned} \quad (4.43)$$

with

$$\Lambda_T(\theta) = \frac{d\theta_{pert}}{d\theta}(\theta, 0), \quad (4.44)$$

and as long as

$$\frac{d\theta_{pert}}{d\theta}(\theta, 0) \neq 0, \quad \theta \in \mathbb{T}, \quad (4.45)$$

which is guaranteed by hypothesis **H2**, one could produce an iteration procedure to construct an approximated splitting which makes Γ_0 to be approximately Normally Hyperbolic (see Definition 4.2.1) and apply the results in [7], which give that F_A will have an invariant curve Γ_A near Γ_0 .

A more direct argument consists in considering the map F_A in the variables (θ, σ) in (4.22), denoted by \tilde{F}_A in (4.25) and apply the results in [62] (see also [63]) to this map. Thanks to hypothesis **H1**, one can consider a neighbourhood of Γ_0 where the change of variables $(x, y) = K(\theta, \sigma)$ is defined and therefore the map \tilde{F}_A is a smooth diffeomorphism

$$\tilde{F}_A : \mathcal{D}_\rho := \mathbb{T} \times \mathcal{I}_\rho \rightarrow \mathbb{T} \times \mathbb{R},$$

where $\mathcal{I}_\rho = \{\sigma \in \mathbb{R}, |\sigma| \leq \rho\}$, with $\rho > 0$ small, and has the form

$$\tilde{F}_A(\theta, \sigma) = \begin{pmatrix} f_0(\theta) + \hat{f}(\theta, \sigma) \\ g(\theta, \sigma) \end{pmatrix},$$

where

$$f_0(\theta) = \theta_{pert}(\theta, 0) + \frac{T_{rel}}{T}, \quad \hat{f}(\theta, \sigma) = \theta_{pert}(\theta, \sigma) - \theta_{pert}(\theta, 0), \quad g(\theta, \sigma) = \sigma_{pert}(\theta, \sigma)e^{-\lambda T_{rel}}.$$

Hypothesis **H2** ensures that f_0 is a smooth diffeomorphism (and therefore invertible) and, taking T_{rel} large enough, the map \tilde{F}_A strongly contracts in the σ direction. Moreover, for $(\theta, \sigma) \in \mathcal{D}_\rho$, we have

$$\left| \frac{\partial \hat{f}}{\partial \theta} \right| \leq L_{11}, \quad \left| \frac{\partial \hat{f}}{\partial \sigma} \right| \leq L_{12}, \quad \left| \frac{\partial g}{\partial \theta} \right| \leq L_{21}, \quad \left| \frac{\partial g}{\partial \sigma} \right| \leq L_{22},$$

where $L_{11}, L_{12} = O(\rho)$, $L_{21}, L_{22} = O(e^{-\lambda T_{rel}})$ can be made small by taking ρ small and T_{rel} large. One can then apply Theorem 3 in [62], which gives, for T_{rel} large enough (hypothesis **H3**), the existence of the invariant curve in the form (4.28), where the function S_A must satisfy

$$\tilde{F}_A^2(\theta, S_A(\theta)) = S_A(\tilde{F}_A^1(\theta, S_A(\theta))),$$

and $S_A = O(e^{-\lambda T_{rel}})$. Again \tilde{F}_A^1 and \tilde{F}_A^2 correspond to the θ and σ component of \tilde{F}_A , respectively.

Returning to the original variables $x = K(\theta, \sigma)$ defined in (4.22) and using that $\Gamma_A \subset \mathcal{M}$, we obtain the parameterization K_A of Γ_A as in (4.29). Moreover, an analogous reasoning to (4.30), once we have bounded the size of S_A , gives

$$|K_A(\theta) - K_0(\theta)| \leq Ce^{-T_{rel}}. \quad (4.46)$$

End of the Proof of Theorem 4.2.2 for $A = \mathcal{O}(1)$

To finish the proof of Theorem 4.2.2 we need to show that the internal dynamics f_A in Γ_A is close to the PRC of Γ_0 for system (4.1).

This can be done analogously to the case A small using (4.46) instead of (4.21) arriving to

$$PRC(A, \theta) = f_A(\theta) - f_0(\theta) + \mathcal{O}(e^{-\lambda T_{rel}}). \quad (4.47)$$

This concludes the proof, using that for $A = \mathcal{O}(1)$, $\mathcal{O}(e^{-\lambda T_{rel}}) = \mathcal{O}(Ae^{-\lambda T_{rel}})$.

4.3 Computation of the PRC by means of the parameterization method. Computational results

4.3.1 Computation of the invariant curve

Theorem 4.2.2 establishes that the PRC can be obtained from the dynamics on the invariant curve Γ_A of the stroboscopic map F_A . This allows us to take advantage of the existing algorithms based on the parameterization method [13, 42] to compute the parameterization of the invariant curve K_A as well as its internal dynamics f_A . The algorithms, which we describe in what follows, are based on a Newton-like method to solve the invariance equation (4.20) for the unknowns K_A and f_A . Indeed, given an approximation of the parameterization K_A of the invariant curve Γ_A and its internal dynamics f_A , the method provides improved solutions that solve the invariance equation up to an error which is quadratic with respect to the initial one at each step. Moreover, the method requires to compute alongside the invariant normal bundle of the invariant curve and its linearised dynamics.

Given a map $F : \mathbb{R}^2 \rightarrow \mathbb{R}^2$ having an invariant curve Γ_A , we look for a parameterization of the invariant curve $K : \mathbb{T} \rightarrow \mathbb{R}^2$ by solving the following invariance equation

$$F(K(\theta)) = K(f(\theta)), \quad (4.48)$$

where both, the parametrization of the curve $K(\theta)$ and the dynamics inside the curve $f(\theta)$ are unknown. Differentiating (4.48) we find the invariance equation for the tangent bundle $DK(\theta)$:

$$DF(K(\theta))DK(\theta) = DK(f(\theta))Df(\theta) = DK(f(\theta))\Lambda_T(\theta), \quad (4.49)$$

where we have defined $\Lambda_T(\theta) := Df(\theta)$. Besides this, by imposing the invariance of the normal (stable) bundle of $K(\theta)$, denoted by $N(\theta)$, we have the following invariance equation

$$DF(K(\theta))N(\theta) = N(f(\theta))\Lambda_N(\theta), \quad (4.50)$$

where $\Lambda_N(\theta)$ denotes the linearised dynamics over $N(\theta)$.

We introduce the matrices

$$P(\theta) = \begin{pmatrix} DK(\theta) & N(\theta) \end{pmatrix}, \quad (4.51)$$

and

$$\Lambda(\theta) = \text{diag}(\Lambda_T(\theta), \Lambda_N(\theta)), \quad (4.52)$$

in order to express in a more compact way the invariance equations (4.49) and (4.50):

$$DF(K(\theta))P(\theta) = P(f(\theta))\Lambda(\theta). \quad (4.53)$$

Therefore, if we express the linear map $DF(K(\theta))$ in the basis provided by $P(\theta)$, it becomes the diagonal matrix $\Lambda(\theta)$. One can use this adapted invariant frame to design an efficient Newton method to solve (4.48). As it is usual in the Newton method, we assume an approximation for the unknowns $K(\theta)$, $f(\theta)$, $N(\theta)$ and $\Lambda_N(\theta)$ is known and we compute improved approximations:

$$\bar{K}(\theta) = K(\theta) + \Delta K(\theta), \quad (4.54)$$

$$\bar{f}(\theta) = f(\theta) + \Delta f(\theta), \quad (4.55)$$

$$\bar{N}(\theta) = N(\theta) + \Delta N(\theta), \quad (4.56)$$

$$\bar{\Lambda}_N(\theta) = \Lambda_N(\theta) + \Delta \Lambda_N(\theta). \quad (4.57)$$

To determine the correction terms $\Delta K(\theta)$, $\Delta f(\theta)$, $\Delta N(\theta)$, $\Delta \Lambda_N(\theta)$, the Newton method is split in two substeps. In the first one, we look for corrections $\Delta K(\theta)$ and $\Delta f(\theta)$. We begin by substituting expressions (4.54) and (4.55) into the invariance equation (4.48), and then expanding in Taylor series around K and f , obtaining

$$\begin{aligned} 0 &= F(\bar{K}(\theta)) - \bar{K}(\bar{f}(\theta)) \\ &= F(K(\theta) + \Delta K(\theta)) - K(f(\theta) + \Delta f(\theta)) - \Delta K(f(\theta) + \Delta f(\theta)) \\ &= F(K(\theta)) + DF(K(\theta))\Delta K(\theta) - K(f(\theta)) - DK(f(\theta))\Delta f(\theta) - \Delta K(f(\theta)) + \mathcal{O}_2 \\ &= E(\theta) + DF(K(\theta))\Delta K(\theta) - DK(f(\theta))\Delta f(\theta) - \Delta K(f(\theta)) + \mathcal{O}_2, \end{aligned}$$

where $E(\theta) = F(K(\theta)) - K(f(\theta))$ is the error for the approximated solution. Neglecting quadratically small terms \mathcal{O}_2 and writing the resulting equations in the adapted frame provided by $P(\theta)$, that is, writing $\Delta K(\theta) = P(\theta)\xi(\theta)$, we get the cohomological equation

$$\eta(\theta) = \Lambda(\theta)\xi(\theta) - \xi(f(\theta)) - \begin{pmatrix} \Delta f(\theta) \\ 0 \end{pmatrix}, \quad (4.58)$$

where $\eta(\theta) = -(P(f(\theta)))^{-1}E(\theta)$ is the error of the approximate solution in the adapted frame. If we express $\eta(\theta)$ in (4.58) in tangent and normal components, we have

$$\eta^T(\theta) = \Lambda_T(\theta)\xi^T(\theta) - \xi^T(f(\theta)) - \Delta f(\theta), \quad (4.59)$$

$$\eta^N(\theta) = \Lambda_N(\theta)\xi^N(\theta) - \xi^N(f(\theta)), \quad (4.60)$$

whose solutions $\Delta f(\theta)$, ξ^T and ξ^N will be computed separately. The normal cohomological equation will be solved by means of a fixed point method. As $K(\theta)$ is normally attracting hyperbolic, $\Lambda_N(\theta)$ must satisfy $\|\Lambda_N(\theta)\| < 1$. Therefore, iterating the fixed point equation

$$\xi^N(\theta) = \Lambda_N(f^{-1}(\theta))\xi^N(f^{-1}(\theta)) - \eta^N(f^{-1}(\theta)),$$

with $\xi^N = 0$ as initial seed, it will converge to its solution $\xi^N(\theta)$.

By contrast, the tangent cohomological equation has two unknowns, $\xi^T(\theta)$ and $\Delta f(\theta)$. Observe that the tangent homological equation (4.59) has not an unique solution. This reflects the fact that, even if the invariant curve is unique, this is not the case for the parameterization $K(\theta)$, which has several possibilities. To solve this undetermined system we choose the simplest solution:

$$\xi^T(\theta) = 0, \quad \Delta f(\theta) = -\eta^T(\theta).$$

After all these computations one finds that $\bar{K}(\theta)$ and $\bar{f}(\theta)$ are defined as

$$\begin{aligned} \bar{K}(\theta) &= K(\theta) + N(\theta)\xi^N(\theta), \\ \bar{f}(\theta) &= f(\theta) - \eta^T(\theta). \end{aligned}$$

The first substep of the method ends by computing an expression of $\bar{f}^{-1}(\theta)$. Defining

$$e(\theta) = f^{-1}(\bar{f}(\theta)) - \theta,$$

and writing $\bar{f}^{-1}(\theta)$ as $f^{-1}(\theta) + \Delta f^{-1}(\theta)$, we use that $\bar{f}^{-1}(\bar{f}(\theta)) - \theta = 0$, to obtain the following expression for $\bar{f}^{-1}(\theta)$:

$$\bar{f}^{-1}(\theta) = f^{-1}(\theta) - e(f^{-1}(\theta)).$$

In the second substep, we use $\bar{K}(\theta)$, $\bar{f}(\theta)$ and $\bar{f}^{-1}(\theta)$ for the computation of $\bar{N}(\theta)$ and $\bar{\Lambda}_N(\theta)$. To avoid stodgy notation, from now on we redefine $K := \bar{K}$, $f := \bar{f}$, $DK := D\bar{K}$ and $\Lambda_T := \bar{\Lambda}_T = D\bar{f}(\theta)$. We define the error $E_N(\theta)$ from the invariance equation (4.50) as

$$E_N(\theta) = DF(K(\theta))N(\theta) - N(f(\theta))\Lambda_N(\theta),$$

and look for $\bar{N}(\theta)$ and $\bar{\Lambda}_N(\theta)$ of the following form:

$$\begin{aligned} \bar{N}(\theta) &= N(\theta) + \Delta N(\theta), \\ \bar{\Lambda}_N(\theta) &= \Lambda_N(\theta) + \Delta\Lambda_N(\theta). \end{aligned}$$

Working analogously as in the previous substep we have

$$\begin{aligned} 0 &= DF(K(\theta))\bar{N}(\theta) - \bar{N}(f(\theta))\bar{\Lambda}_N(\theta), \\ &= DF(K(\theta))(N(\theta) + \Delta N(\theta)) - (N(f(\theta)) + \Delta N(f(\theta)))(\Lambda_N(\theta) + \Delta\Lambda_N(\theta)), \\ &= E_N(\theta) + DF(K(\theta))\Delta N(\theta) - N(f(\theta))\Delta\Lambda_N(\theta) - \Delta N(f(\theta))\Lambda_N(\theta) + \mathcal{O}_2, \end{aligned}$$

and neglecting quadratically small terms and working again in the frame provided by $P(\theta) = (DK(\theta), N(\theta))$, that is, $\Delta N(\theta) = P(\theta)Q(\theta)$, the following cohomological expression is obtained

$$-\tilde{E}_N(\theta) = \Lambda(\theta)Q(\theta) - Q(f(\theta))\Lambda_N(\theta) - \begin{pmatrix} 0 \\ \Delta\Lambda_N(\theta) \end{pmatrix},$$

where

$$\tilde{E}_N(\theta) = \begin{pmatrix} \tilde{E}_N^T(\theta) \\ \tilde{E}_N^N(\theta) \end{pmatrix} := P^{-1}(f(\theta))E_N(\theta).$$

This cohomological equation can be split in components. Analogously to the first substep procedure, that is choosing the simplest expression possible, one can find that, choosing $Q(\theta)$ of the form

$$Q(\theta) = \begin{pmatrix} Q^T(\theta) \\ 0 \end{pmatrix},$$

we obtain that $Q^T(\theta)$ can be found by solving the fixed point equation

$$Q^T(\theta) = (\Lambda_T(\theta))^{-1}(Q^T(f(\theta))\Lambda_N(\theta) - \tilde{E}_N^T(\theta)),$$

and

$$\Delta\Lambda_N(\theta) = \tilde{E}_N^N(\theta).$$

Thus $\bar{N}(\theta)$ and $\bar{\Lambda}_N(\theta)$ are obtained as follows:

$$\begin{aligned} \bar{N}(\theta) &= N(\theta) + DK(\theta)Q^T(\theta), \\ \bar{\Lambda}_N(\theta) &= \Lambda_N(\theta) + \tilde{E}_N^N(\theta). \end{aligned}$$

Continuation of Invariant Curves

In order to obtain accurate seeds for the Newton's method, one can use expansions of the solutions with respect to the parameters. In [14] a continuation scheme for the parameterization $K_A(\theta)$ of the curve Γ_A and its internal dynamics $f_A(\theta)$ is proposed. The aim will be to solve the equation:

$$F_A(K_A(\theta)) - K_A(f_A(\theta)) = 0. \quad (4.61)$$

Assume that for a given A^* we have computed $K_{A^*}(\theta)$ and $f_{A^*}(\theta)$, and we want to compute the corresponding solutions for $A^* + h$. We can take as seeds for the Newton's method the first order approximations of $K_{A^*+h}(\theta)$ and $f_{A^*+h}(\theta)$, that is

$$\begin{aligned} K_{A^*+h}(\theta) &\simeq K_{A^*}(\theta) + h \frac{\partial K_A(\theta)}{\partial A} \Big|_{A=A^*}, \\ f_{A^*+h}(\theta) &\simeq f_{A^*}(\theta) + h \frac{\partial f_A(\theta)}{\partial A} \Big|_{A=A^*}, \end{aligned}$$

where the computation of $\frac{\partial K_A}{\partial A}(\theta)$ and $\frac{\partial f_A}{\partial A}(\theta)$ is discussed below.

Differentiating equation (4.61) with respect to A we have,

$$DF_A(K_A(\theta))\frac{\partial K_A}{\partial A}(\theta) - \frac{\partial K_A(f_A(\theta))}{\partial A} - DK_A(f_A(\theta))\frac{\partial f_A}{\partial A}(\theta) = -\frac{\partial F_A}{\partial A}(K_A(\theta)). \quad (4.62)$$

Then, we write $\frac{\partial K_A}{\partial A}(\theta)$ in the $P_A(\theta)$ basis (see Eq. (4.51)), that is, $\frac{\partial K_A}{\partial A}(\theta) = P_A(\theta)\eta_A$, and take

$$\eta_A(\theta) = \begin{pmatrix} 0 \\ \eta_A^N(\theta) \end{pmatrix},$$

so that we just correct the torus in the normal direction. Let

$$E_A(\theta) = \frac{\partial F_A(K_A(\theta))}{\partial A}, \quad \tilde{E}_A(\theta) = (P_A(f_A(\theta)))^{-1}E_A(\theta).$$

Then, multiplying both sides of (4.62) by $P_A(f(\theta))$ and performing the standard computations of the Newton's method, we obtain the following identities for $\eta_A^N(\theta)$ and $\frac{\partial f_A}{\partial A}(\theta)$:

$$\eta_A^N(\theta) = \Lambda_{NA}(f_A^{-1}(\theta))\eta_A^N(f_A^{-1}(\theta)) + \tilde{E}_A^N(f_A^{-1}(\theta)), \quad (4.63)$$

$$\frac{\partial f_A(\theta)}{\partial A} = \tilde{E}_A^T(\theta). \quad (4.64)$$

Again, as Γ_A is normally hyperbolic, the fixed point equation for $\eta_A^N(\theta)$ given in (4.63) has a unique solution. Finally, after computing the corrections, we can take the following initial seeds for $K_{A^*+h}(\theta)$ and $f_{A^*+h}(\theta)$:

$$\begin{aligned} K_{A^*+h}(\theta) &= K_{A^*}(\theta) + N_{A^*}(\theta)\eta_{A^*}^N(\theta)h, \\ f_{A^*+h}(\theta) &= f_{A^*}(\theta) + \tilde{E}_{A^*}^T(\theta)h, \end{aligned}$$

and then proceed with the Newton-like method described above.

We have reviewed the principal steps of the method. Next, we provide some details on the computation of the initial seeds for the Newton's method. That is, to find an invariant curve for the stroboscopic map (2.4) near the limit cycle of (2.1) for $A = 0$. For a small value of A , we use as initial seed the invariant curve of the unperturbed system. More precisely, having an unperturbed system which displays a limit cycle $\bar{\gamma}(t)$ of period T , we can define $\theta = \frac{t}{T}$ as an angular variable which parameterizes the limit cycle. Therefore, we take $K_0(\theta) = \bar{\gamma}(\theta T)$ and $f_0(\theta) = \theta + \frac{T'}{T}$ as an initial seed for the parameterization K and the dynamics f on it, for A is small.

In order to find an initial seed for the normal bundle and its dynamics, we need to compute the derivative of the limit cycle with respect to its normal bundle direction. To that aim we use the

methods in [39], which provide an analytical solution for the value of that derivative. Although these methods will be profusely reviewed in Chapter 3, we introduce them briefly here in order to explain how to find the initial seeds. The stable manifold \mathcal{M} , in our case, the domain of attraction of the unperturbed limit cycle Γ , can be parameterized by using an angular variable θ corresponding to the phase on the limit cycle and a variable σ called amplitude which moves along the transverse direction to the limit cycle. Dynamics of both variables θ and σ are given by:

$$\begin{aligned}\dot{\theta} &= 1/T \\ \dot{\sigma} &= \lambda\sigma/T,\end{aligned}\tag{4.65}$$

where T and λ are the period and the characteristic exponent of the limit cycle Γ , respectively. The parameterization $K(\theta, \sigma)$ of \mathcal{M} , satisfies

$$\left(\frac{1}{T}\partial_\theta + \frac{\lambda\sigma}{T}\partial_\sigma\right)K(\theta, \sigma) = X(K(\theta, \sigma)),\tag{4.66}$$

where X is the vector field. Expanding $K(\theta, \sigma)$ in σ one gets

$$K(\theta, \sigma) = K_0(\theta) + \sigma K_1(\theta) + \mathcal{O}(\sigma^2),\tag{4.67}$$

where it is clear that the invariant curve $\Gamma_0 = \{K_0(\theta) \mid \theta \in \mathbb{T}\}$. Using equations (4.65) it is easy to see that the stroboscopic map (2.4) with $A = 0$ satisfies:

$$F_0(K(\theta, \sigma)) = K\left(\theta + \frac{T'}{T}, \sigma e^{\frac{\lambda T'}{T}}\right),\tag{4.68}$$

and therefore, differentiating (4.68) with respect to σ we obtain

$$\left.\frac{\partial}{\partial\sigma}\left(F_0(K(\theta, \sigma))\right)\right|_{\sigma=0} = DF_0(K_0(\theta))K_1(\theta) = e^{\frac{\lambda T'}{T}}K_1(\theta).\tag{4.69}$$

Comparing expressions (4.69) and (4.50) it is clear that over the unperturbed limit cycle, $N(\theta) = K_1(\theta)$ and $\Lambda_N(\theta) = e^{\frac{\lambda T'}{T}}$.

In order to obtain $K_1(\theta)$, it is only necessary to compute the fundamental matrix $\Phi(t)$ ($\Phi(0) = Id$) of the variational equations of system (2.1) along the periodic orbit $\bar{\gamma}(t)$. Indeed, if we denote by v the eigenvector of the monodromy matrix $\Phi(T)$ associated to the eigenvalue e^λ , $K_1(\theta)$ is given by $K_1(\theta) = e^{-\lambda\theta}\Phi(T\theta)v$ and $\Lambda_N(\theta) = e^\lambda$.

4.3.2 Computation of PRCs beyond the existence of the invariant curve

The results of Theorem 4.2.2 rely on the computation of an invariant curve for the stroboscopic map F_A of an 'artificially' constructed periodic perturbation (4.11). In some cases, as we will see

in the numerical examples presented in Section 4.4, the invariant curve Γ_A does not exist. This can happen if $F_{pert}(\Gamma_0)$ leaves the basin of attraction \mathcal{M} of the limit cycle Γ_0 (breaking hypothesis **H1**) or if $\theta_{pert}(\theta, 0)$ has a critical point θ^* and therefore $d\theta_{pert}/d\theta(\theta^*, \sigma) = 0$ (breaking hypothesis **H2**). However, in the case that hypothesis **H2** fails it is still possible to design an algorithm based on the parameterization method [15] to compute the PRC with enough accuracy by means of solving an approximate invariance equation which provide fast algorithms. This is also advantageous as for values near the breakdown of the curve, techniques in [42] have a very high computational cost.

Using (4.38) with $\sigma = 0$ we have

$$F_A(K_0(\theta)) = K \left(\theta_{pert}(\theta, 0) + \frac{T_{rel}}{T}, \sigma_{pert}(\theta, 0)e^{-\lambda T_{rel}} \right) = K(\bar{f}_A(\theta), \bar{C}_A(\theta)),$$

where $\bar{f}_A(\theta)$ is given in (4.36) and

$$\bar{C}_A(\theta) := \sigma_{pert}(\theta, 0)e^{-\lambda T_{rel}}. \quad (4.70)$$

Taylor expanding $K(\theta, \sigma)$ with respect to sigma we obtain

$$F_A(K_0(\theta)) = K_0(\bar{f}_A(\theta)) + \mathcal{O}(e^{-\lambda T_{rel}}). \quad (4.71)$$

Of course, expression (4.71) only has sense if $F_{pert}(\Gamma_0) \in \mathcal{M}$ (hypothesis **H1**), but we do not impose that Γ_0 is approximately normally hyperbolic. Nevertheless, we will use the ideas in the algorithms reviewed in previous Section 4.3.1 and we will design a quasi-Newton method to compute a function g_A that satisfies

$$F_A(K_0(\theta)) - K_0(g_A(\theta)) = E(\theta), \quad (4.72)$$

where the error E will not be smaller than the terms $\mathcal{O}(e^{-\lambda T_{rel}})$ that we have dropped.

Assume that g_A satisfies the equation (4.72), then we look for an improved solution $\hat{g}_A(\theta) = g_A(\theta) + \Delta g_A(\theta)$ such that \hat{g}_A solves the approximate invariance equation up to an error which is quadratic in E . Thus, if we linearise about g_A we have

$$\begin{aligned} F_A(K_0(\theta)) - K_0(\hat{g}_A(\theta)) &= F_A(K_0(\theta)) - K_0(g_A(\theta)) - DK_0(g_A(\theta))\Delta g_A(\theta) + \mathcal{O}(|\Delta g_A|^2) \\ &= E(\theta) - DK_0(g_A(\theta))\Delta g_A(\theta) + \mathcal{O}(|\Delta g_A|^2). \end{aligned} \quad (4.73)$$

Therefore, we look for Δg_A satisfying the equation

$$E(\theta) = DK_0(g_A(\theta))\Delta g_A(\theta),$$

which provides

$$\Delta g_A(\theta) = \frac{\langle DK_0(g_A(\theta)), E(\theta) \rangle}{\langle DK_0(g_A(\theta)), DK_0(g_A(\theta)) \rangle}, \quad (4.74)$$

where $\langle \cdot, \cdot \rangle$ denotes the dot product.

The algorithm to compute the PRC is then:

Algorithm 4.3.1. Computation of the PRC. Given $K_0(\theta)$ a parameterization of the limit cycle, and $g_A(\theta)$ an approximate solution of equation (4.72) perform the following operations:

1. Compute $E(\theta) = F_A(K_0(\theta)) - K_0(g_A(\theta))$.
2. Compute $DK_0(g_A(\theta))$.
3. Compute $\Delta g_A = \frac{\langle DK_0(g_A(\theta)), E(\theta) \rangle}{\langle DK_0(g_A(\theta)), DK_0(g_A(\theta)) \rangle}$.
4. Set $g_A(\theta) \leftarrow g_A(\theta) + \Delta g_A(\theta)$.
5. Repeat steps 1-4 until the error E is smaller than the established tolerance. Then $PRC(\theta) = g_A(\theta) - (\theta + T'/T)$.

In Section 4.4, we apply Algorithm 4.3.1 to several numerical examples illustrating the convergence of the method and the good agreement of the results with the standard approach.

4.3.3 Computation of the PRC and ARC

In the previous Section 4.3.2 we have used that K_0 satisfies equation (4.71). Notice that we could be more precise and include the exact expression for the terms of $\mathcal{O}(e^{-\lambda T_{rel}})$. That is,

$$F_A(K_0(\theta)) = K_0(\bar{f}_A(\theta)) + K_1(\bar{f}_A(\theta))\bar{C}_A(\theta) + \mathcal{O}(e^{-2\lambda T_{rel}}),$$

with $K_1(\theta)$ as in (4.41).

We already know that the function $\bar{f}_A(\theta)$ provides the PRC through the relation (4.36). We would like to emphasize here that the function $\bar{C}_A(\theta)$ defined in (4.70) provides the Amplitude Response Curve [17, 85] (ARC) defined in (3.27) and use it to obtain an analogous curve to the PRC for the amplitude value σ , where $ARC(\theta) = \sigma_{pert}(\theta, 0)$, that is the value of σ at x_{pert} (see (4.7)). Therefore, since $\sigma_{pert}(\theta, 0) = \bar{C}_A(\theta)e^{\lambda T_{rel}}$, the function $\bar{C}_A(\theta)$ provides the ARC through $ARC(\theta) = \bar{C}_A(\theta)e^{-\lambda T_{rel}}$.

As in the previous Section, it is possible to design a quasi-Newton method to compute the functions g_A and C_A that satisfy

$$F_A(K_0(\theta)) - K_0(g_A(\theta)) - C_A(\theta)K_1(g_A(\theta)) = E(\theta), \quad (4.75)$$

where the error E will not be smaller than the terms of order $\mathcal{O}(e^{-2\lambda T_{rel}})$ that we have dropped.

Proceeding as in the previous Section, we assume that g_A and C_A satisfy equation (4.75) and we look for an improved solution $\hat{g}_A(\theta) = g_A(\theta) + \Delta g_A(\theta)$ and $\hat{C}_A(\theta) = C_A(\theta) + \Delta C_A(\theta)$ such that \hat{g}_A and \hat{C}_A solve the approximate invariance equation up to an error which is quadratic in E . Thus, if we linearise about g_A and C_A we have

$$\begin{aligned} F_A(K_0(\theta)) - K_0(\hat{g}_A(\theta)) - K_1(\hat{g}_A(\theta))\hat{C}_A \\ &= F_A(K_0(\theta)) - K_0(g_A(\theta)) - DK_0(g_A(\theta))\Delta g_A(\theta) - K_1(g_A(\theta))C_A(\theta) \\ &\quad - DK_1(g_A(\theta))\Delta g_A(\theta)C_A(\theta) - K_1(g_A(\theta))\Delta C_A(\theta) + \mathcal{O}(\Delta^2, e^{-2\lambda T_{rel}}) \\ &= E(\theta) - DK_0(g_A(\theta))\Delta g_A(\theta) - DK_1(g_A(\theta))\Delta g_A(\theta)C_A(\theta) \\ &\quad - K_1(g_A(\theta))\Delta C_A(\theta) + \mathcal{O}(\Delta^2). \end{aligned} \quad (4.76)$$

Thus, we are left with the following equation for Δg_A and ΔC_A ,

$$E(\theta) = [DK_0(g_A(\theta)) + DK_1(g_A(\theta))C_A(\theta)]\Delta g_A(\theta) + K_1(g_A(\theta))\Delta C_A(\theta). \quad (4.77)$$

Therefore, the unknown Δg_A corresponds to the projection of the error E onto the direction $R := DK_0 \circ g_A + C_A \cdot DK_1 \circ g_A$ and $\Delta C_A(\theta)$ corresponds to the projection onto the K_1 direction. Of course, DK_0 and K_1 are transversal since K_1 is tangent to the isochrons of the unperturbed limit cycle which are always transversal to the limit cycle. Since $C_A = \mathcal{O}(e^{-\lambda T_{rel}})$, assuming that T_{rel} is large enough we can always guarantee that R and K_1 are transversal. Therefore, multiplying (4.77) by $K_1^\perp(g_A(\theta))$ we have

$$\Delta g_A(\theta) = \frac{\langle K_1^\perp(g_A(\theta)), E(\theta) \rangle}{\langle K_1^\perp(g_A(\theta)), R(\theta) \rangle}, \quad (4.78)$$

whereas by multiplying by $R(\theta)^\perp$ we obtain

$$\Delta C_A(\theta) = \frac{\langle R^\perp(\theta), E(\theta) \rangle}{\langle R^\perp(\theta), K_1(g_A(\theta)) \rangle}, \quad (4.79)$$

where $\langle \cdot, \cdot \rangle$ denotes the dot product.

Remark 4.3.2. Notice that $C_A(\theta) = \mathcal{O}(e^{-\lambda T_{rel}})$, and if we disregard the terms of order $\mathcal{O}(e^{-\lambda T_{rel}})$ in expression (4.78) we obtain

$$\Delta g_A(\theta) = \frac{\langle K_1^\perp(g_A(\theta)), E(\theta) \rangle}{\langle K_1^\perp(g_A(\theta)), DK_0(g_A(\theta)) \rangle}, \quad (4.80)$$

which is equivalent to the expression obtained in (4.74). Indeed, in this case E and DK_0 have the same direction, and expression (4.74) can be replaced by

$$\Delta g_A(\theta) = \frac{\langle v, E(\theta) \rangle}{\langle v, DK_0(g_A(\theta)) \rangle},$$

where v can be any vector as long as v is not perpendicular to $DK_0(g_A(\theta))$.

Thus, the algorithm to compute the PRC and the ARC is:

Algorithm 4.3.3. Computation of the PRC and the ARC. Given $K_0(\theta)$ a parameterization of the limit cycle, $K_1(\theta)$ the tangent vector to the isochrons of the limit cycle, and $g_A(\theta)$, $C_A(\theta)$ an approximate solution of equation (4.75), perform the following operations:

1. Compute $E(\theta) = F_A(K_0(\theta)) - K_0(g_A(\theta)) - C_A(\theta)K_1(g_A(\theta))$.
2. Compute $R(\theta) = DK_0(g_A(\theta)) + DK_1(g_A(\theta))C_A(\theta)$.
3. Compute $\Delta g_A(\theta) = \frac{\langle K_1^\perp(g_A(\theta)), E(\theta) \rangle}{\langle K_1^\perp(g_A(\theta)), R(\theta) \rangle}$.
4. Compute $\Delta C_A(\theta) = \frac{\langle R^\perp(\theta), E(\theta) \rangle}{\langle R^\perp(\theta), K_1(g_A(\theta)) \rangle}$.
5. Set $g_A(\theta) \leftarrow g_A(\theta) + \Delta g_A(\theta)$.
6. Set $C_A(\theta) \leftarrow C_A(\theta) + \Delta C_A(\theta)$.
7. Repeat steps 1-6 until the error E is smaller than the established tolerance. Then,

$$PRC(\theta) = g_A(\theta) - (\theta + T'/T)$$

and

$$ARC(\theta) = C_A(\theta)e^{\lambda T_{rel}}.$$

4.4 Numerical Examples

In this Section we apply the algorithms based on the parameterization method introduced in Section 4.3 to compute the PRC to some relevant models in neuroscience, namely the Wilson-Cowan model [87] and the Morris-Lecar model [61].

We will use the same perturbation for both models of the form

$$p(t) = \sin^6\left(\frac{\pi t}{T_{pert}}\right),$$

for $0 \leq t \leq T_{pert}$ and $T_{pert} = 10$. The value of T_{rel} is different for each model and its value will be indicated later together with other parameters of the model.

In order to validate the results we will compare the results obtained using the parameterization method with the *standard method* using formula (4.10). We remark the good agreement between both methods.

The Wilson-Cowan model. As we discussed in Chapter 1, the Wilson-Cowan model describes the behaviour of a coupled network of excitatory and inhibitory neurons. The perturbed model has the form (see [87]):

$$\begin{aligned}\dot{E} &= -E + S_e(c_1 E - c_2 I + P + Ap(t)), \\ \dot{I} &= -I + S_i(c_3 E - c_4 I + Q),\end{aligned}\tag{4.81}$$

where the variables E and I are the firing rate activity of the excitatory and inhibitory populations, respectively, and

$$S_k(x) = \frac{1}{1 + e^{-a_k(x - \theta_k)}}, \quad \text{for } k = E, I\tag{4.82}$$

is the input-output function. As we did in Chapter 1, we choose the parameters for the model (4.81) from the set \mathcal{P} in (1.17)

$$\mathcal{P} = \{c_1 = 13, c_2 = 12, a_e = 1.3, \theta_e = 4, c_3 = 6, c_4 = 3, a_i = 2, \theta_i = 1.5\}.\tag{4.83}$$

as we know that for that parameters' choice, the system (4.81) displays a limit cycle for $A = 0$.

Similarly as we did in Chapters 2 and 3, we consider two sets of parameters (P, Q) for which the system displays a limit cycle. For the first set of parameters the limit cycle is born from a Hopf bifurcation and for the second one from a saddle-node on invariant circle (SNIC) bifurcation. As the choice of P, Q is slightly different from the choice we did for Γ_{HB} and Γ_{SN} in Chapter 1, in this Section we refer to them as WC-Hopf and WC-SNIC, respectively. Table 4.1, lists P, Q values, together with the period T , the characteristic exponent λ of each periodic orbit, and the relaxation time T_{rel} of the perturbation.

In Figs. 4.3 and 4.4 we show the comparison between the standard method and the parameterization method for parameters (P, Q) close to a Hopf bifurcation and a SNIC bifurcation, respectively. We remark the good agreement between both methods.

Parameter	Hopf	SNIC
P	2.5	1.45
Q	0	-0.75
T	5.26	13.62
T_{rel}	15T	6T
$-\lambda$	-0.157	-0.66

Table 4.1: (P, Q) parameter values for the Wilson-Cowan model close to the corresponding type of bifurcation. For the indicated parameter values and $A = 0$, the system (4.81) has a stable limit cycle of period T and characteristic exponent $-\lambda$.

Other elements of the computation of the PRCs obtained using the parameterization method, namely the invariant curve Γ_A , the internal dynamics f_A and the derivative of f_A are shown in Fig. 4.5 for the WC-Hopf and in Fig. 4.6 for the WC-SNIC. Notice that as A increases, the shape of the PRCs shows a sudden increase for certain phase values (see panel A in Figs. 4.5 and 4.6). A more detailed discussion about this phenomenon will be given in Section 4.4.1.

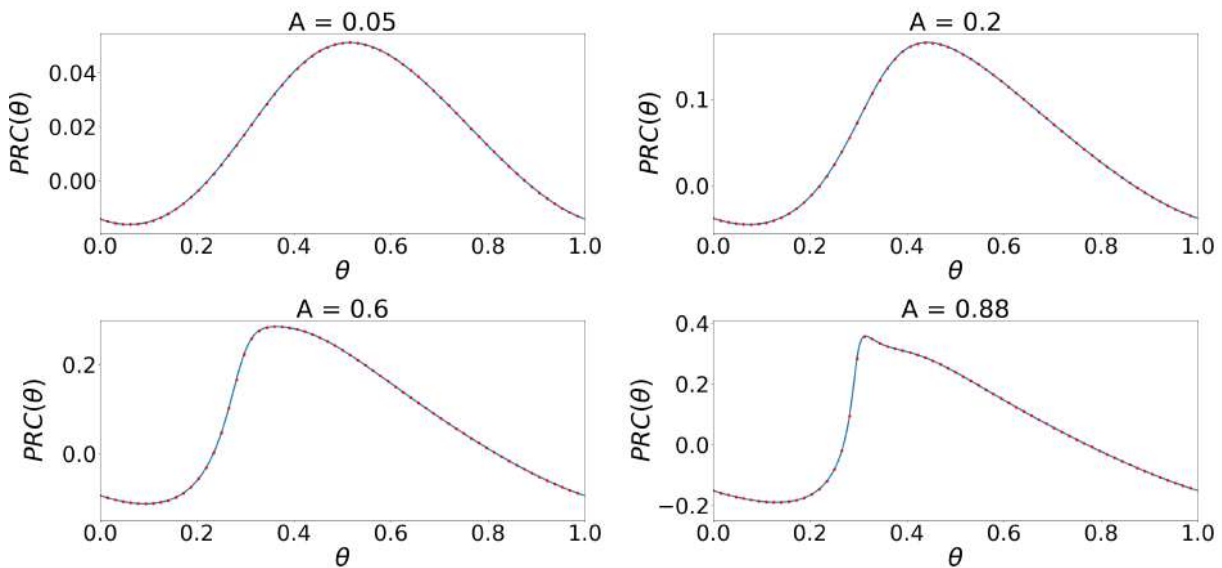


Figure 4.3: PRCs for the Wilson-Cowan model near a Hopf bifurcation (WC-Hopf) for different values of the amplitude A (as indicated in each panel) showing the comparison between the parameterization method (solid blue line) and the *standard method* (red dots).

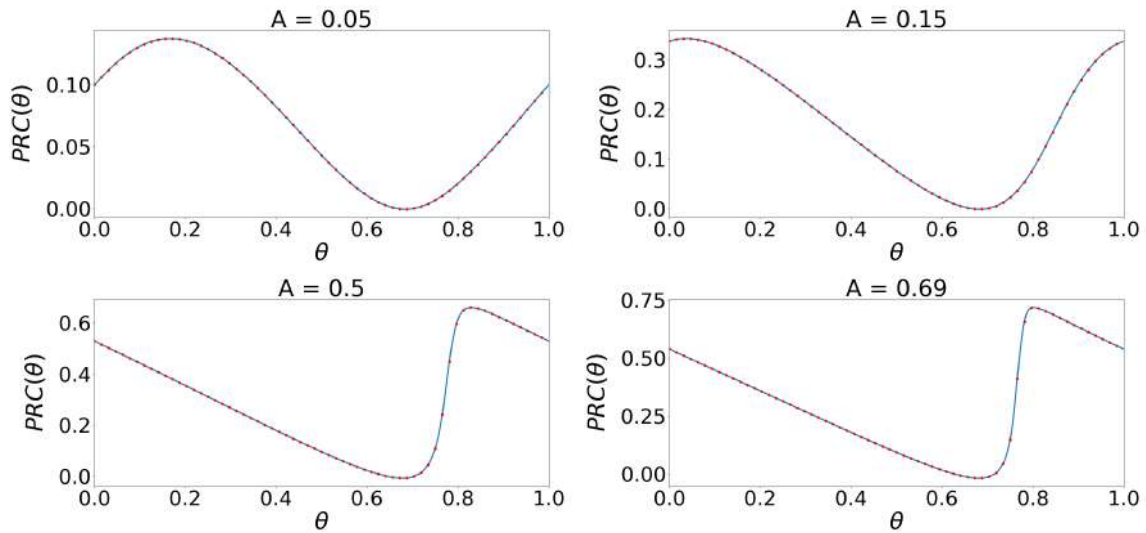


Figure 4.4: PRCs for the Wilson-Cowan near a SNIC bifurcation (WC-SNIC) for different values of the amplitude A (as indicated in each panel) showing the comparison between the parameterization method (solid blue line) and the *standard method* (red dots).

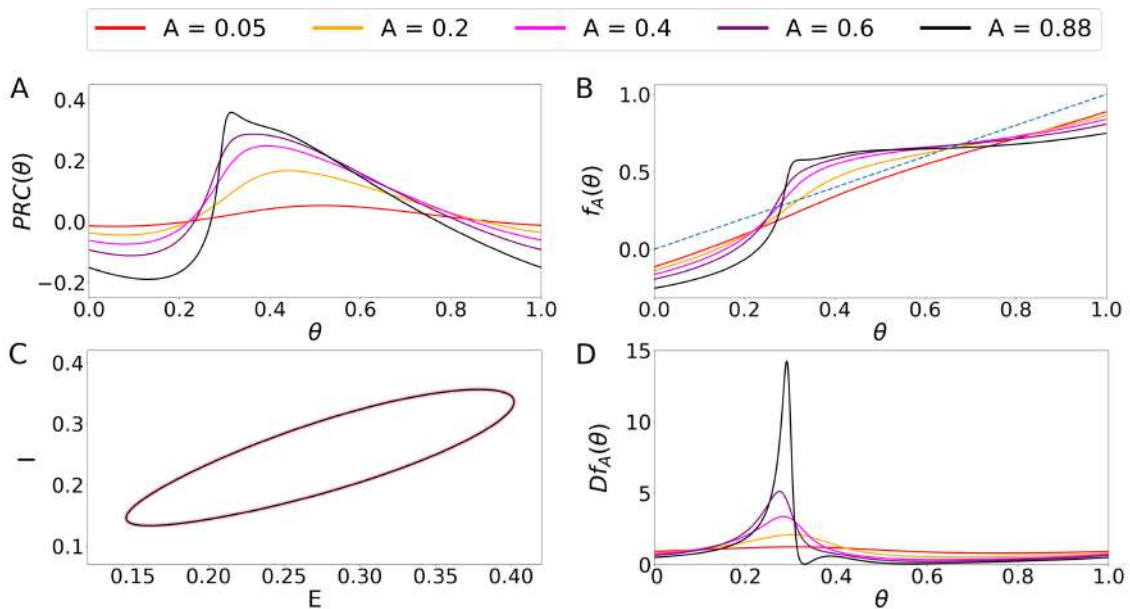


Figure 4.5: For the Wilson-Cowan model near a Hopf bifurcation (WC-Hopf) and different amplitude values A we show: (A) the PRCs, (B) the dynamics $f_A(\theta)$ on the invariant curve Γ_A , (C) the invariant curve Γ_A , (D) the derivative of $f_A(\theta)$. The blue dashed line in panel B corresponds to the identity function.

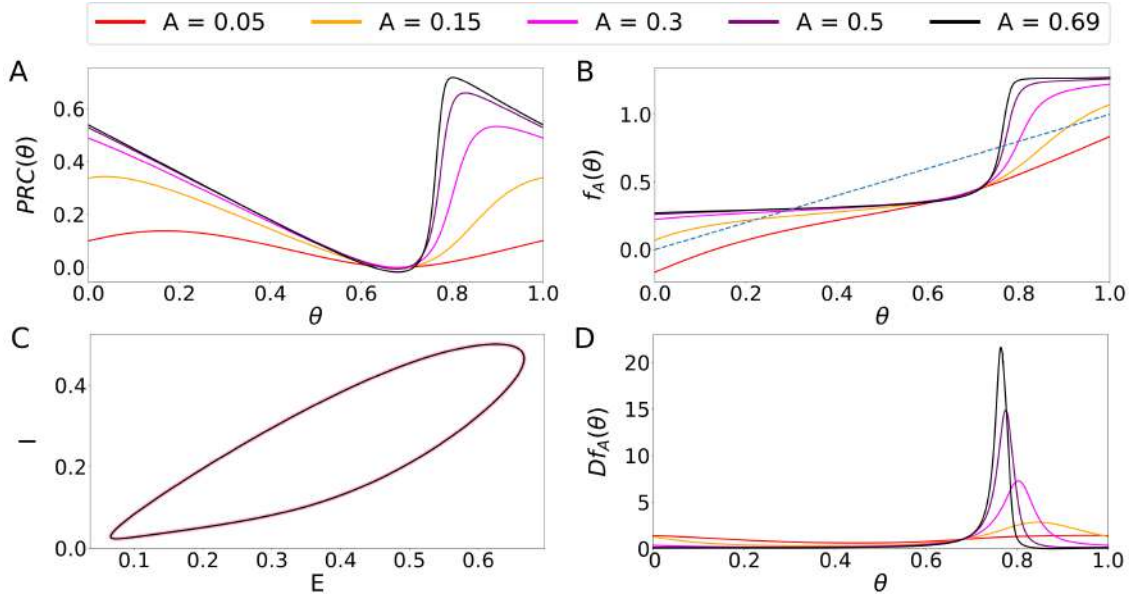


Figure 4.6: For the Wilson-Cowan model near a SNIC bifurcation (WC-SNIC) and different amplitude values we show: (A) the PRCs, (B) the dynamics $f_A(\theta)$ on the invariant curve Γ_A , (C) the invariant curve Γ_A , (D) the derivative of $f_A(\theta)$. The blue dashed line in panel B corresponds to the identity function.

The Morris-Lecar model. It was originally developed as a model to study the changes in excitability properties for the muscle fiber of the giant barnacle, and it has been established as a paradigm for the study of different neuronal excitability types [70]. The perturbed model has the form (see [61]):

$$\begin{aligned} C\dot{V} &= I_{app} - g_L(V - V_L) - g_K w(V - V_K) - g_{Ca} m_\infty(V)(V - V_{Ca}) + Ap(t), \\ \dot{w} &= \phi \frac{w_\infty(V) - w}{\tau_w(V)}, \end{aligned} \quad (4.84)$$

where

$$\begin{aligned} m_\infty(V) &= \frac{1}{2}(1 + \tanh((V - V_1)/V_2)), \\ w_\infty(V) &= \frac{1}{2}(1 + \tanh((V - V_3)/V_4)), \\ \tau_w(V) &= (\cosh((V - V_3)/(2V_4)))^{-1}. \end{aligned} \quad (4.85)$$

Parameter	Hopf	SNIC
ϕ	0.04	0.067
g_{Ca}	4.4	4
V_3	2	12
V_4	30	17.4
I_{app}	91	45
T	99.27	99.192
T_{rel}	6T	5T
$-\lambda$	-0.0919	-0.1198

Table 4.2: Parameter values for the Morris-Lecar model close to the corresponding type of bifurcation. For the indicated parameter values and $A = 0$, the system (4.84) has a stable periodic orbit of period T and characteristic exponent $-\lambda$.

As in the previous example, we consider two sets of parameters for which the system displays a limit cycle across a Hopf and a SNIC bifurcation [24, 71]. We will refer to them as MC-Hopf and MC-SNIC, respectively. Some parameters of the model will be common for both cases, namely

$$\mathcal{P}_{ML} = \{C = 20, V_L = -60, V_K = -84, V_{Ca} = 120, \\ V_1 = -1.2, V_2 = 18, g_L = 2, g_K = 8\}. \quad (4.86)$$

The other parameter values are listed in Table 4.2.

We compute the PRC for the limit cycle of the Morris-Lecar model and for different values of the amplitude A . In Figs. 4.7 and 4.8 we show the comparison between the standard method and the parameterization method for parameters close to a Hopf bifurcation and a SNIC bifurcation, respectively. Again, we remark the good agreement between both methods. Other elements of the computation of the PRCs using the parameterization method are shown in Figures 4.9 and 4.10. Again, both cases show a sharp rise in the PRC for certain phase values as the amplitude increases. We refer the reader to Section 4.4.1 for a more detailed discussion.

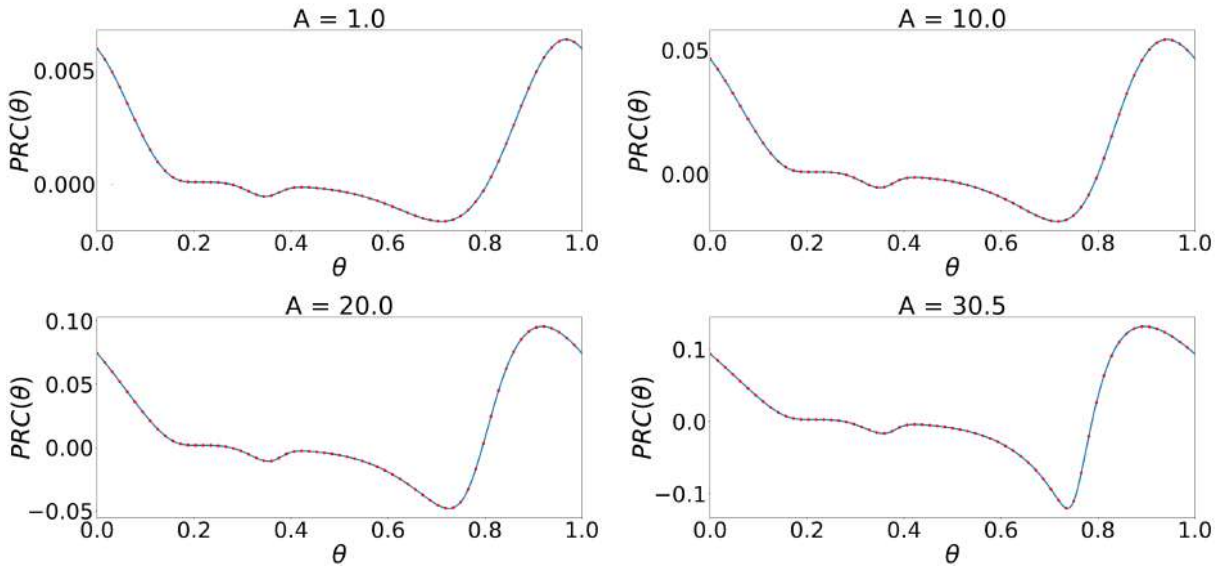


Figure 4.7: PRCs for the Morris-Lecar model near a Hopf bifurcation (ML-Hopf) for different values of the amplitude (indicated in each panel) showing the comparison between the parameterization method (solid blue line) and the *standard method* (red dots).

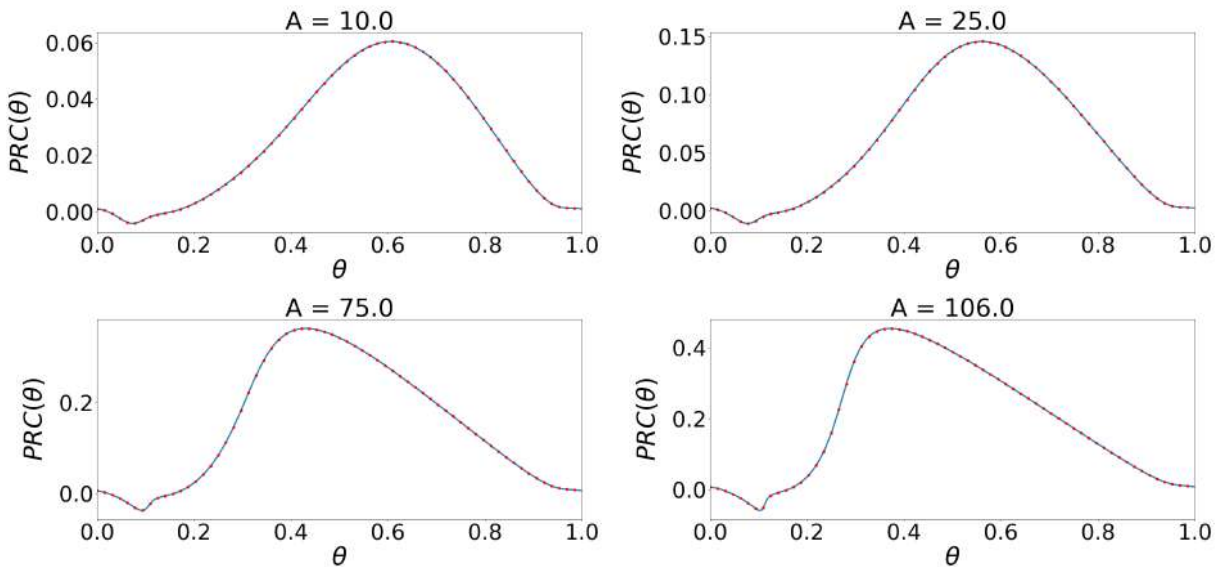


Figure 4.8: PRCs for the Morris-Lecar model near a SNIC bifurcation (ML-SNIC) for different values of the amplitude (indicated in each panel) showing the comparison between the parameterization method (solid blue line) and the *standard method* (red dots).

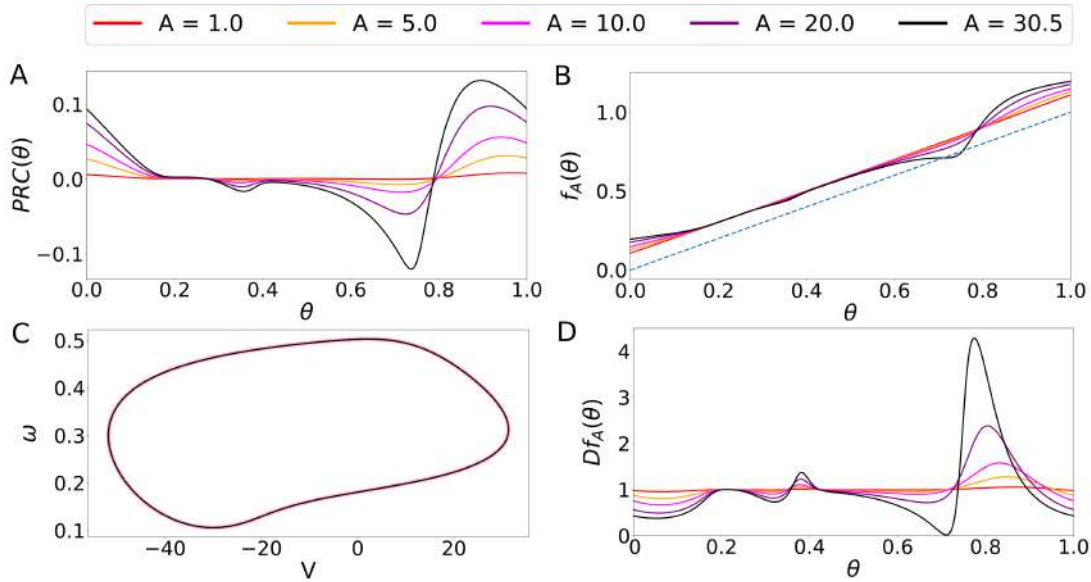


Figure 4.9: For the Morris-Lecar near a Hopf bifurcation (ML-Hopf) and different amplitudes we show: (A) the PRCs, (B) the dynamics $f_A(\theta)$ on the invariant curve Γ_A , (C) the invariant curve Γ_A , (D) the derivative of $f_A(\theta)$. The blue dashed line in panel B corresponds to the identity function.

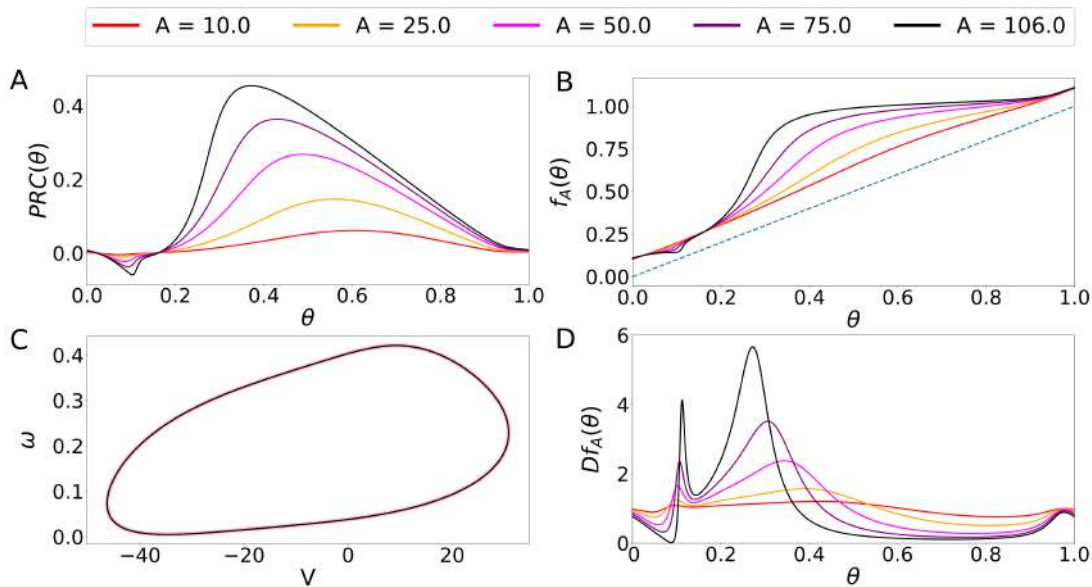


Figure 4.10: For the Morris-Lecar near a SNIC bifurcation (ML-SNIC) and different amplitudes we show: (A) the PRCs, (B) the dynamics $f_A(\theta)$ on the invariant curve Γ_A , (C) the invariant curve Γ_A , (D) the derivative of $f_A(\theta)$. The blue dashed line in panel B corresponds to the identity function.

4.4.1 Large Amplitude Perturbations

The application of the parameterization method (see Section 4.3.1) strongly relies on the existence of an invariant curve Γ_A for the stroboscopic map of an 'artificially' constructed periodic perturbation (see Theorem 4.2.2). In the numerical examples shown in Figs. 4.5, 4.6, 4.9 and 4.10 the computation of the invariant curve fails when the amplitude becomes large and approaches a certain value A^* (which is different for each example), and so does the computation of the PRC using this method. In this Section we will discuss how changes in the waveform of the PRC might be related to normally hyperbolic properties of the invariant curve. We will first focus our discussion on the WC-Hopf model.

First, notice that as the amplitude A increases, the PRC becomes steeper (see Fig 4.5A). By looking at the internal dynamics f_A on the invariant curve Γ_A (see Fig. 4.5B), we observe that, as the amplitude increases, the curve f_A shows a sharp rise followed by a flat region. Moreover, there appear a stable and an unstable fixed point on the invariant curve Γ_A (intersection of f_A with the identity line on Fig. 4.5B). Thus, the curve Γ_A preserves its normal hyperbolicity as long as the contraction/expansion rates on the invariant curve are weaker than the contraction rates on the normal directions (see equation (4.45)). Since the contraction rate is $\mathcal{O}(e^{-\lambda T_{rel}})$, see (4.44), this means that $Df_A(\theta) = d\theta_{pert}/d\theta$ must remain bounded away from 0. However, we observe that as A increases the value of Df_A approaches 0 for a certain θ (see Fig. 4.5D), thus causing the loss of the normal hyperbolicity property and the breakdown of the curve. For values of A slightly smaller than the one for which $Df_A(\theta)$ vanishes, the numerical method in Section 4.3.1 fails to converge. However, we can apply the modified parameterization method provided by the algorithms in Appendix 4.3 and compute the function g_A (see equation (4.72)) and the PRC beyond the existence of an invariant curve (see Figs. 4.11 B, C, D right).

Notice that the method also works if the invariant curve exists (see Fig. 4.11A right). In this case g_A is $\mathcal{O}(e^{-\lambda T_{rel}})$ -close to f_A (see equations (4.36), (4.47), (4.71), (4.75)). Therefore, for practical purposes, the modified method is faster and accurate enough to compute the PRC.

It is possible to describe the phenomenon of the breakdown of the curve in a geometric way using the concept of isochrons (curves of constant phase) and phaseless sets of the original limit cycle. For the model considered, the isochrons for the unperturbed limit cycle are shown in Fig. 4.11 left. Notice that the unperturbed system has an unstable focus P for which the isochrons are not defined (the phaseless set). Now, we consider the image of the curve Γ_0 under the map F_{pert} introduced in (4.33) for different values of A . Of course, the intersection of the curve $\Gamma_{pert} = F_{pert}(\Gamma_0)$ with the isochrons provides the new phases. For small values of A , Γ_{pert} will intersect all the isochrons transversally leading to every possible new phase in a one-to-one correspondence (see Fig. 4.11A). Accordingly, the functions $f_A(\theta)$ and $g_A(\theta)$ are diffeomorphisms.

However, as A increases, there exists a value A^* for which the curve Γ_{pert} becomes tangent to some isochrons and therefore the curve Γ_{pert} intersects some isochrons more than once (see Fig. 4.11B). Thus, the map g_A is no longer one-to-one, which means that Dg_A vanishes for certain phases, causing the loss of normal hyperbolicity and the breakdown of the curve.

Clearly, the function g_A for $A = 0.95$ shows a local maximum and minimum (see Fig. 4.11B), thus corresponding to an isochron tangency. When A is increased further the function g_A splits in two. Indeed, the curve Γ_{pert} will first intersect the phaseless point P for a certain value $A \approx 1.0355$ (see Fig. 4.11 C) and after that it will no longer enclose the point P , thus it will not cross all the isochrons of the limit cycle (see Figure 4.11D). The map g_A will then be discontinuous at the point where the curve Γ_{pert} intersects the phaseless set. After that, the function g_A will be continuous again when we take modulus 1, but, of course, the images will not span the whole interval $[0, 1)$. Regarding to the winding number classification for PRCs, defined as the number of times the curve Γ_{pert} traverses a complete cycle as defined by the isochrons of the unperturbed limit cycle [32, 33], for $A \approx 1.0355$ there is a transition from a type 1 PRC to a type 0 PRC.

The modified parameterization method introduced in Section 4.3.2 also allows for the computation of the Amplitude Response Curve (ARC) (see Algorithm 4.3.3). The ARCs for the amplitude values considered in Fig. 4.11 are shown in Fig. 4.12. The ARC provides information about how "far" in time the perturbation displaces the trajectory away from the limit cycle. That is, the larger the value of the ARC, the longer it will take for the displaced trajectory to relax back to the limit cycle (and therefore one should consider a larger T_{rel}).

Notice that when the curve Γ_{pert} intersects the phaseless set (point P), which occurs for a critical amplitude $A_c \approx 1.035$, there exists a perturbed trajectory which never returns to the limit cycle, and the ARC would show an essential discontinuity. Thus, the ARC, for smaller values of the amplitude $A < A_c$ shows a peak at this phase whose size increases as the amplitude A is increased towards A_c (see Figs 4.12A,B,C). However, for amplitude values larger than A_c (Fig 4.12D), the ARC magnitude decreases again with A , because Γ_{pert} moves away from the neighbourhood of the phaseless point P .

A similar phenomenon as discussed for the WC-Hopf occurs for the WC-SNIC and ML-SNIC examples. The Morris-Lecar model near a Hopf bifurcation (ML-Hopf) is slightly different, since in this case the phaseless set is larger compared to the WC-Hopf case: it is a positive measure set bounded by an unstable limit cycle Γ_u which determines the basin of attraction of the equilibrium point which is in its interior (see Fig.4.13A). As in the WC-Hopf case, the invariant curve Γ_A for the ML-Hopf disappears due to an isochron tangency of Γ_{pert} . Consistently with this tangency Γ_{pert} for $A = 33$ crosses some isochrons more than once (see Fig.4.13A and zoom in B) and as Figs.4.13 C, D show, the function g_A changes its monotonicity. Nevertheless one can still compute the PRC by means of Algorithm 4.3.1. By contrast, for larger amplitude values several points of Γ_{pert} leave the basin of attraction of the stable limit cycle (see Fig.4.13A and zoom in B for

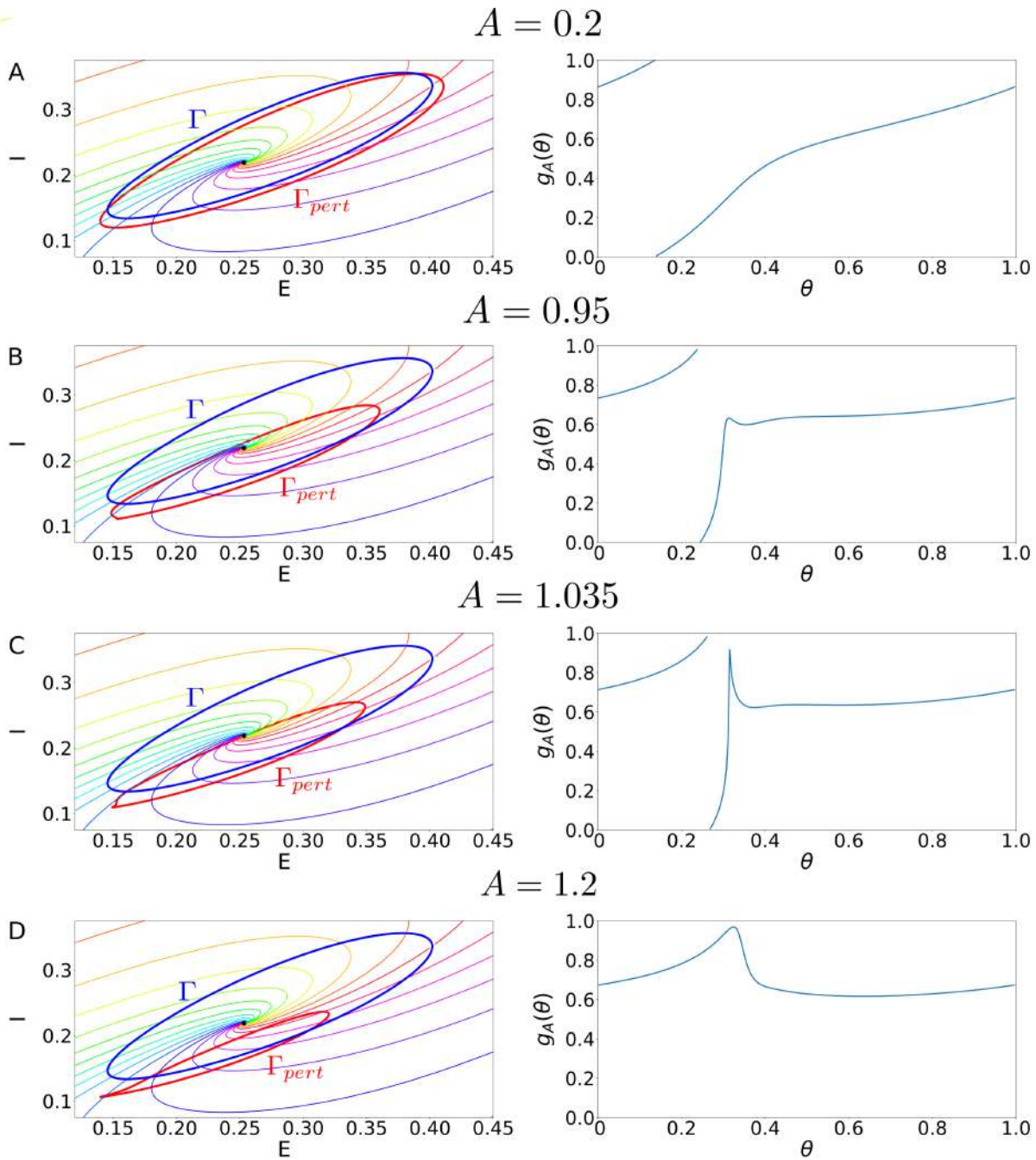


Figure 4.11: For different values of the amplitude (indicated in each panel) we show the isochrons of the unperturbed limit cycle for the Wilson-Cowan model near a Hopf bifurcation (WC-Hopf), together with the curves Γ_{pert} (left) and the functions g_A obtained with the modified parameterization method. The amplitudes selected cover the breakdown of the curve Γ_A and a transition from type 1 to type 0 PRCs (see text).

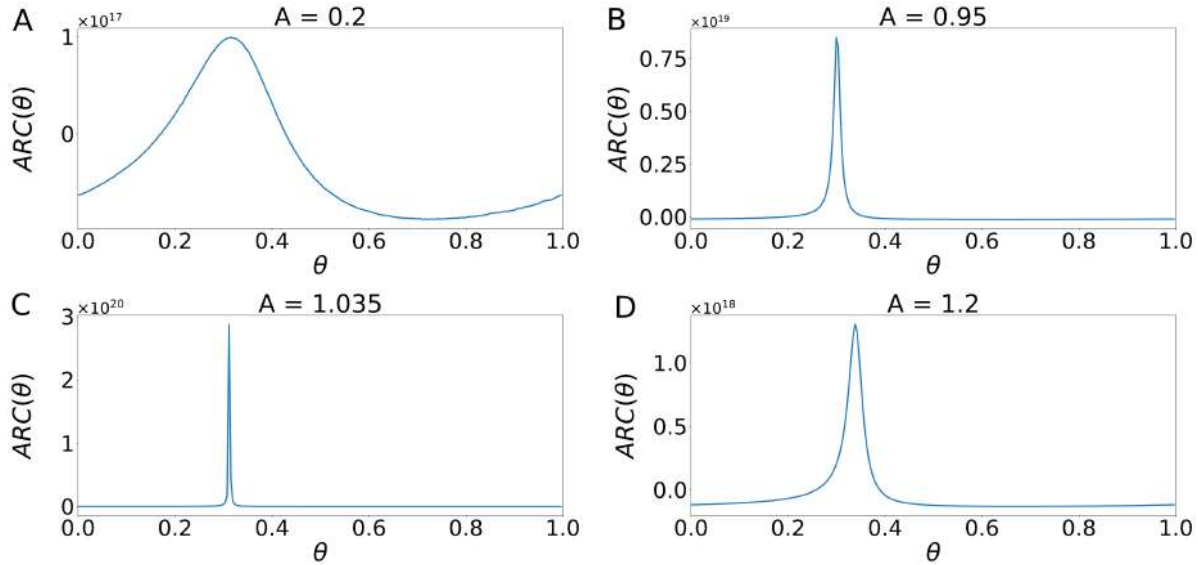


Figure 4.12: ARCs for the Wilson-Cowan model near a Hopf bifurcation (WC-Hopf) and different values of the amplitude (same as in Fig. 4.11).

$A = 40$). Thus, the PRC can be no longer computed even with the modified method.

4.5 Discussion

In this Chapter we have introduced a new approach to PRCs based on the parameterization method. The main idea of the method is to introduce a periodic perturbation consisting of the actual perturbation followed by a relaxation time T_{rel} that repeats periodically. This periodic perturbation allows us to define the corresponding stroboscopic map F_A of the periodically perturbed system. The main result of this paper is Theorem 4.2.2, where we prove the existence of an invariant curve Γ_A for the map F_A and we link its internal dynamics f_A with the PRC. The proof relies on the parameterization method, which defines an invariance equation for the invariant curve and its internal dynamics [13, 14, 44, 45], and provides a numerical algorithm to compute both.

Moreover, Theorem 4.2.2 establishes conditions for the existence of the curve Γ_A . More precisely, although the range of amplitude values A for which the invariant curve exists can be increased by considering a sufficiently large T_{rel} , there is a limitation established by the geometry of the isochrons. Indeed, whenever the curve Γ_{pert} (the displacement of the limit cycle due to the active part of the perturbation) becomes tangent to some isochron of Γ_0 , the invariant curve Γ_A loses its normal hyperbolic properties and breaks down. Moreover, we can explain how the isochrons

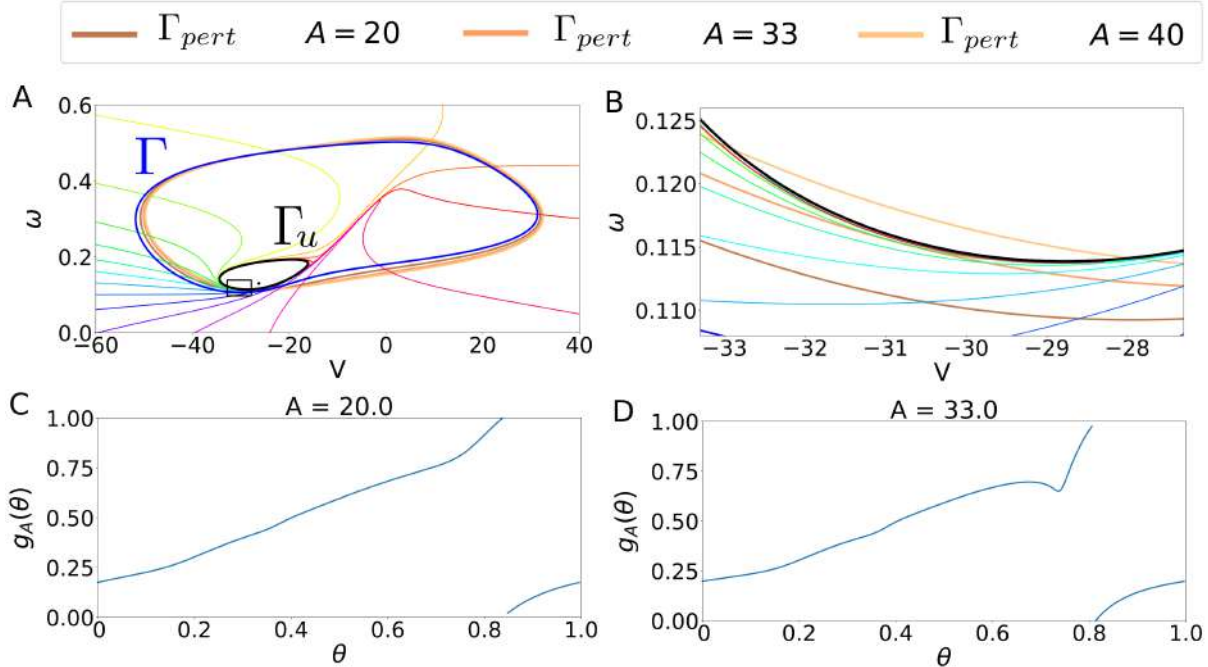


Figure 4.13: ML-Hopf phase space showing the stable limit cycle Γ , its isochrons, and the unstable limit cycle Γ_u determining the basin of attraction of a stable focus P . For different values of the amplitude we show the curves Γ_{pert} (A) and a zoom close to the isochron tangency (B). Panels C and D show the functions g_A obtained with the modified parameterization method for $A = 20$ (C) and $A = 33$ (D). For $A = 40$ some points on Γ_{pert} intersect the basin of attraction of the stable focus P , and the function g_A can not be computed.

of the unperturbed system and the perturbation interact to shape the waveform of the PRC as the amplitude of the perturbation is increased.

Besides theoretical results, we present some strategies to compute the PRC. In [42] one can find algorithms that implement a quasi-Newton method to solve the above mentioned invariance equation. The method though relies on the existence of an invariant curve. Nevertheless, as the PRC still exists beyond the breakdown of the curve Γ_A , we have developed a modified numerical method to compute PRCs inspired by the parameterization method. This method solves a modified invariance equation, which avoids the computation of the invariant curve (thus making the computations faster), and is able to compute PRCs beyond the breakdown of the curve Γ_A and the transition from type 1 to type 0 PRCs. In addition, this algorithm computes not only PRCs but also ARC, which provide information about the effects of the perturbation onto the amplitude variables (or alternatively, the displacement away from the limit cycle). We show examples of the computed ARCs and the relationship between its shape and the transitions experienced by the

PRC.

In order to assess the validity of the method, we have applied it to two models in neuroscience: a neural population model (Wilson-Cowan) and a single neuron model (Morris-Lecar). Moreover, we have studied both of them for values of the parameters near two different bifurcations: Hopf and Saddle Node on Invariant Circle (SNIC) bifurcations. Recall that PRCs are classified as type 1 or type 2 according to their shape, and this property is linked to a particular bifurcation: type 1 PRCs mainly advance phase, and they are related to a SNIC bifurcation, while type 2 PRCs can either advance or delay the phase and they are related to a Hopf bifurcation [23, 64, 76]. The numerical examples presented show the evolution of both PRC shapes for large amplitude values. In all examples PRCs preserve its type as the amplitude is increased but the phase shifts tend to increase.

In this work, we have mainly developed the theory and numerical examples for two-dimensional systems. However, the underlying theorems and numerical algorithms have a straightforward extension for the case $n > 2$.

Chapter 5

The uncoupled limit of identical Hopf bifurcations

In the previous Chapters 2, 3 and 4 we perturbed an oscillator with external non-autonomous perturbations. In this Chapter, we consider a more realistic model: the case of two mutually coupled oscillators. The main difference with the previous Chapters is that now both oscillators can influence each other.

The study of coupled oscillators has been widely studied in the context of neuroscience [80, 5] and it can address a wide range of brain functions including memory and attention [59, 81], among others. The reason why these models are so useful is because under the assumption of weak coupling one can perform reductions to a phase oscillator description suitable for answering several questions about synchronization of system oscillations [1, 48].

We will consider a system composed by two identical subsystems undergoing a Hopf bifurcation that have an uncoupling limit. As noted by several authors, networks of oscillators near a Hopf bifurcation allow one to explore not just the collective phase dynamics but also amplitude behaviour, [3, 34] where richer dynamics can be found. To study this problem we will use the results from a recent paper [6] presenting the normal form near a Hopf bifurcation for N identical and identically interacting smooth (C^∞) vector fields.

We use these results to understand the behaviour of a pair of Wilson-Cowan oscillators, with special interest in the possible synchronization regimes that may arise depending on the nature of the coupling. The study of this system may find applications in perceptual bistability as the synchrony of oscillatory activity is known to play a role in the encoding of perceptually ambiguous stimuli [31].

The structure of the Chapter is as follows: in Section 5.1 we review theoretical results in [6] and write the normal form of a system of two weakly coupled identical oscillators near a Hopf bifurcation. In Section 5.2 we perform a qualitative analysis of the system given by the dominant terms of the normal form. We give a dimension reduction via group-invariant coordinates in order to simplify dynamics. In Section 5.3 we identify different dynamical regimes depending on specific coefficients of the normal form and study the bifurcation diagrams. In particular we follow the appearance and stability of the periodic orbits arising at Hopf bifurcations. We also discuss some invariant tori which appear in the system through several bifurcations. In particular we find some bistability situations between periodic orbits.

In Section 5.4 we write the equations for two mutually inhibiting Wilson-Cowan oscillators near a Hopf bifurcation and we perform a change of coordinates to put the system in the normal form discussed in Section 5.1. For this example, we compare the theoretical predictions given by the normal form analysis with a bifurcation diagram computed numerically. Finally, we note that the results are of broad interest, extending beyond the study of neural oscillators and perceptual bistability to the study of any system involving two coupled oscillators.

This work has been developed in collaboration with Peter Ashwin and James Rankin at the University of Exeter during a research stay of A. Pérez Cervera during summer 2017 and it has been submitted for publication [66].

5.1 Study of two coupled identical systems undergoing Hopf Bifurcations

In this Chapter, we will consider systems of the form:

$$\begin{aligned} \frac{dx_1}{dt} &= H_\lambda(x_1) + \epsilon h_{\lambda,\epsilon}(x_1; x_2), \\ \frac{dx_2}{dt} &= H_\lambda(x_2) + \epsilon h_{\lambda,\epsilon}(x_2; x_1). \end{aligned} \quad x_i \in \mathbb{R}^2, \quad i = 1, 2 \quad \epsilon, \lambda \in \mathbb{R} \quad (5.1)$$

Observe that system (5.1) has S_2 permutation symmetry. Notice that when $\epsilon = 0$, system (5.1) consists of two identical uncoupled subsystems.

We assume that for the uncoupled system (5.1) ($\epsilon = 0$), each subsystem undergoes a Hopf bifurcation at $x = 0$ when the parameter λ crosses zero. More precisely, we assume that the system

$$\frac{dx}{dt} = H_\lambda(x), \quad x \in \mathbb{R}^2$$

has a stable focus at $x = 0$ for $\lambda < 0$ that undergoes a supercritical Hopf bifurcation for $\lambda = 0$ which gives rise to a small amplitude stable limit cycle for $\lambda > 0$. For simplicity, we assume that the eigenvalues of $DH_\lambda(0)$ are $\lambda \pm i\omega$ with $\omega \neq 0$. Moreover, without loss of generality, we assume that $(x_1, x_2) = (0, 0)$ is an equilibrium point of system (5.1) for (λ, ϵ) in some neighbourhood of $(0, 0)$.

5.1.1 Normal Form of system (5.1)

In *Ashwin & Rodrigues* [6] it is shown that systems as in (5.1) having \mathcal{S}_2 symmetry and undergoing a supercritical Hopf bifurcation for $\lambda = 0$, can be written in the following normal form

$$\begin{aligned}\dot{z}_1 &= z_1 \Phi_{\lambda, \epsilon}^1(|z_1|^2, |z_2|^2, z_1 \bar{z}_2) + z_2 \Phi_{\lambda, \epsilon}^2(|z_1|^2, |z_2|^2, \bar{z}_1 z_2), \\ \dot{z}_2 &= z_2 \Phi_{\lambda, \epsilon}^1(|z_2|^2, |z_1|^2, z_2 \bar{z}_1) + z_1 \Phi_{\lambda, \epsilon}^2(|z_2|^2, |z_1|^2, \bar{z}_2 z_1),\end{aligned}\quad (5.2)$$

where the functions $\Phi_{\lambda, \epsilon}^1$ and $\Phi_{\lambda, \epsilon}^2$ are given by

$$\begin{aligned}\Phi_{\lambda, \epsilon}^1 &= \alpha_0(\lambda, \epsilon) + \alpha_1(\lambda, \epsilon)|z_1|^2 + \alpha_2(\lambda, \epsilon)|z_2|^2 + \alpha_3(\lambda, \epsilon)\bar{z}_2 z_1 + \mathcal{O}_4(z_1, z_2, \bar{z}_1, \bar{z}_2), \\ \Phi_{\lambda, \epsilon}^2 &= \beta_0(\lambda, \epsilon) + \beta_1(\lambda, \epsilon)|z_1|^2 + \beta_2(\lambda, \epsilon)|z_2|^2 + \beta_3(\lambda, \epsilon)\bar{z}_1 z_2 + \mathcal{O}_4(z_1, z_2, \bar{z}_1, \bar{z}_2).\end{aligned}\quad (5.3)$$

Moreover, we assume that the coefficients $\alpha_i(\lambda, \epsilon)$ and $\beta_i(\lambda, \epsilon)$ for $i = 0, \dots, 3$, are complex and are written as

$$\begin{aligned}\alpha_i(\lambda, \epsilon) &= \alpha_{0i} + \lambda \alpha_{\lambda i} + \epsilon \alpha_{\epsilon i} + \mathcal{O}_2(\lambda, \epsilon), \\ \beta_i(\lambda, \epsilon) &= \beta_{0i} + \lambda \beta_{\lambda i} + \epsilon \beta_{\epsilon i} + \mathcal{O}_2(\lambda, \epsilon).\end{aligned}\quad (5.4)$$

From now on and to avoid stodgy notation we skip the (λ, ϵ) dependence of the coefficients α_i, β_i .

By substituting the expansion (5.3) in (5.2), we have

$$\begin{aligned}\dot{z}_1 &= z_1 (\alpha_0 + \alpha_1 |z_1|^2 + \alpha_2 |z_2|^2 + \alpha_3 \bar{z}_2 z_1) + z_2 (\beta_0 + \beta_1 |z_1|^2 + \beta_2 |z_2|^2 + \beta_3 \bar{z}_1 z_2) + \mathcal{O}_5(z, \bar{z}), \\ \dot{z}_2 &= z_2 (\alpha_0 + \alpha_1 |z_2|^2 + \alpha_2 |z_1|^2 + \alpha_3 \bar{z}_1 z_2) + z_1 (\beta_0 + \beta_1 |z_2|^2 + \beta_2 |z_1|^2 + \beta_3 \bar{z}_2 z_1) + \mathcal{O}_5(z, \bar{z}).\end{aligned}\quad (5.5)$$

Then, as the system (5.1) has two independent Hopf bifurcations for $\epsilon = 0$ at $\lambda = 0$, it follows that the normal form for $\epsilon = 0$ is given by

$$\begin{aligned}\frac{d}{dt} z_1 &= U_\lambda(z_1), \\ \frac{d}{dt} z_2 &= U_\lambda(z_2),\end{aligned}\quad \text{where } U_\lambda(z) = z(\lambda + i\omega + a_1 |z|^2) + \mathcal{O}_4(z) \quad (5.6)$$

and $a_1 \in \mathbb{C}$.

Therefore, from $U_\lambda(z)$ in (5.6) and using (5.4) we have $\alpha_0(\lambda, 0) = \lambda + i\omega = \alpha_{00} + \lambda\alpha_{\lambda 0}$, and $\alpha_1(\lambda, 0) = \alpha_{01} + \lambda\alpha_{\lambda 1} = a_1$, thus

$$\begin{aligned}\alpha_{00} &= i\omega, & \alpha_{01} &= a_1, \\ \alpha_{\lambda 0} &= 1, & \alpha_{\lambda 1} &= 0.\end{aligned}\tag{5.7}$$

Since for $\epsilon \neq 0$ the normal form has to be $\mathcal{O}(\epsilon)$ -close to (5.6), we also can match the following coefficients

$$\begin{aligned}\alpha_{0i} &= \alpha_{\lambda i} = 0 & \text{for } i = 2, 3, \\ \beta_{0i} &= \beta_{\lambda i} = 0 & \text{for } i = 0, 1, 2, 3.\end{aligned}\tag{5.8}$$

So, in the end, the truncated normal form up to order $\mathcal{O}_3(z)$ is

$$\begin{aligned}\frac{dz_1}{dt} &= z_1 \left(\lambda + i\omega + \alpha_{01}|z_1|^2 \right) + \epsilon \left[z_1 \left(\alpha_{\epsilon 0} + \alpha_{\epsilon 1}|z_1|^2 + \alpha_{\epsilon 2}|z_2|^2 + \alpha_{\epsilon 3}\bar{z}_2 z_1 \right) \right. \\ &\quad \left. + z_2 \left(\beta_{\epsilon 0} + \beta_{\epsilon 1}|z_1|^2 + \beta_{\epsilon 2}|z_2|^2 + \beta_{\epsilon 3}\bar{z}_1 z_2 \right) \right], \\ \frac{dz_2}{dt} &= z_2 \left(\lambda + i\omega + \alpha_{01}|z_2|^2 \right) + \epsilon \left[z_2 \left(\alpha_{\epsilon 0} + \alpha_{\epsilon 1}|z_2|^2 + \alpha_{\epsilon 2}|z_1|^2 + \alpha_{\epsilon 3}\bar{z}_1 z_2 \right) \right. \\ &\quad \left. + z_1 \left(\beta_{\epsilon 0} + \beta_{\epsilon 1}|z_2|^2 + \beta_{\epsilon 2}|z_1|^2 + \beta_{\epsilon 3}\bar{z}_2 z_1 \right) \right],\end{aligned}\tag{5.9}$$

where the constants $\alpha_{01}, \alpha_{\epsilon i}, \beta_{\epsilon i} \in \mathbb{C}$ ($i = 0, \dots, 3$) with the restriction $Re(\alpha_{01}) < 0$ because the Hopf bifurcation is supercritical.

5.1.2 Normal Form Computation

In this Section is to derive the formal procedure to compute the change of variables which from (5.1) to the normal form in (5.9). To start, as we will work with complex coordinates, we perform the following change to x_1, x_2 in (5.1)

$$y = (y_1, y_2) = (x_1^1 + ix_1^2, \quad x_2^1 + ix_2^2) \in \mathbb{C}^2.\tag{5.10}$$

Then, expressing system (5.1) in power series expansion

$$\begin{aligned}\dot{y} &= Ay + P_2(y, \bar{y}) + P_3(y, \bar{y}) + \mathcal{O}_4(y, \bar{y}), \\ \dot{\bar{y}} &= \bar{A}\bar{y} + \bar{P}_2(y, \bar{y}) + \bar{P}_3(y, \bar{y}) + \mathcal{O}_4(y, \bar{y}),\end{aligned}\tag{5.11}$$

where $A = \text{diag}(i\omega, i\omega, -i\omega, -i\omega)$ is a diagonal matrix and $P_i = (P_i^1, P_i^2)^\top$ are homogeneous polynomial of degree i . We remark that P_2 and P_3 in (5.11) have the following expressions,

$$\begin{aligned} P_2(y, \bar{y}) &= \prod_{i,j=1}^4 a_{ij} y_i y_j, \\ P_3(y, \bar{y}) &= \prod_{i,j,k=1}^4 a_{ijk} y_i y_j y_k, \end{aligned} \quad (5.12)$$

where $y_3 = \bar{y}_1$ and $y_4 = \bar{y}_2$.

The goal in the normal form theory is to find a change of variables

$$y = z + Q_2(z, \bar{z}) + Q_3(z, \bar{z}), \quad (5.13)$$

such that the vector field in the new variables is as simple as possible. That is, we impose that the vector field given by

$$\dot{z} = Az + f_2(z, \bar{z}) + f_3(z, \bar{z}) + \mathcal{O}_4(z, \bar{z}) \quad (5.14)$$

satisfies that the polynomials f_2 and f_3 have as many monomials as possible that are zero.

We introduce the following notation for the polynomials $Q_2(z, \bar{z})$ and $Q_3(z, \bar{z})$:

$$\begin{aligned} Q_2(z, \bar{z}) &= \prod_{i,j=1}^4 q_{ij} z_i z_j, \\ Q_3(z, \bar{z}) &= \prod_{i,j,k=1}^4 q_{ijk} z_i z_j z_k, \end{aligned} \quad (5.15)$$

where again $z_3 = \bar{z}_1$ and $z_4 = \bar{z}_2$.

By substituting the change of coordinates in (5.13) in equation (5.11) we have the following equation

$$\begin{aligned} \dot{y} &= A(z + Q_2(z, \bar{z}) + Q_3(z, \bar{z})) \\ &\quad + P_2(z + Q_2(z, \bar{z}) + Q_3(z, \bar{z}), \bar{z} + \bar{Q}_2(z, \bar{z}) + \bar{Q}_3(z, \bar{z})) \\ &\quad + P_3(z + Q_2(z, \bar{z}) + Q_3(z, \bar{z}), \bar{z} + \bar{Q}_2(z, \bar{z}) + \bar{Q}_3(z, \bar{z})) + \mathcal{O}_4(z, \bar{z}) \\ &= A(z + Q_2(z, \bar{z}) + Q_3(z, \bar{z})) \\ &\quad + P_2(z, \bar{z}) + D_z P_2(z, \bar{z}) Q_2(z, \bar{z}) + D_{\bar{z}} P_2(z, \bar{z}) \bar{Q}_2(z, \bar{z}) + P_3(z, \bar{z}) + \mathcal{O}_4(z, \bar{z}). \end{aligned} \quad (5.16)$$

On the other hand, differentiating (5.13) with respect to time and using (5.14) we have

$$\begin{aligned} \dot{y} &= \dot{z} + D_z Q_2(z, \bar{z}) \dot{z} + D_{\bar{z}} Q_2(z, \bar{z}) \dot{\bar{z}} + D_z Q_3(z, \bar{z}) \dot{z} + D_{\bar{z}} Q_3(z, \bar{z}) \dot{\bar{z}} + \mathcal{O}_4(z, \bar{z}) \\ &= (Az + f_2(z, \bar{z}) + f_3(z, \bar{z})) \\ &\quad + D_z Q_2(z, \bar{z})(Az + f_2(z, \bar{z})) + D_{\bar{z}} Q_2(z, \bar{z})(A\bar{z} + \bar{f}_2(z, \bar{z})) \\ &\quad + D_z Q_3(z, \bar{z})Az + D_{\bar{z}} Q_3(z, \bar{z})A\bar{z} + \mathcal{O}_4(z, \bar{z}). \end{aligned} \quad (5.17)$$

So in order to find the coefficients q_{ij} and q_{ijk} in (5.15), we equal the right hand side of equalities (5.16) and (5.17) and solve order by order. Thus the equation for order two is given by

$$AQ_2(z, \bar{z}) - D_z Q_2(z, \bar{z})Az - D_{\bar{z}} Q_2(z, \bar{z})\bar{A}\bar{z} = f_2(z, \bar{z}) - P_2(z, \bar{z}). \quad (5.18)$$

Notice that it is possible to select all the q_{ij} coefficients in $Q_2(z, \bar{z})$ such that all the coefficients f_{ij} for $f_2(z, \bar{z})$ in (5.14) are equal to zero.

Once we have found an expression for Q_2 , we proceed to obtain the equation for order three, which, using that $f_2(z, \bar{z}) = \bar{f}_2(z, \bar{z}) = 0$ is given by

$$\begin{aligned} AQ_3(z, \bar{z}) - D_z Q_3(z, \bar{z})Az - D_{\bar{z}} Q_3(z, \bar{z})\bar{A}\bar{z} &= f_3(z, \bar{z}) - P_3(z, \bar{z}) \\ &- D_z P_2(z, \bar{z})Q_2(z, \bar{z}) - D_{\bar{z}} P_2(z, \bar{z})\bar{Q}_2(z, \bar{z}). \end{aligned} \quad (5.19)$$

In this case, for some monomials, the combination $AQ_3(z, \bar{z}) - D_z Q_3(z, \bar{z})Az - D_{\bar{z}} Q_3(z, \bar{z})\bar{A}\bar{z}$ is equal to zero. Because of this, it is not possible to determine the q_{ijk} values which make zero its corresponding f_{ijk} coefficients. In particular, writing $f_3(z, \bar{z}) = (f_3^1, f_3^2)^\top$, the following monomials in f_3^i survive: $z_i|z_i|^2$, $z_i^2\bar{z}_j$, $z_j|z_i|^2$, $z_i|z_j|^2$, $z_j^2\bar{z}_i$, $z_j|z_j|^2$, $i, j = 1, 2$ and can be found using the following expression

$$f_3(z, \bar{z}) = D_z P_2(z, \bar{z})Q_2(z, \bar{z}) + D_{\bar{z}} P_2(z, \bar{z})\bar{Q}_2(z, \bar{z}) + P_3(z, \bar{z}). \quad (5.20)$$

after these changes of variables the system (5.1) has the form (5.5).

It is important to remark that some of the surviving monomials could be suppressed if the imaginary part of the eigenvalues (the frequencies) at the Hopf bifurcations were not the same. In particular one could get rid of all the monomials except $z_i|z_i|^2$ and $z_i|z_j|^2$ $i, j = 1, 2$.

5.1.3 Numerical computations

In this Section, we explain how to find numerically the coefficients of the normal form (5.5). That is, we explain how to compute the change of variables (5.13) that transforms system (5.1) in system (5.5).

We start by considering the case when $\epsilon = 0$. Notice that in this case both systems, (5.1) and (5.5), are uncoupled. This means that the Jacobian matrices are block diagonal. Moreover, as the uncoupled systems are identical those blocks will be identical as well.

Let us denote by M the Jacobian matrix of the original system (5.1) for $\lambda = \epsilon = 0$. Therefore, there exists a matrix S such that $A = S^{-1}MS$ where A is diagonal and has the following

eigenvectors

$$\begin{aligned}
v_1 &= (a, b, 0, 0) & \text{with associated eigenvalue} & i\omega, \\
\bar{v}_1 &= (\bar{a}, \bar{b}, 0, 0) & \text{with associated eigenvalue} & -i\omega, \\
v_2 &= (0, 0, a, b) & \text{with associated eigenvalue} & i\omega, \\
\bar{v}_2 &= (0, 0, \bar{a}, \bar{b}) & \text{with associated eigenvalue} & -i\omega,
\end{aligned} \tag{5.21}$$

where $a, b \in \mathbb{C}$.

Notice that, since the eigenvalues have multiplicity 2, the matrix is not only diagonal for this basis, but also for any linear combination of eigenvectors v_1 and v_2 , \bar{v}_1 and \bar{v}_2 in (5.21), that is,

$$\begin{aligned}
w_1^0 &= \alpha v_1 + \beta v_2 & \text{with associated eigenvalue} & i\omega, \\
\bar{w}_1^0 &= \bar{\alpha} \bar{v}_1 + \bar{\beta} \bar{v}_2 & \text{with associated eigenvalue} & -i\omega, \\
w_2^0 &= \gamma v_1 + \mu v_2 & \text{with associated eigenvalue} & i\omega, \\
\bar{w}_2^0 &= \bar{\gamma} \bar{v}_1 + \bar{\mu} \bar{v}_2 & \text{with associated eigenvalue} & -i\omega,
\end{aligned} \tag{5.22}$$

for any $\alpha, \beta, \gamma, \mu \in \mathbb{C}$.

For $\epsilon \neq 0$, one can see that the Jacobian matrix has the following eigenvectors and eigenvalues,

$$\begin{aligned}
v_1^\epsilon &= \alpha v_1 + \beta v_2 + \epsilon u_1 & \text{with associated eigenvalue} & i(\omega + \epsilon\omega_1), \\
\bar{v}_1^\epsilon &= \bar{\alpha} \bar{v}_1 + \bar{\beta} \bar{v}_2 + \epsilon \bar{u}_1 & \text{with associated eigenvalue} & -i(\omega + \epsilon\omega_1), \\
v_2^\epsilon &= \gamma v_1 + \mu v_2 + \epsilon u_2 & \text{with associated eigenvalue} & i(\omega + \epsilon\omega_2), \\
\bar{v}_2^\epsilon &= \bar{\gamma} \bar{v}_1 + \bar{\mu} \bar{v}_2 + \epsilon \bar{u}_2 & \text{with associated eigenvalue} & -i(\omega + \epsilon\omega_2),
\end{aligned} \tag{5.23}$$

for some unique (up to normalization) $\alpha, \beta, \gamma, \mu \in \mathbb{C}$ and $u_1, u_2 \in \mathbb{C}^4$.

Then, from all possible eigenvector combinations in the uncoupled case (see (5.22)), there exists only one which is $\mathcal{O}(\epsilon)$ -close to the one in the perturbed case (see (5.23)).

Remark As we discussed in Section 5.1.2, for $\epsilon = 0$, one can not find a change of coordinates that eliminates the following monomials in f_3^i : $z_i |z_i|^2$, $z_i^2 \bar{z}_j$, $z_j |z_i|^2$, $z_i |z_j|^2$, $z_j^2 \bar{z}_i$ and $z_j |z_j|^2$ $i, j = 1, 2$. By contrast, for $\epsilon \neq 0$ and fixed, one could eliminate all of them except $z_i |z_i|^2$ and $z_i |z_j|^2$. Nevertheless, when we consider the coupled system ($\epsilon \neq 0$), in order to have a normal form which is $\mathcal{O}(\epsilon)$ -close to the uncoupled one, one must retain the same monomials although it is possible to kill some of them.

Thus, to obtain the coefficients in (5.5) one just has to consider the coupled case and follow the steps in Section 5.1.2 to obtain a system

$$\dot{z} = A(\epsilon)z + f_3^i(z, \bar{z}; \epsilon) + \mathcal{O}_4(z, \bar{z}), \tag{5.24}$$

where $A(\epsilon)$ is a diagonal matrix having the eigenvectors and eigenvalues in (5.23) and $f_3^i(z, \bar{z}; \epsilon)$ is a third order polynomial containing the monomial terms $z_i|z_i|^2$, $z_i^2\bar{z}_j$, $z_j|z_i|^2$, $z_i|z_j|^2$, $z_j^2\bar{z}_i$ and $z_j|z_j|^2$ $i, j = 1, 2$.

Notice that the linear part of the normal form in (5.9) at $z_1 = z_2 = \bar{z}_1 = \bar{z}_2 = 0$ is given by

$$\begin{pmatrix} \lambda + i\omega + \epsilon\alpha_{\epsilon 0} & \epsilon\beta_{\epsilon 0} & 0 & 0 \\ \epsilon\beta_{\epsilon 0} & \lambda + i\omega + \epsilon\alpha_{\epsilon 0} & 0 & 0 \\ 0 & 0 & \lambda - i\omega + \epsilon\bar{\alpha}_{\epsilon 0} & \epsilon\bar{\beta}_{\epsilon 0} \\ 0 & 0 & \epsilon\bar{\beta}_{\epsilon 0} & \lambda - i\omega + \epsilon\bar{\alpha}_{\epsilon 0} \end{pmatrix}, \quad (5.25)$$

which is not diagonal. Thus, one has to apply the change of variables $Cw = z$ to system (5.24), where

$$C = \frac{1}{\sqrt{2}} \begin{pmatrix} 1 & 1 & 0 & 0 \\ 1 & -1 & 0 & 0 \\ 0 & 0 & 1 & 1 \\ 0 & 0 & 1 & -1 \end{pmatrix}. \quad (5.26)$$

Then, we obtain a system which is exactly in the form (5.9) and from which one can extract the value of the coefficients.

5.2 Dynamical analysis of the truncated normal form

This Section is devoted to analyse the dynamics of system (5.9) taking (λ, ϵ) as bifurcation parameters. In particular, we will analyse its oscillatory solutions.

5.2.1 Normal Form in Polar Coordinates

As it is known, using polar coordinates simplifies the analysis of oscillatory solutions. To express the truncated normal form given in (5.9), in polar coordinates we write $z_n = r_n e^{i\varphi_n}$ with $r_n > 0$ and $\varphi_n \in \mathbb{T}$, so that

$$\dot{z}_n = (\dot{r}_n + ir_n\dot{\varphi}_n)e^{i\varphi_n} = U_\lambda(r_n e^{i\varphi_n}) + \epsilon F_3(r_n e^{i\varphi_n}, r_{3-n} e^{i\varphi_{3-n}}, \epsilon) \quad n = 1, 2. \quad (5.27)$$

Matching imaginary and real parts in (5.27), we obtain the following set of equations for r_n and

φ_n

$$\begin{aligned}
\dot{r}_1 &= r_1 \left(\lambda + \alpha_{01R} r_1^2 \right) + \epsilon f_r(r_1, r_2, \Delta\varphi), \\
\dot{r}_2 &= r_2 \left(\lambda + \alpha_{01R} r_2^2 \right) + \epsilon f_r(r_2, r_1, -\Delta\varphi), \\
r_1 \dot{\varphi}_1 &= r_1 \left(\omega + \alpha_{01I} r_1^2 \right) + \epsilon f_\varphi(r_1, r_2, \Delta\varphi), \\
r_2 \dot{\varphi}_2 &= r_2 \left(\omega + \alpha_{01I} r_2^2 \right) + \epsilon f_\varphi(r_2, r_1, -\Delta\varphi),
\end{aligned} \tag{5.28}$$

where $\Delta\varphi = \varphi_2 - \varphi_1$ and the subscript $X = R, I$ in α_{01} refers to its real and imaginary parts, respectively. The expression for the functions f_r and f_φ is

$$\begin{aligned}
f_r(r_1, r_2, \Delta\varphi) &= r_1^2 r_2 [(\beta_{\epsilon 1R} + \alpha_{\epsilon 3R}) \cos(\Delta\varphi) - (\beta_{\epsilon 1I} - \alpha_{\epsilon 3I}) \sin(\Delta\varphi)] \\
&\quad + r_2^2 r_1 [\alpha_{\epsilon 2R} + \beta_{\epsilon 3R} \cos(2\Delta\varphi) - \beta_{\epsilon 3I} \sin(2\Delta\varphi)] + r_1 \alpha_{\epsilon 0R} + r_1^3 \alpha_{\epsilon 1R} \\
&\quad + r_2^3 [\beta_{\epsilon 2R} \cos(\Delta\varphi) - \beta_{\epsilon 2I} \sin(\Delta\varphi)] + r_2 [\beta_{\epsilon 0R} \cos(\Delta\varphi) - \beta_{\epsilon 0I} \sin(\Delta\varphi)],
\end{aligned} \tag{5.29}$$

$$\begin{aligned}
f_\varphi(r_1, r_2, \Delta\varphi) &= r_1^2 r_2 [(\beta_{\epsilon 1I} + \alpha_{\epsilon 3I}) \cos(\Delta\varphi) + (\beta_{\epsilon 1R} - \alpha_{\epsilon 3R}) \sin(\Delta\varphi)] \\
&\quad + r_2^2 r_1 [\alpha_{\epsilon 2I} + \beta_{\epsilon 3I} \cos(2\Delta\varphi) + \beta_{\epsilon 3R} \sin(2\Delta\varphi)] + r_1 \alpha_{\epsilon 0I} + r_1^3 \alpha_{\epsilon 1I} \\
&\quad + r_2^3 [\beta_{\epsilon 2I} \cos(\Delta\varphi) + \beta_{\epsilon 2R} \sin(\Delta\varphi)] + r_2 [\beta_{\epsilon 0I} \cos(\Delta\varphi) + \beta_{\epsilon 0R} \sin(\Delta\varphi)].
\end{aligned}$$

where again the subscript $X = R, I$ refers to the real and imaginary parts of the coefficients $\alpha_{\epsilon i}, \beta_{\epsilon i}$ $i = 0, \dots, 3$.

System (5.28) can be also written in terms of $\Delta\varphi$ variable, thus obtaining

$$\begin{aligned}
\dot{r}_1 &= r_1 \left(\lambda + \alpha_{01R} r_1^2 \right) + \epsilon f_r(r_1, r_2, \Delta\varphi), \\
\dot{r}_2 &= r_2 \left(\lambda + \alpha_{01R} r_2^2 \right) + \epsilon f_r(r_2, r_1, -\Delta\varphi), \\
\dot{\Delta\varphi} &= \alpha_{01I} (r_2^2 - r_1^2) + \epsilon f_{\Delta\varphi}(r_1, r_2, \Delta\varphi), \\
\dot{\varphi}_1 &= \omega + \alpha_{01I} r_1^2 + \frac{\epsilon}{r_1} f_\varphi(r_1, r_2, \Delta\varphi),
\end{aligned} \tag{5.30}$$

where the expression for the function $f_{\Delta\varphi}$ is:

$$\begin{aligned}
f_{\Delta\varphi}(r_1, r_2, \Delta\varphi) &= f_\varphi(r_2, r_1, -\Delta\varphi)/r_2 - f_\varphi(r_1, r_2, \Delta\varphi)/r_1 = \\
&= (r_1^2 - r_2^2) [\alpha_{\epsilon 2I} - \alpha_{\epsilon 1I} + \beta_{\epsilon 3I} \cos(2\Delta\varphi)] - 2r_1 r_2 (\beta_{\epsilon 1R} - \alpha_{\epsilon 3R}) \sin(\Delta\varphi) \\
&\quad - (r_1^2 + r_2^2) \beta_{\epsilon 3R} \sin(2\Delta\varphi) + \left(\frac{r_1^3}{r_2} - \frac{r_2^3}{r_1} \right) \beta_{\epsilon 2I} \cos(\Delta\varphi) - \left(\frac{r_1^3}{r_2} + \frac{r_2^3}{r_1} \right) \beta_{\epsilon 2R} \sin(\Delta\varphi) \\
&\quad + \left(\frac{r_1}{r_2} - \frac{r_2}{r_1} \right) \beta_{\epsilon 0I} \cos(\Delta\varphi) - \left(\frac{r_1}{r_2} + \frac{r_2}{r_1} \right) \beta_{\epsilon 0R} \sin(\Delta\varphi).
\end{aligned} \tag{5.31}$$

5.2.2 The uncoupled system ($\epsilon = 0$)

Let us start by considering system (5.30) in the uncoupled case ($\epsilon = 0$),

$$\begin{aligned} \dot{r}_1 &= r_1 \left(\lambda + \alpha_{01R} r_1^2 \right), \\ \dot{r}_2 &= r_2 \left(\lambda + \alpha_{01R} r_2^2 \right), \\ \dot{\Delta\varphi} &= \alpha_{01I} (r_2^2 - r_1^2), \\ \dot{\varphi}_1 &= \omega + \alpha_{01I} r_1^2. \end{aligned} \quad (5.32)$$

As we consider two identical systems having a supercritical Hopf bifurcation for $\lambda = 0$, the solutions of system (5.32) for $\lambda > 0$ will correspond to all the Cartesian product of the solutions of each 2-dimensional system.

We observe that, even if the solutions $r_1 = 0$ or $r_2 = 0$ are admissible for system (5.32), they will be singular when we consider the whole system (5.30). For this reason, when we work with these solutions, we refer to system (5.9). Thus, the solution $r_1 = r_2 = 0$ ($\forall \varphi_2, \varphi_1 \in \mathbb{T}$) will be denoted by \mathcal{S}_0 and correspond to the fixed point of system (5.9)

$$\mathcal{S}_0 = \left\{ z_1 = z_2 = 0 \right\}, \quad (5.33)$$

the eigenvalues of the linearization of system (5.9) at \mathcal{S}_0 are $\lambda \pm i\omega$ with multiplicity 2. Therefore, the origin will be a stable focus for $\lambda < 0$ and an unstable focus for $\lambda > 0$.

As $\alpha_{01R} < 0$, for $\lambda > 0$, we have $\forall \varphi_2^0, \varphi_1^0 \in \mathbb{T}$,

$$\mathcal{S}_1(\varphi_2^0) = \left\{ r_1 = r_2 = \sqrt{\frac{-\lambda}{\alpha_{01R}}}, \quad \Delta\varphi = \varphi_2^0 - \varphi_1^0, \quad \varphi_1(t) = \varphi_1^0 + \left(\omega - \lambda \frac{\alpha_{01I}}{\alpha_{01R}} \right) t \right\} \quad (5.34)$$

is a solution of system (5.32), corresponding to the periodic orbit

$$z_1 = \sqrt{\frac{-\lambda}{\alpha_{01R}}} e^{i\varphi_1(t)} = \sqrt{\frac{-\lambda}{\alpha_{01R}}} e^{i(\varphi_1^0 + (\omega - \lambda \frac{\alpha_{01I}}{\alpha_{01R}})t)}, \quad z_2 = \sqrt{\frac{-\lambda}{\alpha_{01R}}} e^{i(\varphi_1(t) + \Delta\varphi)} = \sqrt{\frac{-\lambda}{\alpha_{01R}}} e^{i(\varphi_2^0 + (\omega - \lambda \frac{\alpha_{01I}}{\alpha_{01R}})t)}$$

of system (5.9).

Moreover, the union of these periodic orbits fills a stable 2-dimensional torus \mathcal{T}_0

$$\mathcal{T}_0 = \bigcup_{\varphi_2^0 \in \mathbb{T}} \mathcal{S}_1(\varphi_2^0) = \left\{ r_1 = r_2 = \sqrt{\frac{-\lambda}{\alpha_{01R}}}, \quad \varphi_1, \varphi_2 \in \mathbb{T}^2 \right\}, \quad (5.35)$$

whose characteristic exponents are the eigenvalues of the fixed point $r_1 = r_2 = \sqrt{\frac{-\lambda}{\alpha_{01R}}}$ associated to the two first equations of system (5.32), which are -2λ double. Therefore, \mathcal{T}_0 is a normally hyperbolic attracting torus of system (5.9) for $\lambda > 0$.

There exists another periodic solution of system (5.9) denoted by \mathcal{S}^2 corresponding to $r_1 = \sqrt{\frac{-\lambda}{\alpha_{01R}}}$, $r_2 = 0$,

$$\mathcal{S}^2 = \left\{ z_1 = \sqrt{\frac{-\lambda}{\alpha_{01R}}} e^{i\varphi_1(t)}, \quad z_2 = 0, \quad \varphi_1(t) = \varphi_1^0 + \left(\omega - \lambda \frac{\alpha_{01I}}{\alpha_{01R}} \right) t \right\}, \quad (5.36)$$

which has characteristic exponents $-2\lambda, \lambda \pm i\omega$. Therefore, it is a unstable periodic orbit of saddle type.

Because of the permutation symmetry of system (5.9), it follows that we have another periodic solution

$$\mathcal{S}^3 = \left\{ z_1 = 0, \quad z_2 = \sqrt{\frac{-\lambda}{\alpha_{01R}}} e^{i\varphi_2(t)}, \quad \varphi_2(t) = \varphi_2^0 + \left(\omega - \lambda \frac{\alpha_{01I}}{\alpha_{01R}} \right) t \right\}, \quad (5.37)$$

which is also of saddle type having characteristic exponents $\lambda \pm i\omega, -2\lambda$.

As the torus \mathcal{T}_0 and the periodic orbits \mathcal{S}^2 and \mathcal{S}^3 are hyperbolic for $\lambda > 0$, we have the following result thanks to Fenichel's theorem [27]:

Lemma 5.2.1. *For a fixed value of $\lambda > 0$, there exists $\epsilon_0 = \epsilon_0(\lambda)$, such that for any $0 \leq \epsilon \leq \epsilon_0$, system (5.9) has a stable 2-dimensional torus \mathcal{T}_ϵ and two periodic orbits of saddle type \mathcal{S}_ϵ^2 and \mathcal{S}_ϵ^3 which are ϵ -close to $\mathcal{T}_0, \mathcal{S}^2$ and \mathcal{S}^3 respectively. Moreover, the origin \mathcal{S}_0 also persists as an unstable focus.*

5.2.3 Hopf bifurcations of the origin for $\epsilon > 0$

In the previous Section we have shown that the uncoupled system (5.32) has 4 solutions which we expect to subsist for a small enough coupling $\epsilon > 0$ thanks to Fenichel's theorem. Let us start by analysing the stability of the origin \mathcal{S}_0 given in (5.33). The Jacobian matrix of system (5.9) evaluated at the origin is

$$\begin{pmatrix} \lambda + i\omega + \epsilon\alpha_{\epsilon 0} & 0 & \epsilon\beta_{\epsilon 0} & 0 \\ 0 & \lambda - i\omega + \epsilon\bar{\alpha}_{\epsilon 0} & 0 & \epsilon\bar{\beta}_{\epsilon 0} \\ \epsilon\beta_{\epsilon 0} & 0 & \lambda + i\omega + \epsilon\alpha_{\epsilon 0} & 0 \\ 0 & \epsilon\bar{\beta}_{\epsilon 0} & 0 & \lambda - i\omega + \epsilon\bar{\alpha}_{\epsilon 0} \end{pmatrix}, \quad (5.38)$$

whose its eigenvalues are given by

$$\mu_+ = \lambda + i\omega + \epsilon(\alpha_{\epsilon 0} + \beta_{\epsilon 0}), \quad \mu_- = \lambda + i\omega + \epsilon(\alpha_{\epsilon 0} - \beta_{\epsilon 0}), \quad (5.39)$$

and its complex conjugate pairs $(\bar{\mu}_+, \bar{\mu}_-)$. Therefore, the origin of system (5.9) can undergo two independent Hopf bifurcations, given by $Re(\mu_+) = 0$ and $Re(\mu_-) = 0$. These conditions define the following Hopf bifurcation curves C_{HB}^\pm in the (λ, ϵ) parameter space

$$\begin{aligned} C_{HB}^+ &= \left\{ Re(\mu_+) = 0 \quad \text{or equivalently} \quad \bar{\alpha}^+ := \lambda + \epsilon(\alpha_{\epsilon 0R} + \beta_{\epsilon 0R}) = 0 \right\}, \\ C_{HB}^- &= \left\{ Re(\mu_-) = 0 \quad \text{or equivalently} \quad \bar{\alpha}^- := \lambda + \epsilon(\alpha_{\epsilon 0R} - \beta_{\epsilon 0R}) = 0 \right\}. \end{aligned} \quad (5.40)$$

at each curve C_{HB}^\pm , it will appear a limit cycle denoted in what follows by \mathcal{S}_{osc}^\pm .

To study the stability of the origin of system (5.9), we analyse the sign of the real part of its eigenvalues μ^+ and μ^- given in (5.39) at the previously defined Hopf bifurcation curves C_{HB}^\pm (see Eq. (5.40)),

$$\begin{aligned} \text{if } (\lambda, \epsilon) \in C_{HB}^+ &\rightarrow Re(\mu_+) = 0, \quad Re(\mu_-) = -2\epsilon\beta_{\epsilon 0R}, \\ \text{if } (\lambda, \epsilon) \in C_{HB}^- &\rightarrow Re(\mu_+) = 2\epsilon\beta_{\epsilon 0R}, \quad Re(\mu_-) = 0. \end{aligned} \quad (5.41)$$

Therefore, we conclude that (see Fig. 5.1):

- If $\beta_{\epsilon 0R} > 0$, for $(\lambda, \epsilon) \in C_{HB}^+$ the solution \mathcal{S}_0 changes from a stable-stable focus to unstable-stable focus and a stable limit cycle \mathcal{S}_{osc}^+ emerges from C_{HB}^+ . Moreover, when $(\lambda, \epsilon) \in C_{HB}^-$, the solution \mathcal{S}_0 changes from a unstable-stable focus to an unstable-unstable focus and an unstable limit cycle \mathcal{S}_{osc}^- appears.
- If $\beta_{\epsilon 0R} < 0$, for $(\lambda, \epsilon) \in C_{HB}^-$ the solution \mathcal{S}_0 changes from a stable-stable focus to unstable-stable focus and a stable limit cycle \mathcal{S}_{osc}^- emerges from C_{HB}^- . Moreover, when $(\lambda, \epsilon) \in C_{HB}^+$, the solution \mathcal{S}_0 changes from a stable-unstable focus to an unstable-unstable focus and an unstable limit cycle \mathcal{S}_{osc}^+ appears.
- If $\beta_{\epsilon 0R} = 0$, for $(\lambda, \epsilon) \in C_{HB}^- = C_{HB}^+$, the solution \mathcal{S}_0 changes from a stable-stable focus to an unstable-unstable focus and two stable limit cycles \mathcal{S}_{osc}^+ and \mathcal{S}_{osc}^- , appear.

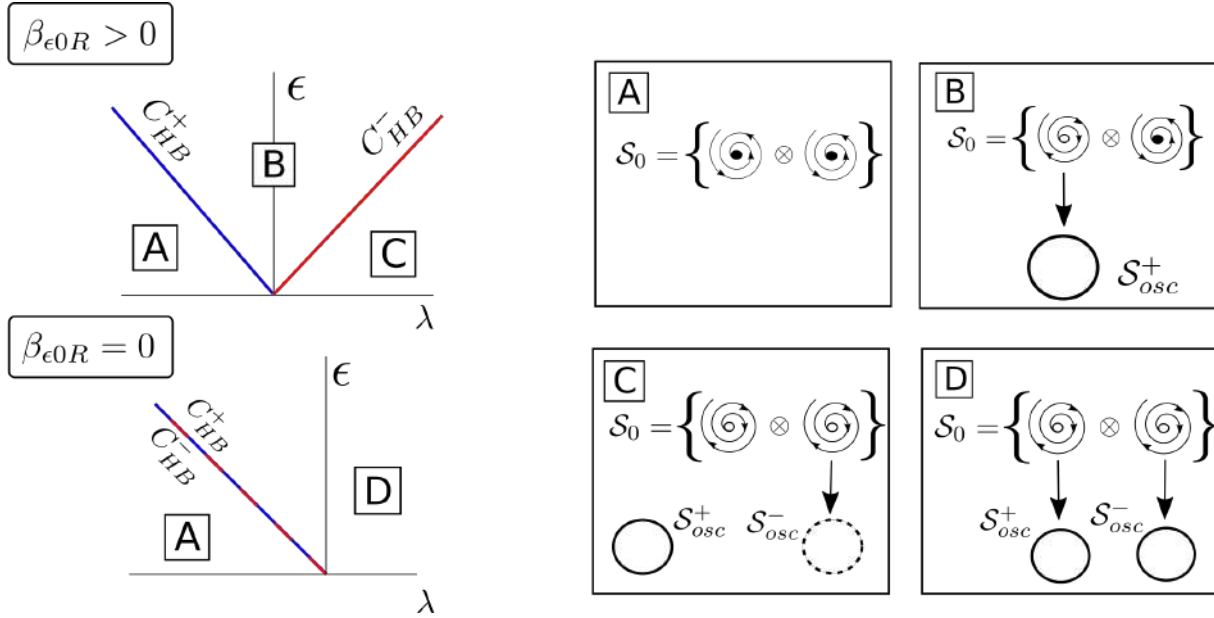


Figure 5.1: Sketch for the curves C_{HB}^{\pm} in (5.9). If $\beta_{\epsilon 0R} > 0$ an stable limit cycle emerges from C_{HB}^+ whereas an unstable limit cycle emerges from C_{HB}^- . For the case $\beta_{\epsilon 0R} < 0$ situation will be the same just reversing \pm by \mp . For the special case $\beta_{\epsilon 0R} = 0$, two stable limit cycles emerge from coincident curves C_{HB}^+ and C_{HB}^- . A $\beta_{\epsilon 0R} > \alpha_{\epsilon 0R} > 0$ value for $\alpha_{\epsilon 0R}$ was chosen to generate this plot.

5.2.4 The Oscillating Solutions S_{osc}^{\pm}

For the coupled case, we have shown the existence of two periodic orbits S_{osc}^{\pm} arising at the Hopf bifurcation curves C_{HB}^{\pm} . Furthermore, Lemma 5.2.1 ensures that the attracting torus \mathcal{T}_0 , which was foliated by the periodic orbits $\mathcal{S}_1(\varphi_0^0)$, persists as a torus \mathcal{T}_{ϵ} when $\epsilon > 0$. The aim of this Section is to relate the existence of the torus \mathcal{T}_{ϵ} and the limit cycles S_{osc}^{\pm} in the coupled case.

To simplify the analysis we exploit the \mathcal{S}_2 permutation symmetry of the system. Let us define the following permutation map

$$K(r_1, r_2, \Delta\varphi) \rightarrow (r_2, r_1, -\Delta\varphi) \quad \text{and} \quad K^2 = Id, \quad (5.42)$$

which in the basis $s = r_1 + r_2$, $d = r_1 - r_2$, $\Delta\varphi$, with $s, d \in \mathbb{R}^+ \times \mathbb{R}$ writes as

$$\tilde{K}(s, d, \Delta\varphi) \rightarrow (s, -d, -\Delta\varphi), \quad (5.43)$$

so we have it diagonal. Thus, we take advantage of this symmetry and express the three first

equations in system (5.30) in the variables $(s, d, \Delta\varphi)$

$$\begin{aligned}\dot{s} &= s\left(\lambda + \frac{\alpha_{01R}}{4}(s^2 + 3d^2)\right) + \epsilon g_s(s, d, \Delta\varphi), \\ \dot{d} &= d\left(\lambda + \frac{\alpha_{01R}}{4}(d^2 + 3s^2)\right) + \epsilon g_d(s, d, \Delta\varphi), \\ \dot{\Delta\varphi} &= -\alpha_{01I}sd + \epsilon g_{\Delta\varphi}(s, d, \Delta\varphi).\end{aligned}\tag{5.44}$$

System (5.44), which will be referred to as the *reduced system*, considers only the first three equations of system (5.30) as they are independent of the variable φ_1 . The expressions for functions g_s , g_d and $g_{\Delta\varphi}$ are given by:

$$\begin{aligned}g_s(s, d, \Delta\varphi) &= f_r\left(\frac{s+d}{2}, \frac{s-d}{2}, \Delta\varphi\right) + f_r\left(\frac{s-d}{2}, \frac{s+d}{2}, -\Delta\varphi\right) = \\ &= s(\cos(\Delta\varphi)\beta_{\epsilon 0R} + \alpha_{\epsilon 0R}) + d\sin(\Delta\varphi)\beta_{\epsilon 0I} + \frac{s}{4}(s^2 + 3d^2)(\beta_{\epsilon 2R}\cos(\Delta\varphi) + \alpha_{\epsilon 1R}) \\ &+ \frac{s}{4}(s^2 - d^2)[(\beta_{\epsilon 1R} + \alpha_{\epsilon 3R})\cos(\Delta\varphi) + \alpha_{\epsilon 2R} + \beta_{\epsilon 3R}\cos(2\Delta\varphi)] \\ &+ \frac{d}{4}(s^2 - d^2)[\beta_{\epsilon 3I}\sin(2\Delta\varphi) - (\beta_{\epsilon 1I} - \alpha_{\epsilon 3I})\sin(\Delta\varphi)] + \frac{d}{4}(3s^2 + d^2)\beta_{\epsilon 2I}\sin(\Delta\varphi), \\ g_d(s, d, \Delta\varphi) &= f_r\left(\frac{s+d}{2}, \frac{s-d}{2}, \Delta\varphi\right) - f_r\left(\frac{s-d}{2}, \frac{s+d}{2}, -\Delta\varphi\right) = \\ &= -d(\cos(\Delta\varphi)\beta_{\epsilon 0R} - \alpha_{\epsilon 0R}) - s\sin(\Delta\varphi)\beta_{\epsilon 0I} - \frac{d}{4}(d^2 + 3s^2)(\beta_{\epsilon 2R}\cos(\Delta\varphi) - \alpha_{\epsilon 1R}) \\ &+ \frac{d}{4}(s^2 - d^2)[(\beta_{\epsilon 1R} + \alpha_{\epsilon 3R})\cos(\Delta\varphi) - \alpha_{\epsilon 2R} - \beta_{\epsilon 3R}\cos(2\Delta\varphi)] \\ &- \frac{s}{4}(s^2 - d^2)[\beta_{\epsilon 3I}\sin(2\Delta\varphi) + (\beta_{\epsilon 1I} - \alpha_{\epsilon 3I})\sin(\Delta\varphi)] - \frac{s}{4}(3d^2 + s^2)\beta_{\epsilon 2I}\sin(\Delta\varphi), \\ g_{\Delta\varphi}(s, d, \Delta\varphi) &= f_{\Delta\varphi}\left(\frac{s+d}{2}, \frac{s-d}{2}, \Delta\varphi\right) = \\ &= \beta_{\epsilon 0I}\cos(\Delta\varphi)\left(\frac{4sd}{s^2 - d^2}\right) - 2\beta_{\epsilon 0R}\sin(\Delta\varphi)\left(\frac{s^2 + d^2}{s^2 - d^2}\right) \\ &- \beta_{\epsilon 2R}\sin(\Delta\varphi)\left(\frac{(s^2 + d^2)^2}{(s^2 - d^2)} - \frac{(s^2 - d^2)}{2}\right) + \beta_{\epsilon 2I}\cos(\Delta\varphi)\frac{2sd(s^2 + d^2)}{(s^2 - d^2)} \\ &- \beta_{\epsilon 3R}\sin(2\Delta\varphi)\frac{(s^2 + d^2)}{2} - (\beta_{\epsilon 1R} - \alpha_{\epsilon 3R})\sin(\Delta\varphi)\frac{(s^2 - d^2)}{2} \\ &+ (\alpha_{\epsilon 2I} + \beta_{\epsilon 3I}\cos(2\Delta\varphi) - \alpha_{\epsilon 1I})sd.\end{aligned}\tag{5.45}$$

Dynamical analysis of the reduced system for $\epsilon = 0$

Let us start by analysing system (5.44) in the uncoupled case ($\epsilon = 0$). That is,

$$\begin{aligned} \dot{s} &= s \left(\lambda + \frac{\alpha_{01R}}{4}(s^2 + 3d^2) \right), \\ \dot{d} &= d \left(\lambda + \frac{\alpha_{01R}}{4}(d^2 + 3s^2) \right), \\ \dot{\Delta\varphi} &= -\alpha_{01I}sd. \end{aligned} \quad (5.46)$$

Notice that in this case, the first two equations uncouple from the third one and can be studied independently. As the variables (s, d) are defined in $\mathbb{R}^+ \times \mathbb{R}$, the fixed points of the two first equations of system (5.46) are given by

$$(0, 0), \quad \left(\sqrt{\frac{-4\lambda}{\alpha_{01R}}}, 0 \right), \quad \left(+\sqrt{\frac{-\lambda}{\alpha_{01R}}}, -\sqrt{\frac{-\lambda}{\alpha_{01R}}} \right), \quad \left(+\sqrt{\frac{-\lambda}{\alpha_{01R}}}, +\sqrt{\frac{-\lambda}{\alpha_{01R}}} \right), \quad (5.47)$$

then, as the Jacobian matrix for the system given by the first two equations of system (5.46) is given by

$$\begin{pmatrix} \lambda + \frac{3\alpha_{01R}}{4}(s^2 + d^2) & \frac{\alpha_{01R}}{4}6ds \\ \frac{\alpha_{01R}}{4}6ds & \lambda + \frac{3\alpha_{01R}}{4}(s^2 + d^2) \end{pmatrix}, \quad (5.48)$$

it is straightforward to see that the eigenvalues of (5.48) for $(s, d) = (0, 0)$ are λ (double), for $(s, d) = \left(\sqrt{\frac{-4\lambda}{\alpha_{01R}}}, 0 \right)$ are -2λ (double) and for $(s, d) = \left(\sqrt{\frac{-\lambda}{\alpha_{01R}}}, \pm\sqrt{\frac{-\lambda}{\alpha_{01R}}} \right)$ are λ and -2λ .

Thus, when $\lambda = 0$, the origin undergoes a bifurcation and change from stable to unstable while three new points appear: one stable corresponding to $(s, d) = \left(\sqrt{\frac{-\lambda}{\alpha_{01R}}}, 0 \right)$ plus two unstable corresponding to $(s, d) = \left(\sqrt{\frac{-\lambda}{\alpha_{01R}}}, \pm\sqrt{\frac{-\lambda}{\alpha_{01R}}} \right)$.

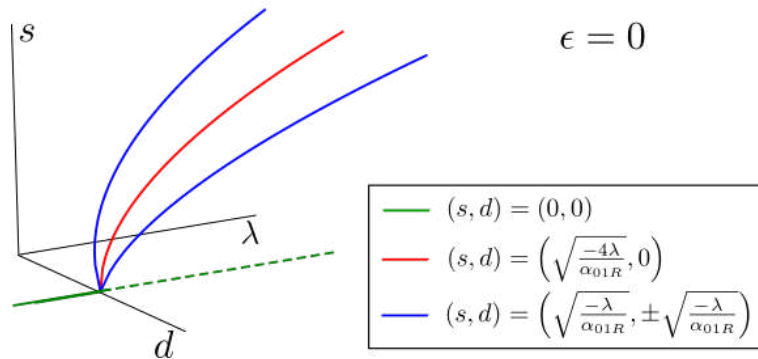


Figure 5.2: Bifurcation diagram of system (5.46) for $\epsilon = 0$ as a function of λ . For the critical value $\lambda = 0$ the system undergoes a bifurcation.

Now let us consider the points given in (5.47) when we also consider the variable $\Delta\varphi$. The (singular) solution

$$\bar{\mathcal{S}}_0 = \left\{ s = d = 0, \quad \Delta\varphi \in \mathbb{T} \right\}, \quad (5.49)$$

with eigenvalues $\lambda > 0$ double, which corresponds to the origin of system (5.9), which is a focus, with eigenvalues $\lambda \pm i\omega$ (double).

For any value of $\Delta\varphi_0$, the solution

$$\bar{\mathcal{S}}_1(\Delta\varphi_0) = \left\{ s = \sqrt{\frac{-4\lambda}{\alpha_{01R}}}, \quad d = 0, \quad \Delta\varphi = \Delta\varphi_0 \right\}, \quad (5.50)$$

is a fixed point with eigenvalues -2λ (double) and 0. They foliate the invariant curve

$$\bar{\mathcal{T}}_0 = \left\{ s = \sqrt{\frac{-4\lambda}{\alpha_{01R}}}, \quad d = 0, \quad \Delta\varphi \in \mathbb{T} \right\}, \quad (5.51)$$

whose characteristic exponents are -2λ (double). Then, $\bar{\mathcal{S}}_1(\Delta\varphi_0)$ and $\bar{\mathcal{T}}_0$ correspond in the system (5.9) to the periodic orbits $\mathcal{S}_1(\varphi_0^2)$ which foliate the torus $\bar{\mathcal{T}}_0$.

The other two fixed points give rise to the following periodic orbits

$$\begin{aligned} \bar{\mathcal{S}}^2 &= \left\{ s = d = \sqrt{\frac{-\lambda}{\alpha_{01R}}}, \quad \Delta\varphi = \Delta\varphi_0 - \frac{\alpha_{01I}}{\alpha_{01R}} \lambda t \right\}, \\ \bar{\mathcal{S}}^3 &= \left\{ s = -d = \sqrt{\frac{-\lambda}{\alpha_{01R}}}, \quad \Delta\varphi = \Delta\varphi_0 + \frac{\alpha_{01I}}{\alpha_{01R}} \lambda t \right\}, \end{aligned} \quad (5.52)$$

whose characteristic exponents are λ and -2λ so they are unstable. These solutions correspond to solutions \mathcal{S}^2 and \mathcal{S}^3 of system (5.9).

In conclusion, (see Fig. 5.3), the phase space for system (5.46) shows for $\lambda > 0$, two invariant curves filled of fixed points, $\bar{\mathcal{S}}_0$ and $\bar{\mathcal{T}}_0$, and two unstable periodic orbits denoted by $\bar{\mathcal{S}}_2$ and $\bar{\mathcal{S}}_3$.

Dynamical analysis of the reduced system in the coupled case ($\epsilon > 0$)

We can take advantage of the \mathcal{S}_2 symmetry of the system (5.44) to look for solutions which remain invariant under the application of the permutation map \bar{K} in (5.43). Then, if we write these curves in the (s, d) coordinates

$$\Xi^+ = \left\{ (s, d, \Delta\varphi) = (s, 0, 0) \right\}, \quad \Xi^- = \left\{ (s, d, \Delta\varphi) = (s, 0, \pi) \right\}, \quad (5.53)$$

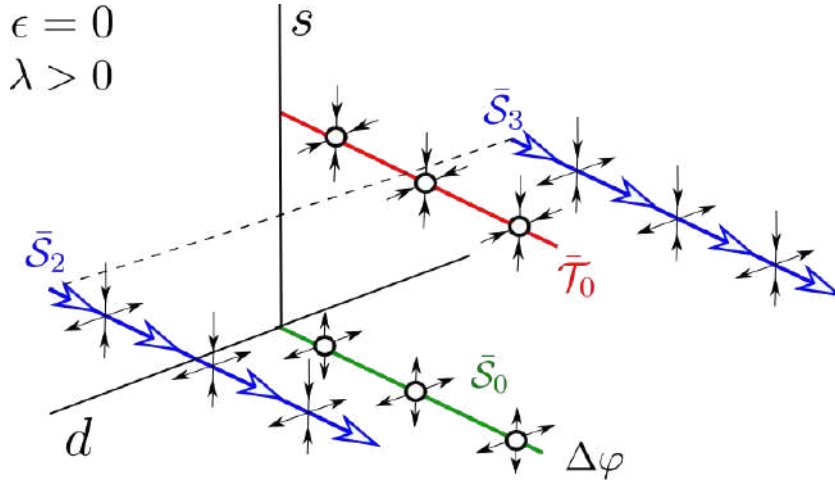


Figure 5.3: Phase space for the unperturbed system (5.46) for $\lambda > 0$. There appear 2 invariant curves, \bar{S}_0 (which is unstable) and \bar{T}_0 (which is stable), filled of fixed points. Moreover there exist two unstable limit cycles \bar{S}_2 and \bar{S}_3 .

the dynamics for system (5.44) when restricted to Ξ^\pm , become simplified to

$$\begin{aligned} \dot{s} &= \lambda s + \frac{s^3 \alpha_{01R}}{4} + \epsilon \left[(\alpha_{\epsilon 0R} \pm \beta_{\epsilon 0R}) s + \frac{s^3}{4} \overbrace{(\alpha_{\epsilon 2R} + \alpha_{\epsilon 1R} + \beta_{\epsilon 3R} \pm (\beta_{\epsilon 2R} + \beta_{\epsilon 1R} + \alpha_{\epsilon 3R}))}^{K_{stb}^\pm} \right], \\ \dot{d} &= 0, \\ \dot{\Delta\varphi} &= 0, \end{aligned} \tag{5.54}$$

where the \pm sign corresponds to $\Delta\varphi = 0, \pi$, respectively.

It is straightforward to check that Eq. for s in (5.54) has three steady solutions, namely, $s = 0$, which corresponds to the previously studied solution \bar{S}_0 , and s_{osc}^\pm given by

$$s_{osc}^\pm = \sqrt{\frac{-4(\lambda + \epsilon(\alpha_{\epsilon 0R} \pm \beta_{\epsilon 0R}))}{\alpha_{01R} + \epsilon K_{stb}^\pm}}. \tag{5.55}$$

Notice that since $s \in \mathbb{R}^+$, we have discarded the negative solutions for the square root.

Taking into account that $\alpha_{01R} < 0$, solutions s_{osc}^\pm in (5.55) are only admissible when $\bar{\alpha}^\pm = \lambda + \epsilon(\alpha_{\epsilon 0R} \pm \beta_{\epsilon 0R}) > 0$. This restriction defines the following conditions for the bifurcation

$$\begin{aligned} \bar{\alpha}^+ &= \epsilon(\alpha_{\epsilon 0R} + \beta_{\epsilon 0R}) + \lambda = 0 & \text{for } \Delta\varphi = 0, \\ \bar{\alpha}^- &= \epsilon(\alpha_{\epsilon 0R} - \beta_{\epsilon 0R}) + \lambda = 0 & \text{for } \Delta\varphi = \pi, \end{aligned} \tag{5.56}$$

which are exactly the conditions defining curves C_{HB}^{\pm} in (5.40) corresponding to the Hopf bifurcations of the origin.

Therefore, for (λ, ϵ) values on the right-hand-side of curves C_{HB}^{\pm} we can define, respectively, the following fixed points of system (5.44)

$$\begin{aligned}\bar{\mathcal{S}}_{osc}^+ &= (s, d, \Delta\varphi) = (s_{osc}^+, 0, 0), \\ \bar{\mathcal{S}}_{osc}^- &= (s, d, \Delta\varphi) = (s_{osc}^-, 0, \pi),\end{aligned}\tag{5.57}$$

which appear across a pitchfork bifurcation (whose character will be discussed below) of the origin in the s direction. Fixed points in (5.57) correspond to the periodic orbits \mathcal{S}_{osc}^{\pm} of system (5.9) that appear at the Hopf bifurcation curves. Next, we will study its stability and possible bifurcations by using the reduced system (5.44).

The Jacobian matrix evaluated at the fixed points $\bar{\mathcal{S}}_{osc}^{\pm}$ is block diagonal

$$\begin{pmatrix} c_s^s & 0 & 0 \\ 0 & c_d^d & c_{\Delta\varphi}^d \\ 0 & c_d^{\Delta\varphi} & c_{\Delta\varphi}^{\Delta\varphi} \end{pmatrix},\tag{5.58}$$

the terms c_s^s , c_d^d , $c_{\Delta\varphi}^d$, $c_d^{\Delta\varphi}$ and $c_{\Delta\varphi}^{\Delta\varphi}$ are different from zero, and their precise expressions are given by

$$\begin{aligned}c_s^s &= \lambda + \epsilon(\alpha_{\epsilon 0R} \pm \beta_{\epsilon 0R}) + \frac{3s^2}{4} \left(\alpha_{01R} + \epsilon(\alpha_{\epsilon 1R} \pm (\beta_{\epsilon 2R} + \beta_{\epsilon 1R} + \alpha_{\epsilon 3R}) + \alpha_{\epsilon 2R} + \beta_{\epsilon 3R}) \right), \\ c_d^d &= \lambda + \epsilon(\alpha_{\epsilon 0R} \mp \beta_{\epsilon 0R}) + \frac{s^2}{4} \left(3\alpha_{01R} + \epsilon(3(\alpha_{\epsilon 1R} \mp \beta_{\epsilon 2R}) \pm (\beta_{\epsilon 1R} + \alpha_{\epsilon 3R}) - \alpha_{\epsilon 2R} - \beta_{\epsilon 3R}) \right), \\ c_{\Delta\varphi}^d &= \epsilon \left(-\frac{s^3}{4} (2\beta_{\epsilon 3I} \pm (\beta_{\epsilon 1I} - \alpha_{\epsilon 3I}) \pm \beta_{\epsilon 2I}) \mp \beta_{\epsilon 0IS} \right), \\ c_d^{\Delta\varphi} &= -\alpha_{01I} s + \epsilon \left(s(\alpha_{\epsilon 2I} - \alpha_{\epsilon 1I} + \beta_{\epsilon 3I} \pm 2\beta_{\epsilon 2I}) \pm 4\frac{\beta_{\epsilon 0I}}{s} \right), \\ c_{\Delta\varphi}^{\Delta\varphi} &= \epsilon \left(\frac{s^2}{2} (\mp(\beta_{\epsilon 1R} - \alpha_{\epsilon 3R}) - 2\beta_{\epsilon 3R} \mp \beta_{\epsilon 2R}) \mp 2\beta_{\epsilon 0R} \right).\end{aligned}\tag{5.59}$$

where $s = s_{osc}^{\pm}$.

Because of the block diagonal form of the Jacobian matrix, it is straightforward to check the stability in the s direction as it corresponds to the 1x1 block. Thus, the eigenvalue $\bar{\mu}_1^{\pm}$ takes the form

$$\bar{\mu}_1^{\pm} = c_s^s = -2(\epsilon(\alpha_{\epsilon 0R} \pm \beta_{\epsilon 0R}) + \lambda),\tag{5.60}$$

and therefore, the solutions \bar{S}_{osc}^\pm are always stable in the s direction as they appear for $\bar{\alpha}^\pm = \epsilon(\alpha_{\epsilon 0R} \pm \beta_{\epsilon 0R}) + \lambda > 0$. Therefore, the pitchfork bifurcations of the origin are supercritical (see Fig. 5.4).

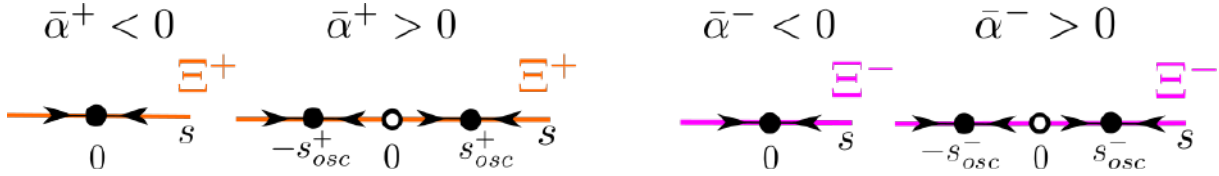


Figure 5.4: Solutions s_{osc}^\pm appear through a supercritical pitchfork bifurcation of the origin in the s direction which takes place at the critical value $\bar{\alpha}^\pm = 0$ of the bifurcation parameter $\bar{\alpha}^\pm = \lambda + \epsilon(\alpha_{\epsilon 0R} \pm \beta_{\epsilon 0R})$.

As the solutions \bar{S}_{osc}^\pm are always stable in the s direction, one has to study the eigenvalues of the 2×2 block, corresponding to the transverse directions, in order to study possible bifurcations of the symmetric solutions \bar{S}_{osc}^\pm . The trace (Tr^\pm) and the determinant (Det^\pm) of the 2×2 block of (5.58) at \bar{S}_{osc}^\pm are given up to order 2 in (λ, ϵ) by:

$$Tr^\pm(\lambda, \epsilon) = c_d^d + c_{\Delta\varphi}^{\Delta\varphi} = -2(\lambda + \epsilon(\alpha_{\epsilon 0R} \pm 3\beta_{\epsilon 0R})), \quad (5.61)$$

$$Det^\pm(\lambda, \epsilon) = \pm 4\epsilon(\lambda + \epsilon(\alpha_{\epsilon 0R} \pm \beta_{\epsilon 0R}))(C_{det} + \beta_{\epsilon 0R}) + 4\epsilon^2(\beta_{\epsilon 0I}^2 + \beta_{\epsilon 0R}^2), \quad (5.62)$$

where

$$C_{det} := \frac{\beta_{\epsilon 0I}\alpha_{01I}}{\alpha_{01R}}. \quad (5.63)$$

So, computing the discriminant

$$\Delta^\pm = (Tr^\pm)^2 - 4Det^\pm = (\lambda + \epsilon(\alpha_{\epsilon 0R} \pm \beta_{\epsilon 0R}))(\lambda + \epsilon(\alpha_{\epsilon 0R} \pm \beta_{\epsilon 0R}) \mp 4\epsilon C_{det}) - 4\epsilon^2\beta_{\epsilon 0I}^2, \quad (5.64)$$

we find that the eigenvalues of the 2×2 block of the Jacobian matrix (5.58) writes as,

$$\begin{aligned} \bar{\mu}_2^\pm &= -(\lambda + \epsilon(\alpha_{\epsilon 0R} \pm 3\beta_{\epsilon 0R})) - \sqrt{(\lambda + \epsilon(\alpha_{\epsilon 0R} \pm \beta_{\epsilon 0R}))(\lambda + \epsilon(\alpha_{\epsilon 0R} \pm \beta_{\epsilon 0R}) \mp 4\epsilon C_{det}) - 4\epsilon^2\beta_{\epsilon 0I}^2}, \\ \bar{\mu}_3^\pm &= -(\lambda + \epsilon(\alpha_{\epsilon 0R} \pm 3\beta_{\epsilon 0R})) + \sqrt{(\lambda + \epsilon(\alpha_{\epsilon 0R} \pm \beta_{\epsilon 0R}))(\lambda + \epsilon(\alpha_{\epsilon 0R} \pm \beta_{\epsilon 0R}) \mp 4\epsilon C_{det}) - 4\epsilon^2\beta_{\epsilon 0I}^2}. \end{aligned} \quad (5.65)$$

Next, we study the stability of the solutions \bar{S}_{osc}^\pm given in (5.57) when the parameters λ, ϵ lie in the area

$$\mathcal{A} := \left\{ (\lambda, \epsilon) \in \mathbb{R}^2 \mid \bar{\alpha}^\pm \geq 0, \quad \epsilon > 0 \right\}, \quad (5.66)$$

which correspond to the region between the right hand side of curves C_{HB}^{\pm} and the horizontal axis (see Fig. 5.1 left).

In particular, for $\bar{\alpha}^{\pm} = 0$, that is $(\epsilon, \lambda) \in C_{HB}^{\pm}$, the eigenvalues of the Jacobian matrix (5.58) at the fixed points $\bar{\mathcal{S}}_{osc}^{\pm}$ are given by

$$\begin{aligned}\bar{\mu}_1^{\pm} &= 0, \\ \bar{\mu}_2^{\pm} &= \mp 2\beta_{\epsilon 0R} - i2\epsilon\beta_{\epsilon 0I}, \\ \bar{\mu}_3^{\pm} &= \mp 2\beta_{\epsilon 0R} + i2\epsilon\beta_{\epsilon 0I}.\end{aligned}\tag{5.67}$$

Therefore, when the parameters (λ, ϵ) cross the curves C_{HB}^{\pm} from left to right, if $\beta_{\epsilon 0R} > 0$, $\bar{\mathcal{S}}_{osc}^+$ is a stable focus whereas $\bar{\mathcal{S}}_{osc}^-$ is a saddle-focus with a 1-dimensional stable manifold (corresponding to the s dimension which is always stable) and vice versa if $\beta_{\epsilon 0R} < 0$.

For ϵ small and $\bar{\alpha}^{\pm} \geq 0$ the eigenvalues of the Jacobian matrix (5.58) at the fixed points $\bar{\mathcal{S}}_{osc}^{\pm}$ are given by

$$\begin{aligned}\bar{\mu}_1^{\pm} &= -2\lambda + \mathcal{O}(\epsilon), \\ \bar{\mu}_2^{\pm} &= -2\lambda + \mathcal{O}(\epsilon), \\ \bar{\mu}_3^{\pm} &= \mp 2\epsilon(\beta_{\epsilon 0R} + C_{det}) + \mathcal{O}(\epsilon^2),\end{aligned}\tag{5.68}$$

which are $\mathcal{O}(\epsilon)$ close to the ones for the uncoupled case, -2λ (double) and 0. In particular, depending on the sign of $(\beta_{\epsilon 0R} + C_{det})$, one fixed point is a stable node whereas the other is a saddle with a 1-dimensional unstable manifold. We remark that consistently with Fenichel's theory we can show that the invariant curve $\bar{\mathcal{T}}_{\epsilon}$ persists for ϵ small as a perturbation of the unperturbed one $\bar{\mathcal{T}}_0$ in (5.51). Indeed, by using the variables $(s, d, \Delta\varphi)$, we show that for $\beta_{\epsilon 0R} > 0$, $\bar{\mathcal{T}}_{\epsilon}$ consists of the union of the saddle point $\bar{\mathcal{S}}_{osc}^-$, its unstable 1-dimensional manifold and the stable node $\bar{\mathcal{S}}_{osc}^+$ (and vice versa if $\beta_{\epsilon 0R} < 0$), so $\bar{\mathcal{S}}_{osc}^{\pm} \in \bar{\mathcal{T}}_{\epsilon}$ for $\epsilon > 0$ small (see Fig. 5.5).

To conclude, we link the results for the reduced 3D system (5.44) with the full system (5.9). In this Section we have shown that fixed points $\bar{\mathcal{S}}_{osc}^{\pm}$ of system (5.44) correspond to the periodic orbits \mathcal{S}_{osc}^{\pm} of the full system (5.28). Therefore, as we have argued that for ϵ small $\bar{\mathcal{S}}_{osc}^+$ and $\bar{\mathcal{S}}_{osc}^-$ are contained in an invariant curve $\bar{\mathcal{T}}_{\epsilon}$, for the 4D system there exists a torus \mathcal{T}_{ϵ} . That torus contains two periodic orbits, \mathcal{S}_{osc}^+ and \mathcal{S}_{osc}^- with $\Delta\varphi = 0$ and $\Delta\varphi = \pi$, respectively whose stability depends on the sign of $\beta_{\epsilon 0R} + C_{det}$. Furthermore, these periodic orbits collapse to a fixed point at different Hopf bifurcation curves C_{HB}^+ and C_{HB}^- given in (5.40), and the stability of these periodic orbits before the bifurcation depends on the sign of $\beta_{\epsilon 0R}$.

In the next Section we will study the evolution of fixed points \bar{S}_{osc}^+ and \bar{S}_{osc}^- in the area \mathcal{A} in (5.66) for different combinations of the signs $\beta_{\epsilon 0R} + C_{det}$ and $\beta_{\epsilon 0R}$.

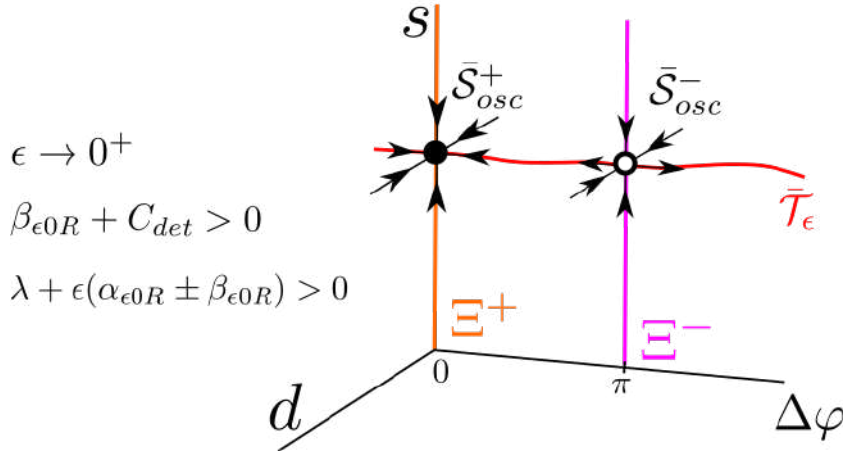


Figure 5.5: Phase space of system (5.44) for $\epsilon \neq 0$, $\beta_{\epsilon 0R} + C_{det} > 0$ and $\lambda + \epsilon(\alpha_{\epsilon 0R} \pm \beta_{\epsilon 0R}) > 0$. There exist two fixed points \bar{S}_{osc}^\pm , a stable node and a saddle point whose unstable invariant manifold form the invariant curve \bar{T}_ϵ . Due to the coupling term there are only two fixed points on \bar{T}_ϵ whereas we had an infinite number in the unperturbed case. Notice that the dynamics on the s direction is always attracting.

5.3 Bifurcation diagrams of the reduced system

In the previous Sections we have shown that when ϵ is small and $\bar{\alpha}^\pm \geq 0$ there exist two critical points \bar{S}_{osc}^\pm belonging to the curve \bar{T}_ϵ which disappear at curves C_{HB}^\pm . The points \bar{S}_{osc}^\pm undergo several bifurcations in the parameter region \mathcal{A} defined in (5.66). Table 5.1 shows which are the values for the trace Tr^\pm in (5.61), the determinant Det^\pm in (5.62) and the discriminant Δ^\pm in (5.64) of the 2x2 block of the Jacobian matrix (5.58) of system (5.44) at \bar{S}_{osc}^\pm near the curves C_{HB}^\pm (given by the condition $\bar{\alpha}^\pm = 0$) and for $\bar{\alpha}^\pm \geq 0$ and ϵ small.

	$\bar{\mathcal{S}}_{osc}^+$		$\bar{\mathcal{S}}_{osc}^-$		
	$\bar{\alpha}^+ \rightarrow 0^+$	$\epsilon \rightarrow 0^+$	$\bar{\alpha}^- \rightarrow 0^+$	$\epsilon \rightarrow 0^+$	
Tr^+	$-4\epsilon\beta_{\epsilon 0R}$	-2λ	$4\epsilon\beta_{\epsilon 0R}$	-2λ	Tr^-
Det^+	$4\epsilon^2(\beta_{\epsilon 0I}^2 + \beta_{\epsilon 0R}^2)$	$4\epsilon\lambda(C_{det} + \beta_{\epsilon 0R})$	$4\epsilon^2(\beta_{\epsilon 0I}^2 + \beta_{\epsilon 0R}^2)$	$-4\epsilon\lambda(C_{det} + \beta_{\epsilon 0R})$	Det^-
Δ^+	$-4\epsilon^2\beta_{\epsilon 0I}^2$	λ^2	$-4\epsilon^2\beta_{\epsilon 0I}^2$	λ^2	Δ^-

Table 5.1: Values for the trace, the determinant and the discriminant of the linearisation of the 2x2 block of the Jacobian matrix (5.58) of system (5.44) at $\bar{\mathcal{S}}_{osc}^\pm$ near the curves C_{HB}^\pm and in the limit $\epsilon \rightarrow 0$ and $\bar{\alpha}^\pm = \lambda + \epsilon(\alpha_{\epsilon 0R} \pm \beta_{\epsilon 0R}) \geq 0$.

Notice that the sign of the constants $\beta_{\epsilon 0R}$ and $C_{det} + \beta_{\epsilon 0R}$ is relevant to determine the local dynamics around fixed points. In particular,

- $\beta_{\epsilon 0R}$ determines which of the two solutions $\bar{\mathcal{S}}_{osc}^\pm$ can have a null trace. For $\beta_{\epsilon 0R} > 0$, is $\bar{\mathcal{S}}_{osc}^+$, whereas for $\beta_{\epsilon 0R} < 0$ is $\bar{\mathcal{S}}_{osc}^-$.
- The sign of $C_{det} + \beta_{\epsilon 0R}$ determines which of the two solutions $\bar{\mathcal{S}}_{osc}^\pm$ can have a null determinant. For $C_{det} + \beta_{\epsilon 0R} > 0$, is $\bar{\mathcal{S}}_{osc}^-$, whereas for $C_{det} + \beta_{\epsilon 0R} < 0$ is $\bar{\mathcal{S}}_{osc}^+$.
- Moreover, as ϵ increases the discriminant always changes from negative to positive. That is, consistently with the eigenvalues obtained in (5.67) and (5.68), the fixed points $\bar{\mathcal{S}}_{osc}^\pm$ change from a stable node and a saddle point to stable focus and a saddle-focus.

Depending on the sign of $\beta_{\epsilon 0R}$ and $C_{det} + \beta_{\epsilon 0R}$ we consider three different cases: (1) $\beta_{\epsilon 0R} > 0$, $C_{det} + \beta_{\epsilon 0R} > 0$; (2) $\beta_{\epsilon 0R} < 0$, $C_{det} + \beta_{\epsilon 0R} > 0$ and (3) $\beta_{\epsilon 0R} = 0$, $C_{det} > 0$. The cases $\beta_{\epsilon 0R} < 0$, $C_{det} + \beta_{\epsilon 0R} < 0$; $\beta_{\epsilon 0R} > 0$, $C_{det} + \beta_{\epsilon 0R} < 0$ and $\beta_{\epsilon 0R} = 0$, $C_{det} < 0$ are analogous to (1), (2) and (3), respectively just replacing $\bar{\mathcal{S}}_{osc}^\pm$ by $\bar{\mathcal{S}}_{osc}^\mp$. For each case, we study in detail the different bifurcations of the solutions $\bar{\mathcal{S}}_{osc}^\pm$ in the (λ, ϵ) parameter space, we link results obtained for the 3D system (5.44) with the complete 4D system (5.9) and we discuss the areas of bistability.

5.3.1 Case $\beta_{\epsilon 0R} > 0$ and $C_{det} + \beta_{\epsilon 0R} > 0$ (or $\beta_{\epsilon 0R} < 0$ and $C_{det} + \beta_{\epsilon 0R} < 0$)

Dynamics of \bar{S}_{osc}^+

For $\bar{\alpha}^+ \geq 0$, λ fixed and ϵ small (see Fig. 5.6), the fixed point \bar{S}_{osc}^+ for system (5.44) is a stable node contained in the invariant curve \bar{T}_ϵ (region B in Fig. 5.6), and as ϵ increases it becomes a stable focus at the curve $\Delta^+ = 0$ (region A in Fig. 5.6). It disappears at a pitchfork bifurcation of the origin in the s -direction at C_{HB}^+ .

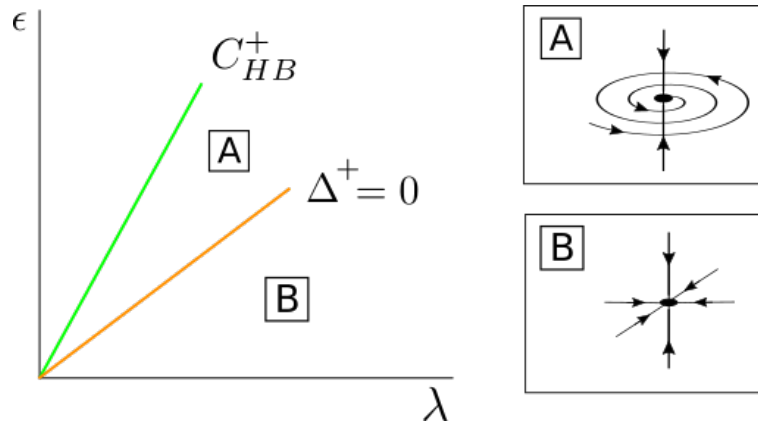


Figure 5.6: Bifurcation diagram for \bar{S}_{osc}^+ in the case $\beta_{\epsilon 0R} > 0$ and $C_{det} + \beta_{\epsilon 0R} > 0$. In this case \bar{S}_{osc}^+ has a supercritical pitchfork bifurcation of the origin in the s direction coinciding with the curve C_{HB}^+ .

Going back to the original 4D system (5.9) we have that for ϵ small there exists a stable periodic orbit S_{osc}^+ , (which belongs to the invariant torus \mathcal{T}_ϵ) which disappears at a Hopf bifurcation of the origin in C_{HB}^+ .

Dynamics of \bar{S}_{osc}^-

\bar{S}_{osc}^- changes from a saddle-focus with a 1-dimensional stable manifold near C_{HB}^- to a saddle with a 2-dimensional stable manifold for ϵ small and $\bar{\alpha}^- > 0$. Moreover, in this case the trace for \bar{S}_{osc}^- vanishes ($Tr^- = 0$). Therefore, if

$$\beta_{\epsilon 0R} < -C_{det} + \sqrt{C_{det}^2 + \beta_{\epsilon 0I}^2}, \quad (5.69)$$

then $Tr^- = 0$ and $\Delta^- < 0$ and \bar{S}_{osc}^- undergoes a Hopf bifurcation.

So, we will distinguish two cases:

1) **Case** $\beta_{\epsilon 0R} < -C_{det} + \sqrt{C_{det}^2 + \beta_{\epsilon 0I}^2}$,

For $\bar{\alpha}^+ \geq 0$, λ fixed and ϵ small (see Fig. 5.7) $\bar{\mathcal{S}}_{osc}^-$ is a saddle with a 1-dimensional unstable manifold (in the $\Delta\varphi$ direction) contained in the invariant curve $\bar{\mathcal{T}}_\epsilon$ (region D). When crossing the curve $Det^- = 0$ (region C), the point $\bar{\mathcal{S}}_{osc}^-$ becomes a stable node. As the coupling ϵ is increased, $\bar{\mathcal{S}}_{osc}^-$ crosses the curve $\Delta^- = 0$ and $\bar{\mathcal{S}}_{osc}^-$ becomes a stable focus. When the parameters cross the curve $Tr^- = 0$, $\bar{\mathcal{S}}_{osc}^-$ undergoes a Hopf bifurcation $\bar{\mathcal{H}}$ in the $d, \Delta\varphi$ directions and $\bar{\mathcal{S}}_{osc}^-$ becomes a saddle focus with a 1-dimensional unstable manifold (region A). At this bifurcation there appears or disappears a periodic orbit $\bar{\mathcal{T}}^-$ depending whether the Hopf bifurcation is supercritical or subcritical. Finally the fixed point disappears at a pitchfork bifurcation of the origin in the s -direction at the curve C_{HB}^- .

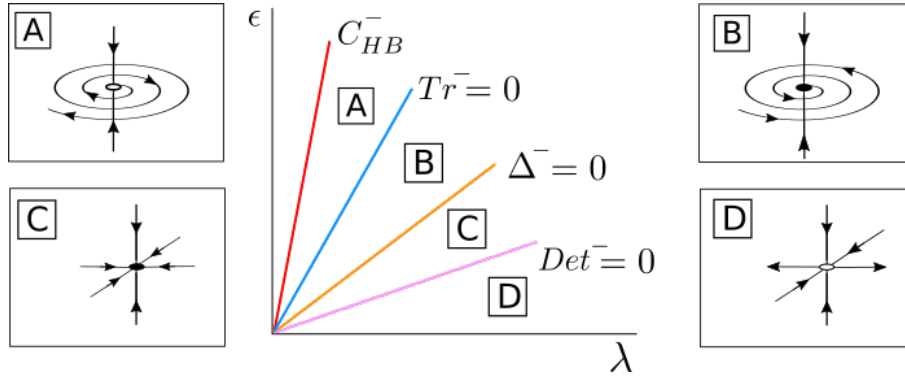


Figure 5.7: Bifurcation diagram for $\bar{\mathcal{S}}_{osc}^-$ in the case $\beta_{\epsilon 0R} > 0$, $C_{det} + \beta_{\epsilon 0R} > 0$ and $\beta_{\epsilon 0R} < -C_{det} + \sqrt{C_{det}^2 + \beta_{\epsilon 0I}^2}$. In this case $\bar{\mathcal{S}}_{osc}^-$ has a supercritical pitchfork bifurcation from the origin in the s direction coinciding with the curve C_{HB}^- , a Hopf bifurcation $\bar{\mathcal{H}}$ of undetermined type at the curve $Tr^- = 0$, and a bifurcation at the curve $Det^- = 0$.

Going back to the original full 4D system (5.9), for ϵ small enough, there exists an unstable periodic orbit \mathcal{S}_{osc}^- , belonging to the torus \mathcal{T}_ϵ , which will become stable at the curve $Det^- = 0$. The periodic orbit undergoes a Torus bifurcation and \mathcal{S}_{osc}^- becomes unstable at the curve $Tr^- = 0$ and a new torus \mathcal{T}^- appears or disappears depending whether the Torus bifurcation is subcritical or supercritical. Finally, \mathcal{S}_{osc}^- will disappear at a Hopf bifurcation of the origin occurring at C_{HB}^- .

2) Case $\beta_{\epsilon 0R} > -C_{det} + \sqrt{C_{det}^2 + \beta_{\epsilon 0I}^2}$

For $\bar{\alpha}^+ \geq 0$, λ fixed and ϵ small (see Fig. 5.8) \bar{S}_{osc}^- is a saddle with a 1-dimensional unstable manifold (in the $\Delta\varphi$ direction) contained in the invariant curve \bar{T}_ϵ (region C). As ϵ increases, \bar{S}_{osc}^- becomes a saddle with a 2-dimensional unstable manifold at the curve $Det^- = 0$ (region B). When further increasing the coupling ϵ , \bar{S}_{osc}^- becomes a saddle-focus point at the curve $\Delta^- = 0$ which disappears at a pitchfork bifurcation of the origin in the s -direction at the curve C_{HB}^- .

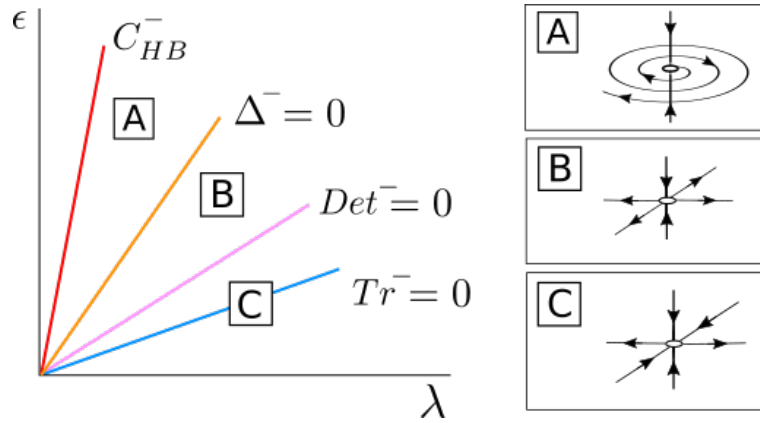


Figure 5.8: Bifurcation diagram for \bar{S}_{osc}^- in the case $\beta_{\epsilon 0R} > 0$, $C_{det} + \beta_{\epsilon 0R} > 0$ and $\beta_{\epsilon 0R} > -C_{det} + \sqrt{C_{det}^2 + \beta_{\epsilon 0I}^2}$. In this case \bar{S}_{osc}^- has a supercritical pitchfork bifurcation from the origin in the s direction coinciding with the curve C_{HB}^- and a bifurcation at the curve $Det^- = 0$.

Going back to the original full 4D system (5.9), for ϵ small enough, there exists an unstable periodic orbit S_{osc}^- , belonging to the torus \mathcal{T}_ϵ . The periodic orbit undergoes a bifurcation and the curve $Det^- = 0$ in which a stable manifold becomes unstable. Finally, S_{osc}^- will disappear at a Hopf bifurcation of the origin occurring at C_{HB}^- .

Bistability Areas

Since \bar{S}_{osc}^+ is always stable, bistability between fixed points will appear in those regions where \bar{S}_{osc}^- is also stable. As in the case $\beta_{\epsilon 0R} > -C_{det} + \sqrt{C_{det}^2 + \beta_{\epsilon 0I}^2}$, the fixed point \bar{S}_{osc}^- is never stable, it is no possible to find bistable regions. By contrast, if $\beta_{\epsilon 0R} < -C_{det} + \sqrt{C_{det}^2 + \beta_{\epsilon 0I}^2}$, there exist a region in the (ϵ, λ) -plane given by

$$Tr^-(\lambda, \epsilon) < 0 \quad \text{and} \quad Det^-(\lambda, \epsilon) > 0, \quad (5.70)$$

for which \bar{S}_{osc}^- can be either a stable node or a stable focus (see Fig. 5.7). So the system is bistable in region (5.70).

Moreover, in the case $\beta_{\epsilon 0R} < -C_{det} + \sqrt{C_{det}^2 + \beta_{\epsilon 0I}^2}$, the point \bar{S}_{osc}^- undergoes a Hopf bifurcation \bar{H} . If the Hopf bifurcation is supercritical, then \bar{S}_{osc}^- becomes unstable and a stable limit cycle \bar{T}^- appears. This generates a bistability situation between \bar{S}_{osc}^+ and \bar{T}^- whose detailed analysis is beyond of the scope of this paper.

Finally we remark that the same bistability scenarios can be found in the full system (5.9) by changing the fixed points \bar{S}_{osc}^\pm by the limit cycles S_{osc}^\pm and the periodic orbit \bar{T}^- by the torus \mathcal{T}^- .

5.3.2 Case $\beta_{\epsilon 0R} < 0$ and $C_{det} + \beta_{\epsilon 0R} > 0$ (or $\beta_{\epsilon 0R} > 0$ and $C_{det} + \beta_{\epsilon 0R} < 0$)

Dynamics of \bar{S}_{osc}^+

In this case the trace for \bar{S}_{osc}^+ vanishes ($Tr^+ = 0$). Therefore, as

$$\beta_{\epsilon 0R} < -C_{det} < -C_{det} + \sqrt{C_{det}^2 + \beta_{\epsilon 0I}^2}, \quad (5.71)$$

then $Tr^+ = 0$ and $\Delta^+ < 0$ and \bar{S}_{osc}^+ will always undergo a Hopf bifurcation \bar{H} .

For $\bar{\alpha}^+ \geq 0$, λ fixed and ϵ small (see Fig. 5.9), the fixed point \bar{S}_{osc}^+ is a stable node (region C) and becomes a stable focus when the parameters cross the curve $\Delta^+ = 0$ (region B). For larger ϵ values \bar{S}_{osc}^+ undergoes a Hopf bifurcation \bar{H} at the curve $Tr^+ = 0$ and becomes a saddle-focus (region A). At this bifurcation there appears or disappears a limit cycle \bar{T}^+ depending whether this Hopf bifurcation is subcritical or supercritical. For larger values of ϵ , \bar{S}_{osc}^+ disappears at a pitchfork bifurcation of the origin in the s -direction at the curve C_{HB}^+ .

Going back to the original 4D system (5.9), for ϵ small enough there exists a stable periodic orbit S_{osc}^+ . This stable periodic orbit will lose its stability across a torus bifurcation occurring at the curve $Tr^+ = 0$ line. At this bifurcation there appears or disappears a new torus \mathcal{T}^+ depending whether the Torus bifurcation is subcritical or supercritical. Finally the unstable limit cycle S_{osc}^+ collapses to the origin at across a Hopf bifurcation occurring at the curve C_{HB}^+ .

Dynamics of \bar{S}_{osc}^-

For $\bar{\alpha}^- \geq 0$, λ fixed and ϵ small (see Fig. 5.10), the fixed point \bar{S}_{osc}^- of system (5.44) is a saddle point with a 1-dimensional unstable manifold in the $\Delta\varphi$ direction contained in \bar{T}_ϵ (region

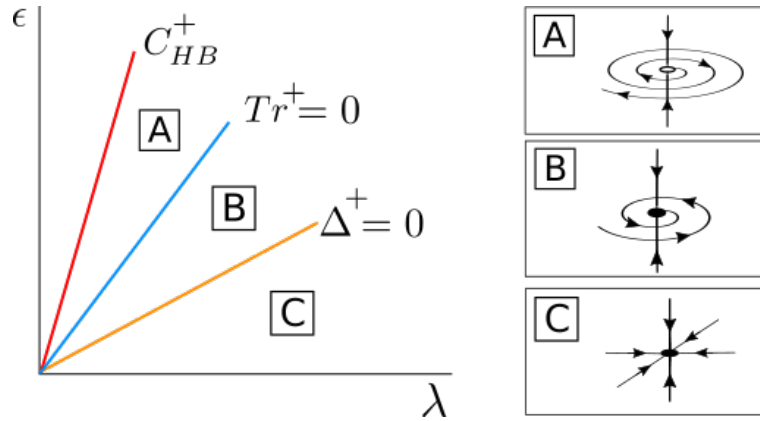


Figure 5.9: Phase space for \bar{S}_{osc}^+ in the case $\beta_{\epsilon 0 R} < 0$ and $C_{det} + \beta_{\epsilon 0 R} > 0$. In this case \bar{S}_{osc}^+ has a supercritical pitchfork bifurcation from the origin in the s direction coinciding with the C_{HB}^+ curve, and a Hopf bifurcation \bar{H} of undetermined type at the curve $Tr^+ = 0$.

C), and as ϵ increases it becomes a stable node when ϵ crosses the curve $Det^- = 0$ (region B). For larger values of ϵ , \bar{S}_{osc}^- becomes a stable focus at the curve $\Delta^- = 0$ (region A) and disappears at a pitchfork bifurcation of the origin in the s direction at the curve C_{HB}^- .

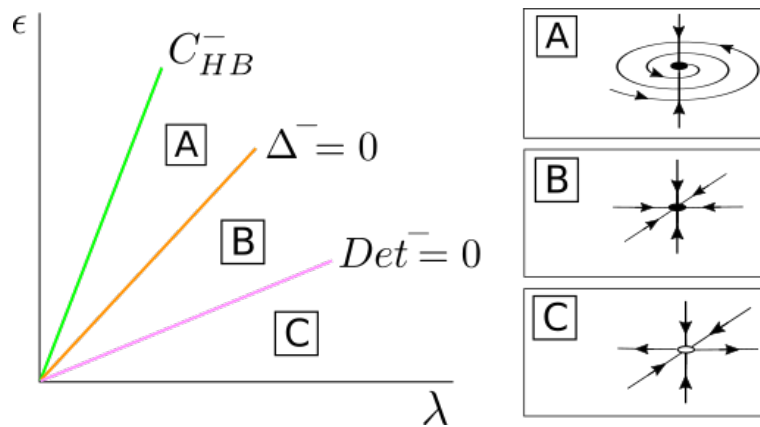


Figure 5.10: Bifurcation diagram for \bar{S}_{osc}^- in the case $\beta_{\epsilon 0 R} < 0$ and $C_{det} + \beta_{\epsilon 0 R} > 0$. In this case \bar{S}_{osc}^- has a supercritical pitchfork bifurcation from the origin in the s direction coinciding with C_{HB}^- line, and a bifurcation at $Det^- = 0$.

Going back to the original 4D system (5.9), for ϵ small there exists an unstable periodic orbit S_{osc}^- . This unstable periodic orbit becomes stable at the curve $Det^- = 0$. Finally, the stable limit cycle S_{osc}^- collapses to the origin at a Hopf bifurcation occurring at the curve C_{HB}^- .

Bistability Areas

There exist a region in the (λ, ϵ) -plane given by

$$Tr^+(\lambda, \epsilon) < 0 \quad \text{and} \quad Det^-(\lambda, \epsilon) > 0, \quad (5.72)$$

in which both fixed points \bar{S}_{osc}^\pm are stable. If the Hopf bifurcation is supercritical, then \bar{S}_{osc}^+ becomes unstable and a stable limit cycle \bar{T}^+ appears. This generates a bistability situation between \bar{S}_{osc}^- and \bar{T}^+ whose detailed analysis is beyond of the scope of this paper.

Finally we remark that the same bistability scenarios can be found in the full system (5.9) by changing the fixed points \bar{S}_{osc}^\pm by the limit cycles S_{osc}^\pm and the periodic orbit \bar{T}^+ by the torus \mathcal{T}^+ .

5.3.3 Case $\beta_{\epsilon 0R} = 0$ and $C_{det} > 0$ (or $\beta_{\epsilon 0R} = 0$ and $C_{det} < 0$)

In this case, the curves C_{HB}^\pm coincide. Moreover, the trace in (5.61) is identically zero for $(\lambda, \epsilon) \in C_{HB}^\pm$. To obtain the sign of Tr^\pm , we compute Tr^\pm when $\lambda + \epsilon\alpha_{\epsilon 0R} \rightarrow 0^+$. We have

$$Tr(\lambda, \epsilon) = (\lambda + \epsilon\alpha_{\epsilon 0R})(-2 + \mathcal{O}_2(\epsilon)), \quad (5.73)$$

so, near the C_{HB}^\pm curves, both fixed points \bar{S}_{osc}^\pm are stable.

Dynamics of \bar{S}_{osc}^+

For $\bar{\alpha}^+ \geq 0$, λ fixed and ϵ small (see Fig. 5.11) \bar{S}_{osc}^+ is a stable node (region B), and as ϵ increases becomes a stable focus when the parameters cross the curve $\Delta^+ = 0$ (region A). For larger ϵ values \bar{S}_{osc}^+ disappear at a pitchfork bifurcation of the origin in the s direction at the curve C_{HB}^+ .

Going back to the original 4D system (5.9), for ϵ small there exists a stable periodic orbit S_{osc}^+ , which collapses at Hopf bifurcation occurring at the curve C_{HB}^+ .

Dynamics of \bar{S}_{osc}^-

For $\bar{\alpha}^+ \geq 0$, λ fixed and ϵ small (see Fig. 5.12), the fixed point \bar{S}_{osc}^- appears as a 1 dimensional unstable saddle (region C), and as ϵ increases becomes a stable node when the parameters cross the curve $Det^- = 0$ (region B). For larger ϵ values the fixed point \bar{S}_{osc}^- becomes a stable focus at

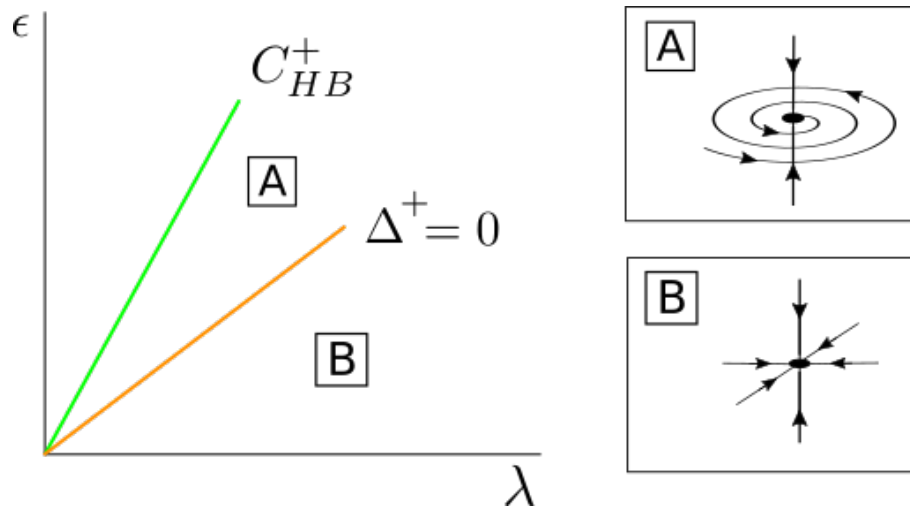


Figure 5.11: Bifurcation diagram for \bar{S}_{osc}^+ in the case $\beta_{\epsilon 0R} = 0$ and $C_{det} > 0$. The fixed point \bar{S}_{osc}^+ has a supercritical pitchfork bifurcation from the origin in the s direction coinciding with the curve C_{HB}^+ .

$\Delta^- = 0$ (region A) which collapses at a pitchfork bifurcation of the origin in the s direction at the curve C_{HB}^- .

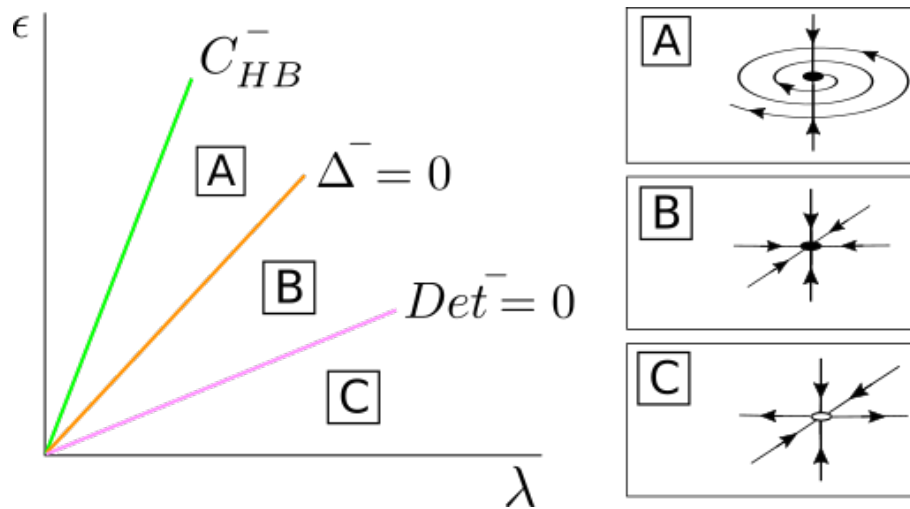


Figure 5.12: Phase space for the \bar{S}_{osc}^- fixed point in the case $\beta_{\epsilon 0R} = 0$ and $C_{det} > 0$. The fixed point \bar{S}_{osc}^- has a supercritical pitchfork bifurcation from the origin in the s direction coinciding with the curve C_{HB}^- , and a bifurcation at the curve $Det^- = 0$.

Going back to the original 4D system (5.9), for ϵ small there exists a unstable periodic orbit \mathcal{S}_{osc}^- whose stability changes at a bifurcation coinciding with the curve $Det^- = 0$. Finally the stable periodic orbit \mathcal{S}_{osc}^- collapses to the origin at a Hopf bifurcation at the curve C_{HB}^- .

Bistability Areas

In the region in the (λ, ϵ) -plane given by

$$Det^-(\lambda, \epsilon) > 0, \quad (5.74)$$

both fixed points $\bar{\mathcal{S}}_{osc}^+$ and $\bar{\mathcal{S}}_{osc}^-$ are stable.

We remark that the same bistability scenarios can be found in the full system (5.9) by changing the fixed points $\bar{\mathcal{S}}_{osc}^\pm$ by the limit cycles \mathcal{S}_{osc}^\pm .

5.4 Application to two coupled Wilson-Cowan oscillators

In this Section, we will consider a 4D system consisting of a pair of Wilson-Cowan oscillators (E-I pair) coupled with strength ϵ :

$$\begin{aligned} \tau \dot{E}_1 &= -E_1 + S(c_1 E_1 - c_2 I_1), \\ \tau \dot{I}_1 &= -I_1 + S(c_3 E_1 - c_4 I_1 + \epsilon(E_2 - b_{sp} I_2)), \\ \tau \dot{E}_2 &= -E_2 + S(c_1 E_2 - c_2 I_2), \\ \tau \dot{I}_2 &= -I_2 + S(c_3 E_2 - c_4 I_2 + \epsilon(E_1 - b_{sp} I_1)). \end{aligned} \quad (5.75)$$

In this case, instead of using the sigmoidal function S defined in (1.2), we redefine it as

$$S(x) = \frac{1}{1 + e^{-\lambda x + \theta}} - \frac{1}{1 + e^\theta}, \quad (5.76)$$

so $S(0) = 0$, which is more convenient. The function S satisfies $S'(0) = \lambda S_1$, where $S_1 = \frac{e^\theta}{(1+e^\theta)^2}$. Therefore, for the uncoupled case ($\epsilon = 0$), each subsystem generically has a steady state $(E, I) = (0, 0)$ which undergoes a Hopf bifurcation at $\lambda_c = \frac{2}{(a-d)S_1}$.

For this study, we will consider the following set of parameters:

$$\bar{\mathcal{P}} = \{c_1 = 7, c_2 = 5.25, c_3 = 5, c_4 = 0.7, \theta = 2, \tau = 1\}, \quad (5.77)$$

whereas λ and ϵ will be the bifurcation parameters. By considering $b_{sp} = -0.03, 0.03, 0.0$ we will study different types of dynamics. For each case we will write system (5.75) in the normal form (5.9) by numerically computing its corresponding coefficients (see Section 5.1.3). Next, by using numerical continuation we will compute bifurcation diagrams for system (5.75), so we can check the theoretical predictions in Section 5.3 and complete the bifurcation diagrams for large values of λ and ϵ , where the normal form approximation breaks down.

	b_{sp}				b_{sp}		
	-0.03	0.03	0		-0.03	0.03	0
α_{01R}	-21.94	-21.94	-21.94	ω	1.073	1.073	1.073
α_{01I}	-20.94	-20.94	-20.94	$\beta_{\epsilon 0R}$	0.0047	-0.0047	0
$\alpha_{\epsilon 0R}$	0	0	0	$\beta_{\epsilon 0I}$	0.252	0.241	0.246
$\alpha_{\epsilon 0I}$	0	0	0	$\beta_{\epsilon 1R}$	-12.91	-13.18	-13.05
$\alpha_{\epsilon 1R}$	0	0	0	$\beta_{\epsilon 1I}$	19.36	16.76	18.06
$\alpha_{\epsilon 1I}$	0	0	0	$\beta_{\epsilon 2R}$	7.16	6.46	6.52
$\alpha_{\epsilon 2R}$	8.4	9.02	8.72	$\beta_{\epsilon 2I}$	-5.56	-5.47	-5.52
$\alpha_{\epsilon 2I}$	6.34	6.8	6.57	$\beta_{\epsilon 3R}$	14.29	13.33	13.81
$\alpha_{\epsilon 3R}$	-24.02	-22.3	-23.2	$\beta_{\epsilon 3I}$	10.02	10.3	10.16
$\alpha_{\epsilon 3I}$	-46.36	-44.92	-45.46				

Table 5.2: Coefficients of the normal form (5.9) for the three considered cases, namely $b_{sp} = -0.03, 0.03$ and 0 . These coefficients have been computed using the procedure described in Section 5.1.3.

5.4.1 Case $b_{sp} < 0$

We consider the case $b_{sp} = -0.03$. The coefficients of the normal form, which were computed using the techniques described in Section 5.1.3, are given in Table 5.2 and satisfy the conditions $\beta_{\epsilon 0R} > 0$, $C_{det} + \beta_{\epsilon 0R} > 0$ and $\beta_{\epsilon 0R} < -C_{det} + \sqrt{C_{det}^2 + \beta_{\epsilon 0I}^2}$. Therefore, this case corresponds to the one considered in Section 5.3.1. Fig. 5.13 shows the bifurcation diagram of system (5.75) for $b_{sp} = -0.03$ obtained numerically. The results match the theoretical predictions obtained in Section 5.3.1. More precisely, for a fixed ϵ value and varying the bifurcation parameter λ we have:

- A stable in-phase (IP) solution corresponding to \mathcal{S}_{osc}^+ will emerge from the Hopf bifurcation at C_{HB}^+ . Moreover when varying the bifurcation parameter, the IP solution will maintain its stability (see Fig. 5.6).
- An unstable anti-phase (AP) solution corresponding to \mathcal{S}_{osc}^- will emerge from the Hopf bifurcation at C_{HB}^- . For a fixed ϵ and varying the bifurcation parameter AP solution gains stability across a Torus bifurcation, but when further increasing the bifurcation parameter it will lose it again across a pitchfork bifurcation (corresponding respectively to the lines $Tr^- = 0$ and $Det^- = 0$ in Fig. 5.7).

5.4.2 Case $b_{sp} > 0$

We consider the case $b_{sp} = 0.03$. The coefficients of the normal form, which were computed using the techniques described in Section 5.1.3, are given in Table 5.2 and satisfy the conditions $\beta_{\epsilon 0R} < 0$ and $C_{det} + \beta_{\epsilon 0R} > 0$. Therefore, this case corresponds to the one considered in Section 5.3.2. Fig. 5.14 shows the bifurcation diagram of system (5.75) for $b_{sp} = 0.03$ obtained numerically. The results match the theoretical predictions in Section 5.3.2. More precisely, for a fixed ϵ value and varying the bifurcation parameter λ we have:

- A stable anti-phase (AP) solution corresponding to \mathcal{S}_{osc}^- will emerge from a Hopf bifurcation at C_{HB}^- whereas an unstable in-phase (IP) solution corresponding to \mathcal{S}_{osc}^+ will emerge from the Hopf bifurcation at C_{HB}^+
- The stability of both solutions is reversed as the bifurcation parameter grows. Moreover, the bifurcations giving rise to these stability changes are of the same type as we predicted: IP solution becomes stable across a torus bifurcation (corresponding to the Hopf bifurcation \mathcal{H} at the $Tr^+ = 0$ line in Fig. 5.9) whereas the AP solution loses stability across a pitchfork bifurcation of limit cycles (corresponding to the $Det^- = 0$ line in Fig. 5.10).

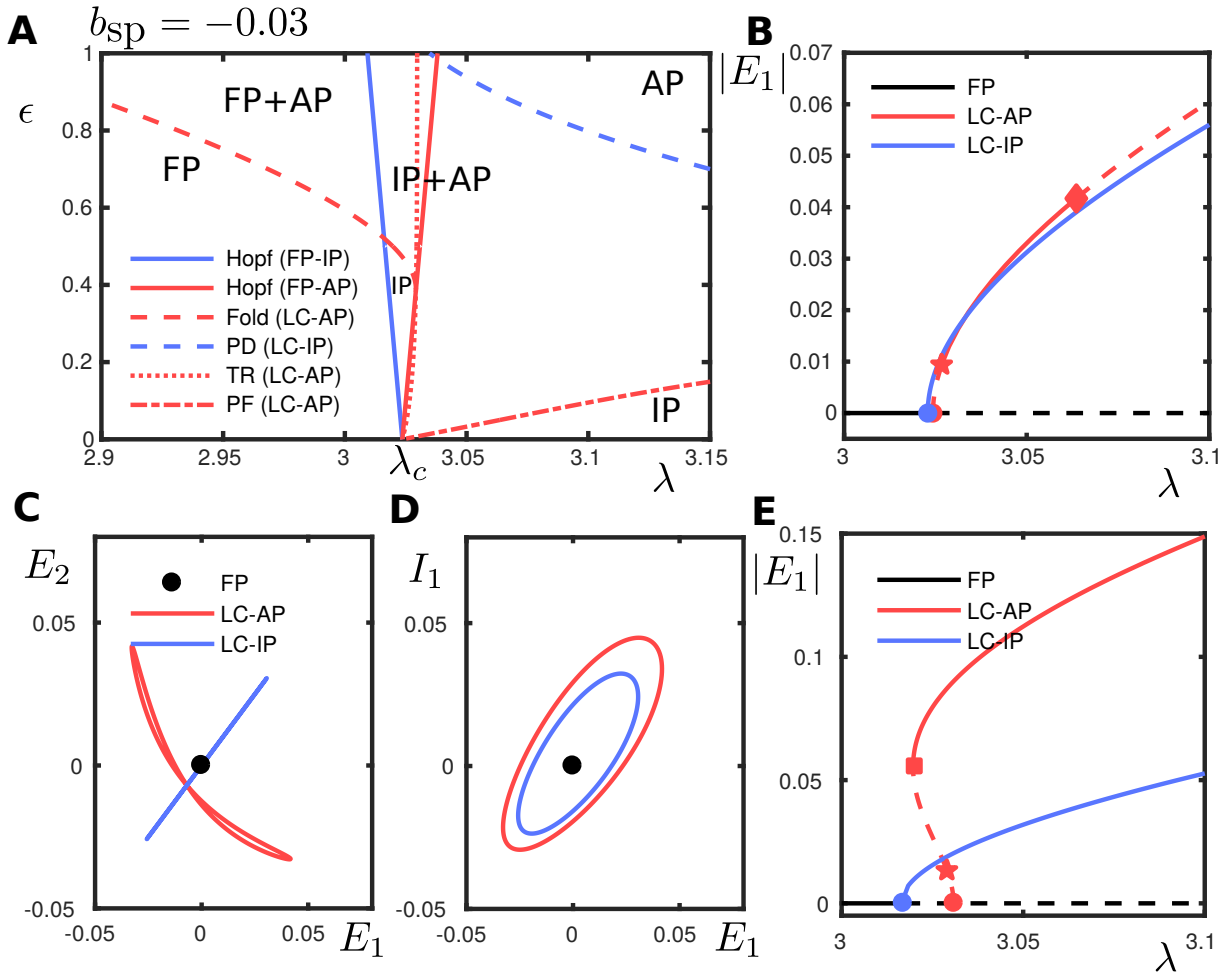


Figure 5.13: Bifurcation diagram with parameters \bar{P} and $b_{sp} = -0.03$ in (5.75) (corresponding to the case $\beta_{\epsilon 0R} > 0$, $C_{det} + \beta_{\epsilon 0R} > 0$ and satisfying $\beta_{\epsilon 0R} < -C_{det} + \sqrt{C_{det}^2 + \beta_{\epsilon 0I}^2}$ as described in Section 5.3.1). **A:** Two-parameter bifurcation diagram in the (λ, ϵ) -plane. The legend indicates bifurcations of a fixed point (FP) or a limit cycle (LC) giving rise to or involving the $\Delta\varphi = 0$ in-phase (IP) or $\Delta\varphi = \pi$ anti-phase (AP) solution branches; PD: period doubling; PF: pitchfork; TR: torus bifurcation. Text labels indicate the solutions that are stable in a given region, e.g. ‘IP+AP’ is a region with coexisting, stable IP and AP solutions. **B:** One-parameter bifurcation diagram at $\epsilon = 0.05$ showing the FP branch, IP branch and AP branch; dashed segments are unstable. The IP and AP branches bifurcate from the FP branch in subsequent Hopf bifurcations (bullet) for λ increasing. The IP branch emerges stable and remains stable. For increasing λ the AP branch is initially unstable, gains stability at a torus bifurcation (star) and loses stability at a pitchfork bifurcation (diamond). **C:** Coexisting solutions at $\lambda \approx 3.05$ and $\epsilon = 0.05$ in the (E_1, E_2) -plane. Motion on the diagonal (blue) corresponds to in-phase oscillations. **D:** As **C** in the (E_1, I_1) -plane for one E-I oscillator. **E:** As **C** at $\epsilon = 0.5$, where a torus bifurcation (star) is on an unstable branch that gains stability at a Fold of limit cycle (square).

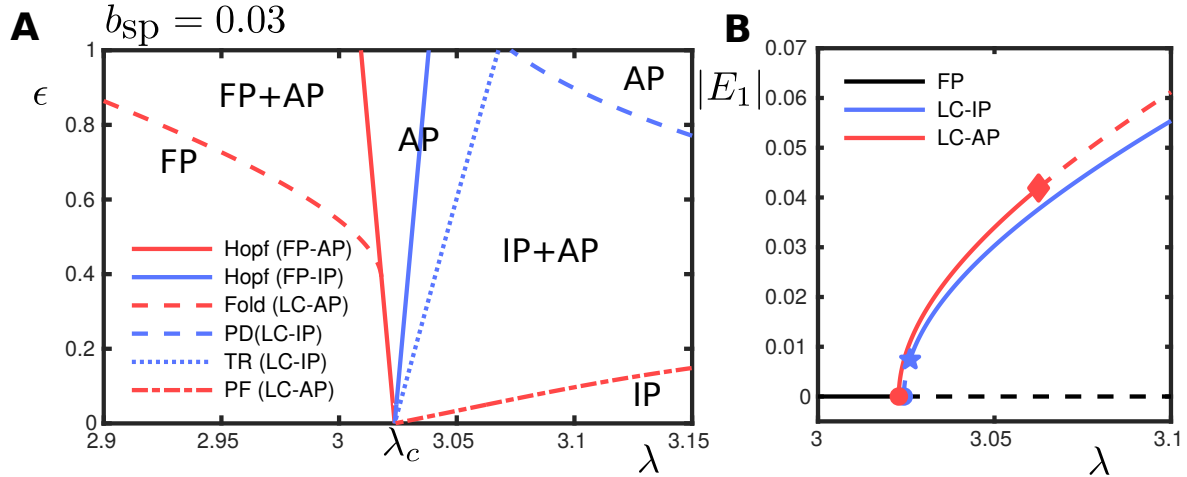


Figure 5.14: Bifurcation diagram with parameters $\bar{\mathcal{P}}$ and $b_{sp} = 0.03$ in (5.75) (corresponding to the case $\beta_{\epsilon 0R} < 0$ and $C_{det} + \beta_{\epsilon 0R} > 0$, as described in 5.3.2). **A**: Two-parameter bifurcation diagram in the (μ, ϵ) -plane. Legends and labelling as in Fig. 5.15; TR: torus bifurcation. **B**: One-parameter bifurcation diagram showing the FP branch, IP branch and AP branch; dashed segments are unstable. The AP and IP branches bifurcate from the FP branch in subsequent Hopf bifurcations (bullet) for μ increasing. The AP branch loses stability in a pitchfork bifurcation (diamond). The IP branch is initially unstable and gains stability at a torus bifurcation (star).

5.4.3 Case $b_{sp} = 0$

We consider the case $b_{sp} = 0.0$. The coefficients of the normal form, which were computed using the techniques described in Section 5.1.3, are given in Table 5.2 and satisfy the conditions $\beta_{\epsilon 0R} = 0$ and $C_{det} > 0$. Therefore, this case corresponds to the “degenerated case” discussed in Section 5.3.3. Fig. 5.15 shows the bifurcation diagram of system (5.75) for $b_{sp} = 0$ obtained numerically. Notice that it matches the theoretical predictions, namely:

- Both Hopf bifurcation curves C_{HB}^{\pm} coincide and give rise to a bistable situation. On one side of the double Hopf curve there exists bistability between the in-phase (IP) solution $\Delta\varphi = 0$ corresponding to \mathcal{S}_{osc}^+ and the anti-phase (AP) $\Delta\varphi = \pi$ solution corresponding to \mathcal{S}_{osc}^- .
- For ϵ fixed and increasing the bifurcation parameter λ , the \mathcal{S}_{osc}^- (AP) solution loses stability across a Pitchfork bifurcation of limit cycles that we found for the 3D system as the line having $Det^- = 0$ (see Fig. 5.12).

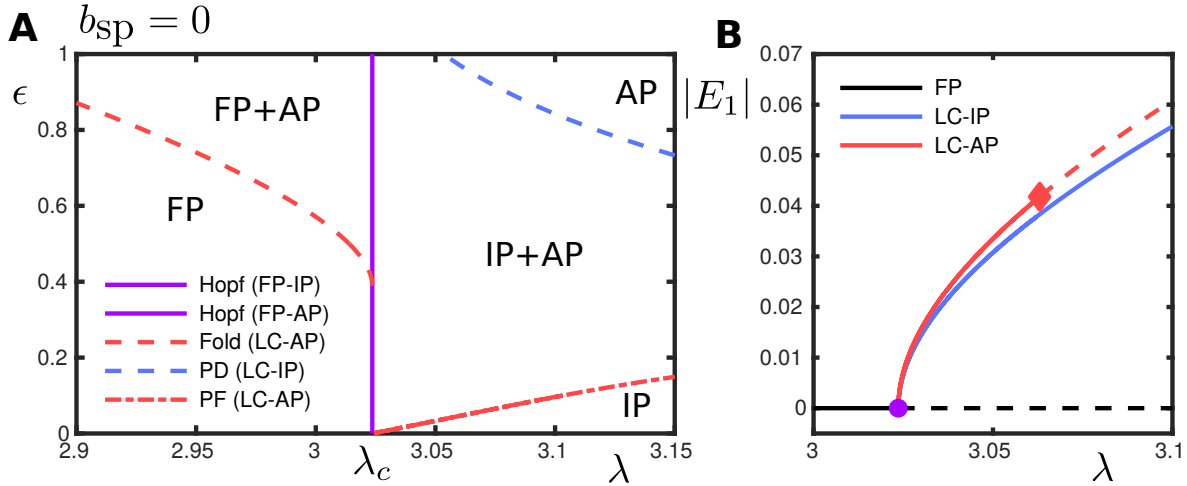


Figure 5.15: Bifurcation diagram with parameters \bar{P} and $b_{sp} = 0$ in (5.75) (corresponding to the case in Section 5.3.3). **A**: Two-parameter bifurcation diagram where curves are the locus of bifurcations in the (μ, ϵ) -plane. The legend indicates bifurcations of a fixed point (FP) or a limit cycle (LC) giving rise to or involving the $\Delta\varphi = 0$ in-phase (IP) or $\Delta\varphi = \pi$ anti-phase (AP) solution branches; PD: period doubling; PF: pitchfork. Text labels indicate the solutions that are stable in a given region, e.g. ‘IP+AP’ is a region with coexisting, stable IP and AP solutions. **B**: One-parameter bifurcation diagram for fixed $\epsilon = 0.05$ showing the fixed point branch, IP branch and AP branch; dashed segments are unstable. The IP and AP branches bifurcate from the FP branch at a degenerate Hopf bifurcation (bullet). The AP branch loses stability in a pitchfork bifurcation (diamond).

5.4.4 Dynamics beyond the weak coupling limit

Our numerical bifurcation analysis has revealed the possibility for richer dynamics, whilst noting a wide range of parameters for which the IP and AP solutions are stable and coexist. Furthermore, a Bautin bifurcation on the AP Hopf branch for $\epsilon_{BT} \approx 0.4$ as seen in Figures 5.13, 5.14 and 5.15 gives rise to a region of parameter space for $\lambda \lesssim \lambda_c$ where a stable AP solution coexists with a stable fixed point. The bifurcation point ϵ_{BT} separates branches of sub- and supercritical Hopf bifurcations in the parameter space. As we can see, for nearby λ, ϵ parameter values, the system has two limit cycles which collide and disappear via a Fold bifurcation of periodic orbits. Although the analysis done in Sections 5.2 and 5.3 is restricted to the weak coupling case, we briefly discuss how the reduced system (5.44) can provide some insight about this bifurcation.

In the weak coupling regime, the denominator in the formula (5.55) for the s_{osc}^\pm solutions, is given by $\alpha_{01R} + \epsilon K_{stb}^\pm$ and is assumed to be negative. Therefore, s_{osc}^\pm solutions appear for $\alpha^\pm = \lambda +$

$\epsilon(\alpha_{\epsilon 0R} \pm \beta_{\epsilon 0R}) > 0$ at a supercritical pitchfork bifurcation of the origin (see Fig. 5.4). Nevertheless, writing the equation for s in (5.54) in the following way

$$\dot{s} = A(\lambda, \epsilon)s + B(\lambda, \epsilon)s^3,$$

we clearly see that at the curve $A(\lambda, \epsilon) = 0$, the origin undergoes a pitchfork bifurcation that is supercritical or subcritical depending on the sign of $B(\lambda, \epsilon)$. Consequently, the point (λ, ϵ) satisfying $A(\lambda, \epsilon) = 0$ and $B(\lambda, \epsilon) = 0$ corresponds to a Bautin bifurcation. Thus, using the expression for A and B (which are known up to first order in ϵ and λ), we can estimate that a Bautin bifurcation occurs for

$$\epsilon_{BT} \approx -\frac{\alpha_{01R}}{K_{stb}^-}, \quad (5.78)$$

assuming that $K_{stb}^- > 0$ and for λ_{BT} such that $(\lambda_{BT}, \epsilon_{BT}) \in C_{HB}^-$. Although an accurate derivation is beyond the scope of this work, this transition from subcritical to supercritical involves the appearance of a curve of saddle-node bifurcations of fixed points for the system (5.44) for nearby values of the parameters. More precisely, if we consider the exact expression of the determinant of the 2x2 block of Jacobian Matrix (5.58) given by:

$$Det(s_{osc}^-) = c_d^d c_\varphi^\varphi - c_d^\varphi c_\varphi^d \quad (5.79)$$

where the constants are given by Eqs. (5.59) with $s = s_{osc}^-$ in (5.55), one can see that it is singular at $B(\lambda, \epsilon) = 0$. Therefore, we consider the curve

$$B(\lambda, \epsilon) Det(s_{osc}^-) = 0,$$

and one can see that the Bautin point $(\lambda_{BT}, \epsilon_{BT})$ belongs to it. Moreover, for $\epsilon > \epsilon_{BT}$ as $B(\lambda, \epsilon) > 0$ this curve corresponds to the saddle-node bifurcations of the solutions s_{osc}^- outside the C_{HB}^- curve.

Using the numerical values given in Table 5.2, $K_{stb}^- > 0$. Thus, we can estimate from the normal form that the Bautin bifurcation occurs for $\epsilon_{BT} \approx 0.42, 0.43, 0.42$ for $b_{sp} = -0.03, 0.03, 0$, respectively, which matches the results obtained numerically (see Figures 5.13, 5.14 and 5.15). Recall that in the original 4D system (5.9) the pitchfork and saddle-node bifurcations correspond to Hopf and fold of limit cycles bifurcations, respectively.

Besides this previous behaviour, we also remark that the IP solution undergoes a period-doubling bifurcation for large ϵ and λ leading to richer dynamical behaviour away from the analytically-investigated uncoupling limit.

5.5 Discussion

The study of identical coupled oscillators near a Hopf bifurcation is applicable to a wide range of systems where near-identical units undergo oscillatory instability. These systems may in general be represented by very different vector fields. Using the normal form theory in [6], we are able to predict universal aspects of the mathematical behaviour for such systems. The analysis performed in this work for two oscillators reveals that, as is often the case in normal forms, although (5.9) involves a big number of parameters, in the weak coupling limit, just a few of them govern and determine the possible bifurcations of the system.

We have seen that, because of the symmetry of the system, there appears naturally two oscillating solutions: an in-phase ($\Delta\varphi = 0$) and anti-phase ($\Delta\varphi = \pi$). As theoretical and computational analysis shows, depending on parameters all the possible combinations between different stabilities of both solutions are possible. Our numerical analysis has shown that away from the coupling limit, richer dynamical behaviour is possible, with secondary bifurcations from the anti-phase branch and regions of coexistence between fixed-point and anti-phase solutions mediated by a fold of cycles.

We finally discuss the possible implications of this work for models of perceptual bistability and neural competition. These models are widely based on the assumption of strong mutual inhibition between populations of neurons that encode different perceptual interpretations of ambiguous stimulus. In general, this assumes that populations associated with different percepts are separated in some featured spaces (e.g. orientation in binocular rivalry) and that these populations enter into competition through mutual inhibition. However, when stimuli are periodic and the two possible perceptual interpretations involve the same features, it is less clear how competition between percepts might arise. In this work we explored how synchrony properties of oscillations entrained at the rate of a rapidly alternating stimulus could be the mechanism by which different perceptual interpretations emerge and coexist as bistable states. Indeed, encoding of perceptual interpretations through oscillations allows for complete synchronisation of the network with all incoming inputs (in-phase) or for partial synchronisation of different parts of a network with separate elements (here in anti-phase). This encoding mechanism does not rely on strong mutual inhibition, widely assumed between the abstracted percept-based neural populations in competition models.

Bibliography

- [1] J. A. Acebrón, L. L. Bonilla, C. J. P. Vicente, F. Ritort, and R. Spigler. The Kuramoto model: A simple paradigm for synchronization phenomena. *Reviews of Modern Physics*, 77:137–185, 2005.
- [2] E. L. Allgower and K. Georg. *Introduction to numerical continuation methods*. SIAM, 2003.
- [3] D. G. Aronson, G. B. Ermentrout, and N. Kopell. Amplitude response of coupled oscillators. *Physica D: Nonlinear Phenomena*, 41(3):403–449, 1990.
- [4] D. K. Arrowsmith and C. M. Place. *An introduction to dynamical systems*. Cambridge University Press, 1990.
- [5] P. Ashwin, S. Coombes, and R. Nicks. Mathematical frameworks for oscillatory network dynamics in neuroscience. *The Journal of Mathematical Neuroscience*, 6(1):2, Jan 2016.
- [6] P. Ashwin and A. Rodrigues. Hopf normal form with sn symmetry and reduction to systems of nonlinearly coupled phase oscillators. *Physica D: Nonlinear Phenomena*, 325:14–24, 2016.
- [7] P. W. Bates, K. Lu, and C. Zeng. Approximately invariant manifolds and global dynamics of spike states. *Inventiones mathematicae*, 174(2):355–433, 2008.
- [8] H. Berger. Über das elektroencephalogramm des menschen. *European Archives of Psychiatry and Clinical Neuroscience*, 87(1):527–570, 1929.
- [9] R. M. Borisyuk and A. B. Kirillov. Bifurcation analysis of a neural network model. *Biological Cybernetics*, 66(4):319–325, 1992.
- [10] G. Buzsáki. *Rhythms of the Brain*. Oxford University Press, 2006.
- [11] X. Cabré, E. Fontich, and R. de la Llave. The parameterization method for invariant manifolds I: manifolds associated to non-resonant subspaces. *Indiana University mathematics journal*, pages 283–328, 2003.

- [12] X. Cabré, E. Fontich, and R. de la Llave. The parameterization method for invariant manifolds II: regularity with respect to parameters. *Indiana University mathematics journal*, pages 329–360, 2003.
- [13] X. Cabré, E. Fontich, and R. De La Llave. The parameterization method for invariant manifolds III: overview and applications. *Journal of Differential Equations*, 218(2):444–515, 2005.
- [14] M. Canadell and A. Haro. Parameterization method for computing quasi-periodic reducible normally hyperbolic invariant tori. In *Advances in Differential Equations and Applications*, pages 85–94. Springer, 2014.
- [15] M. Canadell and À. Haro. A newton-like method for computing normally hyperbolic invariant tori. In *The Parameterization Method for Invariant Manifolds*, pages 187–238. Springer, 2016.
- [16] C. C. Canavier and S. Achuthan. Pulse coupled oscillators and the phase resetting curve. *Mathematical biosciences*, 226(2):77–96, 2010.
- [17] O. Castejón, A. Guillamon, and G. Huguet. Phase-amplitude response functions for transient-state stimuli. *The Journal of Mathematical Neuroscience*, 3(1):13, 2013.
- [18] R. Castelli, J.-P. Lessard, and J. D. Mireles James. Parameterization of invariant manifolds for periodic orbits I: Efficient numerics via the floquet normal form. *SIAM Journal on Applied Dynamical Systems*, 14(1):132–167, 2015.
- [19] F. Devalle, A. Roxin, and E. Montbrió. Firing rate equations require a spike synchrony mechanism to correctly describe fast oscillations in inhibitory networks. *PLoS computational biology*, 13(12):e1005881, 2017.
- [20] J. C. Dunlap, J. J. Loros, and P. J. DeCoursey. *Chronobiology: biological timekeeping*. Sinauer Associates, 2004.
- [21] P. Dyan and L. Abbott. *Theoretical Neuroscience. Computational Modeling of Neural Systems*. Cambridge, Mass.: MIT Press, 2001.
- [22] B. Ermentrout. An adaptive model for synchrony in the firefly pteroptyx malaccaea. *Journal of Mathematical Biology*, 29(6):571–585, 1991.
- [23] B. Ermentrout. Type I membranes, phase resetting curves, and synchrony. *Neural computation*, 8(5):979–1001, 1996.
- [24] B. Ermentrout and D. Terman. *Mathematical foundations of neuroscience*. New York : Springer, 2010.

- [25] G. B. Ermentrout and N. Kopell. Multiple pulse interactions and averaging in systems of coupled neural oscillators. *Journal of Mathematical Biology*, 29(3):195–217, 1991.
- [26] G. B. Ermentrout and D. H. Terman. *Mathematical foundations of neuroscience*, volume 35. Springer Science & Business Media, 2010.
- [27] N. Fenichel. Persistence and smoothness of invariant manifolds for flows. *Indiana Univ. Math. J.*, 21:193–226, 1971/1972.
- [28] N. Fenichel. Asymptotic stability with rate conditions. *Indiana Univ. Math. J.*, 23:1109–1137, 1973/74.
- [29] G. Floquet. Sur les equations differentielles lineaires. *Ann. ENS [2]*, 12(1883):47–88, 1883.
- [30] P. Fries. A mechanism for cognitive dynamics: neuronal communication through neuronal coherence. *Trends in cognitive sciences*, 9(10):474–480, 2005.
- [31] P. Fries, P. R. Roelfsema, A. K. Engel, P. König, and W. Singer. Synchronization of oscillatory responses in visual cortex correlates with perception in interocular rivalry. *Proceedings of the National Academy of Sciences*, 94(23):12699–12704, 1997.
- [32] L. Glass and M. C. Mackey. *From clocks to chaos: the rhythms of life*. Princeton University Press, 1988.
- [33] L. Glass and A. . T. Winfree. Discontinuities in phase-resetting experiments. *American Journal of Physiology-Regulatory, Integrative and Comparative Physiology*, 246(2):R251–R258, 1984.
- [34] M. Golubitsky and I. Stewart. *The symmetry perspective: from equilibrium to chaos in phase space and physical space*, volume 200. Springer Science & Business Media, 2003.
- [35] W. Govaerts and B. Sautois. Computation of the phase response curve: a direct numerical approach. *Neural Computation*, 18(4):817–847, 2006.
- [36] A. Griewank and A. Walther. *Evaluating derivatives: principles and techniques of algorithmic differentiation*, volume 105. Siam, 2008.
- [37] J. Guckenheimer. Isochrons and phaseless sets. *Journal of Mathematical Biology*, 1(3):259–273, 1975.
- [38] J. Guckenheimer and P. Holmes. *Nonlinear oscillations, dynamical systems, and bifurcations of vector fields*, volume 42. Springer Science & Business Media, 2013.
- [39] A. Guillamon and G. Huguet. A computational and geometric approach to phase resetting curves and surfaces. *SIAM Journal on Applied Dynamical Systems*, 8(3):1005–1042, 2009.

- [40] D. Hansel, G. Mato, and C. Meunier. Synchrony in excitatory neural networks. *Neural computation*, 7(2):307–337, 1995.
- [41] A. Haro. Automatic differentiation tools in computational dynamical systems. *Univ. of Barcelona Preprint*, 2008.
- [42] À. Haro, M. Canadell, J.-L. Figueras, A. Luque, and J.-M. Mondelo. *The Parameterization Method for Invariant Manifolds*. Springer, 2016.
- [43] A. Haro and R. de la Llave. Persistence of normally hyperbolic invariant manifolds, Personal communication.
- [44] A. Haro and R. de la Llave. A parameterization method for the computation of invariant tori and their whiskers in quasi-periodic maps: numerical algorithms. *Discrete and Continuous Dynamical Systems Series B*, 6(6):1261, 2006.
- [45] A. Haro and R. de La Llave. A parameterization method for the computation of invariant tori and their whiskers in quasi-periodic maps: explorations and mechanisms for the breakdown of hyperbolicity. *SIAM Journal on Applied Dynamical Systems*, 6(1):142, 2007.
- [46] M. Hirsch, C. Pugh, and M. Shub. *Invariant manifolds*, volume 583 of *Lecture Notes in Math*. Springer-Verlag, Berlin, 1977.
- [47] A. L. Hodgkin and A. F. Huxley. A quantitative description of membrane current and its application to conduction and excitation in nerve. *The Journal of physiology*, 117(4):500–544, 1952.
- [48] F. C. Hoppensteadt and E. M. Izhikevich. *Weakly connected neural networks*, volume 126. Springer Science & Business Media, 2012.
- [49] G. Huguet and R. de la Llave. Computation of limit cycles and their isochrons: fast algorithms and their convergence. *SIAM Journal on Applied Dynamical Systems*, 12(4):1763–1802, 2013.
- [50] G. Huguet, A. Pérez-Cervera, and T. M. Seara. A geometric approach to phase response curves and its numerical computation through the parameterization method. *arXiv preprint arXiv:1809.07318*, 2018.
- [51] E. M. Izhikevich. *Dynamical systems in neuroscience*. MIT press, 2007.
- [52] Z. P. Kilpatrick. Wilson-cowan model. *Encyclopedia of Computational Neuroscience*, pages 3159–3163, 2015.
- [53] Y. Kuramoto. *Chemical oscillations, waves, and turbulence*, volume 19. Springer Science & Business Media, 2012.

- [54] C. Liu, D. R. Weaver, S. H. Strogatz, and S. M. Reppert. Cellular construction of a circadian clock: period determination in the suprachiasmatic nuclei. *Cell*, 91(6):855–860, 1997.
- [55] A. Mauroy and I. Mezić. On the use of fourier averages to compute the global isochrons of (quasi) periodic dynamics. *Chaos: An Interdisciplinary Journal of Nonlinear Science*, 22(3):033112, 2012.
- [56] A. Mauroy and I. Mezić. Global computation of phase-amplitude reduction for limit-cycle dynamics. *arXiv preprint arXiv:1803.07379*, 2018.
- [57] A. Mauroy, I. Mezić, and J. Moehlis. Isostables, isochrons, and koopman spectrum for the action–angle representation of stable fixed point dynamics. *Physica D: Nonlinear Phenomena*, 261:19–30, 2013.
- [58] D. C. Michaels, E. P. Matyas, and J. Jalife. Mechanisms of sinoatrial pacemaker synchronization: a new hypothesis. *Circulation Research*, 61(5):704–714, 1987.
- [59] R. Miller. Cortico-hippocampal interplay: Self-organizing phase-locked loops for indexing memory. *Psychobiology*, 17(2):115–128, 1989.
- [60] E. Montbrió, D. Pazó, and A. Roxin. Macroscopic description for networks of spiking neurons. *Physical Review X*, 5(2):021028, 2015.
- [61] C. Morris and H. Lecar. Voltage oscillations in the barnacle giant muscle fiber. *Biophysical journal*, 35(1):193–213, 1981.
- [62] K. Nipp and D. Stoffer. Attractive invariant manifolds for maps: existence, smoothness and continuous dependence on the map. In *Research report/Seminar für Angewandte Mathematik*, volume 1992. Eidgenössische Technische Hochschule, Seminar für Angewandte Mathematik, 1992.
- [63] K. Nipp and D. Stoffer. Invariant manifolds in discrete and continuous dynamical systems. *EMS tracts in mathematics*, 21, 2013.
- [64] S. A. Oprisan and C. C. Canavier. The influence of limit cycle topology on the phase resetting curve. *Neural computation*, 14(5):1027–1057, 2002.
- [65] H. M. Osinga and J. Moehlis. Continuation-based computation of global isochrons. *SIAM Journal on Applied Dynamical Systems*, 9(4):1201–1228, 2010.
- [66] A. Pérez-Cervera, P. Ashwin, G. Huguet, T. M. Seara, and J. Rankin. The uncoupling limit of identical hopf bifurcations with an application to perceptual bistability. *arXiv preprint arXiv:1901.07283*, 2019.

- [67] A. Pérez-Cervera, G. Huguet, and T. M. Seara. Computation of invariant curves in the analysis of periodically forced neural oscillators. In *Nonlinear Systems, Vol. 2*, pages 63–81. Springer, 2018.
- [68] D. J. Pinto, J. C. Brumberg, D. J. Simons, G. B. Ermentrout, and R. Traub. A quantitative population model of whisker barrels: re-examining the wilson-cowan equations. *Journal of computational neuroscience*, 3(3):247–264, 1996.
- [69] J. Rankin, E. Sussman, and J. Rinzel. Neuromechanistic model of auditory bistability. *PLoS computational biology*, 11(11):e1004555, 2015.
- [70] J. Rinzel and G. B. Ermentrout. *Analysis of neural excitability and oscillations*. Cambridge, MA: MIT Press, 1989.
- [71] J. Rinzel and G. Huguet. Nonlinear dynamics of neuronal excitability, oscillations, and coincidence detection. *Comm. Pure Appl. Math.*, 66(9):1464–1494, 2013.
- [72] J. E. Rubin and D. Terman. High frequency stimulation of the subthalamic nucleus eliminates pathological thalamic rhythmicity in a computational model. *Journal of computational neuroscience*, 16(3):211–235, 2004.
- [73] N. W. Schultheiss, A. A. Prinz, and R. J. Butera. *Phase response curves in neuroscience: theory, experiment, and analysis*. Springer Science & Business Media, 2011.
- [74] T. M. Seara and J. Villanueva. On the numerical computation of diophantine rotation numbers of analytic circle maps. *Physica D: Nonlinear Phenomena*, 217(2):107–120, 2006.
- [75] C. Simó. On the analytical and numerical approximation of invariant manifolds. In *Les Méthodes Modernes de la Mécanique Céleste. Modern methods in celestial mechanics*, volume 1, pages 285–329, 1990.
- [76] R. M. Smeal, G. B. Ermentrout, and J. A. White. Phase-response curves and synchronized neural networks. *Philosophical Transactions of the Royal Society of London B: Biological Sciences*, 365(1551):2407–2422, 2010.
- [77] P. Tiesinga, J.-M. Fellous, and T. J. Sejnowski. Regulation of spike timing in visual cortical circuits. *Nature reviews neuroscience*, 9(2):97, 2008.
- [78] P. Tiesinga and T. J. Sejnowski. Cortical enlightenment: are attentional gamma oscillations driven by ing or ping? *Neuron*, 63(6):727–732, 2009.
- [79] P. H. Tiesinga and T. J. Sejnowski. Mechanisms for phase shifting in cortical networks and their role in communication through coherence. *Frontiers in human neuroscience*, 4:196, 2010.

- [80] J. L. P. Velazquez. Brain research: a perspective from the coupled oscillators field. *Neuro-Quantology*, 4(2), 2007.
- [81] O. Vinogradova, E. Brazhnik, V. Stafekhina, and A. Belousov. Septo-hippocampal system. rhythmic oscillations and information selection. *Neurocomputers and Attention I: Neurobiology, Synchronization and Chaos*, pages 129–148, 1991.
- [82] K. C. Wedgwood, K. K. Lin, R. Thul, and S. Coombes. Phase-amplitude descriptions of neural oscillator models. *The Journal of Mathematical Neuroscience*, 3(1):2, 2013.
- [83] M. A. Whittington, R. Traub, N. Kopell, B. Ermentrout, and E. Buhl. Inhibition-based rhythms: experimental and mathematical observations on network dynamics. *International journal of psychophysiology*, 38(3):315–336, 2000.
- [84] D. Wilson and B. Ermentrout. Greater accuracy and broadened applicability of phase reduction using isostable coordinates. *Journal of mathematical biology*, 76(1-2):37–66, 2018.
- [85] D. Wilson and J. Moehlis. Extending phase reduction to excitable media: theory and applications. *SIAM Review*, 57(2):201–222, 2015.
- [86] D. Wilson and J. Moehlis. Isostable reduction of periodic orbits. *Physical Review E*, 94(5):052213, 2016.
- [87] H. R. Wilson and J. D. Cowan. Excitatory and inhibitory interactions in localized populations of model neurons. *Biophysical journal*, 12(1):1–24, 1972.
- [88] A. Winfree. Patterns of phase compromise in biological cycles. *Journal of Mathematical Biology*, 1(1):73–93, 1974.
- [89] A. T. Winfree. Biological rhythms and the behavior of populations of coupled oscillators. *Journal of theoretical biology*, 16(1):15–42, 1967.